DISCRETE MICROMECHANICS OF RANDOM FIBROUS ARCHITECTURES

ABHILASH ANJALY SUKUMARAN NAIR

(Bachelor of Technology, Mechanical Engineering)
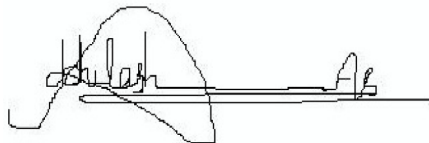
UNIVERSITY OF CALICUT 2005

A THESIS SUBMITTED

FOR THE DEGREE OF DOCTOR OF PHILOSOPHY

DEPARTMENT OF MECHANICAL ENGINEERING

NATIONAL UNIVERSITY OF SINGAPORE

2012

Declaration

I hereby declare that the thesis is my original work and it has been written by me in its entirety.

I have duly acknowledged all the sources of information which have been used in the thesis.

This thesis has also not been submitted for any degree in any university previously.

Abhilash Anjaly Sukumaran Nair

24 December 2012

To my beloved Amma & Achan

Acknowledgements

I gratefully acknowledge the excellent guidance provided by my supervisor Dr. Shailendra Joshi. I deeply appreciate the meticulous care and huge amount of time he spent with me every time I stumbled. I thank him for all the advice on academic and non-academic matters; and above all, for making me realize the importance of going that extra mile.

I also wish to thank Prof. J. N. Reddy for offering me PhD admission and welcoming me to this intellectual world, which has changed my life all over. I would also like to express my gratitude towards my thesis committee members, Prof. Vincent Tan and Dr. Erik Birgersson for their advice and comments on my work.

I was lucky to have interacted with prolific researchers from all around the globe; Prof. Abhijit Mukherjee (Thapar University, India), Dr. Leon Mishnaevsky (RisøNational Laboratory, Denmark), Dr. Prashant Purohit (University of Pennsylvania, USA) and Prof. Narasimhan Ramarathinam (IISc Bangalore, India). Sincere thanks to all of them for the enriching discussions and valuable contributions to my PhD.

It has been a pleasure working with the members of the close-knit Joshi research group; Dr. Jing, Dr. Ramin, Hamid and several short term undergraduate students. Most of the time I spent during the last four years was with them, and

Contents

Summary

Fibrous micro-architectures are subscale motifs ubiquitously found in structures ranging from eukaryotic cells to laminated composites. The mechanics of such microstructures, including their stiffening, strengthening and the failure are enriched by the nonlinearities and stochastic effects arising from the underlying topological randomness coupled with constituent properties. This thesis investigates the mechanics of two types of fibrous architectures with stiffness and length scales that span over several orders: (i) soft, filamentous networks mimicking biopolymers, and (ii) stiff, fiber-reinforced polymers employed in many engineering applications. The primary focus is on the role of microstructural discreteness in the evolution of elasticity and failure of the above-mentioned exemplars. Three major steps involved in this task are: (i) generation and characterization of random microstructures, (ii) study of the mechanical response including damage and (iii) making connections between the characterization parameters defined in step (i) and the response obtained in step (ii).

Discrete micromechanical models encompass the spatial heterogeneities and the finer resolution offers avenues to understand various deformation mechanisms. In-house algorithms are developed for the generation and characterization of random topologies. A discrete network (DN) model is developed for filamentous networks that explicitly models the individual filaments and crosslinks that

connect these filaments together at a discrete level. Statistical parameters that are used to characterize the networks showed correlation with the overall mechanical response. The experimentally observed stochastic crosslink scission of F-actin networks is incorporated through Kinetic Monte Carlo algorithms. DN model predicts the characteristic response of the biopolymeric networks; rate dependent stiffening, identification of peak stiffness and softening followed by failure. The model is further extended over to a wide range of filament stiffness in an attempt to develop a general predictive response model for filamentous networks.

A micromechanical model is developed for the interface damage of fiber reinforced composites under mechanical and environmental stimuli. Moisture attacks the interfaces and the degradation of the interface strength is incorporated into the modeling. The response obtained with this approach is weaker compared to the pristine interface cases. The interplay between the randomness in fiber arrangement and the interface damage is elucidated through its correlation with the measure of fiber clustering.

List of Abbreviations

2D	Two Dimensional
3D	Three Dimensional
ABPs	Actin Binding Proteins
b.c.	Boundary Condition
CNTs	Carbon Nanotubes
DM	Discrete Microstructure
DN Model	Discrete Network Model
F-actin	Filamentous actin
FE	Finite Element
FRC	Fiber Reinforced Composite
G-actin	Globular actin
GUI	Graphical User Interface
KMC	Kinetic Monte Carlo
RC	Random Cluster
RVE	Representative Volume Element
SC	Square Cluster
SEM	Scanning Electron Microscopy
SR	Square Regular
TEM	Transmission Electron Microscopy
WLC	Worm Like Chain

List of Symbols

A_F	Alignment factor
$\bar{v}$	Average velocity, $\mathrm{ms^{-1}}$
l_b	Bending length, nm
κ	Bending rigidity, $\mathrm{Nm^2}$
k_B	Boltzmann constant, $\mathrm{m^2 kgs^{-2} K^{-1}}$
l^*	Characteristic thermal length, nm
C_v	Coefficient of variation
ζ_0	Continuum non-affinity parameter
F_{cr}	Critical breaking force, N
k	Crosslink dissociation rate, $\mathrm{s^{-1}}$
k_0	Crosslink dissociation rate at zero force, $\mathrm{s^{-1}}$
X_F	Crosslink factor
l_0	Crosslink length
$\hat{t}$	Crosslink life time, s
X_M	Crosslink moment, $\mu\mathrm{m}$
r_c	Cut off radius, $\mu\mathrm{m}$
$\dot{\phi}$	Damage evolution rate, $\mathrm{s^{-1}}$
δ	Displacement vector, $\mu\mathrm{m}$
l_c	Distance between crosslinks, $\mu\mathrm{m}$
d	Distance from reference axis, $\mu\mathrm{m}$

E	Elastic modulus, $\mathrm{Nm^{-2}}$	
F_F	Fabric factor	
γ_f	Failure strain	
v_f	Fiber volume fraction	
K_b	Filament bending stiffness, $\mathrm{Nm^{-1}}$	
$\bar{\rho}$	Filament density	
Γ	Filament distribution function	
μ_F	Filament modulus, $\mathrm{Nm^{-2}}$	
θ	Filament orientation angle	
K_s	Filament stretching stiffness, $\mathrm{Nm^{-1}}$	
f_f	Filament volume fraction	
F	Force, N	
ϕ_m	Fraction of chains broken (damage- Epoxy)	
ϕ	Fraction of crosslinks broken (damage- DN model)	
ψ	Fraction of interface debonding	
G	Fracture energy, $\mathrm{Jm^{-2}}$	
K_0	Initial stiffness, $\mathrm{Nm^{-1}}$	
a	Interaction distance, nm	
ϕ_{int}	Interface damage parameter (damage- Micromechanics model)	
L	Length of filaments, $\mu\mathrm{m}$	
ξ	Mean value	
μ_M	Mechanical modulus	
ζ	Mesh size, $\mu\mathrm{m}$	
c	Moisture concentration, $\mathrm{mol^1 m^{-3}}$	
D_m	Moisture diffusivity, $\mathrm{m^2 s^{-1}}$	
$beta$	Moisture expansion coefficient	
λ_{na}	Non-affinity length	

K_n	Normalized stiffness
N	Number of filaments
θ_p	Orientation parameter
l_p	Persistence length, μm
ζ_1	Phenomenological stress sensitivity parameter
v	Poissons ratio
γ	Shear strain
$\dot{\gamma}$	Shear strain rate
τ	Shear stress, Nm^{-2}
W	Size of RVE, μm
Σ	Standard deviation
K	Stiffness, Nm^{-1}
ε	Strain
$\dot{\varepsilon}$	Strain rate, s^{-1}
σ	Stress, Nm^{-2}
λ	Stretch
μ	Stretching rigidity, N
T	Temperature, K
μ_T	Thermal modulus, Nm^{-2}
t	Time, s
t	Traction vector
γ_T	Transition strain
F_{ult}	Ultimate breaking force, N
r	Uniformly distributed random number

List of Tables

List of Figures

xxiii

xxiv

xxvi

Chapter 1

Introduction

1.1 Background

In recent decades, microstructural engineering has received unprecedented focus in the realm of materials engineering encompassing nearly all functional applications imaginable. This is because, microstructural details including, the choice of materials, their topological arrangements, presence of defects and their distribution, play key roles in determining the functional efficiency of the systems they constitute. Examples include, but are not limited to, materials used in mechanical, thermal, electrical, optical and electronic applications [1, 2]. The universe of expectations for such applications is unsatiably expanding, necessitating the design of complex architectures that are manipulated from macroscopic to atomic length scales. In devising strategies for functional architectures (whether micro or macro), the primary aim is to produce robust designs. For example, in structural systems i.e., systems whose primary (or an important) function is to adequately support mechanical stimuli (a focal aspect of this thesis), it is highly desirable to reduce the material volume by using high-strength, tough materials.

However, it is imperative to retain sufficient redundancy in such structures, ideally at multiple scales, that would ensure their *graceful* performance, even in the event of a failure. Such requirements or expectations although ubiquitous in protean systems, often give rise to conflicting design situations that are extremely difficult to meet simultaneously.
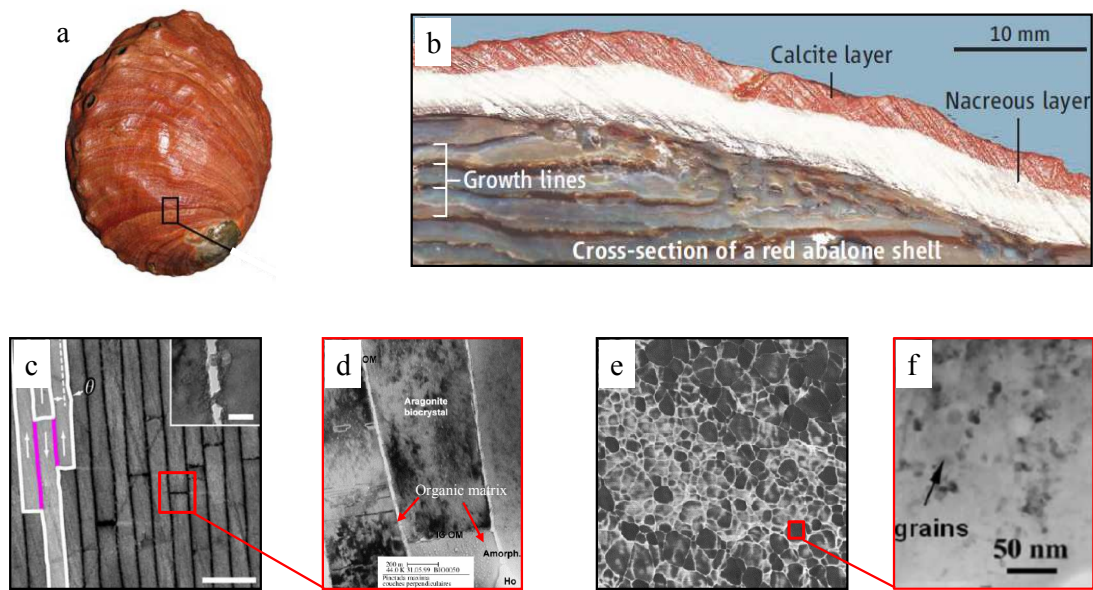
Figure 1.1: The brick mortar structure of the nacre. (a) Red abalone shell. (b) A cross-section showing the layered structure. (c) Scanning electron micrograph of the nacre showing the ceramic tablets which are stacked like bricks with a lining of the biopolymer at the interfaces. (d) Interfaces of the tablets reveling the organic (biopolymer) layer. (e) AFM image showing the top view of the tablets. (f) TEM image showing the nano-grains of the single tablet (adapted from Espinosa *et al.* [3] and Rousseau *et al.* [4]). Wood, bone,chitin etc. have similar hierarchical structures.

A great source of inspiration for designing efficient structures through microstructural engineering comes from examples in the natural world [5, 6]. It is rather

intriguing to note how nature grows efficient structures like nacre with building blocks of organic and inorganic materials, such as biopolymers, ceramics/minerals and crosslinking agents [3, 4]. Figure 1.1 shows various hierarchies in nacre made from the brick mortar arrangements of the aragonite tablets glued together by biopolymeric interfaces. Perhaps, one of the most exciting lessons from myriad natural examples is that nearly all macroscopic structures comprise microstructures with exceptional hierarchies at different length scales [7, 8]. Often, properties at each length scale are obtained by judicious combination and arrangement of single or multiple constituent materials, rendering them as highly engineered composite materials. Numerous examples of such natural composites may be cited, e.g., bone, nacre, chitin in the exoskeleton of arthropods etc. [9, 10], that appropriately combine hard and soft constituents to provide the necessary strength and toughness [1].
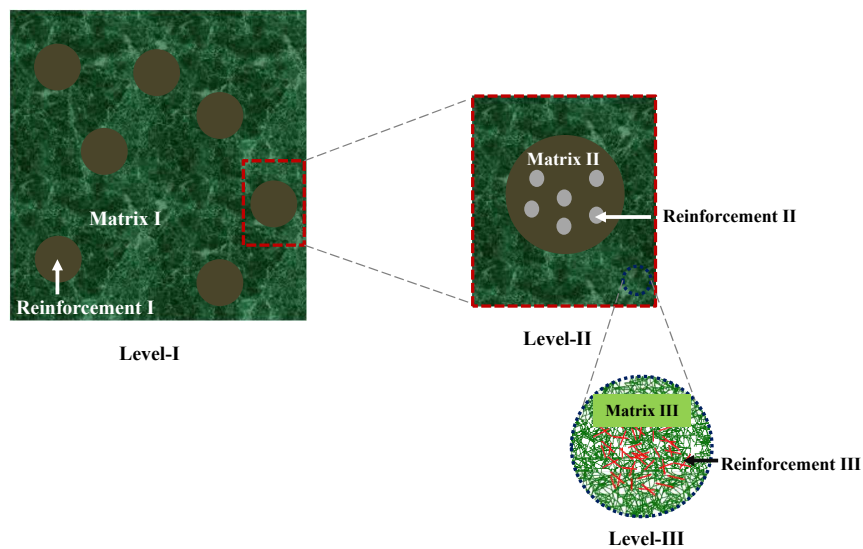
Figure 1.2: Schematic representation of a hierarchical composite showing various levels of reinforcements. Both biological and synthetic materials show such levels of hierarchies.

---

[1]Bone is an excellent example of this. It exhibits a range of stiffness and strength depending upon its function - skull, verterbrae, femur, etc.

Another feature in the aforementioned natural hierarchical microstructures is that often they comprise fibrous topologies at various length scales that may be dispersed, entangled or connected through binders or crosslinking agents. Through intelligent use of these networks at various hierarchical scales, these systems adapt to an optimal strength-to-weight ratio for the designed purpose [11, 12]. Figure 1.2 shows the toy model of a *hierarchical composite*, i.e., a composite within a composite. As an example, at a coarse length scale (e.g., observable by optical or low resolution scanning electron microscopes (SEM)) the level-II structure could be a reinforced polymer comprising strong fibers speckled in a regular or random arrangement. As one examines the structure of this reinforcement at a finer scale (e.g., high resolution SEM), it may itself be a composite (level-I) of fibers coated or embedded with finer, stronger fibers. Indeed, this has been a motivating factor in many examples of artificial composite structures processed using a combination of materials that bear fibrous architectures at subscales. There have been several successful recipes of artificial microstructures mimicking such natural examples that result in strong and ductile materials by exploiting the interplay between the material properties and fibrous topological arrangements [13–17]. In our schematic example (Fig. 1.2), the polymer matrix may also be construed as a dense filamentous network at the finest resolution, which may be reinforced by stiffer nano-scaled fibers (shown as red lines). Examples of such architectures include epoxies reinforced with CNTs for the purpose of matrix strengthening [18, 19].

Bao and Suresh discuss about the deformation of single cells and bio-molecules and appropriately places various materials based on the stiffness and length scales [20]. Figure 1.3 schematically shows the approximate range of values for the stiffness and length scales of different materials (adapted from Bao and Suresh [20]). All these microstructures render anisotropy in the elasticity (and

4

perhaps even inelasticity, including damage). *In vivo* F-actin networks in biological cells possess capability to rearrange dynamically thereby adjusting their stiffness actively. Wood, bone and composites are typically strong in the direction of the reinforcements, but exhibits very low transverse strength [21, 22].
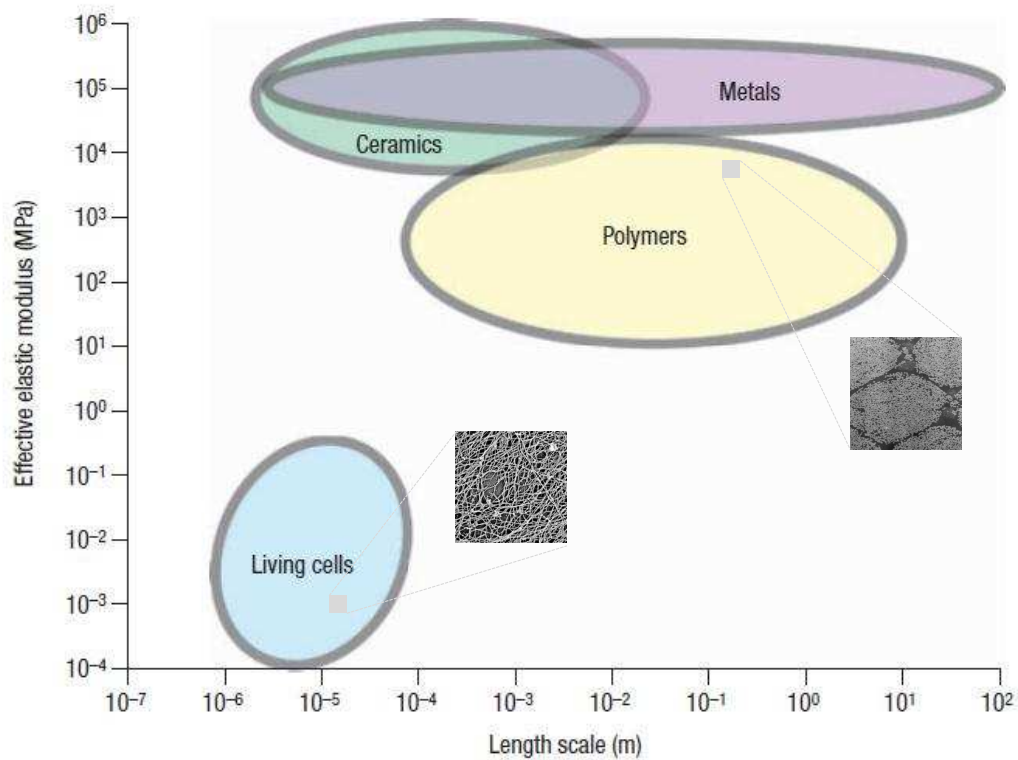
Figure 1.3: Schematic diagram showing the approximate range of the elastic modulus and length scales of various materials having random microstructures. We chose materials at two ends of the spectrum, F-actin networks for biological cells and epoxies reinforced with glass fibers for composites. (main figure adapted from Bao *et al.* [20] and microstructures from refs [23, 24]).

The ubiquity of fibrous architectures in natural and artificial structures across a range of length scales and stiffnesses provides the motivation for this thesis. It focuses on some of the aspects concerning the mechanics of fibrous networks, including their elasticity and failure. Of particular interest is modeling the spatial

and temporal dynamics arising from topological interactions under protean mechanical stimuli. The approach taken is based on the notion that microstructural discreteness plays a vital role in determining the responses of such architectures and must be carefully understood in order to develop robust homogenized approaches.

1.2 Examples of Fibrous Architectures

The examples highlighted in the Introduction brings to the fore a description of what we mean by "Fibrous" microstructures. A working definition that serves the purpose of this thesis is as follows: **fibrous architectures**[2] may indicate microstructures that are made of filaments forming an interconnected network through entanglements and/or physical/chemical crosslinks, or those that embed fibers within a binding matrix, or a combination thereof. The following two sections shed some light on some of the commonly found fibrous architectures that fall within these categories. The examples are not exhaustive, but illustrative.

1.2.1 Random Filamentous Networks

Filamentous networks form structural motifs for a variety of systems ranging from macroscopic to atomistic, for example, felt, paper, cotton, dish scrubbers, biopolymers, elastomers, hydrogels, and so on [25–35]. Figure 1.4 shows some examples of fibrous networks observable at different resolutions. Figure 1.4a shows the network structure of an epoxy, which can be resolved at atomic scales [25]. Figure 1.4b shows a CNT network, which has applications as conducting devices in flexible electronics [29]. Biological cell structures are abundant

---

[2]We use the terms "microstructure", "architecture" and "micro-architecture" interchangeably.

with such architectures, e.g., actin network (Figure 1.4c [26]) whose mechanical rigidity provides important clues about cell functioning. Figure 1.4d shows the network of electrospun polymers used as scaffolds in tissue engineering [28]. Nanowires may be grown on substrates as a network with applications as electrodes in Li-ion batteries (Fig. 1.4e) [30]. Finally, at reasonably coarse resolution the network of cellulose fibers in paper is revealed (Fig. 1.4f) [27].
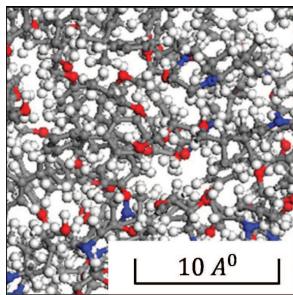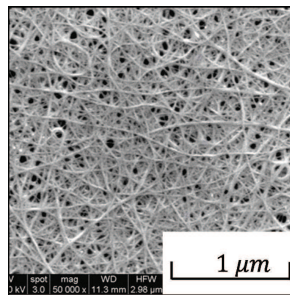
(a) Epoxy network [25]   (b) CNT network [29]   (c) Cytoskeletal network [26]
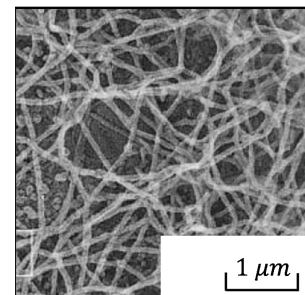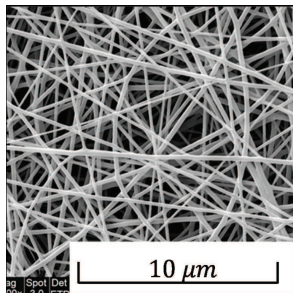
(d) Electrospun scaffolds [28]   (e) Battery electrodes [30]   (f) Paper [27]
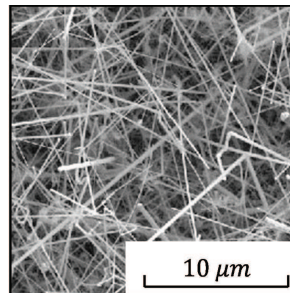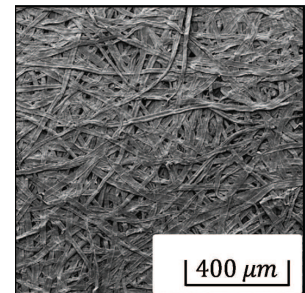
Figure 1.4: Network structures of different materials with the corresponding length scales.

1.2.2   Random Fiber Composites

A fiber reinforced composite (FRC) is another example of fibrous architecture that are widely used in several applications including aerospace, marine, energy and bio-medical systems. In most FRCs, fibers are randomly arranged inside

the matrix. Figure 1.5 shows examples of FRC microstructures. In Fig. 1.5a, a laminated composite with plies having reinforcement in different directions are shown [36], while Fig. 1.5b shows an example of unidirectional FRC with randomly arranged fiber bundles. Although, FRC microstructures are distinct from the examples of network architectures mentioned in the preceding section, some of the issues pertaining to elasto-plasticity and failure bear semblance; for example, the role of topology in response variability is critical to FRC structure performance.
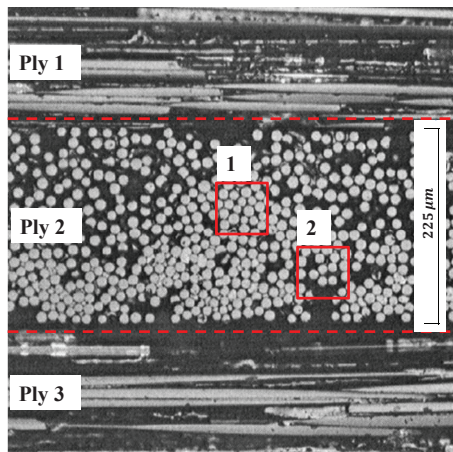
(a) Laminated composite [36]   (b) Random fiber bundles [37]
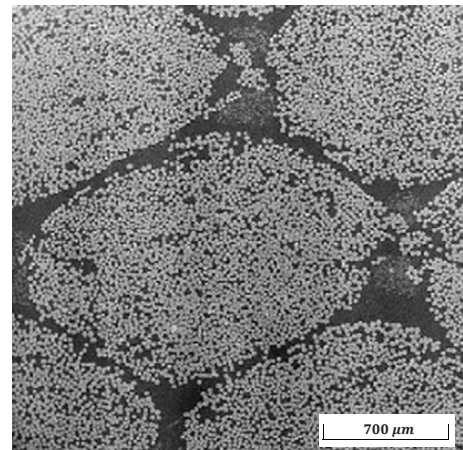
Figure 1.5: Examples of FRC microstructures. (a) A cross-section of plies in a laminated composite with different fiber orientations. Square windows 1 and 2 show typical computational domains used in micromechanical modeling. (b) A cross-sectional view of the unidirectional FRC with randomly arranged fiber bundles.

1.3   Modeling of Random Microstructures

This thesis deals with modeling the mechanical behaviors of the aforementioned exemplars of fibrous architectures. Although, the underlying approach in principle may be applicable to metallic and polymeric systems alike (the details may differ), the main focus here is on the latter. In particular, it encompasses two types of aforementioned random micro-architectures that sit at the extremes of the elastic stiffnesses in polymeric structures (Fig. 1.3), yet are strongly influenced by the topological arrangements of its constituents. Figure 1.6 shows examples of the artificially generated motifs resembling the real architectures that will appear frequently in this thesis. As mentioned earlier, the central idea is to model the discreteness of such fibrous microstructures and this is achieved by resorting to developing Discrete Network (DN) models for fibrous networks (Fig. 1.6a) and discrete microstructures for the FRC microstructures (Fig. 1.6b).
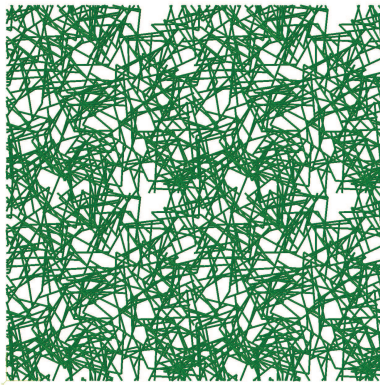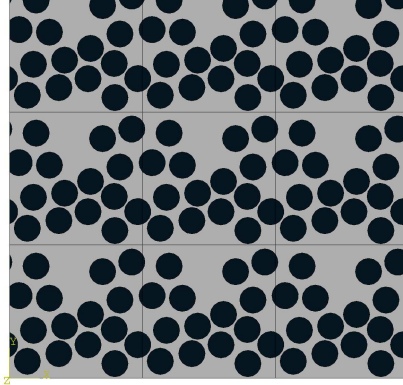
(a) Random filament network   (b) Random fiber composite

Figure 1.6: Examplars of random microstructures considered in this work. (a) Microstructure of a discrete filament network. (b) Cross-section of a unidirectionally fiber reinforced composite.

The elastic, plastic and failure properties of these and similar microstructures observed at the macro-scale are intimately linked to the arrangements of their

building blocks at the sub-scale [38]. For example, if a filamentous microstructure exhibits isotropic elasticity it could signal uniformity in the spatial distribution of filaments, while an anisotropic response of such an architecture could be related to a biased distribution. Likewise, it is common to encounter fiber clustering in FRCs leaving regions that are matrix-rich and matrix-deficient (e.g., dark regions in Fig. 1.5b). In dealing with these aspects, this thesis provides a detailed account of the digital generation of such microstructures, their topological characterization, seamless integration of these topologies into existing finite element code, topology-response correlation, stochastic nature of failure mechanics and the effects of topological variability on the mechanical behaviors.

1.3.1   Meso-scale Modeling

As in metals, atomistic models for polymeric systems provide a strong basis for unraveling the unknown physics of the deformation process; however, these can be computationally prohibitive at microstructural size scales beyond few hundred nanometers and therefore, are limited to interrogating very small volumes [39]. Also, the highest resolution on the time-scale set by the atomic vibrations results in prescription of high deformation rates that may not be realistic. At the other extreme, homogenized continuum models provide a powerful way to describe the macroscopic mechanics, but have to rely on phenomenological constitutive descriptions. While good constitutive models are available for many polymers, they may not capture specific features that are mediated by topological aspects. An important intermediate approach, sometimes referred to as the *meso-scale* may be introduced by choosing a spatial resolution such that it smears out some of the finer details in atomistic models, but retains other important discrete entities not modeled in homogenized continua [40–42]. This is much

like an approach adopted in experimental characterization of materials, where one chooses techniques ranging from high resolution transmission electron microscopy to optical microscopy depending on the queries one needs to find answers to. Meso-scale models form a bridge between the atomistic and continuum models [39, 42–45] providing pathways for multi-scale modeling where specific information is extracted at the finer scale and incorporated into the subsequent coarser scales [42, 46, 47].

In polymeric systems, there are a large number of multi-scale modeling approaches and we cite some of these for the sake of completeness. Gates and coworkers (e.g., [48]) developed an equivalent continuum modeling where the energy equivalence of the molecular structures and their macro-scale equivalent is used to transfer information from lower scales to higher length scales for CNTs and its composites. Monte Carlo and Bond-Fluctuation methods have been developed for flexible chain polymers to map atomistic scales on to coarse-grained models [49, 50]. Barocas and coworkers [51, 52] modeled the mechanics of collagenous gels occurring at length scales smaller than the functional length scales (microns) using volume averaging theories. Breuls *et al.* [53] developed a multi-level finite element (FE) approach for modeling tissue constructs in which detailed nonlinear FE analysis of the microstructure at the integration points were homogenized to obtain the response of large-scale skeletal muscle tissues. A similar multilevel FE approach was used by Smit *et al.* [54] to predict the response of heterogeneous polymeric materials. They studied the influence of microstructural properties on the macroscopic mechanical behavior polystyrene/polycarbonate containing voids/rubbery particles, subjected to unidirectional extension.

1.4 Modeling of Biopolymeric Networks
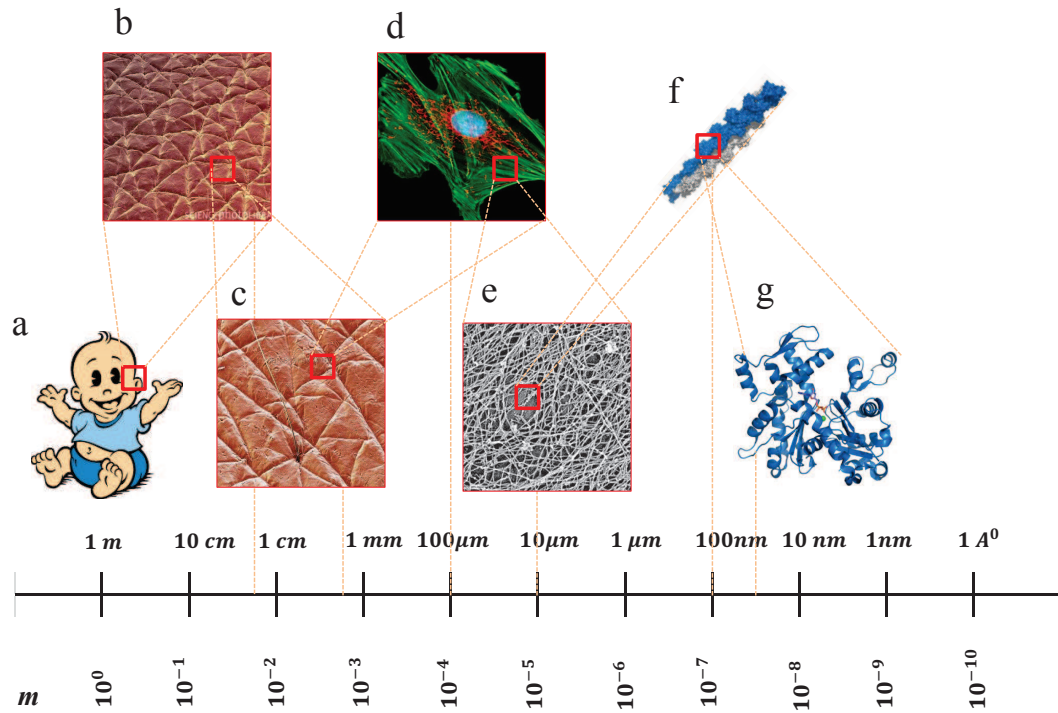
Figure 1.7: Various length scales in biomechanics dealing with human tissues (figures adapted from refs [26, 55–58]).

Figure 1.7 shows typical hierarchical architecture of human tissues [26, 55–58]. Eukaryotic cells (Fig. 1.7d) comprise gel-like cytoplasm, which is bounded by the cell membrane [59, 60]. The cytoplasm holds most of the cell's internal constituents e.g., organelles and a part of it that is devoid of the organelles is called the cytosol. Cytosol houses a network of filaments that provides the structural rigidity to cells. These networks together form the cytoskeleton and hosts three main types of filaments - Actin, Intermediate filaments and Microtubules. All

these filaments are in turn made up of sub-structures made up of protein sub-units called amino acids. The building block of actin is a $42000\ Da$[3] protein called G-actin. Long chains of G-actin are termed as F-actin and it forms double helix of diameter ≈ 7 nm called as *micro filaments* [55]. Networks of F-actin filaments pinned together with crosslinkers (known as Actin Binding Proteins or ABPs for short) in biological cells are an important class of fibrous architectures that help determine the shape of the cell and offer resistance to mechanical stimuli [12, 61–63]. F-actin constitutes $\approx 1\%$ mass of the human body and plays an important role in various cellular functions such as mechanotransduction, mitosis and cell-migration [12, 64–67]. From a mechanics perspective, such fibrous biopolymeric networks are exciting micro-architectures that provide avenues to devise efficient functional solutions for a variety of engineering and biological applications [68].

1.4.1 Mechanics of F-actin Networks

The mechanical behavior of biopolymeric networks ensues from the rich dynamics that arises out of their properties and topological arrangements of their constituents. Under mechanical stimuli, they exhibit a nonlinear stress-strain behavior that is attributed to entropic elasticity and/or bending-stretching transition of the semiflexible filaments that is modulated by the crosslink (ABP) behavior [69]. For example, the network response depends on whether the crosslinking protein is rigid or compliant. Various researchers have modeled the mechanics of F-actin networks through different approaches such as mean-field theory, effective medium theory and discrete network (DN) models [70–73]. In a series of systematic experimental and modeling works, MacKintosh and coworkers [74–77]

---

[3]Dalton (Da) is the unit of atomic mass.

elucidated some of the complex physical mechanisms that govern the mechanical behaviors of F-actin networks. In a pioneering set of experiments on rigidly crosslinked F-actin networks, Gardel *et al.* [33] concluded that the network elasticity has its origins in the filament entropic behavior. Through DN simulations, Head *et al.* [77] constructed a map showing different regimes of the network elastic response. They also developed scaling laws for the initial shear modulus and bending rigidity as a function of stretching modulus of the filament and mean distance between crosslinks. Van der Giessen and coworkers [78, 79] used the DN approach to model the strain stiffening response of networks and attributed it to the non-affine deformation kinematics arising from bending and stretching of individual filaments rather than the entropic elasticity of the filament themselves. The same group adopted an affine network model [80], but modeled the thermal undulations to show that a similar response can be obtained without invoking non-affine kinematics. They also noted the apparent discrepancy that arises in the calculation of the flexural rigidity based on persistence length assumption and physical dimensions of F-actin filament. In the effective medium approach developed by Broedersz *et al.* [81], crosslinks were endowed with nonlinear stiffness instead of assuming highly rigid and a similar nonlinear network stiffening was observed, but attributed to the crosslink response rather than non-affine deformation. Recently, Chen *et al.* [82] explored the effect of molecular motors in the strain stiffening using a finite element based DN model with compliant and rigid crosslinks. They showed that rigid crosslinks resulted in a negligible hardening response compared to the compliant ones as observed in experiments [70, 83].

Irrespective of the type of crosslinking protein, biopolymeric networks ubiquitously exhibit the following salient characteristics - an initial soft response followed by a rate-dependent nonlinear stiffening that culminates into a precipitous

drop in the overall stiffness beyond a critical strain [72, 84–86].
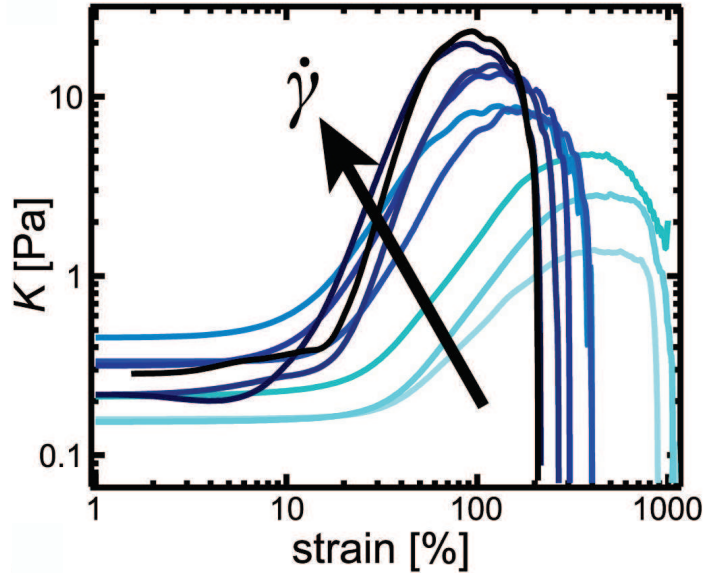
Figure 1.8: Rate sensitivty of F-actin networks cross linked by ABP filamin (adapted from Schmoller *et al.* [72]).

Figure 1.8 shows such a response for F-actin network crosslinked by ABP filamin. Drop in stiffness is mostly irreversible, although in some cases highly reversible softening has been observed, especially those with high F-actin concentration [87]. It is natural to imagine that the underlying mechanisms for the reversible and irreversible softening characteristics would be distinct. Mechanistic arguments based on DN models posit the role of filament buckling [87] in the reversible softening scenarios as has recently also been shown by Su and Purohit [88]. Microscopically, the loss of overall mechanical stability of actin networks should result from the dominance of a softening mechanism over stiffening induced by the elasticity of the network constituents. This competition would naturally lead to the identification of the peak stress and characteristic rupture strain. Further, these network characteristics are expected to be modulated by

15

the mechanical properties of the individual network constituents, network density, topology, and applied deformation rate [70–72]. Unfortunately, most of the aforementioned works, with the exception of Broedersz *et al.* [71] do not model or discuss the irreversible softening mechanics. Even their work only alludes to it by incorporating an additional irreversible strain in a continuum sense, but do not resort to any physically motivated explanation for the same. Experiments indicate that crosslinks dissociate under force [84], which is a likely softening mechanism in networks. DiDonna and Levine [89] proposed a mean-field model enriched with unfolding (saw-tooth) behavior of crosslinkers to model the strain softening response of F-actin networks. In their work, the differential (tangent) modulus exhibits a linear variation with deformation unlike most of the experimental results that indicate highly nonlinear response. They ignored the bending energy of the filament and crosslinks were assumed to possess infinite number of unfolding domains leading to a response that may have repercussions on the non-affine network behavior. Notwithstanding this discrepancy, their model predicts that the degree of softening depends on the softness of the cross-linker.

1.4.2 Discrete Network Modeling

Experimental techniques have evolved to a level where forces in the range of few pico newtons can be measured accurately. Techniques including laser tweezers, atomic force microscopy etc. have enabled researchers to characterize the mechanical properties of F-actin filaments and various crosslinking proteins. Nearly 150 types of ABPs have been identified with each of them exhibiting different characteristics, which may also affect the type of networks formed [90]. These developments have provided sufficient background to develop mathematical models that can capture the response of individual filaments and crosslinks,

and also their collective behaviors as networks. Like some of the literature cited in the previous section, we adopt the DN modeling approach to investigate the response of fibrous networks. In this approach individual filaments and the interaction among filaments are accounted explicitly. Although it is computationally expensive compared to the homogenized continuum models, it provides enriched details of the evolving kinematics that are governed by the local kinetic processes and inter-filament interactions.

One of the aspects that is addressed in this thesis is the failure mechanics of fibrous architectures mimicking semi-flexible F-actin networks. We develop a finite element based DN approach incorporating topological randomness and stochastic crosslink scission kinetics. The DN approach is rendered particularly useful, because failure is governed by local characteristics of a microstructure rather than the overall features. The stochastic approach to modeling the crosslink dissociation process coupled with the topological variations of networks (for the same nominal parameters, e.g., filament density) introduce statistical effects in their mechanical behavior.

The following sections discuss the motivation behind understanding the mechanics of network structures, including the failure.

1.4.3 Biomechanics

Understanding the response of a cell is within the broad scope of biomechanics and it finds novel applications in medicine. Biomechanics aims at bridging the gap between medical and engineering fields and it exploits the overlap between both areas to enable the medical practitioners obtain novel insight from the understanding the physics of the biological response. Few applications of biomechanics in these areas are given below.

Diagnostics of Diseases

The disease-structure-property correlation of the pathogenic basis of certain diseases has been recently unraveled [91]. It has been shown that the mechanical properties of cells change depending upon the pathological conditions that prevail in them. For example, malaria affected red blood cells may stiffen or soften (depending upon the malaria type) by orders of magnitude, while malignant cancer cells exhibit a significantly compliant response compared with the healthy and benign cancer cells [64, 92]. The interaction of the parasitic protein with the spectrin network during the ring stage of infection leads to the stiffening of malaria infected red blood cells [91]. The increased compliance and motility of cancer cells in humans is attributed to the mutation of the filamin gene [12]. This nexus between the mechanics and pathology could be exploited in disease diagnosis along with the conventional diagnostic techniques.

Functional Tissue Engineering

Functional tissue engineering requires extensive understanding of the *in vivo* response of the various tissues [93]. *In vivo* experimental characterization of tissues is rather difficult and one of the solutions to this problem is the modeling of complex loading conditions experienced by the tissues with the knowledge gained from the *in vitro* characterization. Current advances in stem cell research are supported by the learning experience from mechanobiology, both in terms of the cell morphological/structural changes and the substrate/scaffold response. It has been shown that the stiffness of the substrate affects the growth of mesenchymal stem cells in that adapt to the stiffness of their substrate by differentiating toward lineages that reflect the substrate stiffness [94]. For example, on soft substrates mimicking the stiffness of the brain, stem cells tend to evolve into a

18

neuronal structure that are highly elongated, while on much stiffer substrates (e.g., bone-like stiffness) the same cells may grow more isotropically. Understanding the deformation and force transmitting mechanisms of the substrates and scaffolds used in the culture are precursors to such studies. It calls for further understanding of the structural changes and the associated changes in the response of cells so that the efficacy of the methods utilizing structure-property correlation can be improved and mechanobiology will emerge as a mainstream technique along with the conventional ones.

Biomimetics

Biomimetics aims at nature-inspired design of engineering materials in order to obtain high performance ultra-light hierarchical materials [38]. Engineering these new material systems require deep understanding of the mechanisms by which the weakly bonded natural soft materials emerge with intriguingly high strength, toughening and crack blunting [17]. Incorporating hierarchical designs could push the limit of current composite technologies to newer levels. Practical applications of bio-inspired designs require development of physically-based theoretical models that encompass information from various levels of hierarchies. Learning and adapting nature's design is truly a multidisciplinary research area which requires the contribution from all areas of science and technology. The success of above-mentioned applications rely on the accuracy with which the mechanical response of bio-materials can be quantified, which demands developing constitutive theories that cater for complex features such as uncertainty.

In précis, there is a strong motivation to develop sophisticated theoretical and computational modeling approaches that can embed a variety of complex details within them through systematic connections at the sub-scale.

1.5 Meso-scale Modeling of Fiber Composites
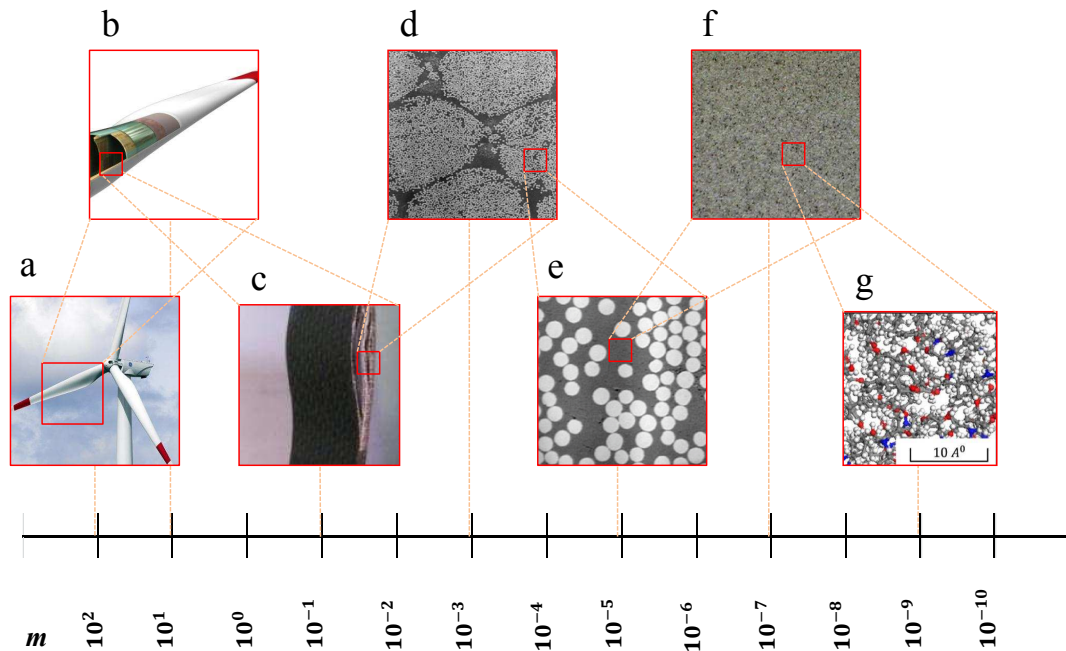
Figure 1.9: Various length scales in modeling the composite used in wind turbines. When the structure changes from the wind turbine to epoxy molecular structure, length scales changes from meters to A^0 (figures adapted from refs [25, 37, 95–98]).

As noted in Section 1.3 and in Fig. 1.3, fiber reinforced polymers (FRPs) sit at the higher end of the stiffness spectrum in the family of polymers. Akin to the various methods in modeling fibrous networks, FRP modeling can also be performed at over a range of spatial resolutions. Figure 1.9 illustrates hierarchical structures that may be resolved in typical FRCs at different length scale [25, 37, 95–98]. Starting with a macroscale structure (Fig. 1.9a and b) the mechanics of laminates (Fig. 1.9c) has been well established. Individual plies within these laminates may exhibit randomly arranged fibers (Fig. 1.9d), which provides a meso-scale resolution where individual fibers and their arrangements can be retained (Fig. 1.9e)

20

and can naturally lead to understanding the role of composite topology under protean loading conditions. In this work, we developed a micromechanics model at this level. Fig. 1.9f zooms into the matrix part which is usually epoxies and Fig. 1.9g reveals the molecular length scale of epoxy which appears to be discrete network of random filament arrangements. Hereafter we focus on modeling the composite at the level of microstructure shown in Fig. 1.9e. Specifically, at the interface damage in epoxy based polymers reinforced with long glass fibers.
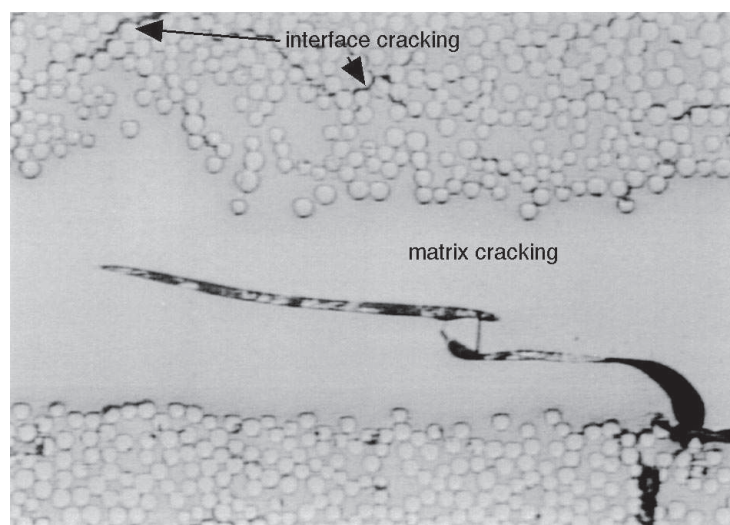
Figure 1.10: Matrix cracking and interface damage in fiber reinforced composites (adapted from [99]).

Composites are prone to damage that could initiate within the matrix, in fibers or at the fiber-matrix interfaces (Fig. 1.10). Damage could be caused by the mechanical load and/or environmental effects during processing and functional life. While microstructural topology generally plays a role in ascribing the severity of damage, it takes prominence in situations where such microstructures experience ambient conditions that set up transients due to diffusion of temperature, moisture etc. through the constituents. For example, dental composites used in root canal implants are continually exposed to moist environments with varying

chemical compositions (acidic/alkaline) [100].

Various meso-scale modeling approaches have been developed to predict the mechanical response of pristine FRCs (no damage) and those that account for damage. Unit cell modeling has been a method of choice for analytical as well as numerical modeling of FRC microstructures. However, these methods work well if the underlying assumption of regularly arranged fibers reasonably describes the real microstructure topologies. In his book [101], Mishnaevsky discusses in great detail the various meso-scale modeling approaches for FRCs and provides some guidelines toward modeling realistic architectures in 2D and 3D. A short report on continuum mechanics by Böhm also discusses the basic guidelines for modeling [102].

A quick survey of the literature on meso-scale modeling of FRCs incorporating damage indicates a large body of work that considers composite degradation under mechanical loads [103–106]. While microstructural topology plays a role in the evolution of damage of FRCs under (quasi-)static mechanical loads comparison and this has been well-addressed through a variety of modeling strategies [101, 102, 107], the situation is much more interesting if damage accrues in random FRC architectures under diffusive processes. With this in mind, the present work discusses the damage evolution and its impact on the mechanical response as a function of FRC microstructural topologies. The idea is to probe an aspect of topologically mediated degradation where microstructural constituents play a vital role.

1.6   Thesis Contributions

The key focus of this thesis is to investigate the mechanics of random microstructures with an emphasize on damage. Two types of random microstructures; discrete filament networks and fiber reinforced composites are considered. The key aspects accomplished in this work are:

- A MATLAB$^{\circledR}$ based FE preprocessing tool kit **NetGen** for the generation of the filamentous microstructures. The capability of the tool kit includes:

  - Generation of 2D random network structures.

  - Topological characterization based on statistical parameters.

  - FE pre-processing including meshing and automated generation of input and sub-routine files for ABAQUS$^{\circledR}$.

- A DN model for F-actin networks. The salient features are:

  - 2D network of filaments and crosslinks.

  - Accounted the variations in topology using fully random network structures.

  - Implemented the failure of crosslinks using KMC algorithm.

  - Developed empirical equations for the damage evolution (cross link scission) that can be used in continuum models.

  - Validated the simulation results with the existing experimental results.

- A non-affine continuum model for filamentous materials:

  - Incorporated the underlying microstructural details using probability distribution functions.

- Tracking of the filament orientation evolution with deformation.

- Non-affine formulation based on the theory of amorphous solids.

- Incorporated the damage evolution equations from the DN model calculations.

- Qualitative modeling of the rate-sensitive mechanical response.

• Parametric study of the mechanical response of filamentous networks with an objective of creating a response map that can be used for different materials having similar microstructures:

- A comprehensive parametric study of networks with filament property ranging from F-actin networks to three orders of magnitude higher.

- Developed contour maps of the hardening response, non-affine deformation and damage.

- Explored the role of the filament stiffness in damage evolution.

• A micromechanics model for the moisture induced degradation of FRC microstructures:

- Considered different microstructures like regular, random and clustered fiber arrangement.

- The topology characterization using statistical parameters.

- Linked the characterization parameters to the interface damage.

- Incorporated the degradation of interfaces with moisture using a degrading traction separation rule .

1.7 Thesis Organization

Chapter 2 discusses in detail the numerical generation of random filamentous networks using algorithms implemented in MATLAB$^{\textregistered}$. Characterization of the random networks based on the topological parameters is the topic of discussion in Chapter 3. It discusses the correlation of the mechanical response with the statistical descriptors of networks. In Chapter 4, the applicability of the D-N approach is shown using a model system of F-actin networks. Stochastic DN simulations capture the qualitative and quantitative rate sensitive response of F-actin networks. A non-affine continuum model which qualitatively captures the experimentally observed rate sensitive response of F-actin networks is discussed towards the end. We expand this work further to account for the effect of filament and crosslink properties in Chapter 5. Specifically, a map is developed which shows the characteristic response of the network with the variation of filament stretching and bending stiffness. The variation in the damage characteristics for a range of filament/crosslink properties is also shown. Micromechanics of fiber reinforced polymeric composite is the topic of discussion in Chapter 6. The first part of the chapter discusses the characterization of the random fiber arrangement and the later parts explain the interface damage and its correlation with the topological factors.

Appendix A discusses the setup for the implementation of single crosslink simulation, details of the time increment independent crosslink scission criterion, role of stochasticity etc. A preliminary probabilistic model developed for the moisture induced degradation due to chain scission in epoxies is briefly discussed in Appendix B. Appendix C lists the publications and conference presentations by the author.

Chapter 2

Discrete Network Approach and Computational Model Development

2.1 Introduction

This chapter focuses on the computational aspects of the generation and characterization of network topologies for modeling filamentous microstructures. It has been shown by experiments that materials like F-actin networks, polymers, paper, fluff etc. have filamentous microstructure and are similar in several aspects vis-á-vis topological randomness, deformation mechanisms, damage etc. We develop a generic model that captures the response of these materials. The model explicitly accounts for the filamentous microstructure and is termed as *discrete network models* (DN models). The capability of the model is demonstrated using a material for which extensive experimental data is available at both filament and network levels. A literature review of the network models developed thus far for materials mentioned above is presented in the first part of this chapter along

26
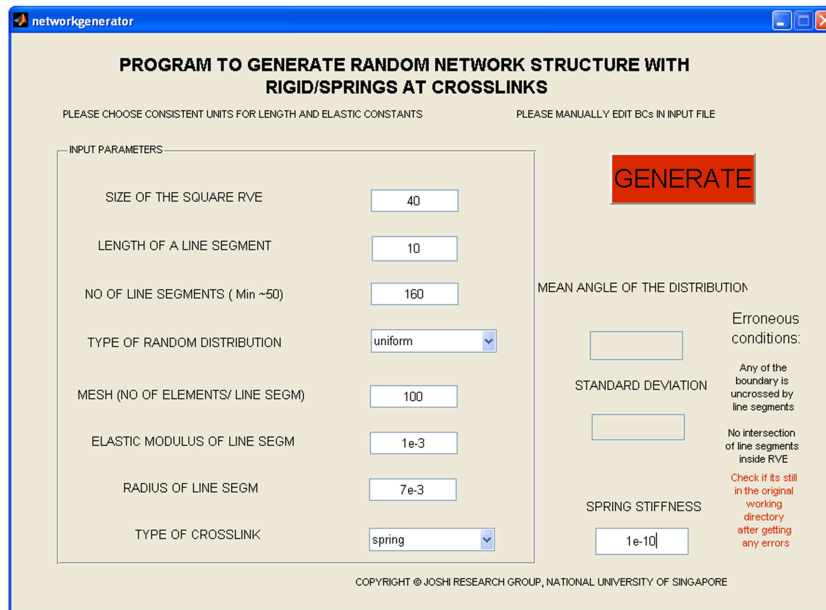
Figure 2.1: GUI of the network generation toolkit, **NetGen** showing the input panel.

with a table summarizing key features. Subsequent part gives a detailed description of the algorithms used for the topology generation of filamentous networks with desired parameters that can approximate the microstructure of any of these materials. A brief discussion about the statistical parameters used to characterize the networks is discussed towards the end. Various algorithms used for network generation and characterization is organized into different modules and is integrated into a graphical user interface (GUI) frame work using MATLAB$^{®}$. The GUI based toolkit (hereafter called **NetGen**) generates the networks with user supplied input, characterize it using statistical parameters and provides the FE models as the output which can be analyzed with the commercial FE package ABAQUS$^{®}$. Fig. 2.1 shows the GUI of **NetGen**.

2.2 DN Modeling of Fibrous Networks: A Review

Discrete network models help to understand the material response from a microstructural viewpoint. The advantage of such models is that the discreteness of the kinematic processes and resulting kinetics of deformation can be tracked in addition to modeling the macroscopic response. As the macroscopic response has underpinnings to local effects observed in the microscopic scale, understanding these mechanisms and processes enables us to better explain the macroscopic response. Furthermore, it gives avenues for understanding mechanisms involved in the damage evolution and helps to design such materials to overcome failure or to engineer failure for our advantage. This can be also used to build predictive models and to develop physically based continuum theories.

As elucidated in Chapter 1, one of the main objectives of this work are to understand the origins of phenomena, such as rate sensitivity, effect of the constituent concentration, filament/crosslink stiffness on the overall response etc. We also study the process of damage evolution in filamentous network under externally applied loads. Damage in these networks could be either damage of filaments or the damage of the crosslinks which connects the filaments together. One of the key assumptions in the model is that there exists a connection between the filaments where they intersects. We assume that the filament remains intact and limit our discussion to the damage of the crosslinks, vis-á-vis crosslink scission.

Depending on the length scales at which the random network structure exists, mechanisms of deformation could be *deterministic* or *stochastic* especially the process of damage. Materials like paper and random composites fall in the broad category of networks with deterministic deformation mechanisms. As thermal undulations and non-bonding interactions are dominant at the scale at which synthetic polymers and biopolymers exhibit network structure, they fall in the

broad category of stochastic showing a strong dependence on the applied force. Due to thermal undulations, crosslinks of F-actin networks are rather transient and are in a process of continuous breakage and reformation. The rate of crosslink reformation is higher than the dissociation when no external force is applied and a net fraction of crosslinks is present at any instant of time. And with the externally applied load the rate of disassociation increases and shows an *Arrhenius* type of dependence to the applied force. Unlike flexible polymer chains which can be approximated by Gaussian chains, F-actin filaments are semiflexible filaments with finite bending stiffness (see Section 2.6 for a discussion about the classification of polymer chains). The model usually adopted for such filaments is the *worm like chain* model (WLC) [108]. Filaments are in consistent thermal undulations and the externally applied force has to pull the the filament straight out of these undulations which costs energy and it adds to the thermal modulus of filaments [77].

At larger length scales, e.g., in the case of paper, thermal undulations are less significant and the crosslinks are rather stationary and the breakage depends on the energy criterion. Another important aspect arises in the deformation of network is non affinity; local deformation of the network differs from the macroscopically applied deformation. Further discussion on non-affinity and other important considerations like isostaticity of the network is given in Chapter 5.

Discrete network models have been developed for materials like paper, biopolymer, synthetic polymers, randomly reinforced composites etc. Depending on the nature of the problem, some of them require a stochastic approach while others are deterministic and our model is capable of modeling both these types [109]. The response of such materials are highly non-linear stiffening, non-affine and shows softening and failure due to failure of filaments and crosslinks.

The mechanisms of elasticity (entropic and thermal contributions) and damage changes with both length scales and materials, and the response becomes either deterministic or stochastic. A review of the DN modeling approach for various materials are given in the next section, categorized based on the types of response.

2.2.1 Discrete Network Models: Deterministic Approach

The entropic and thermal contributions to the elasticity is negligible at length scales of microns or above. In such networks, failure of the crosslink/bond are governed by the strain/stress based criterions. Paper, cotton, cellulose fluff, electrospun networks etc. falls in this category. Models developed for such materials account for the randomness in the topological arrangement and the mechanisms for the filament and bond failure is usually deterministic. The overall response may show the statistical variations which arises entirely due to the random nature of the topology. Few researchers have tried investigating the damage evolution in paper using FE based DN models. Heyden [110] did extensive work in developing DN models for cellulose fluff. Both 2D and 3D models have been developed with both linear and nonlinear bond response. Bond fracture is also accounted in the model and damage evolution was tracked with deformation. Other aspects probed are the effect of filament property, computational window size etc. Isaksson and Hagglund [111] used a similar approach for modeling the response of paper. The focus of that work was the fracture of the bonds connecting the filaments and they compared the simulation results with experimental work and found striking correlations. They observed a randomly distributed damage evolution which subsequently changed to highly localized damage as the deformation progressed. In a subsequent work, same authors embarked on a numerical study

of the damage evolution and identified that the peak stress coincides with the onset of damage localization. They also developed damage evolution laws based on the filament aspect ratio and the bond density [112]. Jan Astron *et al.* [113] developed a DN model for fibrous networks like paper and observed linear dependence of the filament density on the elastic modulus. Wu and Denizen [114] developed an effective medium approach by averaging the strain energy contribution over all directions and compared the results with the FE based DN models. Wei *et al.* [115] modeled the response of electrospun networks incorporating the fusion bonds between the filaments and non-bonding interactions. They used a strain based failure criterion and found that the fusion bonds contribute significantly to the elasticity of networks. Increase in the strength of electrospun networks by the addition of CNTs was studied by Agic *et al.* [116] by experiments and DN models. Chen *et al.* [117] developed a DN model with an activation strain based criterion for filament failure and modeled materials having length scales from a range of 10 to 100 μm. Their model showed excellent correlation with experiments for materials like paper, nanowoven cloth and nanomats.

2.2.2 Discrete Network Models: Stochastic Approach

Networks at submicron or lower length scales are strongly affected by the thermal undulations which contribute to the overall filament modulus. Apart from this, the elasticity could be entropic if the persistence length (l_p) of the filaments is small (see Section 2.6 for a discussion about l_p). Typically biopolymers and synthetic polymers falls in this category. Termonia *et al.* [118–121] pioneered the discrete network modeling approach for linear chain polymers like polyethylene where the individual polymer chains were modeled as linear

springs. These models are based on the kinetic theory of fracture of solids developed by Zhurkov [122]. In his work, Zhurkov developed a universal rate relation between life time of the bonds and the stress after rigorous experiments with various materials like aluminum, plexi glass and several polymers. This work is a pioneering work and has been widely used for modeling bond breaking process both in synthetic and biopolymers[1]. Effect of molecular weight on the tensile strength of ordered polyethylene fibers were probed using a DN model by Termonia and coworkers [118]. They explicitly accounted for the chemical bonds and assumed a stochastic bond breakage process. Both primary and secondary bonds were modeled and the bond scission was incorporated using Kinetic Monte Carlo approach. Various parameters relevant for the bond scission criterion were obtained from experiments.

In a subsequent series of work, Termonia and Smith [119] probed the correlation of molecular parameters like molecular weight, entanglement spacing etc. with the mechanical response. Further, they studied the role of molecular weight on the response of flexible chain polymer using a structured network; along with both primary and secondary bonds, entanglement slippage was accounted in this work. A similar approach was used to study the effect of entanglement spacing on the response and the results were compared with experiments [120]. In another work, they probed the effect of experimental conditions like temperature and the deformation rate [121]. This work was further expended to study the biological problems like spider silk elasticity where crystallites and the soft rubber like polymeric chains were modeled using a DN model [124]. Wang and Jin [125] studied the damage mechanisms in amorphous polymers using a 3D network model considering the entanglements and the sliding points of the polymer chains. In all works mentioned here, a regular structured network was used

---

[1]G. I. Bell proposed a model, widely known as *Bell model* for receptor ligand bond breaking based on the work of Zhurkov [123].

and the bond/crosslink scission mechanism was stochastic. In the next paragraph, a review of the DN model using randomly oriented filaments is given.

Another area where DN models have been widely used is for biopolymeric networks. MacKintosh and coworkers [74,77,126] did extensive experiments to understand the network response and developed models for the response of F-actin networks. Head *et al.* [126] characterized the shear modulus and non-affine response of F-actin networks. They proposed a material length scale ($l_b = \sqrt{\kappa/\mu_s}$) and defined a measure of non-affinity (λ_{na}) based on this length scale. In a subsequent work [77] they developed scaling laws for the network modulus based on the filament property and qualitatively delineated various response regimes based on the filament length and concentration. In doing so, they quantified the role of thermal fluctuation in network response and identified a characteristic length scale below which thermal effects are negligible. In the above two works, crosslinks were fixed at the intersection point and were freely rotating type. Marbini and Picu [127] studied various factors which affect the non-affine response in random fiber networks; found that the non-affinity is independent of the applied deformation and it decreases with the preferential orientation.

Onck *et al.* [78] developed FE based network models with rigid crosslinks and looked at the stress strain response. In a 2D network model, the transition from non-affine to affine response was attributed to the transition from bending dominated to stretching dominated regime in the response of filaments and they ascribed the non-affine response solely to the topological effects [78]. Networks with undulated filaments showed a similar response as that of straight filaments but had a delayed bending-stretching transition. In a 3D network model, similar response was observed but less stiffening due to less constraint effects [128]. A work by Van Dillen *et al.* [80] compared the the DN model approach by Van der Giessen [78] where the stiffening of the network is attributed to the topological

effects and the work of MacKintosh [129] where the stiffening is attributed to more of filament property. They also highlighted the discrepancy between the persistence length[2] and the bending stiffness of the filaments used in DN models. Heussinger and Frey [130] modeled the non-affine response and the different transition regimes of the filamentous networks with freely rotating crosslinks. In another work, they studied the effect of the thermal fluctuations which contribute to the elasticity of networks through entropic stiffness [131]. They looked into the polydispersity and structural randomness those are not present in the athermal modes and highlighted the importance of polymer chain length.

In all works mentioned above, crosslinks were assumed to be rigid/freely rotating. DiDonna and Levine [89] developed DN models where the elasticity and failure of crosslinks were incorporated. The effect of crosslink unfolding was probed using a crosslinks having infinite unfolding domains. Though this work adopted a more realistic representation of the crosslink response, filaments were modeled as linear springs that are incapable of bending. Due to this assumption, the model failed to capture in initial bending dominated compliant response at small strains. Chen and Shenoy [82] incorporated the effect of moelcular motors into a DN model with crosslinks having finite stiffness. Using a computational approach they showed that molecular motors are able to stretch the flexible crosslinks to full extend there by stiffening the network several orders higher than one with rigid crosslinkers.

---

[2]See Section 2.6 for a discussion about persistence length.

Table 2.1: Summary of the literature review of DN models for various materials showing the key features of each models.

Researchers	Material	Key Features
Termonia *et al.* [118–121]	Polyethylene	2D Regular spring network, Stochastic crosslink scission, Effect of molecular weight, entanglement spacing etc., Both primary and secondary bonds, Affine deformation
Termonia [124]	Spider silk	2D Regular spring network, Stochastic crosslink scission, Role of crystallites
Wang and Jin [125]	Amorphous polymers	3D Regular beam network, Entanglement sliding, Non-affine response
Marbini and Picu [127]	Semi- flexible	2D Random beam network, Role of fiber orientation, Non-affine response
Jan Astron *et al.* [113]	Paper	2D Random spring network, Relation between filament modulus and network stiffness
Wu and Denizen [114]	Wool assembly	2D Random beam network, Effective medium model
Heyden [110]	Cellulose fluff	2D and 3D Random spring network, Linear and nonlinear crosslinks, Fracture mechanics based crosslink scission
Isaksson and Hagglund [111]	Paper	2D Random network, Fracture mechanics based crosslink scission
Wei *et al.* [115]	Electrospun network	2D Random bead-spring network, Fusion bonds, strain based failure criterion
Agic and Mijovic [116]	Electrospun network	2D Random beam network, Non-affine, Multiscale model

Table 2.1 – Continued

Researchers	Material	Key Features
Chen *et al.* [117]	Paper, Nanowoven cloth and Nanomat	2D Random beam network, Scaling laws, Non-affine, A general model for a different materials, Activation strain based failure criterion
Head *et al.* [77, 126]	F-actin	2D Random beam network, Scaling laws, Non-affine
Onck *et al.* [78]	F-actin	2D Random beam network, Rigid crosslinks, Nonlinear stiffening, Non-affine
Huisman *et al.* [128]	F-actin	3D Random beam network, Rigid crosslinks, Nonlinear stiffening, Non-affine
Heussinger and Frey [130, 131]	F-actin	2D Random beam network, Freely rotating crosslinks, Polydispersity of filaments, Non-affine
DiDonna and Levine [89]	F-actin	2D Random spring network, Crosslink with finite stiffness, Stochastic failure of crosslinks, Affine
Chen and Shenoy [82]	F-actin	2D Random beam network, Crosslink with finite stiffness, No failure of crosslinks, Non-affine

Table 2.1 summarizes some of the key efforts in network-based modeling for various material systems. From the summary, key features identified are– modeling random filament topologies, accounting for affine/non-affine deformation and incorporating right crosslink breaking mechanism; stochastic or deterministic depending on the problem. Models by Termonia incorporates stochastic crossing scission but restricts the focus to regular networks with linear springs between junctions for polymers. Didonna used random topologies and stochastic cross link scission but ignored the role of filament bending. Further to it, only crosslink unfolding was incorporated, not complete failure of crosslinks. Rest of

36

the works use a DN model but do not account for the crosslink scission.

We develop a DN model for filament networks, which accounts for the actual response of both filaments and crosslinks. Our model has all the three features mentioned above that are considered to be important in modeling the response of polymers. By incorporating the stochastic failure of crosslinks as observed in experiments, it captures both the qualitative and quantitative network response. A detailed overview of algorithms developed for the generation and characterization of networks is given in the next section.

2.3 Network Generation

Network comprises of filaments and crosslinks which binds them together. Based on the type of filament orientation distribution ($\theta_{\bar{p}}$), networks can be broadly classified into two; networks with filaments oriented in all directions (uniformly distributed) and networks with filaments having a preferred orientation (normally distributed with specified mean angle and standard deviation). We do simulations on numerically recreated networks by assuming the filaments to be line segments and the crosslinks to be the intersection points of the line segments (both line segments and filaments are used interchangeably to represent the filaments). For the computational studies of network structures, we developed a MATLAB$^{\circledR}$ based toolkit, **NetGen** that creates filamentous networks with specified filament density, orientation, type of crosslinks etc. It also provides the facility for topology characterization, generation of the necessary FE mesh and storing it as a file that can be seamlessly read into ABAQUS$^{\circledR}$. In a nutshell, it works as a FE preprocessor for filamentous network topologies. The software also creates the part of the subroutine files which are necessary to implement the

crosslink scission algorithms.
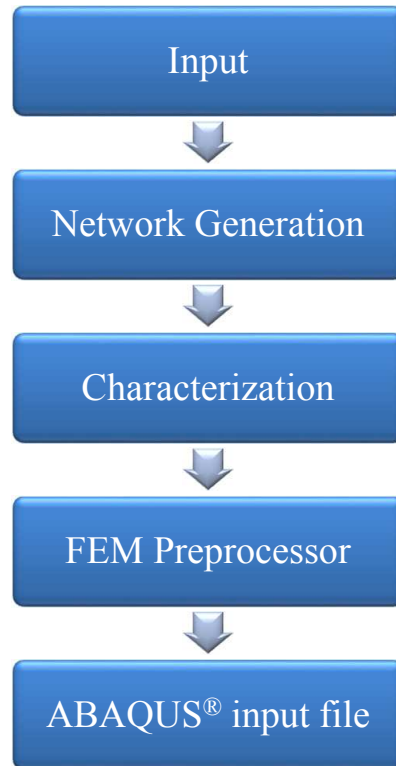
Figure 2.2: The overall work flow of **NetGen**.

Figure 2.2 show the basic structure of the software. The GUI accepts input including the size of representative volume element (RVE), number of filaments, mesh size, type of the filament orientation, type of crosslinks and the material properties. Inputs are passed to a network generating module which generate the networks based on the requested filament density $(\bar{\rho})$[3]. Once the topologies are created, it is passed to the network characterization module where the network statistics about the crosslinks and the orientation are extracted out. After

---

[3] $\bar{\rho} = NL^2/W^2$ is a non-dimensional filament density where N is the number of filaments, L is the length of a filament and W is the size of the computational window. See Section 2.3.2.

this , FE preprocessor module does the operations required to generate an input file amenable for ABAQUS$^{\circledR}$. Each module in Fig. 2.2 consists of a series of operations and it is described in subsequent sections. Before delving into details of the algorithm, a brief introduction about the rigidity percolation is given in next section.

2.3.1   A Note About Rigidity Percolation

One of the important considerations while working with filamentous networks is the concept of percolation. It appears as a generic concept, e.g ., conductivity percolation, rigidity percolation etc. Conductivity percolation refers to the continuity of electric or communication signals. It checks when a signal is supplied at one end of the network whether it reaches other end or not. The percolation relevant in the present context is rigidity percolation which refers to the ability of the network to carry load. If the network is above rigidity percolation threshold, it could resist the applied load which implies that it has filaments connected from end to end, at least a single strand [132]. The percolation of the networks can be measured in terms of the filament density of the network.

Rigidity percolation can be explained with the help of a simple exercise: Consider a RVE of given size where the number of filaments is increased starting from zero. At a very low filament density, initially the individual filaments are stranded in the domain, then it forms small clusters which are not connected to each other and cannot resist any deformation. As the density increases, these remote clusters get interconnected and gradually develops rigidity, the critical density at which this transition takes place is identified as rigidity percolation threshold $\bar{\rho}_c$ and it corresponds to a filament density of $\bar{\rho} = 5.7$ [133]. This is analogous to say that network makes a transition from simple mechanism to a structure when

the number of filaments reaches a critical value. A simple example is a four bar pin joined linkage which cannot resist shear loads, but when a diagonal linkage is added, it could resist shear deformations. For all simulations in this work, $\bar{\rho}$ is above this threshold and the network is a rigid structure which can resist the applied loads.

The percolation mentioned above is in terms of the topological arrangements, which is similar to conductivity percolation. In order to carry load, filaments has to be connected to each other. We are assuming a case where the filaments form physical connections at the topological intersection points. Frictional force at the intersections could also lead to the percolation, but these are not accounted in the current work. In our case, the percolation is entirely due the formation of crosslinks. At densities well above the percolation threshold, the network is a highly redundant structure. One of the examples for such a network is birds nest which is made up of random arrangement of filaments. It has important implications from a failure viewpoint too. Due to the highly redundant nature, failures of few filaments do not result in the failure of the entire structure. Networks with crosslinks that could break, represent such a scenario. Though few crosslinks are broken, the network still remains redundant and carries load, but when a critical fraction of crosslinks breaks, the rigidity is lost and the structure collapses.

2.3.2 Generation of Line Segments

The 2D discrete network model is made up of line segments confined in a single plane. Intersection points of line segments are considered as crosslinks with zero initial length. Line segments are of finite length and are assumed to be straight. The software has the capability to generate networks with uniform/preferred orientations. Uniform distribution means line segments are equally present in

all directions. For the preferred orientation, we use normally distributed line segments with mean angle (μ') in the preferred direction along with the specified standard deviation (Σ). In both cases above, only the orientation distribution($\theta_{\bar{\rho}}$) is varied but the location of the line segments follows uniform distribution.

Input data to **NetGen** are the size of RVE (W), number of line segments (N), length of line segment (L) and type of orientation function (uniform/normal). The filament density is defined as $\bar{\rho} = Nl^2/W^2$ [78]. Rigidity percolation of the networks are ensured by considering a network density of $\bar{\rho} \geq 5.7$. The size of the computational domain is determined in such a ways that the boundary effects are minimum. Unless otherwise stated, all networks have an aspect ratio of $W/L = 4$. A detailed analysis of the boundary effects based on the W/L ratio is given in the dissertation of Heyden [110]. To start with, location of the line segments is determined based on a random seed within the size of RVE. The orientation of the line segment is determined using another random seed and a line segments of length L is generated based on the location and orientation. When a line segment is generated inside RVE, its intersection with other line segments already inside the RVE and the boundaries of the RVE are found to define the crosslinks and the periodic boundary conditions (b.c.'s). The Intersection point P_x, P_y between the line segment L_1 and L_2 is obtained by using Cramer's rule [134].
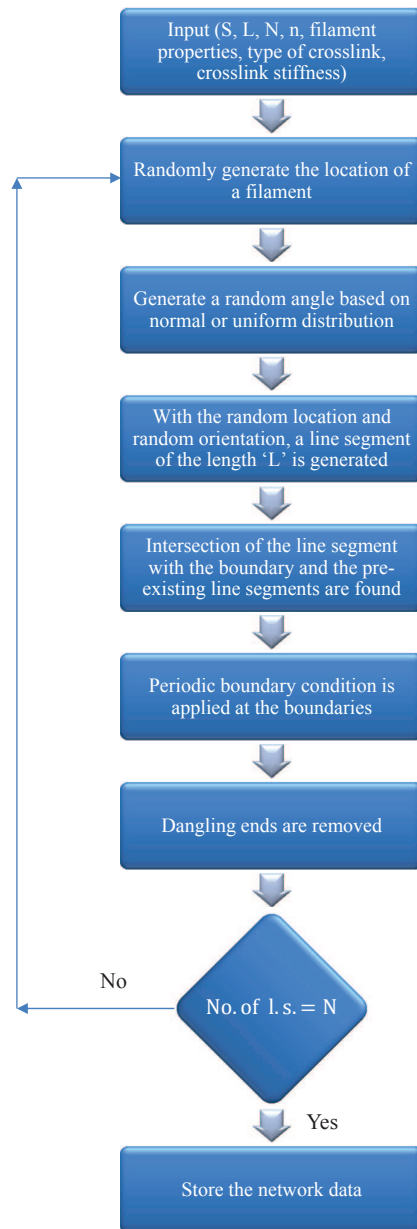
Figure 2.3: Algorithm used for the generation of periodic networks with the desired orientation and density.

$$P_x = \frac{\begin{vmatrix} \begin{vmatrix} x_1 & y_1 \\ x_2 & y_2 \\ x_3 & y_3 \\ x_4 & y_4 \end{vmatrix} & \begin{vmatrix} x_1 & 1 \\ x_2 & 1 \\ x_3 & 1 \\ x_4 & 1 \end{vmatrix} \end{vmatrix}}{\begin{vmatrix} \begin{vmatrix} x_1 & 1 \\ x_2 & 1 \\ x_3 & 1 \\ x_4 & 1 \end{vmatrix} & \begin{vmatrix} y_1 & 1 \\ y_2 & 1 \\ y_3 & 1 \\ y_4 & 1 \end{vmatrix} \end{vmatrix}} \qquad P_y = \frac{\begin{vmatrix} \begin{vmatrix} x_1 & y_1 \\ x_2 & y_2 \\ x_3 & y_3 \\ x_4 & y_4 \end{vmatrix} & \begin{vmatrix} y_1 & 1 \\ y_2 & 1 \\ y_3 & 1 \\ y_4 & 1 \end{vmatrix} \end{vmatrix}}{\begin{vmatrix} \begin{vmatrix} x_1 & 1 \\ x_2 & 1 \\ x_3 & 1 \\ x_4 & 1 \end{vmatrix} & \begin{vmatrix} y_1 & 1 \\ y_2 & 1 \\ y_3 & 1 \\ y_4 & 1 \end{vmatrix} \end{vmatrix}} \qquad (2.1)$$

where $\begin{vmatrix} a & b \\ c & d \end{vmatrix}$ denotes a determinant, (x_1, y_1) and (x_2, y_2) are the points on the line, L_1 and (x_3, y_3) and (x_4, y_4) are the points on the line L_2. The determinant in Eq. 2.1 can be expanded as [134],

$$\begin{aligned} P_x &= \frac{(x_1 y_2 - y_1 x_2)(x_3 - x_4) - (x_1 - x_2)(x_3 y_4 - y_3 x_4)}{(x_1 - x_2)(y_3 - y_4) - (y_1 - y_2)(x_3 - x_4)} \\ P_y &= \frac{(x_1 y_2)(y_3 - y_4) - (y_1 - y_2)(x_3 y_4 - y_3 x_4)}{(x_1 - x_2)(y_3 - y_4) - (y_1 - y_2)(x_3 - x_4)} \end{aligned} \qquad (2.2)$$

This gives the intersection of two infinitely long lines and it is ensured that (P_x, P_y) lies on the line segment considered. Each generated line segment is compared against all existing line segments in the RVE and the RVE boundaries to find out the intersection points. All the intersection points are stored as the

global node numbers to be used in the FE model.

2.3.3   Periodic Boundary Conditions
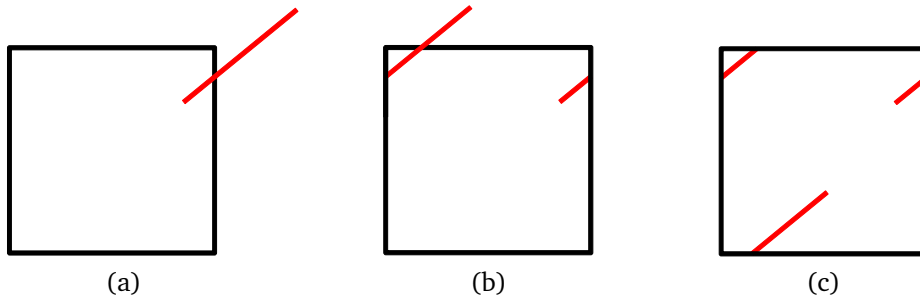
Figure 2.4: Steps involved in applying the periodic boundary condition for a line segment crossing the boundary of the RVE. (a) A line segment is crossing the right boundary. (b) The segment is terminated at the intersection with the boundary and is inserted back at the opposite boundary. (c) The same process is repeated at the top and bottom boundaries.

Networks generated are assumed to be a small sample from a big network structure. To approximate this, we prescribe periodic boundary condition at the edges of the RVE; both topological periodicity and compatible deformation which is ensured by proper kinematic b.c's during the FE simulations. In order to achieve the topological periodicity, we adopted the procedure depicted in Fig. 2.4. For a topology to be periodic, it should be continuous when tiled up in both horizontal and vertical axis which necessitates the continuity of the line segments across the edges. When a line segment crosses the boundary (Fig. 2.4a), it is terminated at the intersection with boundary and is translated to the opposite boundary and the same horizontal level and is continued inside the RVE (Fig. 2.4b). In this particular case, after the first translation the line segment crosses the boundary

at the top, so the same procedure is repeated and the remaining length of the line segment is continued at the bottom boundary. The algorithm has the capability to apply periodic b.c. to line segment of any length crossing the boundary. The deposition of line segments is continued until the required numbers (N) are placed in the RVE to obtain the desired density. Once this condition is satisfied, The generation process is stopped and the coordinates of the line segments and the the crosslinks are stored.

2.3.4 Dangling End Removal
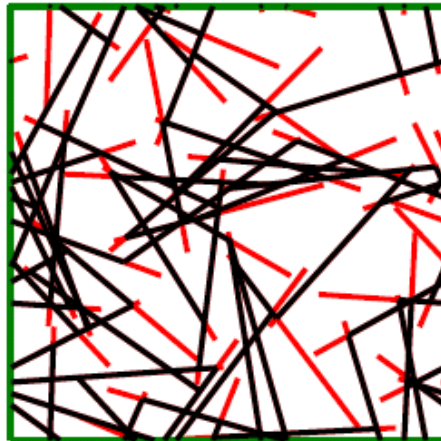
Figure 2.5: A network with periodic b.c. applied and dangling ends removed. Red line segments are dangling ends that extends beyond the end crosslinks which is removed for computational efficiency.

Line segments are present in all orientations and they make multiple contacts with the other segments inside the RVE. A network after applying periodic condition is shown in Fig. 2.5 (red line segments). It can be noted that edges of the line segments project beyond the end crosslinks. Such ends are called *dangling ends*. In the analysis, physical contact and interaction between the line segments other

than at crosslinks are not considered and these ends which do not contribute to the structural rigidity of the networks are removed to enhance the computational efficiency. The final structure of the network is shown by black line segments in Fig. 2.5. Dangling ends are important if frictional, contact or non-bonding forces are accounted, else it may result in underestimating the network rigidity.

After the dangling end removal, the network generation process is complete and the control is passed to the statistical characterization unit. Once the dangling ends are removed, the effective line segment is the distance between two end crosslinks. The distance between two crosslinks are calculated and the average of the distance between crosslinks calculated for the all crosslinks in the RVE and is defined as the *mean distance between crosslinks* (l_c). Cox [135] developed a theoretical expression for l_c, given by $l_c = \pi L / 2\bar{\rho}$. The average value of l_c obtained from networks generated by **NetGen** is comparable with value of l_c from the theoretical expression.

2.4   Network Characterization

Even if the input parameters are held fixed, the randomness in the network generation algorithm results in different realizations. Naturally, one may expect variation in the mechanical response due to differences in network percolation. This necessitates the development of parameters other than $\bar{\rho}$ to characterize the network in terms of their mechanical responses. Networks exhibit highly non-linear and anisotropic responses which are inextricably linked to the topology. The network response could depend on the type of crosslinks, location of the crosslinks, loading direction, orientation of filaments etc. It is also known that the local architecture affects the percolation of the networks and it in turn has

a strong influence on the overall response. This is more dominant in the case of networks with low $\bar{\rho}$. In such cases the overall topological variability among different realization will be very high.

(a) 1×1 compartment   (b) 3×3 compartment
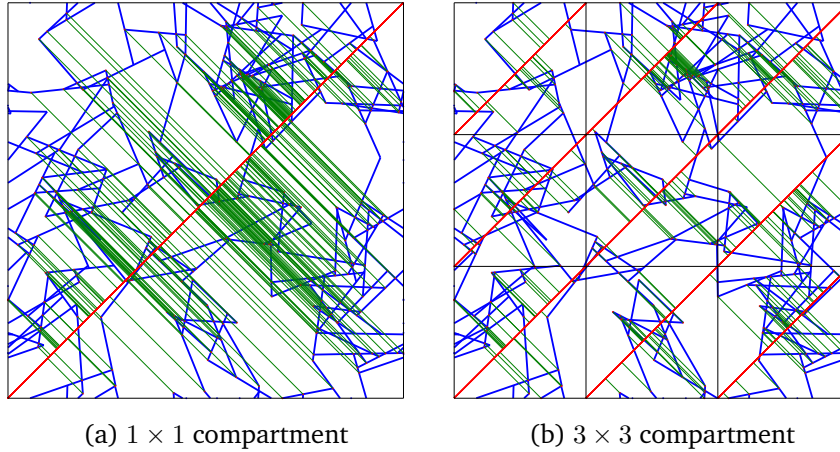
Figure 2.6: Two approaches to calculate the statistical parameters like the number of crosslink, distance of crosslinks from a reference axis (red lines), projected length of the line segments on the axis etc. (a) Shows the distance of crosslinks from the reference axis when the RVE is considered as a single compartment (b) Shows the same network when the RVE is divided into 3×3 compartments.

A method commonly used to find out the statistical descriptors that can characterize the response is nearest neighbor statistics. This method is commonly employed in the characterization of packing of hard spheres, discs and random filament arrangement in composites [136–138]. Kushsch *et al.* [139] developed nearest neighbor statistics for fiber reinforced composites, identified clusters of fibers that are highly stressed regions in the composites. We developed a similar statistical approach based on the center to center distance of fibers in composites and correlated it with the interface debonding [140]. This method also identified clusters of fibers based on the coefficient of variation of the center to center distance of fibers.

47
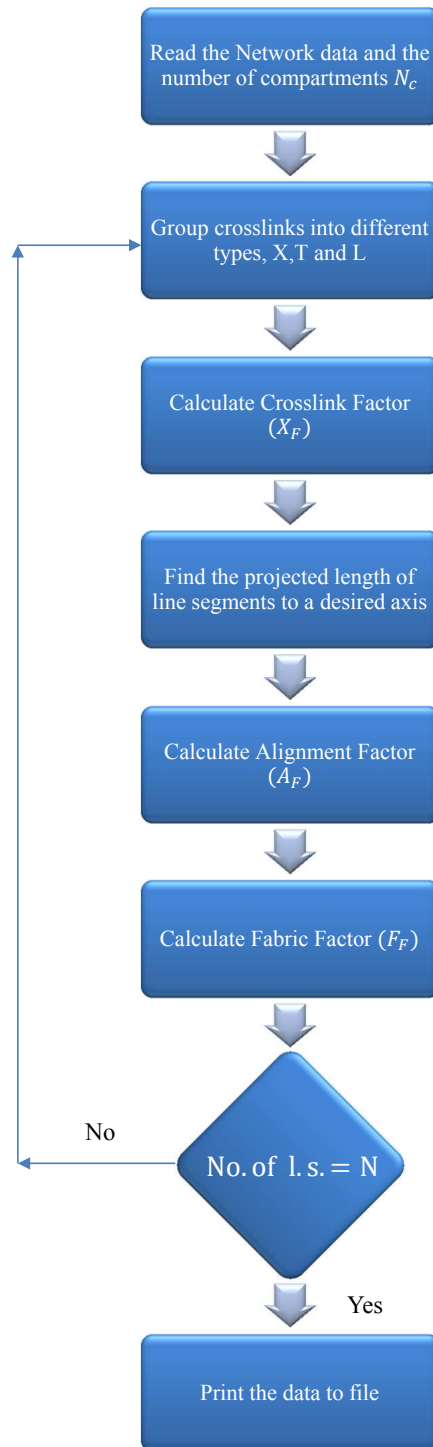
Figure 2.7: The work flow in the network characterization module where the types of crosslinks are identified and parameters like A_F and F_F are calculated.

An approach to account for such local variations in the filament distribution is to compartmentalize a given network into different regions for the calculation of statistical parameters and then find the equivalent (Fig. 2.6). The NetGen software has the capability to divide a given network into any number of compartments for the calculation of the statistical parameters. The characterization module can identify the type of crosslinks, projected length of the line segments onto a reference axis and the distance of the crosslink from the axis.

We define four parameters; X_M, X_F, A_F and F_F to characterize the topology based on the topological information, such as crosslink density and the filament orientation. A detailed discussion about these parameters is given in Chapter 3 in conjunction with the discussion of mechanical response and its correlation. The flow of activities in the characterization module of the **NetGen** is shown in Fig. 2.7. It first identifies the type of crosslinks as X, T or L (Fig. 2.10) and then generates the statistics of X_M, X_F, A_F and F_F in a sequential manner. The output of the module is saved to a Microsoft excel file.
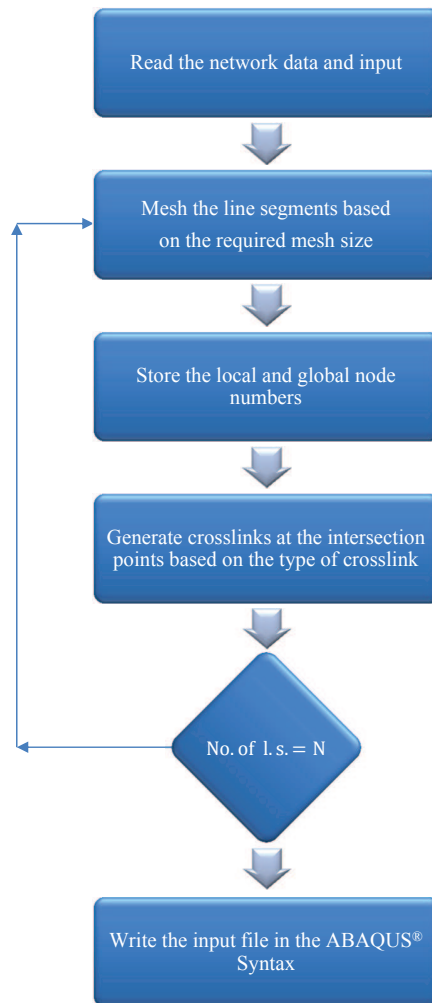
Figure 2.8: Steps involved in the FE preprocessing module.

2.5 FE Preprocessing

Our aim is to develop a computational model for the discrete networks in a finite element framework. The model is implemented in a commercial FE software ABAQUS® for which an input file is written that can be seamlessly read into it. This help us to utilize the solver and post processing capability of ABAQUS®

while focusing ourself on the development the discrete network model.
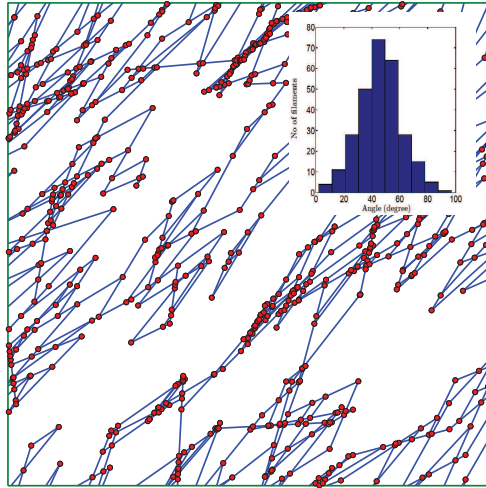
(a) $\mu' = 45^0$ and $\Sigma = 15^0$
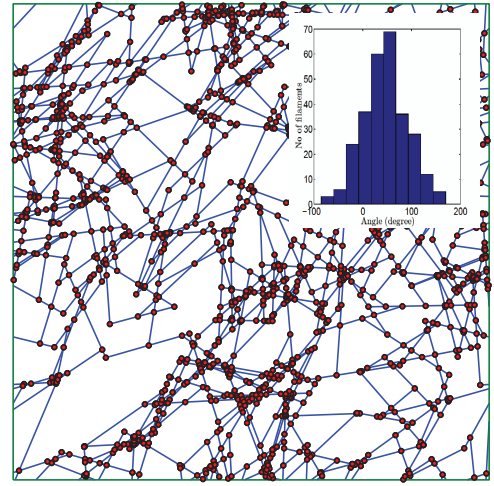
(b) $\mu' = 45^0$ and $\Sigma = 45^0$
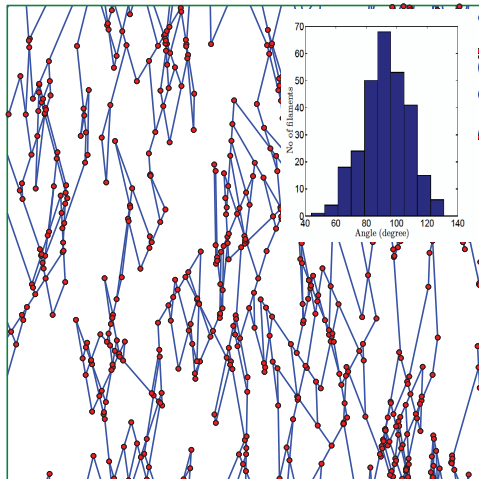
(c) $\mu' = 90^0$ and $\Sigma = 15^0$
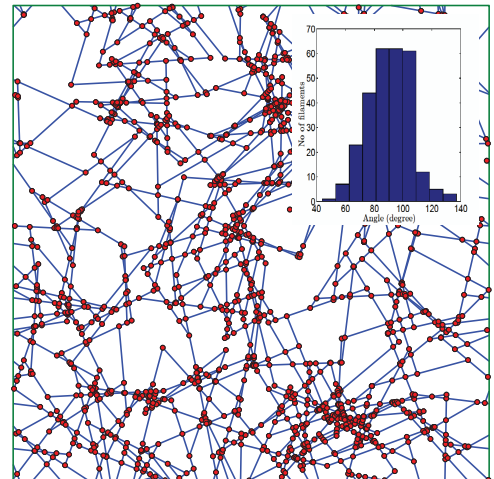
(d) $\mu' = 90^0$ and $\Sigma = 45^0$

Figure 2.9: Networks having normal filament orientation distribution with the orientation histogram in the inset. The mean angle (μ') and standard deviation (Σ) of each network is shown in the label. It can be noted that all filaments are oriented to the mean angle in figures (a) and (c) but the spread of the distribution increases as Σ increases as shown in figures (b) and (d). Networks become more uniformly distributed as Σ increases and the overall number of crosslinks increases.

Figure 2.8 outlines the steps involved in this module. **NetGen** is capable of generating two types of networks based on the filament distribution by selecting the options in the input panel. It also has a provision to generate same topology with rigid and compliant crosslinks. The types of networks that can be generated by **NetGen** are

1. Uniform filament orientation distribution

2. Normal filament orientation distribution

3. Networks with rigid crosslinks

4. Networks with crosslinks having finite stiffness

5. Type 3 and 4 at the same time

Input to the FE preprocessor is the number of mesh per filament, type of crosslink, type of element and the material property of both filaments and crosslinks. Figure 2.9 shows two networks with normal filament orientation distribution, generated using **NetGen**. Figure 2.9a shows a network with a mean angle $\mu' = 45^0$ and a standard deviation of $\Sigma = 15^0$. The network appears to be sparse with most of the filaments oriented along the diagonal along 45^0. When the standard deviation is increased keeping the μ' the same (Fig. 2.9b), the distribution becomes more random and has more crosslinks and the networks appears to be more dense though the $\bar{\rho}$ in both Fig. 2.9a and Fig. 2.9b is the same. Figures 2.9c and d shows a similar case when $\mu' = 90^0$. In Fig. 2.9c, filaments are aligned in the vertical direction and the disorder increases as the Σ increases.

2.5.1 Mesh Generation

The most important step involved in the FE preprocessing is finite element meshing. Filaments in the DN model are modeled using beam elements as the actual filaments show resistance to bending. The element type used is based on the aspect ratio of the beams. For slender beams Euler- Bernoulli finite elements (B23 in ABAQUS®) are used while for stubby beams, lower order element like Timoshenko beam elements (B21) are used. Within **NetGen**, meshing is done based on the number of elements required per filament (user input) and is accomplished in two stages:

First stage: A filament is discretized based on the crosslink locations. This is done after the network generation when the intersection points are identified and they are assigned the node numbers. After the first stage of meshing, the mesh size is of the order of l_c.

Second stage: Filaments are already discretized at all crosslink locations and a new mesh is formed if the distance between two crosslinks are greater than or equal to twice the mesh size. This is done based on the number of elements specified by the user. The algorithm run through each line segment one at a time. In between two crosslinks, a new mesh is formed only if the remaining length is again greater than or equal to twice the input mesh size. This constraint helps to avoid very small elements being formed. Such elements may have effect on the numerical convergence during FE simulations. It calculates the average mesh size based on the filament length and the number of mesh required as $\zeta = L_a/n$ where ζ is the mesh size[4], L_a is the projected length of the filament and n is the number of elements required per filament. This operation is done on the horizontal projection of the filaments and then rotated back to the actual

---

[4]In simple terms, it is the average dimension of the FE mesh created on the filament.

orientation of filaments. Each filament is stored as coordinate pairs in an array with its starting and ending points together with crosslink locations. First, the distance between two points (end point and the next crosslink) is calculated and if the size greater than the mesh size, it is discretized.

The meshing approaches are somewhat different for networks with rigid crosslinks and flimsy crosslinks. For the rigid ones, there entire network is a single instance (it is an ABAQUS$^{\circledR}$ terminology) based on a single coordinate system and all mesh points are global node numbers. In the case of networks with finite stiffness crosslinks, each filament is a separate instance having its own local coordinate system. Crosslinks acts as the global node numbers while the mesh points acts local to a line segment. **NetGen** calculates the statistical parameters of the networks and does the complete FE preprocessing. The output of the FE preprocessor unit is fed to the next module where an input file in ABAQUS$^{\circledR}$ syntax is written and can be directly used for simulations in ABAQUS$^{\circledR}$.

2.5.2   Generation of Input Files

Once the meshing is complete, the next task is to form the crosslink pairs for the crosslink with finite stiffness. Crosslinks are treated as springs and is implemented as Spring2 elements in ABAQUS$^{\circledR}$. Crosslinks are assumed to have a constrained translational degrees of freedom while it is free to rotate about the axis perpendicular to the plane. This is implemented using separate springs along both x and y axis. The line segment edges on the vertical boundaries are identified for the kinematic coupling for the periodic b.c.'s where all degrees of freedom on the left and right edge are tied together. The horizontal edges are identified for applying load b.c.'s. Once all these sets are identified, the output is written to a text file in the format of ABAQUS$^{\circledR}$ input file [141]. During this,

54

the material property is assigned to the filaments/crosslinks and the b.c.'s are applied on the boundaries. It generates and stores the input files, data necessary for the implementation of crosslink breaking algorithms, statistical parameters of the networks and images generated at various stages.
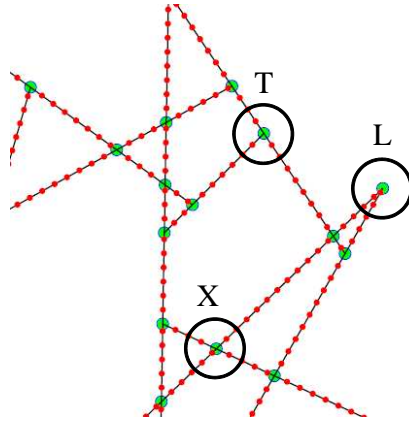
Figure 2.10: A closer look at a network with free ends removed. The green intersections are crosslinks and red dots shows the finite element mesh. X,T and L-types of crosslinks are marked in the figure.

2.6 Mechanical Properties of Constituents

The DN model is a generic and can be used to model a wide range of materials which exhibit the fibrous network structures at any level. The overall macroscopic properties depend on the length scale at which the material exhibit the network structure, properties of the constituents like filaments and crosslinks, presence of external media like fluids, failure mechanisms for filaments and crosslinks etc. If we consider two materials which exhibits the network structure at the same length scales but different macroscopic properties; it could be attributed to the parameters like the $\bar{\rho}$ and/or the properties of the filaments and crosslinks. A brief discussion about the material property of the filaments and crosslinks is

given in this section for the sake of completeness.

Filament Property

Filaments in the network is an approximation of the short segments of *polymer chains*. The physical characteristics and the material properties of the filaments are available from single filament experiments. One of the parameters used to classify the polymers chains is the long range correlation existing in the chains. Based on the bending stiffness of the chains, a length scale referred to as the *persistence length* ($l_p = \kappa/k_B T$) is defined, where κ is the filament bending rigidity, k_B is the Boltzmann constant and T is the temperature. The long - range order in polymers depends on this length scale and based on l_p polymers are broadly classified into three types [60].

- Flexible ($L < l_p$)

- Semi-flexible ($L \sim l_p$) and

- Rigid ($L > l_p$)

where L is the length of the polymer chains. With increasing l_p, the long range correlation in the polymer chains increases and bending deformation requires more energy. In the case of flexible polymer chains, any two points beyond the length of the monomer units are uncorrelated. Gels and rubbers fall in this category and the mechanism of deformation is entropic [34, 60]. During deformation, the number of energetically favorable configurations reduces resulting in higher energetic cost. One of the key differences between entropic elasticity and conventional elasticity is in the case of thermal response. Increasing temperature increases the stiffness in the case of former while the latter becomes more compliant.

When l_p is nearly equal to the polymer chain length, it is called semi-flexible. Semi-flexible polymer chains exhibits rich dynamics due to the bending stiffness of the chains unlike the flexible chains and thermal effects. There are two energy components associated with stretching; *thermal* and *mechanical*. At finite temperature, polymer chains will be in thermal oscillations and to pull out of transverse thermal fluctuations costs additional energy. The overall filament modulus could be the equivalent of the mechanical and thermal modulus [142].

$$\mu = \frac{\mu_M \mu_T}{\mu_M + \mu_T} \tag{2.3}$$

where μ is the effective modulus, μ_M is the mechanical modulus and μ_T is the thermal modulus. For F-actin filaments of diameter d, only if the chain length between two crosslinks is less than a characteristic length $l^* = (d^2 l_p)^{1/3} \sim 100$ nm, thermal fluctuations are insignificant [142]. It implies, for a realistic modeling of biopolymers, one has to account for the thermal effects.

These filaments could be straight, curly or undulated ones. Length of the filaments also pay a significant role in the overall response. Even if the filaments are long, the distance between the crosslinks l_c may be playing a dominant role if the crosslinks are rigid. Usually for the modeling, if the chain segments are smaller than l_p, chains are approximated as straight filaments and thermal effects can be neglected. Van der Giessen and coworkers [78, 79] developed 2D and 3D network models for F-actin filaments using both straight and undulated filaments. They observed that the response remains similar in both cases except delayed bending to stretching transition in the case of undulated filaments. When l_p is infinitely large or the chain segments are shorter than l_p, chains acts like rigid rods. In the current model, we neglect thermal energy and assume that the filaments are straight and of finite length.

Crosslink Property

The overall mechanical response of the network is grossly determined by the interaction (load transfer) between the filaments. This interaction could arise from the presence of crosslinks, friction at the intersections, physical entanglements or the the Van der Waals interaction or combinations thereof. For the sake of simplicity, only crosslinks at the intersection points are considered in the current model. The property of the crosslinks has to be carefully considered for the accurate representation of the actual system considered. The response of the crosslinks could range from linear response to highly nonlinear and flimsy to rigid. In the case of biopolymers like F-actin networks, actin binding proteins (ABPs) forms the crosslinks and it shows very highly nonlinear response elicited by experiments on single ABPs. For the modeling of F-actin network, we used a simplified bi-linear representation for a highly nonlinear hardening response of the crosslinks [82].

Crosslinks are modeled as springs with independent degrees of freedom in both x and y directions (see Section 2.5). For implementing the failure criterion, the resultant forces are calculated and failure implies, loss of stiffness in both the directions.

Conversion of the Filament Concentration to Filament Density

Biopolymers like F-actin is usually expressed in terms of the concentration of F-actin filaments and the crosslinking proteins. In order to develop DN model for biopolymers, the filament concentration has to be converted into filament density. This can be done based on the dimension of the constituent molecules.

F-actin has a dimer structure made up of the two strands of G-actins [60]. G-actin has a spherical structure and the dimensions are known. Total length of the filaments inside RVE for a given $\bar{\rho}$ can be obtained by $\rho = \bar{\rho}/L$. This is translated in to length per unit volume by considering the dimension of the RVE. Using the dimension of G-actin, number of G-actin present in the RVE can be obtained. This information can be converted into number of moles and which in turn can be converted into weight per unit volume. This can be further converted into molecular concentration unit micromolar and can be compared with the given concentration of F-actin. Using this approach, DN models is built for biopolymers where the network desity in experiments is expressed in the concentration of the constituents.

Failure Response of Crosslinks

In the DN model, the failure of networks is through the failure of crosslinks. The mechanisms for the failure of crosslinks is highly dependent on the length scales of the networks. If the network is in a microscopic scales where thermal undulations and non-bonding interactions are dominant, the failure becomes a stochastic process. Such kind of process can be modeled using Kinetic Monte Carlo approach (see Chapter 4 for a discussion about the KMC algorithm). Failure of crosslinks in biopolymers falls into this regime.

If the network structure exists at a larger length scale where the process is more deterministic, fracture mechanics based failure criteria like traction separation rule can be applied [110]. A wide range of materials like paper, felt, electrospun polymers etc. can be approximated into this category. The failure criterion can be written as [110]

$$g(F) = \frac{\overrightarrow{F}}{F_{ult}} - 1 \tag{2.4}$$

where $g(F)$ is the slip criterion, $\overrightarrow{F}$ is the vector sum of the forces and the F_{ult} is the ultimate force in the crosslink.

The overall network stiffness, toughness and ultimate strength depends upon the crosslink response. Rigid crosslinks make the network stiffer and of high strength but it may result in low toughness and low failure strains. Engineering the crosslinks can yield networks having exceptional properties, in a computational study by Salib *et al.* [143], a network with a fraction of the labile crosslinks rendered the network 200% stronger than one with all rigid crosslinks.

The network model developed in this chapter can be used to model the response of a variety of materials having underlying filamentous microstructure. We chose F-actin network as an exemplar to show the capability of the model. Chapter 3 focuses on the variability in the response of networks due to random topological realizations and limiting the size of RVE. Chapter 4 focuses on the rate dependent stochastic failure of F-actin networks. Chapter 5 explores the network response over a wide parametric space, starting with the F-actin networks focusing mainly on the nonlinear stiffening, non-affine response and damage.

Chapter 3

Influence of Topological Characteristics in Network Response

3.1 Introduction

In Chapter 2, we described the computational approach developed in this work to generate fibrous architectures with a given basic set of topological and physical parameters. We also showed that one could obtain myriad realizations even if the basic structural parameters for networks are kept constant. Consequently, for fixed constituent material properties, it is of interest to know how the topological characteristics of a network would influence the overall response. Each realization carved out of a bigger sample could potentially generate a different quantitative response that depends on its domain size (sampling window) W, filament density $\bar{\rho}$ and their orientation distribution with respect to the loading direction. Naturally, these aspects raise a multitude of questions regarding the effect of these topological features on the response variability. While one may paint a qualitative landscape of the range of responses that could be obtained,

e.g., linear/nonlinear, affine/non-affine, stiffening/softening, or a combination thereof, it is important to understand and ideally, predict the variability in the responses as a function of the uncertainties arising from network topology.

(a) Network with $\bar{\rho} = 10$ (b) Filament orientation distribution
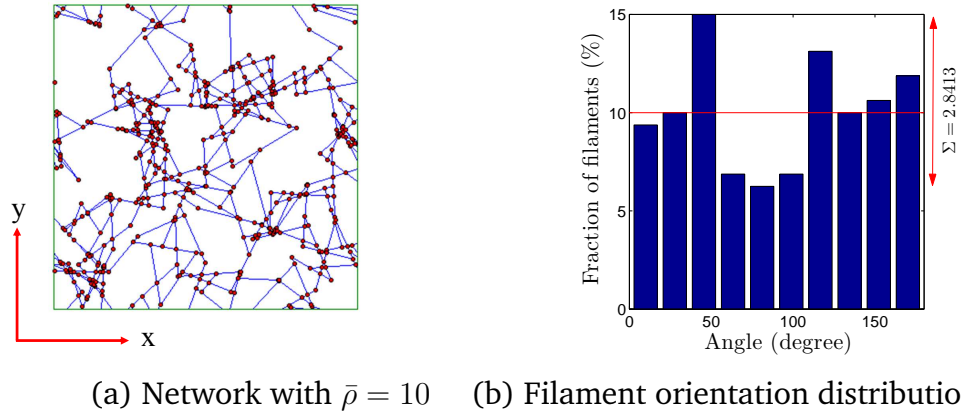
Figure 3.1: (a) A periodic filament network. (b) Filament orientation distribution function $\theta_{\bar{\rho}}$ of the network shown in (a). Though the prescribed $\theta_{\bar{\rho}}$ is uniform, the resulting distribution is not perfectly uniform. Such anomalies lead to variability in the response. The reference axis shown.

We cite two examples to motivate some of the complexities associated with the characterization of the mechanical behaviors of such fibrous networks. Consider the network shown in Fig. 3.1a, generated by prescribing a uniform orientation distribution using **NetGen** (Fig. 2.1). The filament orientation distribution $\theta_{\bar{\rho}}$ corresponding to the network is shown in Fig. 3.1b. For this network, Fig. 3.2a shows the stiffness-strain response when deformed independently in the forward and reverse directions under simple shear. For a topologically isotropic network, one should expect the network to generate near-identical responses whether deformed in the forward direction or its opposite direction. However, as can be seen, the actual result shows some asymmetry indicating the influence of the deviation from an ideal uniform filament orientation distribution. The second case serves as an exemplar of the variability produced by multiple realizations

of network for a given $\bar{\rho}$. Figure 3.2b collates the responses of twelve different realizations ($\bar{\rho} = 10$) deformed under simple shear. Although some results tend overlap, in general, there exists a considerable spread in the response underscoring the role of network topology. Note that here we assume a simple constituent description for the filaments, that of linear elasticity. Nonlinear material models and damage mechanisms further complicate the response characteristics and also the variability.

(a) Anisotropy   (b) Topology dependence
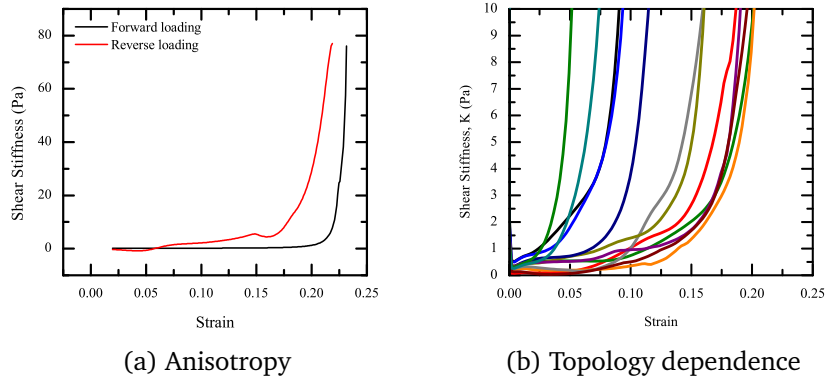
Figure 3.2: Examples of variability in mechanical response for $\bar{\rho} = 10$. (a) Shows the same realization loaded in opposite directions. (b) Shows the different realizations for same $\bar{\rho}$ loaded in same direction.

This chapter discusses some effects arising from the topological characteristics of fibrous networks by considering multiple network realizations where one parameter is varied while others are held fixed. For a given $\bar{\rho}$, increasing the computational domain size improves the topological corroboration with the ideal (expected) one by virtue of the sampling statistics. However, amongst other aspects, the choice of the computational domain size is restricted by the computational effort that can be handled by available computational power at our disposal. Clearly, smaller sampling windows are expected to produce larger variations in the macroscopic behaviors [144–146]. In other words, to obtain a

good statistical measure of the network responses, one has to choose a reasonably large representative volume element (RVE) so that fewer realizations are required or perform simulations on a large number of realizations with smaller domain sizes. The available computational resources during this work indicated that a sampling window of 40 μm allows obtaining results in a reasonable time. Next section discusses the variability in the filament distribution and selection of an optimum sample window size to the reduce this variability.

3.2   Topological Variability

The issue of sampling size is important in constructing artificial microstructures. For example, from the viewpoint of computational cost it may not be possible to simulate large scale specimens (Fig. 3.3). Instead, one may need to choose smaller windows from the large specimen. While on an average, such a windowing procedure is expected to retain global features of the larger architecture, e.g., filament and crosslink density but the local details could vary significantly as shown in Fig. 3.3. In turn, this variability in the local architectures is deemed to influence the mechanical responses. Although, the algorithm attempts to generate networks that adhere to the input characteristics, there is always a possibility of the generated networks deviating from expected features. The deviation is quantified using statistical parameters and suggest methods to achieve perfectly uniform networks. We briefly discuss these statistical aspects with reference to the topological isotropy as a function of computational window size (W) and filament density ($\bar{\rho}$).
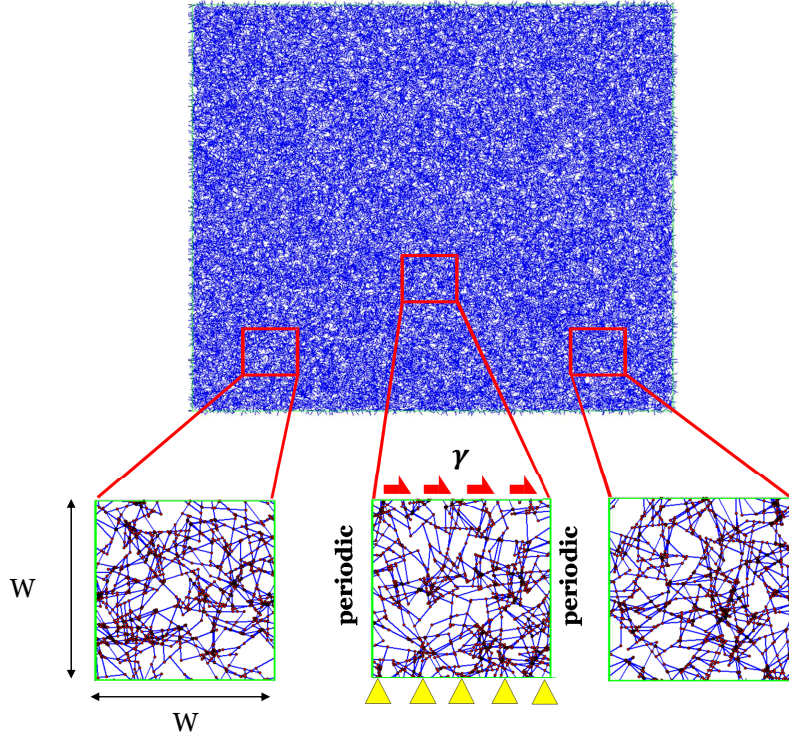
Figure 3.3: Idealization of actual network by smaller computational windows. Depending on the location, filament distribution inside windows could be different. Though nominal network parameters like $\bar{\rho}$ and number of crosslinks are the same, response could vary for different filament realizations.

To begin with, we prescribe a uniform filament distribution for a given window size W. Filaments are randomly placed in the window until the desired $\bar{\rho}$ is obtained. In order to quantify the filament orientation distribution of a given network, filaments are grouped into ten bins of orientations ranging from 0^0 to 180^0 with each bin of width 18^0. The number of filaments in each bin is normalized by the total number of filaments and this filament fraction was used in rest of the calculations. For a given $\bar{\rho}$ or W, we consider five network realizations to obtain the average, μ' and the standard deviation, Σ of the filament fraction . Given that the range of angles considered is from 0^0 to 180^0 and the distribution

is uniform, the average value is always $\approx 10\%$. The Coefficient of variation is $C_v = \mu'/\Sigma$. In the following sections, we discuss the statistical aspects arising from computational window size, W and filament density, $\bar{\rho}$.

3.2.1 Increasing the Computational Window Size

One of the approaches to get the idealized uniformly distributed filament networks is to increase the W for a given $\bar{\rho}$. We considered a case with $\bar{\rho}=10$ and increased the window size, W to find the optimum size at which the filament distribution becomes uniform. Starting with a $W= 30~\mu$m, networks were generated with uniform filament distribution and filaments of length, L=10 μm and the largest W was of 1000 μm (Fig. 3.4). As the W increases distribution tend to be more uniform, reflected as a drop in the value of Σ.

(a) $W = 40\,\mu$m

(b) $W = 1000\,\mu$m
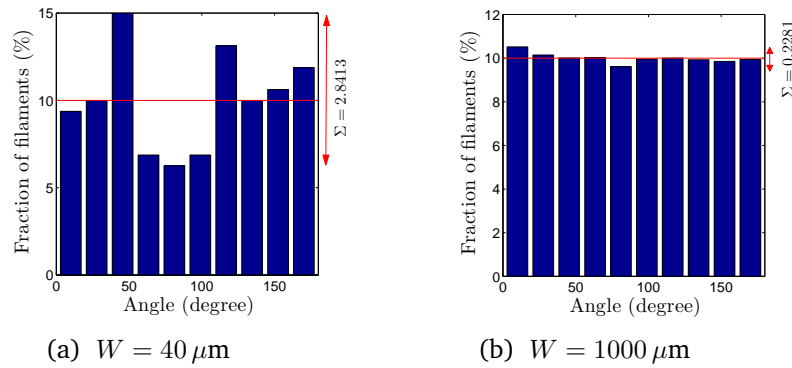
Figure 3.4: Filament distribution with $\bar{\rho}=10$ for two window sizes are shown with the mean (red line) and standard deviation. As the W increases, the distribution becomes more uniform.

Figure 3.5 gives a summary of the parametric study with W ranging from 30 μm to 1000 μm. From the μ' and Σ of each realization, C_v was calculated. Using the C_v of five realizations for a given W, μ' and Σ of the C_v of each W was calculated. From the limited number of realizations considered here, we deduce that

the variability is very high when the W is 30 μm and there is a limitation for the lowest value for W that can be considered due to the fixed filament length of 10 μm and the rigidity percolation requirement. It can be noted that increasing W beyond 200 μm does not yield any substantial increase in the convergence of numerical approximation of uniform distribution (shown by the blue zone in Fig. 3.5). Increase in W is offset by the cost of computation. From a computational cost stand point, for a given $\bar{\rho}$, it would be necessary to consider a large number of realizations to obtain accurate bounds on the response variability, if one chose to use small W. For the present work, we chose $\approx 5 - 8$ realizations to obtain the variability due to topological effects. The accuracy could be further improved with more realizations. The value of W used in the current study is marked in Fig. 3.5.
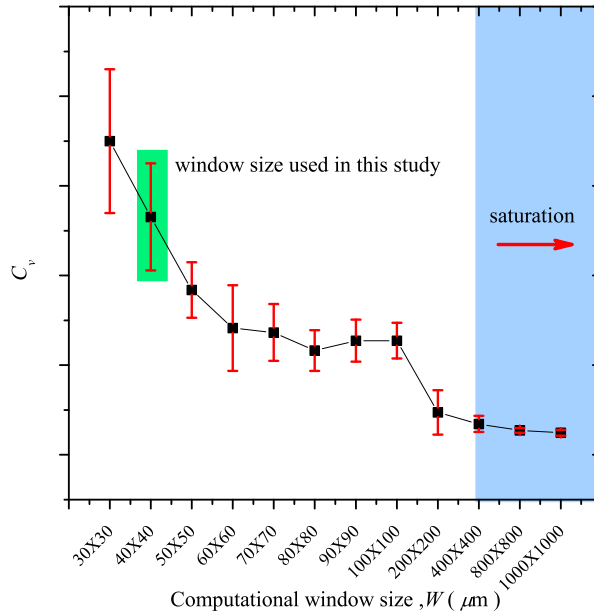
Figure 3.5: Variability in filament distribution decreases as the W increases. Increasing the W beyond $200\,\mu$m does not reduces the variability in filament distribution.

3.2.2 Increasing Filament Density

(a) Network with $\bar\rho=10$ (b) Network with $\bar\rho=8000$
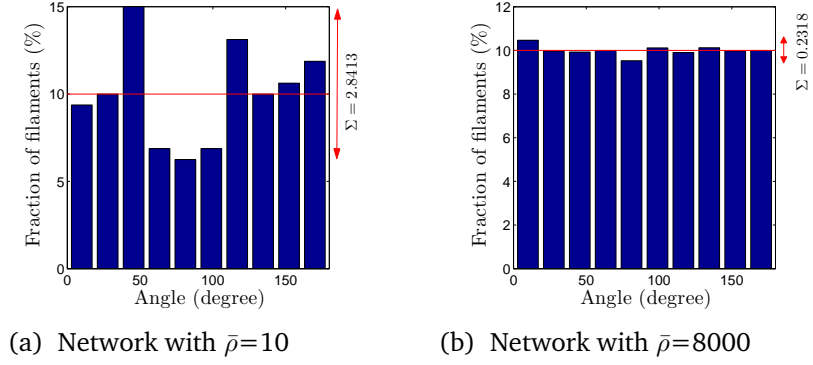
Figure 3.6: The filament distribution for $\bar\rho=10$ and 8000 is shown with the mean (red line) and standard deviation. As $\bar\rho$ increases the distribution becomes more uniform. W remains fixed at $40\,\mu$m.

An allied question that arises is - how would $\bar\rho$ affect the variability if W is fixed. As the filament location and orientation are randomly generated, more the number of filaments, better the chance of approximating the prescribed distribution function. Figure 3.6 shows the filament distribution for two typical realization with limiting values of $\bar\rho$. At a $\bar\rho = 10$, distribution shows large variability and the standard deviation Σ is high. As $\bar\rho$ increases, the distribution becomes more uniform and the standard deviation drops by an order of magnitude but only at a very high filament density, $\bar\rho = 8000$. However, this is a reasonable choice only if the global responses also tend to be independent of $\bar\rho$, e.g., in networks mimicking highly crosslinked synthetic polymers. In problems concerning low density networks, e.g., biopolymers, increasing $\bar\rho$ would not be a natural option, because the responses tend to be a strong function of $\bar\rho$. In such cases, using reasonably large W with fewer realizations or small W with large number of realizations would be the options. To find a good choice of $\bar\rho$ for a given $W = 40\ \mu$m so that the filament distribution approaches theoretical uniform distribution, Networks were generated with $\bar\rho$ ranging from 5 to 8000 and five different realizations for

each $\bar{\rho}$. Using the similar procedure as in Section 3.2.1, Fig. 3.7 shows the variability of C_v on $\bar{\rho}$, for a fixed W. It shows that C_v decreases as the $\bar{\rho}$ increases and there is a saturation value; the blue zone shown in figure. Increasing $\bar{\rho}$ beyond 1000 do not change the distribution any further. It implies that multiple realizations of networks with $\bar{\rho} \geq 400$ would tend to yield nearly identical global responses. Therefore, it may seem that the variability arising from topological differences can be mitigated by choosing a $\bar{\rho}$ for a given W.
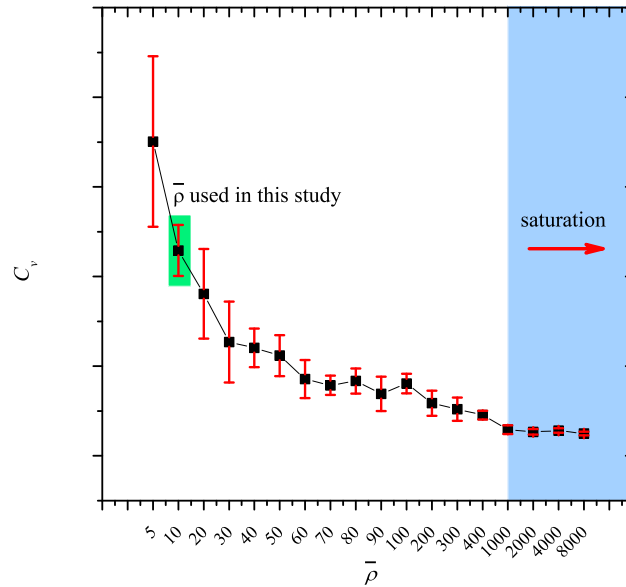
Figure 3.7: Variability in the filament distribution decreases as $\bar{\rho}$ increases. Increasing $\bar{\rho}$ above 1000 brings no change in filament distribution.

3.3　Network Characterization

Reiterating the observation in Fig. 3.2a, we show that even for a network with nominally uniform filament orientation distribution and same $\bar{\rho}$, the overall behavior could be different when the shearing direction is reversed. Likewise, rarely do two networks with same $\bar{\rho}$ exhibit identical characteristics even with nominally similar orientation parameters with respect to the loading directions (Fig. 3.2b). These observations necessitate identification of metrics for network characterization that embed in them the information of the network directionality and topological arrangement. It is seen that one of the reasons for the variability in response is due to the variation of $\theta_{\bar{\rho}}$ (deviations from the prescribed distribution) which could be reduced by choosing a large sampling window. We ask:

1. Why do the network exhibit variation in response despite of having similar $\bar{\rho}$ and crosslink densities?

2. What are the factors which contribute to this variability?

3. Is there any correlation between these factors and the mechanical response?

We examine the networks and quantify variations by characterization of these topologies based on statistical parameters. Some of the readily known factors affecting the network response are i) filament density, ii) crosslink density and iii) filament orientation. The first and second factor are related to each other but depends on the $\theta_{\bar{\rho}}$, vis-á-vis uniformly distributed networks form more crosslinks than normally distributed networks (Section 3.3.2). Characterization of the filament networks is challenging due to the myriad realizations possible and intersection of a filament with multiple other filaments. Many researchers have developed network models using discrete filamentous networks (see Table

2.1 for a summary) however, the applicability of such models are based on the limited statistics. In none of these works, the variability in response due to the microstructure is probed. In order to develop a discrete network model, it is imperative that the variability arising from various factors have to be addressed and quantified.

Analogous problem of network characterization exists in foams, porous materials, concrete etc [147, 148]. Zhu *et al.* [149] studied the role of irregularities in the elastic properties of foams using 2D random Voronoi networks. In their observation, the forms remained isotropic with varying levels of irregularity and the elastic modulus increased with randomness. Bréchet *et al.* [150] probed the role of randomness in the elasticity of cellular solids using Voroni 2D networks. They observed a power law dependence between the Young's modulus and relative density. 2D random networks considered in our work is different from the random Voronoi networks due to the long range order present in the network, the filament length L. Heussinger and Frey [131] showed the importance of underlying network structure on the macroscopic response. They considered networks of varying level of randomness and probed its influence on the elastic properties. Both random and ordered networks were used to study this and developed scaling laws for the modulus.

Network comprises of mainly three types of crosslinks based on the number of filaments intersecting at a crosslink. $\breve{Z}$agar *et al.* [151] categorized crosslinksas X-type if its the intersection of four filaments , T-type if its the intersection of three filaments and L-type if its the intersection of two filaments (Fig. 2.10). In most of the cases L-type forms the end links and X and T-types are formed in the interior of the filaments. The effectiveness of the crosslinks on the overall mechanical response depends on the type and stiffness of the crosslinks. If the crosslinks are stiff, X-type crosslink is the one which dominates the mechanical

response. They identified a topological function based on the mean distance between crosslinks, mesh size and the number of X-type crosslinks and developed scaling laws for the initial shear stiffness of the biopolymeric networks with rigid crosslinks [151]. Such a scaling is applicable only for the networks that are assumed to be uniformly distributed and these statistics fails when the networks have a resulting orientation. We identified statistical parameters in similar lines that can account for both filament orientation and crosslink density and applicable to networks of any orientation an filament density.

3.3.1   Crosslink Moment X_M

One of the reasons for the variation in the response of networks having similar filament and crosslink density is the variation in the distribution of crosslinks rather than the total number of crosslinks. For uniformly distributed networks the, distribution could be macroscopically uniform. However, there could be local regions where the filaments and crosslinks form cluster that alter the response. We identified a parameters which is the moment of the crosslinks with respect to a chosen reference axis[1]. The crosslink moment accounts for not just the number but also the effect of the spacial distribution. If the compartment approach is used in calculating the moment, it gives a better measure about the uniformity of the crosslink distribution. Such an approach is shown in Fig. 2.6 where the moments of the crosslinks are found with the RVE as a whole and after dividing the RVE into 3×3 compartments. The moment of the crosslinks is calculated as

---

[1]Present work focuses on the shear loading of the polymeric networks. The principal loading direction for a square domain will be the diagonal inclined at 45^0. Motivating from these, we are considering an axis inclined at 45^0 for the calculation of crosslink moments. If the deformation mode changes from shear to tension, correspondingly the axis should also be changed.

$$X_M = \frac{1}{n} \sum_{i=1}^{n} d_{p_i} \tag{3.1}$$

where n is the total number of crosslinks and d_{p_i} is the perpendicular distance between the crosslink and a chosen axis. When the RVE is divided into compartments, the equivalent moments can be calculated as in the case of spring networks. This approach could account for the periodic boundary condition of the RVE.

3.3.2 Crosslink Factor X_F

In lines with Žagar *et al.*, we defined *crosslink factor* (X_F) which is the ratio of X-type crosslink to the total number of crosslinks in a RVE.

$$X_F = \frac{n_X}{n_X + n_T + n_L} \tag{3.2}$$

where n_X is the total number of X-type crosslinks and similarly for other types of crosslinks. As the X-type crosslink has the maximum connectivity,it plays a dominant role in the overall network response. Evolution of X_F with density depends on the filament distribution.

Uniform $\theta_{\bar{\rho}}$: Black symbols in Fig. 3.8 show the evolution of X_F. Average of several simulations shows that X_F increases with density and the bounds becomes tighter as the $\bar{\rho}$ increases.

Normal $\theta_{\bar{\rho}}$: Red symbols in Fig. 3.8 show the evolution of X_F and the trend is very similar to that in the case of uniform distribution but the actual value of the X_F for a given density is lower by a factor of 2 and the trend is consistent across various $\bar{\rho}$ considered here. The reason for this lower crosslink density is

the lower spread of the filaments unlike in the case of uniform $\theta_{\bar{\rho}}$ where there is higher chances of a filament making more intersections due to the random nature of the distribution.
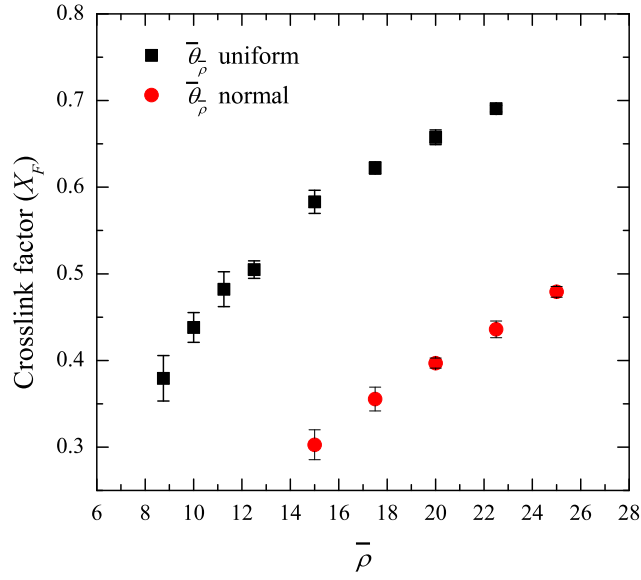
Figure 3.8: Variation of X_F with $\bar{\rho}$ for networks with uniform filament distribution. At lower $\bar{\rho}$, the variation is high and the bounds becomes smaller as $\bar{\rho}$ increases. The error bar shows one standard deviation.

3.3.3 Alignment Factor A_F

The type of crosslinks could give information about the mechanical response pertaining to the crosslink density but it may not give any information about the anisotropic response observed in the network structures. If the same network is subjected to shear deformation in opposite directions, the response could vary drastically depending on the filament alignment although the type and number of crosslinks remains same in both cases (Fig. 3.2a). Another occasion is when

the filament distribution is non uniform. The response of the network with preferred orientation becomes highly anisotropic and the correlation with the (X_F) is not observed in this case (Fig. 3.18). We have used networks with filaments normally distributed in the preferred direction (mean angle μ') with a predetermined standard deviation (Σ). Σ of the orientation determines the spread of the filaments. In order to account for anisotropy, we defined a parameter called the *alignment factor* (A_F) which is the ratio of the sum of projected length of the filaments along a principal loading axis to the total length of filaments.

$$A_F = \frac{\sum_{i=0}^{N} L_{a_i}}{\sum_{i=0}^{N} L_i} \tag{3.3}$$

where L_{a_i} is the projected length of the line segment along an axis considered and L_i is the length of the line segment. When the loading direction changes, the axis considered for A_F changes and its value could be different for different directions. As in the case of X_F, variation of A_F with density is also filament distribution dependent.
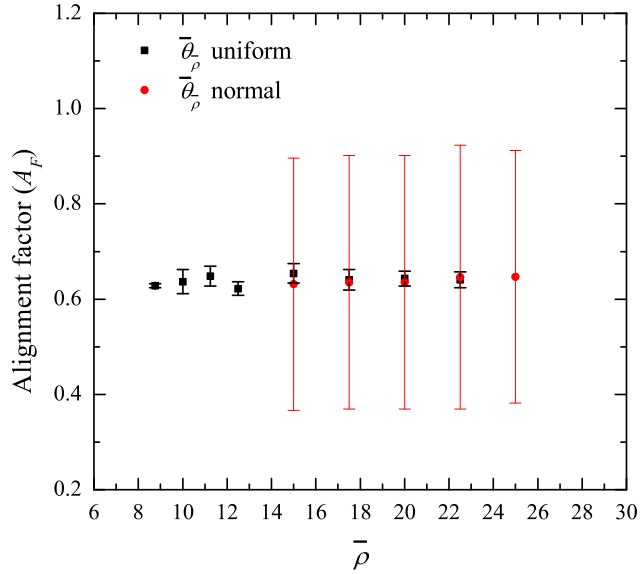
Figure 3.9: Variation of A_F with $\bar{\rho}$. Value of A_F does not change significantly with $\bar{\rho}$ for networks with uniform $\theta_{\bar{\rho}}$ and fluctuates around the mean value of 0.64. The same trend is not observed for networks with uniform $\theta_{\bar{\rho}}$, for the favorable orientation ($\mu' = 45^0$), $A_F \approx 1$ while for unfavorable orientation ($\mu' = 135^0$), $A_F \approx 0$. The error bar shows one standard deviation.

Uniform $\theta_{\bar{\rho}}$: Black symbols in Fig. 3.9 show the variation of A_F with $\bar{\rho}$ for networks with uniform $\theta_{\bar{\rho}}$. Unlike in the case of X_F (Fig. 3.8), A_F does not increase with $\bar{\rho}$ but oscillate abound a mean value of 0.64. Furthermore, the value of A_F remains in the same range if different axis is used for the calculation.

Normal $\theta_{\bar{\rho}}$: A_F changes drastically with the axis considered (black symbols in Fig. 3.9). A network with normal $\theta_{\bar{\rho}}$ with $\mu' = 45^0$ shows a very high value for A_F if the axis used for the calculation is inclined at 45^0 ($A_F \approx 0.9$) but the value of A_F is very low if the axis is changed to one inclined at 135^0 ($A_F \approx 0.2$). The average value with one standard deviation is shown here. This implies the role of A_F in accounting for the resulting orientation of the network.

76

3.3.4 Fabric Factor F_F

In a nutshell, X_F accounts for the role of $\bar{\rho}$ which may be related to the filament density while the A_F accounts for the effect of orientation of the filaments ($\theta_{\bar{\rho}}$). Any of these parameters used alone cannot account for the complete network response. To overcome this shortcoming, we defined a parameter called *fabric factor* (F_F) which is the product of X_F and A_F. F_F accounts for both filament density and orientation.

$$F_F = X_F A_F \qquad (3.4)$$

We found that F_F shows very good correlation with the response (K_0 and γ_T) for a range of filament densities and $\theta_{\bar{\rho}}$. We systematically probed the influence of all these parameters on the mechanical response of networks with rigid crosslinks in the following sections. Failure of crosslinks is not accounted in the results presented in this chapter.

3.4 Overall Network Response

Before delving into understanding the response uncertainty due to microstructural variability, we first discuss the effect of network filament density $\bar{\rho}$ and network orientation distribution on the overall mechanical response. The basic network parameters are chosen and the generated architectures are investigated under simple shear condition. Between all the cases considered here the filament properties as well as the inter-filament junction characteristics (i.e., bonds or crosslinks) are kept fixed[2]. The typical properties considered here are indicative

---

[2]Chapter 5 discusses the effect of filament and crosslink properties.

of F-actin networks where the filament bending and stretching rigidities are not necessarily correlated (unlike in generic truss or framed structures where a prescription of the elastic modulus, cross-sectional shape and dimensions automatically define the member rigidities). This discrepancy arises in nearly all flimsy networks because of the importance of the influence of the thermal fluctuations that introduce the notion of a persistence length that gets intimately connected to the member flexural rigidity [78]. We do not model thermal fluctuations, but use a simple strategy that accommodates this dichotomy between the two rigidities. Rather than providing the filament material and cross-sectional properties separately, we directly prescribe their stiffness properties by assuming a generalized cross-section internally with the FE framework. The flexural rigidity (EI) is set to 8.4×10^{-22} Nm^{-2} and the axial rigidity (EA) is set equal to 1.6×10^{-4} N. These properties resemble those of F-actin filaments that form semi-flexible networks within eukaryotic cells [82]. The crosslinks are assumed to be elastically rigid, which is a reasonable assumption for some biopolymeric networks [33] (as well as some synthetic networks [115]) and for simplicity, they are assumed to be infinitely strong so that failure does not occur[3].

---

[3]Both these assumptions are relaxed in Chapter 5.

3.4.1 Effect of Topological Arrangements for a fixed $\bar{\rho}$ and $\theta_{\bar{\rho}}$
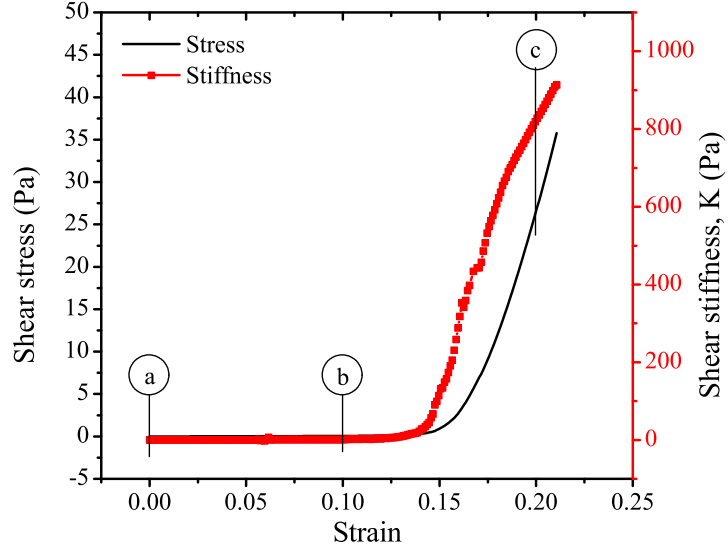
Figure 3.10: Variation of stress and stiffness of a network with $\bar{\rho} = 10$ deformed with a shear rate of $\dot{\gamma} = 1s^{-1}$. The deformed configuration of the network at the three markers shown are given in Fig. 3.11.

Figure 3.10 (black curve) shows the overall shear stress - shear strain $(\tau - \gamma)$ responses of a network realization (with $\bar{\rho} = 10$) subjected to applied shear strain rate $\dot{\gamma} = 1s^{-1}$. From the $\tau - \gamma$ curves, the tangent shear stiffness K is obtained by numerically calculating the derivative $\partial\tau/\partial\gamma$ and is plotted as a function of γ, shown in the same figure (red curve). The overall response is highly nonlinear and shows strain stiffening with a steep increase in stiffness at strain of ≈ 12.5 to 15%. The entire deformation history of the network is explained with help of the stress/stiffness- strain curves and the corresponding snapshots of the deformed configuration of the network taken at three strains.
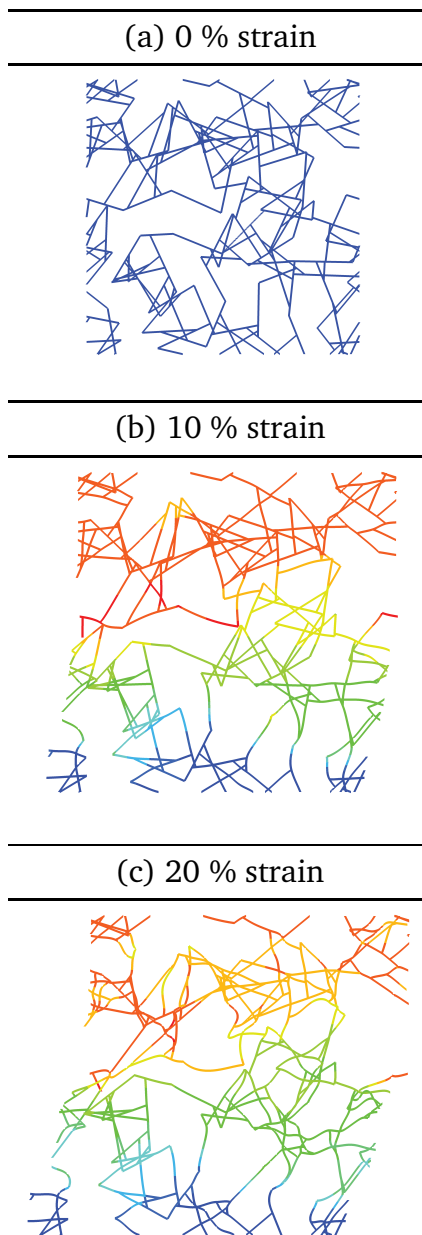
Figure 3.11: Snapshots of the network at three strains. Colors represent the resultant displacement in the network. (a) Shows the initial configuration with straight filaments. (b) At a strain of 10%, filaments reorient to the loading direction by bending and stretching and the network stiffness starts to increase. (c) At a strain of 20% network stiffness increases to ≈600 times of the stiffness in Fig. b (see Fig. 3.10).

Figure 3.11a shows the initial configuration at zero strain. At a strain of 10%, the stress and stiffness of the network does not increase to an appreciable value. Figure 3.11b shows the network at 10% strain, it can be seen that some of the filaments have slightly reoriented and the local deformation is different from the applied macroscopic deformation (colors represent the resultant displacement in the network). Such localized deformation is called *non-affine* deformation and is more evident from the vector plot of the displacement on the deformed network as one shown in Fig. 3.12. Most importantly, the material properties used for the filaments are linear while the response of the network is highly nonlinear. This nonlinearity arises purely out of the non-affine deformation due to the bending and buckling of filaments (a similar argument can be found in the work of Onck *et al.* [78]). At a strain on $< 10\%$ the deformation is predominantly bending dominated.

The sudden jump in stress and corresponding stiffness at a strain range of ≈ 12.5 to 15% marks the change in deformation from bending dominated to stretching dominated. This point is defined at the *transition strain* γ_T. As this process takes place over a range of strain, γ_T is defined as the strain at which $K/K_0 \approx 10$(see Section 3.5.2 for a discussion about γ_T). This transition does not implies the end of non-affine response or bending of filaments but the main mode of deformation changes to stretching rather than bending. At a strain of 20% (point c in Fig. 3.10), the stiffness of the network is nearly ≈ 600 times of the stiffness at 10% strain. The corresponding network configuration is shown in Fig. 3.11c. With further straining, localization/bundling of the filaments takes place and the network stiffness increases even further. This nonlinear stiffening is common to all networks having similar constituent filaments and an example for such a deformation from biological world; stress fibers formed in F-actin networks is a similar bundle of fibers formed to resist the external mechanical stimuli [152–

154]. We verify this concept for a wide range of $\bar{\rho}$ and filament property and a more detailed discussion about the non-affine response is given in Chapter 5. Having said about the overall response of a network, next we consider the role of various factors which affect the network response from a topological perspective.
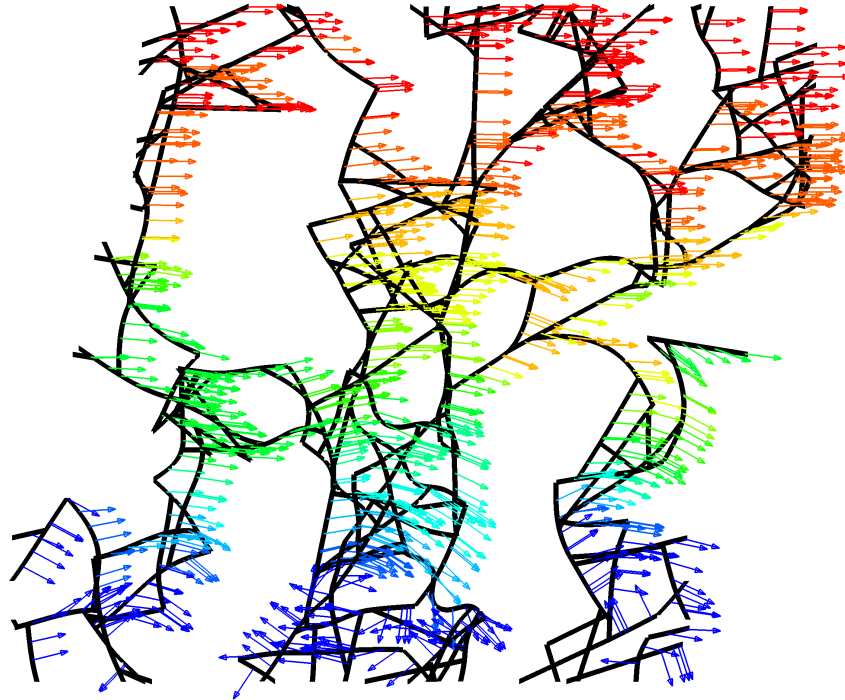
Figure 3.12: Vector plot of the displacement of a network at a strain of 20% showing the non-affine deformation. The applied shear load is in the horizontal direction while some of the filament rotates and the deformation differs from the global applied deformation.

3.4.2 Effect of Filament Density $\bar{\rho}$
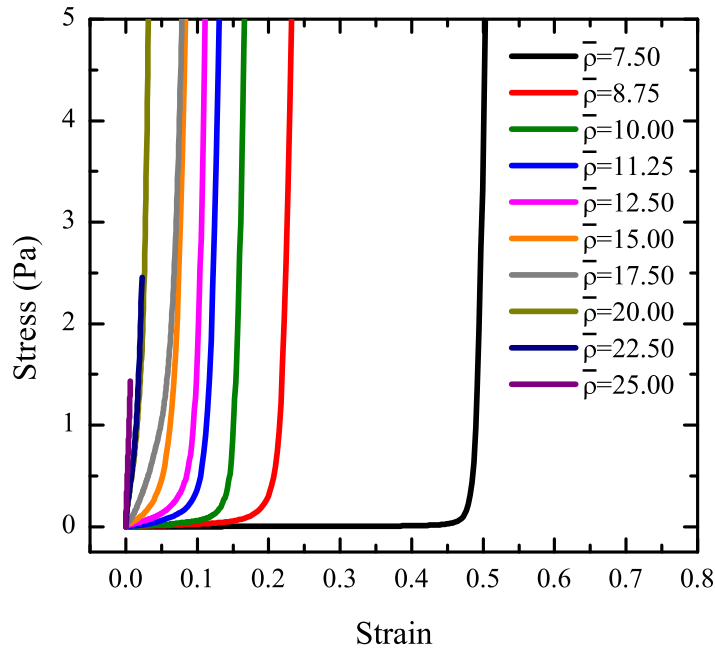
Figure 3.13: Stress-strain response of networks with increasing filament density $\bar{\rho}$. As the filament density increases, the initial response stiffens early and tends to be linear. Typically, biopolymers (low to intermediate $\bar{\rho}$) exhibit nonlinear elastic responses while synthetic polymers (high $\bar{\rho}$) exhibit linear elastic responses.

At a given strain, the overall stiffness of a fibrous network depends on the network connectivity. It is known that fibrous networks support load only if the filament density is above a certain threshold connectivity. This is referred to as the *rigidity percolation*[4] [133]. Below the rigidity percolation, a network may not be a integrally connected structure and therefore, could act like a mechanism. The idea is quite analogous to the truss structures in civil engineering where a given system of truss (bars with hinged joints) has to satisfy a certain criterion for it to be able to support an applied load. For fibrous networks, above the

---

[4]See Section 2.3.1 for a discussion about rigidity percolation.

rigidity percolation, the structural stiffness typically increases with increasing filament density. Increasing the number of filaments results in a better network connectivity resulting in higher stiffness. Increasing the filament density makes the network response more affine; instead of showing initially flimsy response followed by steep stiffening, it tend to be more stiffer and linear in response.

The role of filament density is shown here by increasing density from $\bar{\rho} = 7.5$ to 25. Figure 3.13 shows the stress-strain response of the networks with increasing $\bar{\rho}$. The filament densities considered here are motivated from practical problems, e.g., biopolymers like F-actin networks typically have density $\approx \bar{\rho} = 10$, electospun/paper networks shows intermediate densities and synthetic polymer like epoxies shows very high density[5] [111, 155]. Due to high nonlinearity, the response of different $\bar{\rho}$ cannot be compared easily. Here we make use of the parameters we have defined earlier; K and γ_T. Only a qualitative description is given in this section, for more detailed discussion please refer to Section 3.5. The response of networks is similar to the example explained in the preceding section and characteristics of the deformation are same, non-affine and nonlinear stiffening. An interesting observation is that the response tend to be more of linear at higher densities, e.g.,$\bar{\rho} = 22.5$ and 25 . At a $\bar{\rho} = 7.5$, the response is highly nonlinear and there is a transition at a strain of $\approx 50\%$ and K increases with a steep slope (Fig. 3.13). As the $\bar{\rho}$ increases, γ_T decreases and the response becomes more and more linear. This signifies that the non-affine contributions reduces as $\bar{\rho}$ increases and the deformation is stretching dominated.

---

[5]Material property of the filaments varies with materials. In the present context, we motivate it from a topological perceptive. Chapter 5 discusses the role of filament property in the response.

(a) Stiffness   (b) Normalized Stiffness
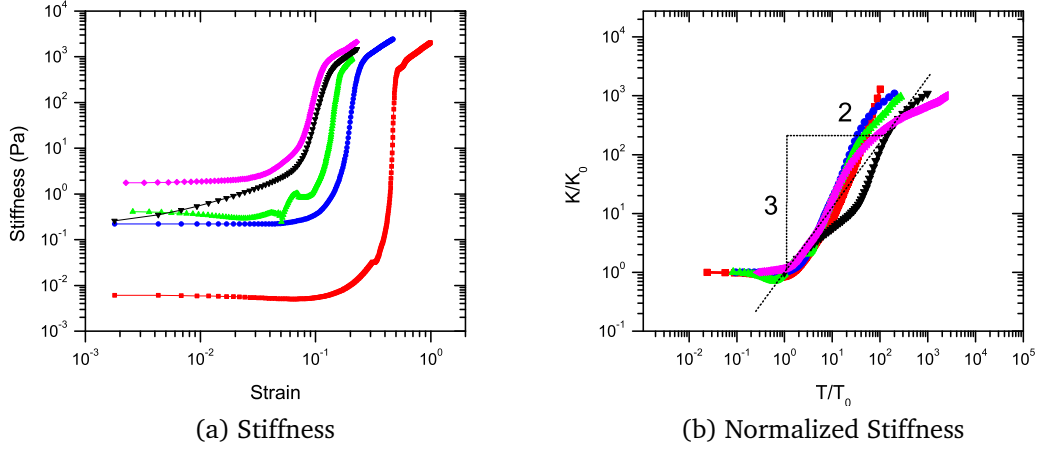
Figure 3.14: Stiffness evolution of networks with increasing $\bar{\rho}$. (a) The network initial stiffness increases with $\bar{\rho}$. (b) Curves collapses when the stiffness is scaled and plotted as a function of scaled stress. The average slope of the curves is 3/2 as shown by Žagar *et al.* [156].

Žagar *et al.* studied such a case of increasing $\bar{\rho}$ or decreasing l_c and developed scaling laws for the long strain response, given by $\tilde{K} \propto \tau^{3/2}$ [156]. To investigate whether such a scaling law also holds for the cases considered in our simulations, we plot the stiffness response when the l_c is decreased. Figure 5.3a shows the stiffness-strain curves and is similar to the cases shown in Fig. 3.10. In Fig. 5.3a, the stiffness is normalized and is plotted as a function of T/T_C as in the work of Žagar, all curves collapses with a mean slope of $3/2$ in the log-log scale [156]. Such a scaling is possible only if the bending length $l_b{}^6$ is similar in all cases as shown in Section 5.2.1.

---

[6]It is a material length scale given by $l_b = \sqrt{(\kappa/\mu_s)}$. See Chapter 5 for a discussion about l_b.

3.4.3 Effect of Filament Distribution

While filament density plays an important role in describing network responses (as shown in the previous section), it may not be a sufficient metric to fully characterize their behaviors. Indeed, network realizations with same filament density but different net orientations with respect to the loading direction can exhibit overall stiffness characteristics that could vary by several orders of magnitude. Filament distribution could range from uniform to highly oriented ones.
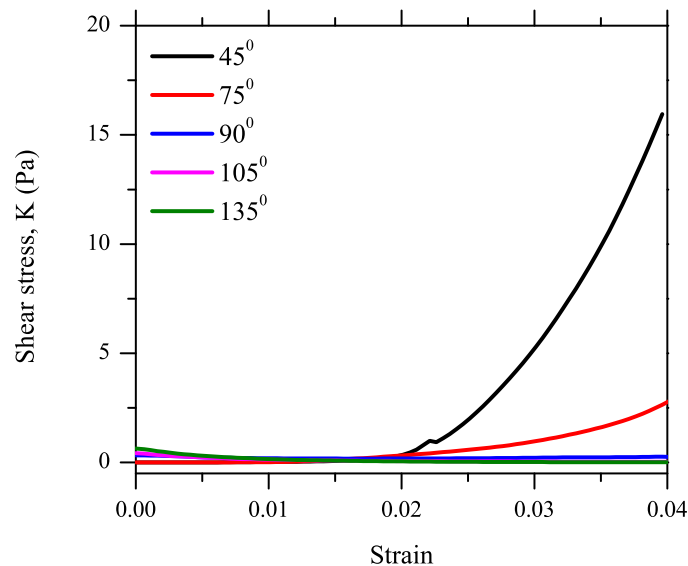
Figure 3.15: Response of normally distributed networks to shear loading. Networks with a net orientation of 45^0 shows stronger response compared to one with net orientation of 135^0.

86
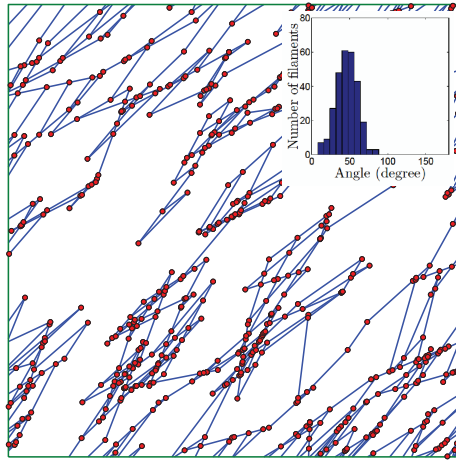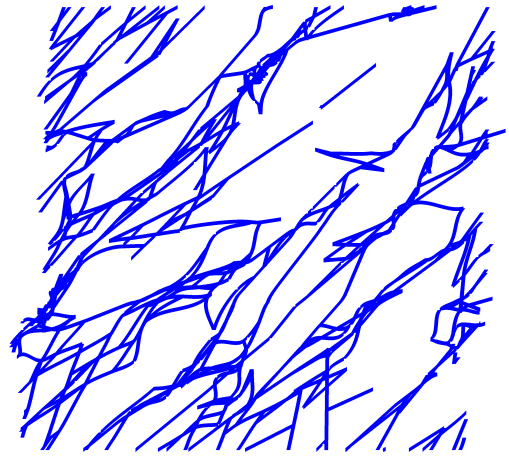
(a) Initial network   (c) Deformed network
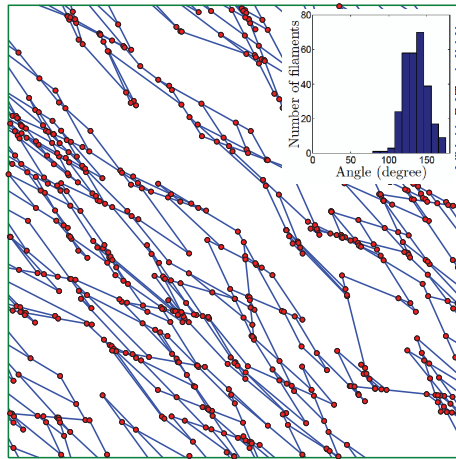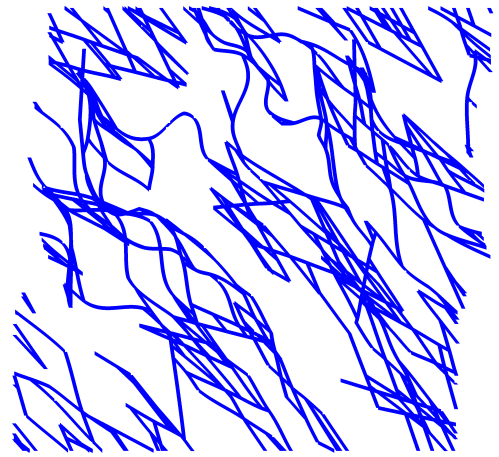
(d) Initial network   (f) Deformed network

Figure 3.16: Networks with normal filament distributions. (a) Shows the initial configuration of a network with $\mu' = 45^0$. The histogram of the filament distribution is shown in the inset. Majority of the filaments are oriented at 45^0. (b) The deformed configuration at a strain of 4%. Figures (c) and (d) shows the same for a network with $\mu' = 135^0$. The clear distinction between the deformation of these two orientations; for $\theta_{\bar{\rho}}$ with $\mu' = 45^0$, filaments get stretched as they are aligned to the shear loading whereas for $\mu' = 135^0$, filaments are not aligned to the loading direction and they bend and rotate to the applied load showing compliant response (Fig. 3.15).

It is seen preceding sections that the filament try to reorient towards the loading

direction by bending and subsequent rotation. The significance of this process can be clearly understood by considering networks with same $\bar{\rho}$ but having different resulting filament orientations. Figure 3.16 shows two such networks with a mean orientation of $\mu' = 45^0$ (Fig. 3.16a) and $\mu' = 135^0$ (Fig. 3.16d) and the corresponding histogram of the $\theta_{\bar{\rho}}$ is shown in Fig. 3.16b and e. For both cases, $\Sigma = 15^0$. At a strain of 4%, the network with $\mu' = 45^0$, filaments are deformed in stretching (Fig. 3.16c) while for the $\mu' = 135^0$, filaments are in bending (Fig. 3.16f) leading to vast difference in the resulting network stiffness K.

Figure3.15 summarizes the results of four such orientations. Network with $\mu' = 45^0$ shows the stiffest response and the stiffness decreases as the orientation becomes more unfavorable and the least stiffness is for $\mu' = 135^0$. When $\mu' = 45^0$, the primary component of the strain energy during deformation is stretching and the bending energy contribution is small. As the μ' changes, the proportion of stretching/bending changes leading to the decrease in stretching and bending contribution increases. At $\mu' = 135^0$, the energy balance is reverse as of $\mu' = 45^0$. We have seen in Section 3.4.2 that the stiffness increases with $\bar{\rho}$. The key difference in the overall response with increasing $\bar{\rho}$ and changing the $\theta_{\bar{\rho}}$ at a fixed $\bar{\rho}$ is the variation in γ_T; for the former, its decreases as the $\bar{\rho}$ increases however, γ_T remains at the same value for different $\theta_{\bar{\rho}}$.

3.4.4 Loading Direction

The direction of shear loading direction has a similar effect on the overall mechanical response as in the case of filament orientation distribution. The response of a network with a net orientation to loading in one direction is nearly same as that of a network with orientation offset by 90^0 and loaded in opposite direction. A network exhibits a highly stiff response (sometimes tending toward linearity) if

its filaments are primarily oriented along the loading direction, with the network stiffness governed by the concerted stretching of the filaments. However, if the same initial network configuration is shear loaded in the reverse sense, it shows a highly compliant response that is now dominated by the relatively much softer bending mode of the filaments (Fig. 3.2a). This is because the filaments tend to buckle because of the alignment with the principal compressive axis.

3.5 Correlation between Network Topology and Mechanical Response

In this section, we describe the results of an extensive set of numerical experiments performed on a range of network realizations comprising varying filament and crosslink densities and filament orientations ($\theta_{\bar{\rho}}$). Two types of $\theta_{\bar{\rho}}$, uniform and normal are used to probe the role of filament orientation (Fig. 3.17). For normal distribution, networks with a mean orientations ranging from 45^0 to 135^0 to the x-axis with a standard deviation $\Sigma=15^0$ are considered. For each type of $\theta_{\bar{\rho}}$ and net orientation, networks with eight different $\bar{\rho}$ and for each of the cases, 5-8 different realizations are considered (see Table 3.1 for the list of cases considered). Altogether ≈ 300 simulations are done. Note that increasing the standard deviation makes the network more disoriented (i.e., randomized architectures tending toward uniform distributions), while smaller standard deviations tends to produce highly oriented networks. The latter may also affect the network connectivity, which is an important issue to consider from the viewpoint of the percolation threshold for a given $\bar{\rho}$.

In what follows, we discuss the results in terms of the network initial stiffness K_0 and transition strain γ_T described in Section 3.4.1. Specifically, we show their
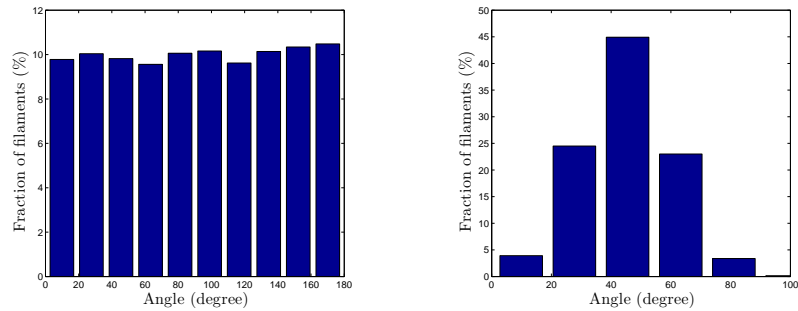
(a) Uniform filament distribution   (b) Normal distribution (45 ± 15^0)

Figure 3.17: Distribution of filament orientation angles in networks (a) Uniform network (b) Normally distributed network with a mean orientation of 45^0 and a standard deviation of 15^0.

dependencies on the network orientation (described by the alignment factor A_F) and the crosslink density (described by the crosslink factor X_F). Then, we utilize a composite factor that embeds the information from A_F and X_F and exhibits good correlation with K_0 and γ_T for a wide range of network characteristics. We discuss the significance and implications of identifying such a unified metric. The relevance of all three (X_F, A_F and F_F) statistical parameters[7] in understanding the network response is explained and its correlation with response is shown for networks with a range of filament distributions and crosslink densities.

3.5.1   Effect on the Initial Stiffness K_0

As discussed in Section 3.4, a filamentous network supports applied loads through a combination of filament bending and stretching. The relative contributions from each of these deformation modes depend on the elastic and geometric properties of the filaments. In situations where the filament bending stiffness dominates a significant portion of the overall response (Fig. 3.13), it is of interest

---

[7]Refer to Section 3.3 for more details.

90

to investigate if K_0 depends on the topological parameters and if so, what is the nature of this dependency[8].

To enable answering this question in terms of A_F and X_F, we consider the a range of networks with mean orientations ranging between 0^0 to 45^0 (describes the role of A_F) for a range of $\bar{\rho}$ (partly affects X_F), subjected to simple shear. Note that increasing A_F indicates increased bias in the network orientation with respect to the loading direction (also referred to here as preferential or favorable orientation). That is, for a given $\bar{\rho}$, a higher A_F indicates that a larger proportion of the filaments are initially oriented along the principal tensile axis.

Table 3.1: Details of the networks used for characterization. In all cases the RVE size was fixed at $40\,\mu$m and the filament length at $L = 10\ \mu$m. For each of the normally distributed cases, 5 filament orientations with $\mu' = 40^0, 75^0, 90^0, 115^0$ and 135^0 with a $\Sigma = 15^0$ is considered.

No. of Filaments (N)	Filament density ($\bar{\rho}$)	Filament distribution ($\theta_{\bar{\rho}}$)
140	8.75	uniform
160	10.00	uniform
180	11.25	uniform
240	15.00	uniform & normal
280	17.50	uniform & normal
320	20.00	uniform & normal
360	22.50	uniform & normal
400	25.00	uniform & normal

[8]If cross links are not rigid, K_0 is modulated by the crosslink stiffness. See Chapter 5, Section 5.3 for a detailed discussion.
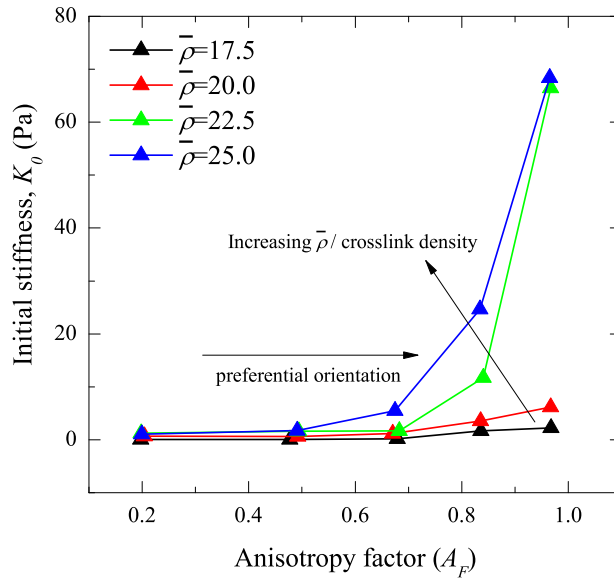
Figure 3.18: Variation of K_0 with A_F for normal $\theta_{\bar{\rho}}$. Higher alignment factor shows the initial orientation of the filament to the loading direction which results in high initial stiffness during loading. Increase in $\bar{\rho}$ also makes the response stiffer.

Figure 3.18 shows the variation of K_0 with A_F for different filament densities with a normal $\theta_{\bar{\rho}}$ (Table 3.1). Each data point is an average of about 5 to 8 simulations. The plot reveals several interesting features: first, the general trend is that K_0 increases with increasing A_F across the entire range of $\bar{\rho}$ considered. This is expected, because for any given $\bar{\rho}$ increasing A_F accentuates the role of filament stretching over its bending counterpart producing an overall stiffer network. Second, the magnitude of this enhancement is highly dependent on the filament density. At higher $\bar{\rho}$ the increase in K_0 is a strongly nonlinear function of A_F and the critical A_F, $(A_F)_{cr}$ beyond which the enhancement is rapid decreases with increasing $\bar{\rho}$. This trend appears because of two reasons: (i) a higher filament density generates a more rigid network as the stiffnesses scale inversely with the effective filament lengths and (ii) a higher A_F means more filaments are

already apportioned along the tensile axis, which is the predominant load carrying direction. Consequently, such networks tend to mitigate the requirement of filament reorientation and hence, K_0 is dictated by the filament stretching mode rather than the bending mode, the limiting case being $A_F \approx 1$. However, this does not happen at all $\bar{\rho}$ and there seems to be a critical filament density that produces a high stiffening effect with increased A_F. In other words, at the other end of the spectrum $(A_F = 0)$ shows the network with net orientation towards the diagonal at 135^0 and shows a flimsy response. K_0 increases with increasing A_F and another observation about the stiffening response is the rate of stiffening; it increases with increasing $\bar{\rho}$. This indicates the role of network density in the overall hardening along with filament orientation.
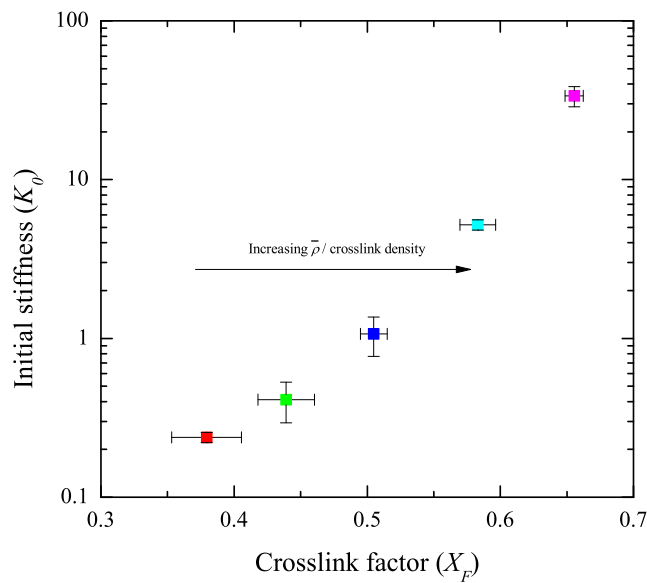
Figure 3.19: Variation of K_0 with X_F for networks having uniform filament orientation. As the $\bar{\rho}$ increases, the fraction of X-type crosslinks increases and the overall network stiffness increases. See Fig. 3.8 for the variation of X_F with $\bar{\rho}$.

One may ask a slightly different question: For a given orientation distribution,

what is the relation between the network connectivity and K_0? Figure 3.19 precisely answers this question for the case of uniform filament distribution (A_F value for networks with uniform $\theta_{\bar{\rho}} \approx 0.64$, see Fig. 3.9). Given that the filament orientation is similar in all the cases, the plot clearly shows that a higher density of X-type crosslinks in a given network (i.e., higher X_F), the stiffer is the initial network response. This is a direct consequence of the fact that amongst a variety of junction types, X-type crosslinks possess the largest coordination number of 4, rendering a more effective network connectivity for load sharing. Thus, even though two networks may possess similar A_F, their responses may vary depending on the value of X_F.
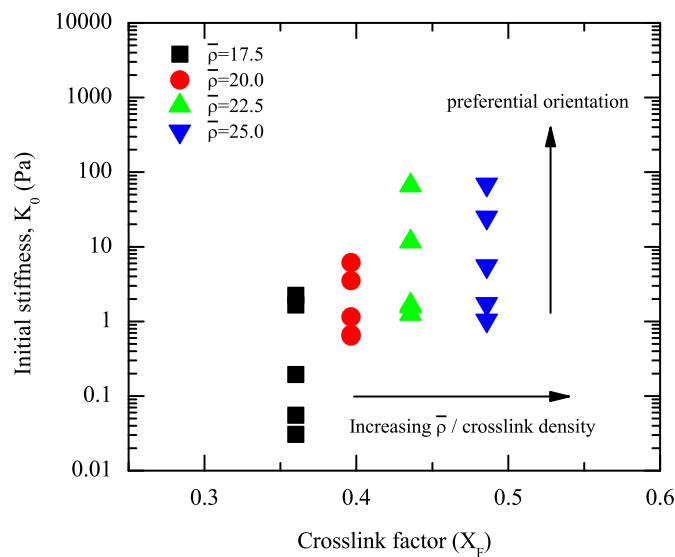
Figure 3.20: Variation of K_0 with X_F for networks having uniform filament orientation. As the $\bar{\rho}$ increases, the fraction of X-type crosslinks increases and the overall network stiffness increases. See Fig. 3.8 for the variation of X_F with $\bar{\rho}$.

In précis, it is clear that for a fixed $\bar{\rho}$, A_F accounts for the filament distribution and exhibits a consistent relationship with K_0 (Fig. 3.18), but it does not account

for the crosslink/filament density. Likewise, X_F accounts for the crosslink density (i.e. network connectivity) and correlates very well with K_0 for networks with uniform $\theta_{\bar{\rho}}$ (Fig. 3.19), but the correlation breaks down when there is a net orientation in the filament distribution. Figure 3.20 shows the variation of K_0 with X_F for networks with normal $\theta_{\bar{\rho}}$. For each $\bar{\rho}$, we have considered 5 filament orientations; $40^0, 75^0, 90^0, 115^0$ and 135^0. It is evident from Fig. 3.20 that the stiffness not only depends on X_F but also on the resultant filament orientation, i.e., on A_F. Due to this dependence of stiffness on both A_F and X_F and to account for both crosslink density and filament orientation, a natural question arises as to whether it is possible to consider a metric that captures the combined effect and whether it would exhibit any correlation. The following section address on this question.

3.5.2 Developing Scaling Law for K_0 and γ_T

A simple-minded way of embedding the effects of A_F and X_F is to use the composite $F_F = A_F X_F$, referred to here as Fabric Factor (see Section 3.3.4). The fact that it is obtained as a product of the filament orientation distribution and network connectivity inherently suggests a synergistic interaction between the two. Continuing from the discussion in the preceding section, Fig. 3.21 combines the results of Figs.3.18, 3.19 and 3.20 into a log-log plot that shows K_0 as a function of F_F. The error bars bounding each average result (average obtained from about 5 to 8 cases for each data point) indicate the variability observed for a given set of topological parameters[9]. However, before discussing the trend, it is informative to comment on the range of F_F that is in turn delineated by the ranges of A_F and X_F. Based on our statistical analysis for several networks with

---

[9]This plot combines the results from ≈ 300 simulations.

uniform filament distribution we obtain that $A_F \approx 0.64$ for axis along both 45^0 and 135^0 diagonals (Eq. 3.3). If we consider such networks above the rigidity percolation (i.e., $\bar{\rho} > 5.6$, which sets the minimum for $X_F \approx 0.3$, see Fig. 3.19), we obtain $F_F \approx 0.2$. Thus, all networks with uniform filament distribution fall in the range $0.2 \leq F_F \leq 0.6$. On the other hand, networks with normal $\theta_{\bar{\rho}}$ tend to exhibit different A_F along its principal diagonals. For a given network, A_F is higher in one direction than in the other, because of the preferential orientation; note that for these cases, X_F depends on $\bar{\rho}$, but is the same irrespective of which principal diagonal is under consideration.

With this background, the results in Figure 3.21 indicate three regimes as we traverse along the F_F axis. These are, Regime 1: $F_F < 0.1$, Regime 2: $0.1 \leq F_F \leq 0.24$ and Regime 3: $F_F > 0.25$. Regime 1 signifies network topologies that are both unfavorably oriented (very low A_F) and poorly connected (low X_F) resulting in low K_0 that indicate flimsy networks. Regime 2 may be designated as an intermediate region where the overall fabric of the network is still poor, but may be because of plethora of topological possibilities that result in an overall flimsy fabric. For example, a network may be highly favorably oriented network ($A_F \to 1$, see Fig. 3.18), but poorly connected ($X_F \to 0.3$, see Fig. 3.19), or reasonably connected, but poorly oriented, and so on. With one or both the parameters working against providing adequate structural support, the initial stiffness responses resemble networks that tend to deform predominantly by filament bending. Regime 3 seems to evolve from a bending dominated behavior at its lower end ($0.25 \leq F_F \leq \approx 0.3$) to a stretching dominated behavior for $F_F \geq 0.3$. An interesting observation in Regime 3 is the range of K_0 exhibited by the networks with uniform distributions (solid squares). Particularly, those that possess high K_0 indicate the response that may be at least as stiff or even stiffer

compared to the normally distributed networks (solid circles). This indirectly indicates that the crosslink density of the uniform distribution is higher and can be attributed to the random nature of the filament orientations (Fig. 3.8). This may be further accentuated with increasing $\bar{\rho}$, and suggests that crosslink density is an important parameter which governing the network response.

Finally, the plot provides scaling laws for networks in each of the regimes. In each of the regimes the $K_0 - F_F$ relationship shows a linear regression indicating a power-law dependence of the initial stiffness on the fabric of a network. This gives a unique estimate of the initial stiffness of a network provided one knows its fabric factor. The scaling exponent of the lines are 4.5, 6 and 10 in regimes 1, 2 and 3, respectively. However, while the uniqueness exists in determining K_0 for a known F_F, there exists ambiguity in unequivocally ascribing a fabric to a network provided one already has information about K_0. This is particularly the case in $0.1 \leq F_F \leq 0.3$ range. For example, if a network has a $K_0 = 1$ Pa, it may resemble a network with $F_F = 0.85, 0.21$ or 0.3. It is only in the regime $F_F \geq 0.32$ that a unique correlation becomes possible, $K_0 \propto F_F^{10}$ (shaded region). However, one could argue that the non-uniqueness in the low F_F regime suggests that for networks that possess low initial stiffness ($K_0 < 2$ Pa) the fabric factor does not matter. Note that in Regimes 1 and 2, value of stiffness is always less than 2 Pa. This could be due to either of the two reasons mentioned earlier in this section; poor network connectivity or unfavorable filament orientation.

A similar scaling law based on the topological parameters for the scaled initial stiffness was given by $\breve{Z}$agar *et al.* with a scaling exponent of 2.5. Their work is limited only to networks with uniform filament orientation as the filament orientation start to play a dominant role when there is a resulting orientation in the network. Heussinger and Frey [131] looked a semiflexible networks with random network to regular lattice structure. They considered the role of filament
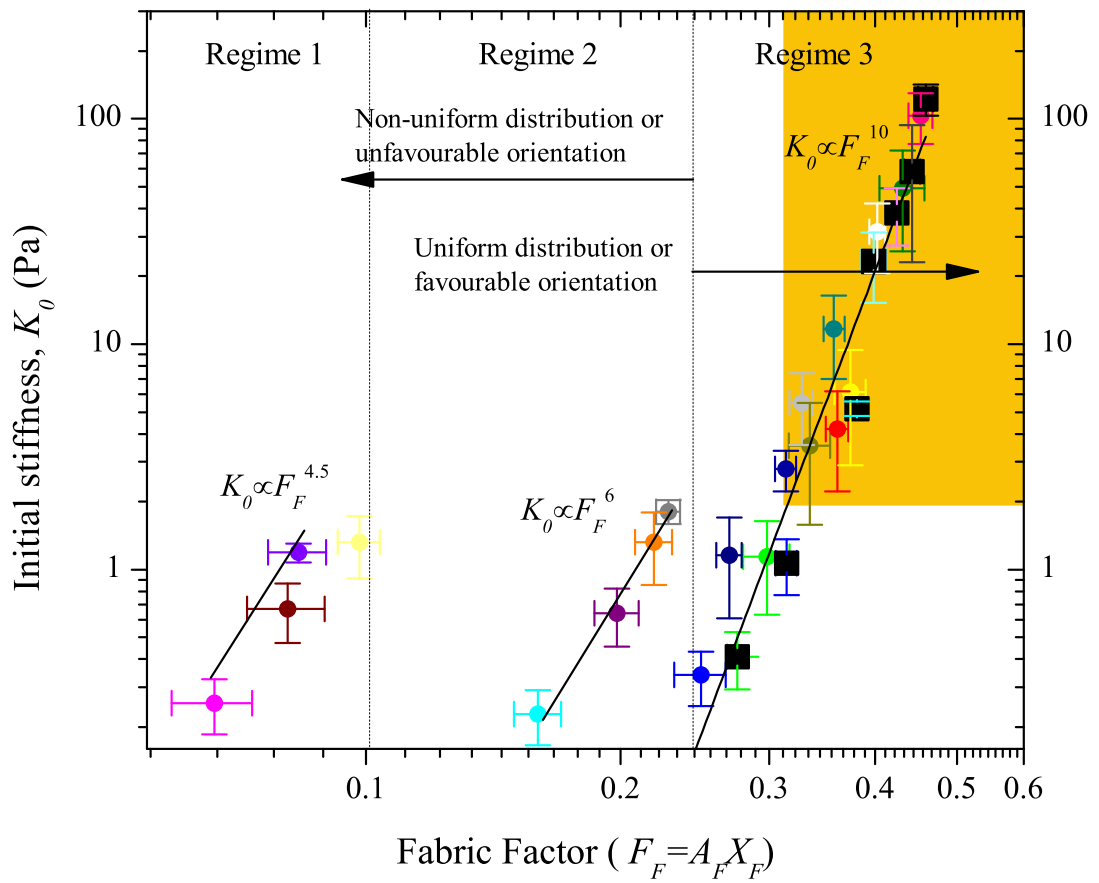
Figure 3.21: Variation of K_0 with F_F. Square symbols corresponds to networks with uniform filament orientation and circles correspond to normally distributed filament orientation. The black lines shows the power law fit for each regimes.

98

length and filament density and developed scaling laws for the stiffness based on the average distance between crosslinks (l_c). They accounted for thermal energy and found that the stiffness scaled with the filament density. The shear modulus showed a scaling with the bending and stretching stiffness with the exponent ranging between 0 to 1 depending on complete bending or stretching. Further to it, they identified two different regimes based on the filament length, one in which the modulus decreased with the increasing filament length and another regime where it remained independent. In similar lines Head *et al.* developed scaling laws for the network modulus based on the average distance between crosslinks. They delineated the response into bending dominated and stretching dominated. In the bending dominated regime, the modulus scaled with the bending stiffness, angle of filament deflection and l_c^{-3}. In the stretching dominated regime, modulus was proportional to stretching stiffness and l_c^{-1}. Similar scaling laws have been developed from experimental observations. Gartel *et al.* used F-actin networks crosslinked by rigid crosslinker Scruin to eliminate the role of crosslinker [157]. Scaling law was developed for Shear modulus based on the average distance between the filaments, average distance between the crosslinks and the bending stiffness. A review paper by Picu summarizes such scaling relationships by various researchers. Based on numerical simulation on extensive set of parameters, he presented excellent scaling relations for the 2D random filament networks. Response was delineated based on the filament density and bending stiffness and provided scaling laws for affine and non-affine regimes [158]. The novelty of our approach is the ability to characterize the networks of all densities and orientations. The contribution from l_c is embedded in our X_F parameter. In the regime where K_0 is uniquely defined by F_F, the nature of the networks (either uniform distribution or favorable orientation) can be predicted if the K_0 is given. If the network is of uniform $\theta_{\bar{\rho}}$, the filament density

99

could be accurately predicted from F_F as A_F is always ≈ 0.64. It becomes a bit equivocal when $\theta_{\bar{\rho}}$ is normal as a single value of F_F could corresponds to more than one $\bar{\rho}$ depending on A_F (orientation).
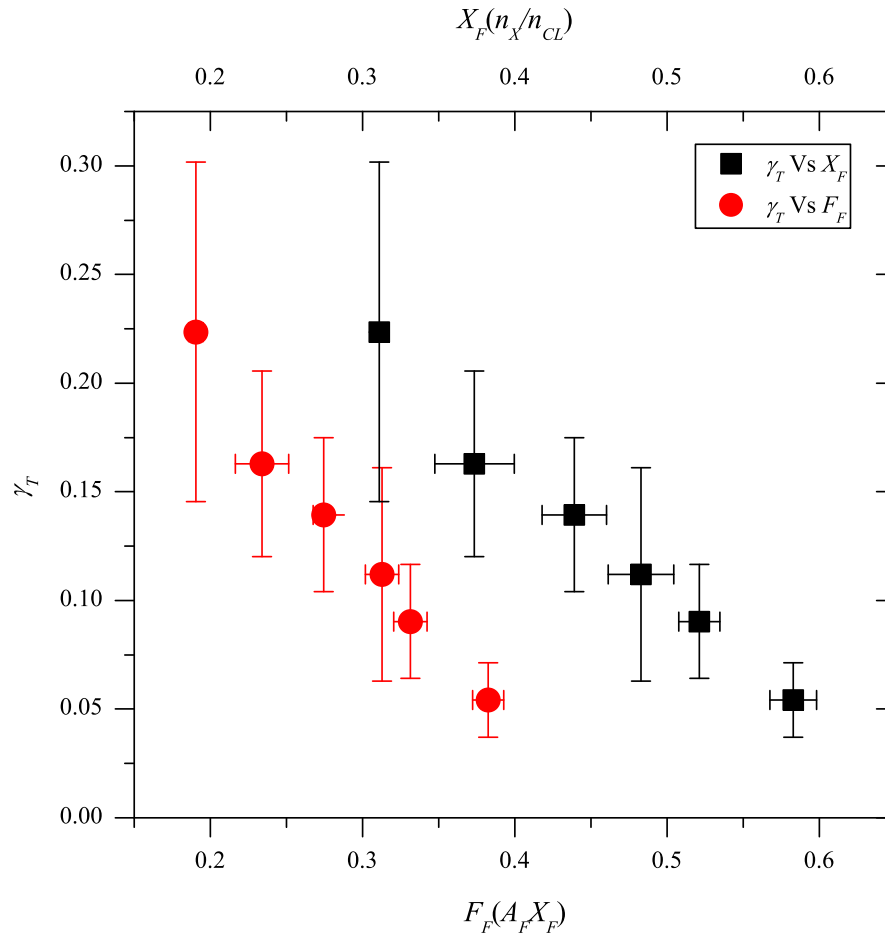
Figure 3.22: Variation of γ_T with X_F for uniform filament distribution. Network density increases as X_F increases and it stiffens at lower strains.

As mentioned in the introductory part of this chapter, to describe the basic characteristics of a network, the information about the network transition from bending to stretching is also important and this is characterized by the transition strain γ_T. It is logical to expect that the transition strain γ_T characterizing a change in

the deformation mode from bending-dominated to stretching-dominated, should also be influenced by the underlying fabric of a network. Indeed, as shown in Fig. 3.22, γ_T shows a nearly linear relationship with F_F. The figure also shows that the linear variation with the crosslink factor X_F. This, together with the linearity in F_F implies that γ_T must be nearly independent of A_F, which is indeed true as the networks considered in arriving this result have a constant A_F (uniform filament orientation distribution). The reason for choosing only uniform orientation space is because for very low $F_F <\approx 0.2$ (i.e. unfavorable orientations) the transition from bending to stretching may either occur at very large strains that are practically difficult to capture, or not occur at all. Notwithstanding this limitation, the result indicates that the fabric characteristics, including the crosslink density and the network topology produce linear scaling for the transition strain.

3.6 Summary

The topological aspects of fibrous networks and its connections with the mechanical response is studied in this chapter. Topological variability arising from the limited computational window size (W) is examined and an ideal window size is proposed for both fixed and varying $\bar{\rho}$. Statistical parameters are identified for the characterization of networks and its correlation with the mechanical response is established. The characteristic network response and the role of various factors in the overall response is also discussed. In a nutshell, the initial stiffness K_0, transition strain γ_T and the overall response depends on the nominal network parameters and topology of the networks. The response of the networks with rigid crosslinks with no failure mechanism for the crosslinks are correlated to topological factors X_F and F_F. K_0 shows a power law dependence to F_F and

γ_T linearly decreases with X_F and F_F. When the failure of crosslinks are account-ed the evolution of topology has to be tracked to derive the statistical parameters and very high variability is expected in such cases. Approximating the filament distribution as uniform/normal itself is prone to statistical variation. It is high-ly dependent on the filament density as well as the size of the computational domain considered.

This chapter has mainly focused on the influence of network statistics on the initial network stiffness. Though it may give indication about the subsequent network response, variation in network architecture and non-affine deformation due to the local rearrangement of filaments could make the response drastically different. For a complete understanding, one has to probe the response over a wide range of strain. First we validate the network model by examining the response of F-actin networks including failure and the results are presented in Chapter 4. We further continue to probe the response of networks over a wide parametric space in Chapter 5. We analyse the networks up to 15% strain and create a deformation map with key focus on non-affine response and failure.

Chapter 4

Stochastic Rate-dependent Elasticity and Failure of Soft Fibrous Networks

4.1   Introduction

This work focuses on modeling the rate sensitive stiffening-to-softening transition in fibrous architectures mimicking crosslinked F-actin networks induced by crosslink unbinding. Using finite element based Discrete Network (DN) modeling approach combined with stochastic crosslink scission kinetics, we correlate the microstructural damage evolution with the macroscopic stress-strain responses of these networks as a function of applied deformation rate. Simulations of multiple DN realizations for fixed filament density indicate that an incubation strain exists, which characterizes the minimum macroscopic deformation that a network should accrue before damage initiates. This incubation strain exhibits a direct relationship with the applied strain rate. Simulations predict that critical damage fraction corresponding to colossal softening is quite low, which may be ascribed to the network non-affinity and filament reorientation. Further, this

critical fraction appears to be independent of applied strain rate. Based on these characteristics, we propose a phenomenological damage evolution law mimicking scission kinetics in an average sense. This law is embedded within an existing continuum model that is extended to include non-affine effects induced by filament bending.

4.2   DN Model of F-actin Networks

Real in-vitro F-actin networks are random architectures of undulated F-actin filaments connected by crosslinking proteins and surrounded by a fluid medium [159]. Apart from the filament length L, another important length-scale in such networks is l_p, the filament persistence length which is in the range of $\approx 10 - 20$ μm [160]. When $l_p \gg L$, undulated filaments act as if they were straight. Van der Giessen and coworkers showed that the macroscopic responses of networks assuming straight filaments is qualitatively similar to those modeled using undulated filaments [80, 128]; initial undulations tend to postpone the transition from flimsy to a stiff behavior. Therefore, we model the networks with straight filaments with individual filament designed to be of length $L \approx l_p$. For a prescribed line (filament) density $\bar{\rho}$, our in-house MATLAB$^{\circledR}$ code generates a 2D network of randomly oriented straight filaments that intersect each other at discrete points within the computational window (Fig. 4.1). These intersection points are considered as crosslinks and are modeled as springs with finite stiffness. We perform a topological analysis to check the randomness of the initial average orientation of a generated network (see Chapter 3, Section3.2 for a brief discussion). The code automatically generates FE mesh on the topology and records the necessary information in a manner that can be seamlessly read into ABAQUS$^{\circledR}$ [141].

Figure 4.1: Initial configuration of a typical network. Dangling ends are removed and the boundary of the computational window (red dashed lines) along with the b.c.'s are shown.

The unfolding characteristics of the crosslinks are approximated by a bi-linear constitutive relationship comprising an initial compliant regime followed by a highly stiff behavior [81,89,161,162]. The unbinding characteristic of a crosslink is tantamount to the scission process beyond which it is incapable of supporting any load. Interestingly, the critical force F_{cr} for scission exhibits rate-dependency that depends logarithmically on the applied loading rate [163, 164]. Another equally striking experimental observation is the variability of F_{cr} for a fixed loading rate[1] [164,165]. This variability even at the single crosslink level is expected to play a role in the overall network response. A noteworthy feature incorporated in the present work is that it explicitly accounts for the rate-dependent stochastic crosslink dissociation process. This is achieved by combining Bell model [166], which gives an exponential relation to the applied force and the dissociation rate, with a Kinetic Monte Carlo (KMC) algorithm [167]. The crosslink dissociation

---

[1]See Appendix A for a discussion about single crossslink simulations.

rate is given by

$$k = k_0 e^{(Fa/k_B T)} \tag{4.1}$$

where k_0 is the characteristic dissociation rate in the absence of applied force, F is the induced local force on a crosslink, a is the interaction distance [168, 169], k_B is the Boltzmann constant and T is the temperature. The stochastic crosslink scission is introduced as a KMC step in that the crosslink life-time is given by

$$t = -\frac{1}{k} \, log(r) \tag{4.2}$$

where $0 < r < 1$ is a uniformly distributed random number. A crosslink may potentially dissociate if it satisfies the criterion

$$t \leq \hat{t} \tag{4.3}$$

where $\hat{t} = \varepsilon_c / \dot{\varepsilon}$ with $\dot{\varepsilon}$ being the local axial strain rate and $\varepsilon_c = a/l_0$ being the critical axial dissociation strain for a crosslink of length $l_0 \approx 160$ nm.

The time-scales associated with the crosslink dissociation kinetics may interact with the time-scale pertaining to the macroscopic deformation rate, producing an overall rate-dependent network response including stiffening and failure [72, 168]. In the model system adopted here, we consider $\bar{\rho} = 10$ that translates to actin concentration of ≈ 0.8 mg/ml [60]. From a numerical viewpoint, we model a square computational domain of fixed size $W = 40$ μm. From this, the total number of filaments N in the computational domain is obtained through the relationship $\overline{\rho} = NL^2/W^2$, where $L = 10$ μm is the filament length [78]. Filaments are meshed using 2D Euler-Bernoulli beam finite elements and each crosslink is modeled using spring element having both axial and transverse degrees of freedom while the rotational degree of freedom is unconstrained. We

adopt the parameters that resemble networks crosslinked by Filamin, which is a relatively compliant ABP among the myriad crosslinkers that have been reported in the literature [90]. The parameters used in the crosslink scission algorithm are $k_{off}^0 = 0.1$ s^{-1}, $a = 0.5$ nm and $l_0 = 160$ nm [169, 170]. Note that at every time-step there may be multiple crosslinks that satisfy Eq. 4.3, but we choose to break only the one with the smallest t. The reader is referred to appendix Bfor the implementation of KMC algorithm in FE framework [167].

4.2.1 KMC Algorithm and Implementation in Finite Element Model

In bio- as well as synthetic polymeric networks the length-scales of interest introduce stochastic effects due to the presence of thermal energy that superposes the mechanical energy. The KMC algorithm implemented in this work addresses this stochastic nature as a first-order reaction. This description is appropriate for an ensemble of similar bonds whose kinetics can be modeled deterministically by a first order ordinary differential equation (ODE) even though the breaking of each bond is a stochastic process. In particular, the probability density function corresponding to the time required to break j^{th} bond can be written as

$$p_j(t) = k_j e^{-k_j t} \tag{4.4}$$

where k_j is dissociation rate of a bond and is given by Eq. 4.1. Dissociation of crosslinks is based on the criterion given in Eq. 4.3. In our FE implementation within ABAQUS$^{\circledR}$, we used a random seed that depends on the physical time at which the simulation was performed. This largely ensured that for a given network topology no two sequences of random numbers were identical.
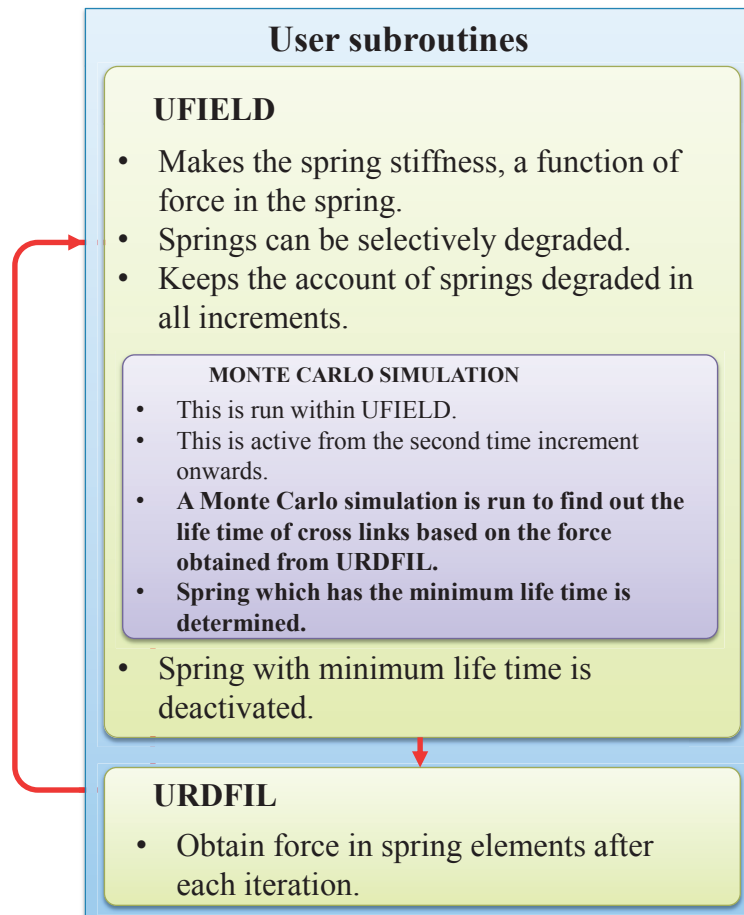
Figure 4.2: Implementation of crosslink scission algorithm within ABAQUS®.

The implementation of KMC algorithm in ABAQUS® is shown in Fig. 4.2. Specifically, we wrote two user-subroutines, which determine the kinetics of each crosslink modeled as bi-linear spring -(a) UFIELD: to incorporate the Bell model that gives a crosslink dissociation rate. Using this subroutine, we related the crosslink stiffness as a function of an appropriate field variable (axial force F in a crosslink) and (b) URDFIL: To enable reading and storing those field variables for each crosslink so that they can be used by UFIELD.

We note here that similar to the scission process, crosslink reformation is also

an important phenomenon that ascertains the network remains structurally viable, e.g., thermally-activated crosslink scission. However, the scission rate is enhanced exponentially in the presence of tension F in a crosslink. More generally, the equilibrium constant of the reaction is given by $\hat{k}(F) = (k_{off}/k_{on}) = \hat{k}_0 e^{(Fa/k_B T)}$, where k_{on} is the rate of crosslink formation, $\hat{k}$ is the equilibrium constant and $\hat{k}_0$ is the value of $\hat{k}$ at zero force [168]. If the tensile force in a filament is large then the reaction is biased toward crosslink scission and may prevail over the relinking process, although the former may provide sites for the latter. The crosslink rebinding phenomenon is rich with complexities [171] and is beyond the scope of this thesis.

4.3   Discrete Network Simulation Results

For the given $\overline{\rho}$, Fig. 4.1 shows the initial configuration of one of the many realizations considered in this work. The kinematic b.c.'s prescribed on the edges of the computational domain are as follows: the bottom edge is fixed while the top edge is sheared horizontally with a constant velocity $\overline{v}$, simulating simple shear condition with a nominal shear strain rate $\dot{\gamma} = \overline{v}/W$. Periodic b.c.'s are applied to the left and right edges so that the microstructure can be considered as representative of an infinitely long slab in the horizontal direction.

4.3.1 Increasing filament bending stiffness
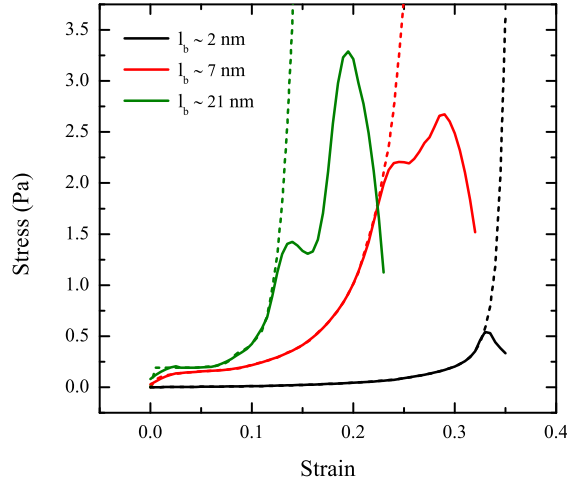
Figure 4.3: Stress-strain response of networks with increasing filament bending stiffness. Response becomes stiffer with increasing filament stiffness. Solid curves show the response with damage and the dotted curves show the undamaged response.

Before delving into the rate sensitivity of the network response, we look into the role of filament bending stiffness in the overall response. The bending nature of the filament dependens on a material length scale called *bending length* $l_b = \sqrt{(\kappa/\mu_s)}$ (see Chapter 5 for a detailed discussion). The ubiquity of the influence of l_b in overall response is verified by considering networks with flexible crosslinks (corresponding to filamin). We also considered the failure of the crosslinks incorporated using KMC Algorithm (Section 4.2.1). Figure 4.3 shows the stiffness response of networks with and without damage for the increasing bending stiffness in such a way that l_b increases from 2 to 21 nm (dotted lines). The snapshots of the deformed configuration of the networks are shown in Fig. 4.4. As l_b increases response becomes more stiffer and a similar response

is observed with damage (solid lines). Note the very low failure stress of the networks when damage is accounted. Even with the increasing filament stiffness, curves show an initially flimsy regime. This is attributed to the bi-linear nature of the crosslinks (Fig. 5.4). And due to the same reason, crosslinks deform at low strains but the contribution to overall network response is small (blue springs in Fig. 4.4). Only after a finite strain, the crosslinks enters the high stiffness regime and then acts as rigid ones and the stiffening of networks takes place. When the crosslinks are in the flimsy regime, the overall network stiffness is very low as it is determined by the minimum of the stiffnesses, i.e., crosslink stiffness. Increase in bending stiffness has a significant effect in the initial stiffness; evident from the jump in stress-strain curves at small strains.

In a typical network, there are three stiffness which determine the overall response; filament stretching, filament bending and crosslink stretching stiffness. Apart from these, buckling of filaments results in local fluctuations in load transfer which is reflected as oscillations in the response curves. When the $l_b = 2$ nm, filament bending is the preferred mode of deformation and it is evident from the curvature of filaments in Fig. 4.4a . As the l_b increases, filament bending becomes more difficult and even at 20% strain, it appears to be straight and crosslink extension becomes the preferred mode of deformation (Fig. 4.4b and c). The bending length of the filaments used in this work is $l_b = 2$ nm which corresponds to F-actin networks.
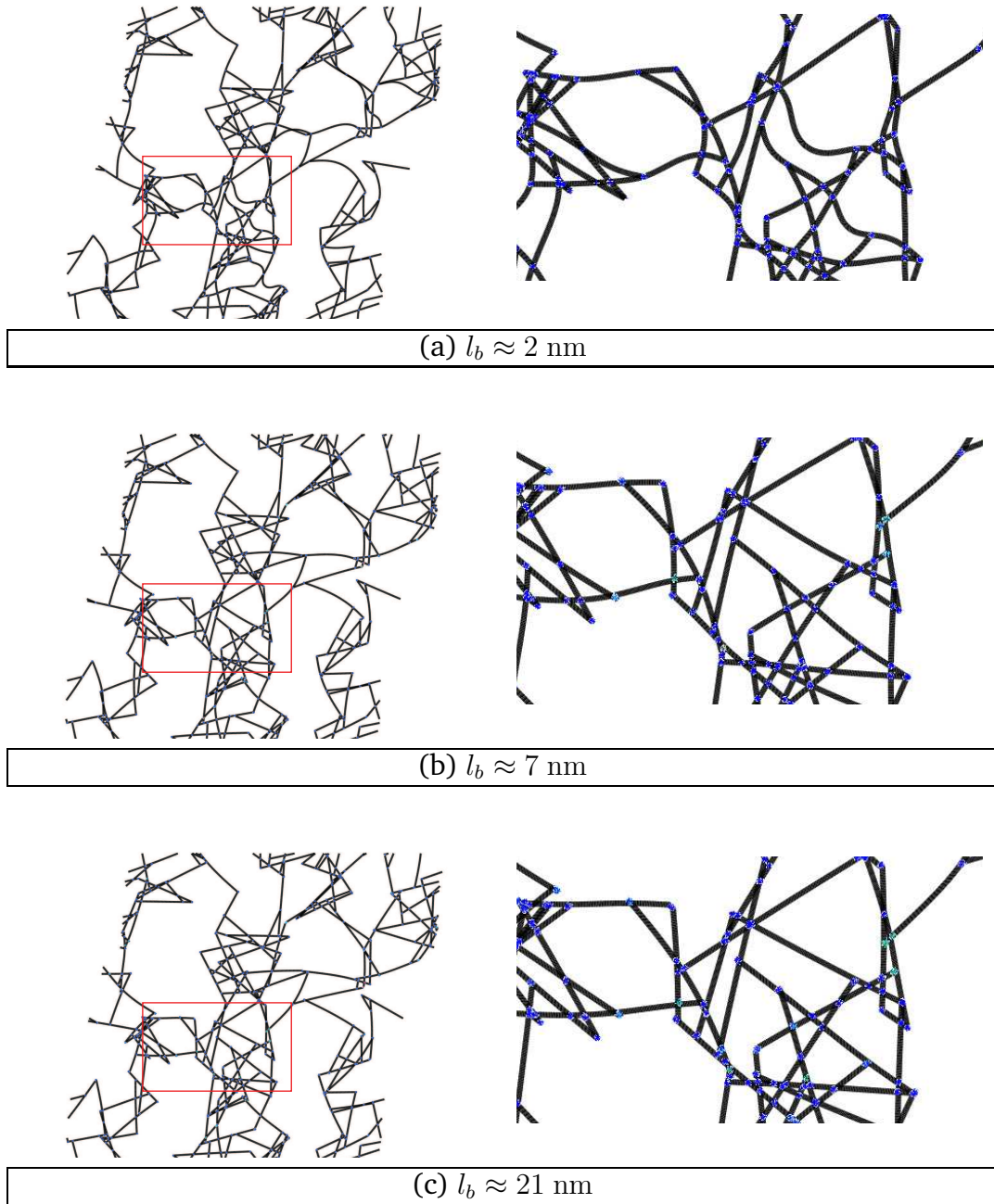
Figure 4.4: Snapshots of networks at a strain of 20%. Black lines shows the filaments and the blue junctions represents the crosslinks. (a) When $l_b \approx 2$ nm, filaments bend with minimum extension of the crosslinks and the resulting response is weaker (Fig. 4.3). (b) As the l_b increases, bending of filaments costs more energy and the crosslink extension becomes more preferred mode of deformation. (c) At an $l_b \approx 21$ nm, the filament bending is even more difficult and the overall network response becomes stiffer.

112

4.3.2   Increasing Filament Density
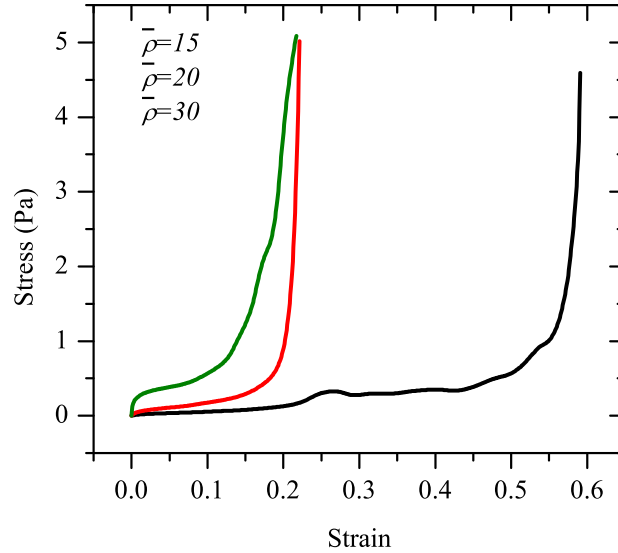
Figure 4.5: Stress-strain response of networks with increasing filament density ($\bar{\rho}$).

Increasing the $\bar{\rho}$ shows a very similar response as seen in Section.4.3.1 when the bending stiffness (or l_b) of the filaments is increased (Fig. 4.5). It shows similar overall response and a similar jump in stress at small strains. Though the results are comparable at a variation of l_b over a small range, in Chapter 5, we see that the correlation breaks down when the range of l_b considered is large. Another factor which modulates the response is the crosslink response. The crosslinks are assumed to be rigid in Chapter 5 when we study the role of filament bending stiffness exclusively. Response of the network with $\bar{\rho} = 15$ shows very delayed hardening response (Fig. 4.5). And this transition takes place at lower strains as $\bar{\rho}$ increases. With the increasing $\bar{\rho}$, network connectivity increases and the average l_c decreases which results in an increased bending resistance. Correlation between the responses in Fig. 4.3 and 4.5 corroborates this hypothesis.

4.3.3   Rate Sensitive Response of F-actin Networks

Having seen the basic mechanics of network response, we chose a $\bar{\rho} = 10$ and $l_b = 2$ nm to further explore more characteristics of the network response. In order to investigate the rate effects, we shear a given network at $\dot{\gamma} = 0.01, 0.1$ and 1.0 s^{-1}. Fig. 4.6 shows snapshots of final configuration of the network for these shear rates. The flexibility of the crosslinks is evident from the extensive deformation at the filament intersection (blue springs in the color version). Some of the crosslinks dissociate during deformation. This is severe for the low rates due to the low critical breaking force. It is interesting to note the tendency of the network to form *stress fibers*, which may be construed as a set of aligned filaments that are closely bundled together, traversing the principal tensile axis. These stress fibers are more commonly observed at higher rates (e.g., Fig. 2c) compared to lower rates.

<div align="center">

(a) $\dot{\gamma} = 0.01$ s^{-1} (b) $\dot{\gamma} = 0.1$ s^{-1} (c)$\dot{\gamma} = 1.0$ s^{-1}

</div>
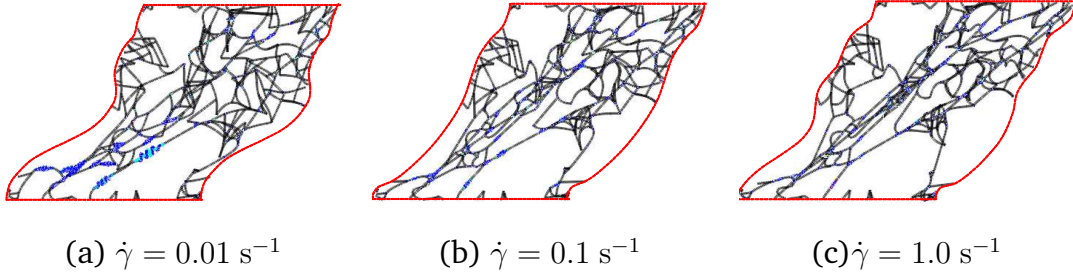
Figure 4.6: Deformed configurations of the network in Fig. 4.1 experiencing macroscopic shear strain of 50% under three different shear rates. Blue springs are dissociated crosslinks.

In what follows, we first discuss the deterministic mechanics of one network topology (Fig. 4.6) in order to provide an insight into the macro-micro nexus. A deterministic analysis implies that the stochastic step (Eq. 4.2) is not activated in the simulations. Then we discuss the rate-dependent behavior of the networks in

terms of the stiffness and evolution crosslink scission fraction ϕ with strain where

$$\phi(t) = \frac{\text{Number of crosslinks broken at time } t}{\text{Total initial number of crosslinks}} \tag{4.5}$$

As shown later the critical fraction of ϕ that causes precipitous collapse of the network stiffness is quite low. The underlying reasons for this are discussed in the next section. Following this we discuss the stochastic effects arising from the KMC procedure and the variability arising from topological randomness (for fixed $\bar{\rho}$). Finally, we present a homogenized continuum model with damage.

Deterministic Network Response

Figure 4.7 shows the evolution of the average shear stress τ, tangent shear stiffness $K = \partial\tau/\partial\gamma$ and damage fraction ϕ as a function of shear strain γ for the network in Fig. 4.1 subjected to $\dot{\gamma} = 1\ \text{s}^{-1}$. In the initial flimsy regime the stress is low owing to the low bending rigidity of the filaments and the low initial stiffness of the crosslinks. This is the regime of filament reorientation that aligns them along the principal stress directions. The damage is also low in this regime, which indicates that at this stage the lifetime of most of the crosslinks is larger than the time-scale associated with the imposed local strain rate.

At $\gamma \approx 0.2$ the stress begins to increase at a faster rate due to preferential alignment of some fraction of filaments along the axis of principal tension together with the fact that the initially flimsy crosslinks get fully stretched to l_c (Eq. 4.3) and lock. As these filaments become taut their stretching stiffness, which is orders of magnitude larger than the bending stiffness, comes into play and determine the overall network response [78]. Consequently, the damage process also accrues faster because the larger forces experienced by the crosslinks dramatically reduce their lifetime (Eq. 4.1) resulting in increased likelihood of satisfying the
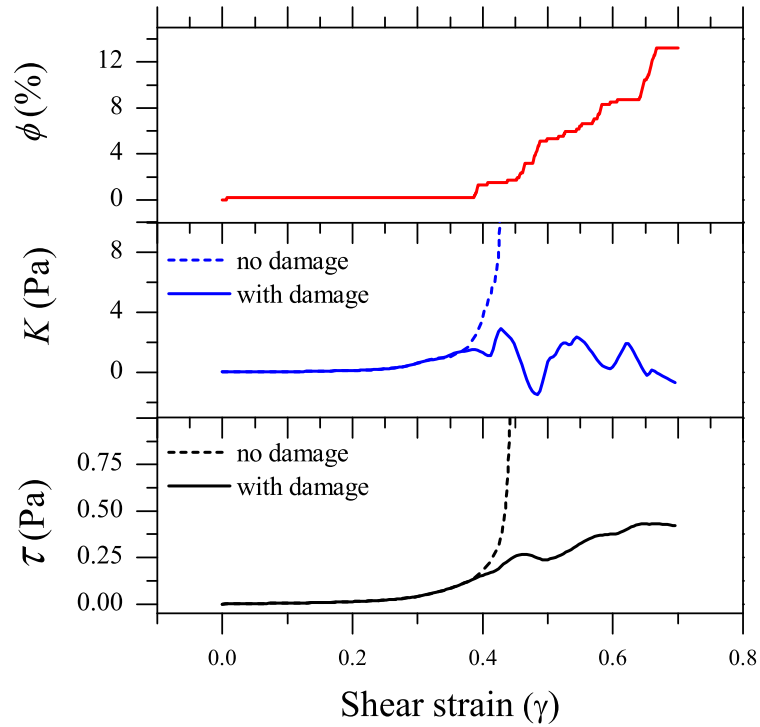
Figure 4.7: Plot of stress, stiffness and damage as a function of strain for $\dot{\gamma} = 1$ s^{-1}. The dotted curves indicate the response of pristine networks.

dissociation criterion. As damage develops the average network stress and tangent stiffness increasingly deviate from their pristine counterparts (shown by the dotted curves). Although the stress continues to rise, the rate of increase slows down over a short strain range ($\gamma \approx 0.4 - 0.42$) that manifests as a *temporary* drop in the network stiffness. As the crosslink scission process starts dominating the response ($\gamma \approx 0.45$) the stiffness drops precipitously. The stress and stiffness do exhibit some recovery, which is due to reorganization of the intact crosslinked filaments into aligned bundles (stress fibers). It is worth noting that there may be situations where a network may soften temporarily, but it may not necessarily lead to a colossal loss of load carrying ability. This indicates a competition between the stiffening mechanism driven by the tendency of a network to reorient

116

majority of the filaments along the principal tensile axis in order to maximize the stretching stiffness and the scission based softening mechanism. As long as there are sufficient number of intact crosslinks, the overall system redundancy helps retain dominance of the stiffening process. Eventually, the softening mechanism prevails over the stiffening mechanism due to increasing force. In fact, to some extent it is a self-cascading process. Each crosslink dissociation brings about an increased tendency of reorientation of the intact network filaments, because these filaments experience weaker constraint from its surrounding. This results in higher forces on the intact crosslinks, which further increases their probability to dissociate even more rapidly. Concomitantly, the damage evolves with strain rapidly beyond $\gamma \approx 0.5$ (Fig. 4.7) .
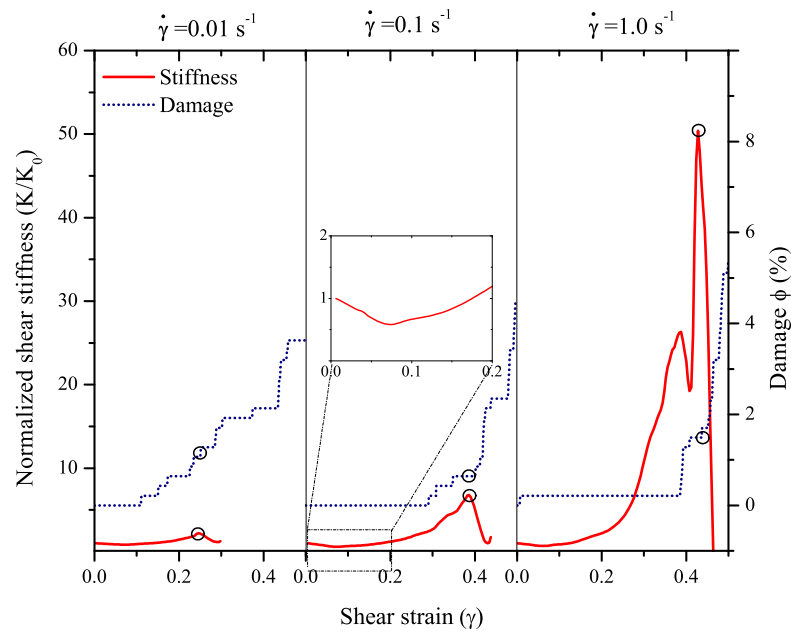
Figure 4.8: Rate-dependent stiffness and damage evolution for three applied rates. Stiffness degradation of networks coincide with the rapid increase in the damage (marked by circles). Inset shows the softening regime at small strains due to filament buckling.

We now discuss the rate-dependent mechanical response of the network. Fig. 4.8 shows evolution of the normalized tangent stiffness K/K_0 (K_0 is the initial stiffness) and damage for the three shear rates. In each case, the network stiffness has an initial flimsy regime as depicted earlier in the Fig. 4.7. It is evident that the network stiffness shows an initial gradual reduction which is present even in the absence of crosslink scission before it begins to increase (see inset in Fig. 4.8). This is so because, as filaments reorient toward the direction of principal stresses, a certain proportion experience tension, while the remaining undergo compression. Given the high flexibility of filaments, compression induces buckling - a structural softening mechanism, which is not necessarily irreversible [78, 87]. Consequently, the entire stress is carried by the filaments under tension after they are fully taut. As noted in the preceding section, the filament straightening is concomitant with the nonlinear increase in the overall network stiffness. Importantly, Fig. 4.8 shows that the degree of nonlinear stiffening is rate-dependent. With increasing applied rate the overall network response increases; higher stiffening and a higher peak before the loss of stiffness occurs. The rate-dependent stiffening and the peak stiffness are a direct result of the interaction between the loading rate and crosslink scission rate (Eq. 4.1). At slow strain rate the dissociation criterion (Eq. 4.3) is more likely to be satisfied even at small strains. Therefore, damage initiates early for lower $\dot{\gamma}$ and extends over the entire strain range up to the point of collapse. With increasing strain rate the damage initiates later, but it evolves more rapidly as can be deduced from the steeper jumps on the damage-strain curves. At higher applied strain rates the induced local rate may exceed the dissociation rate resulting in the crosslink not having sufficient time to break before the force has changed. Naturally, such a delay means that the network remains intact for larger strain values and therefore, exhibits an overall higher stiffness at a given strain compared to those deformed at lower strain

rates. Interestingly, this situation is akin to the dislocation kinetics in metals that exhibit rate-sensitivity at the elastic to plastic transition [172].

Of the three shear rates considered here, the maximum peak normalized stiffness obtained is ≈ 50 for $\dot{\gamma} = 1 \text{ s}^{-1}$ and the minimum of ≈ 2 for $\dot{\gamma} = 0.01 \text{ s}^{-1}$. Soon after the point of maximum stiffness, the network collapses. We characterize this loss of structural functionality of the network by the *failure strain* γ_f at which the $\tau - \gamma$ curve crosses the $K - \gamma$ curve (Fig. 4.7). Although the simulations may continue beyond this point, we consider γ_f as the measure of structural failure, because the subsequent stiffening effect is usually much weaker than the one before the colossal stiffness drop. From a microstructural viewpoint, at the failure strain there is a substantial deterioration of the network integrity brought about by scission of a critical fraction of the total crosslink population.

Stochastic Network Response

The results presented in the preceding section are for a fixed network topology and with deterministic scission kinetics. However, there are at least two sources through which variability may arise in the responses, even in the case of fixed $\overline{\rho}$. First, it is evident from experiments that the crosslink scission is a stochastic process [164, 165]. Thus, at a given deformation rate, F_{cr} for crosslink scission may be scattered about a mean value. Second, one may be able to generate myriad topological realizations for a given orientation distribution function. In this section, we investigate the stochastic effects in the rate-dependent behavior of networks arising from these sources of variabilities.We consider five different realizations of the networks corresponding to $\overline{\rho} = 10$. For each realization, the stochastic nature of crosslink scission is captured through the KMC procedure (Section 4.2), which is invoked for every crosslink in a given network. The

crosslinks are ranked in an ascending order of their lifetimes t and the one with the largest lifetime t_{max} is compared with the critical lifetime $\hat{t}$. We perform five such simulations for each network realization. Thus, for a given $\dot{\gamma}$ we simulate twenty-five cases. We note in passing that the variability arising from the latter is also expected to depend on the size of the computational window, *W*. A discussion about the topological variability due to the filament density and size of the computational window is presented in Section 3.2.
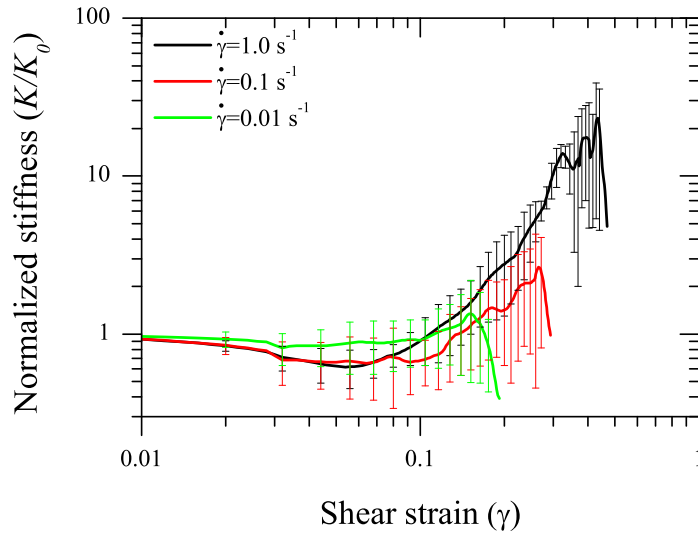
Figure 4.9: Stochastic rate-dependent response of networks.

Figure 4.9 shows the network stiffness evolution with strain for three different applied strain rates. Each curve is an average of 25 simulations and the error bars indicate the variability due to the aforementioned sources of randomness. The responses indicate rate-sensitive stiffening and failure, but also exhibit significant variability as indicated by error bars. The variability is low at small strains ($\gamma \approx 0.05$), but it increases beyond that. Although not shown here, our simulations indicate that topological variations, which are meditated by the computational

domain size, play a bigger role than the stochastic scission and some of this can be reduced by sampling larger regions (Section 3.2). However, microstructural characteristics also mediate this variability. This is primarily due to the fact that as each network topology accrues damage due to crosslink scission, the local rearrangements of the filaments can vary significantly.

A quantitative comparison with experiments is challenging due to the large number of parameters involved: actin concentration, actin-ABP ratio, filament length, distance between crosslinks, rate of loading etc. Figure. 4.10 summarizes experimental data on the peak normalized network stiffness for F-actin networks crosslinked with various ABPs [71, 72, 173–176]. It also superposes the present simulation results (square boxes with error bars). It should be noted however, that the different experimental results in the figure may not directly comparable as the concentration of actin and ABP are not the same; also, the filament lengths may differ. For the data shown in Fig. 4.10, the concentration of F-actin varies from $0.4 - 0.8$ mg/ml. The concentration ratio of ABP to actin varies from 0.003 to 0.01. The experimental result that compares well with the our simulation results are from Kasza *et al.* [174] (black triangle in Fig. 4.10), where the F-actin concentration is ≈ 0.5 mg/mlwith $L \approx 10$ μm, similar to the parameters used here.

Figure 4.11 shows the average rate-dependent evolution of the damage ϕ with strain corresponding to the stiffness evolution in Fig. 4.9. The trend is similar to the one in the deterministic simulations (Fig. 4.8) and given that this result stems from sizable number of simulations, we identify two universal features- (a) incubation strain γ_{in} which characterizes the minimum macroscopic deformation that a network should accrue before crosslinks begin to dissociate and (b) rate of growth $\dot{\phi}$ beyond incubation. As can be noted, γ_{in} has an inverse relationship with the applied rate: networks subjected to lower rates of loading possess
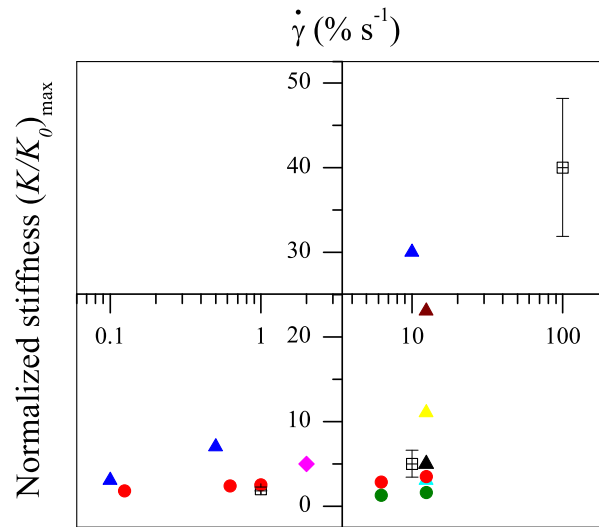
Figure 4.10: Peak normalized stiffness obtained from experiment and the simulation results. The results shown above are for networks formed by various crosslinkers. Triangles corresponds to crosslinker Filamin, circles for Fascin and diamonds for rigor-HMM bonds. Simmulation results are shown by the rectangular boxes [71, 72, 173–176]. The length of the F-actin filaments used in experiments is shown in the legend.

propensity for early initiation of damage, while at higher rates, damage initiation takes place only at large strains. Such information is not available in experimental literature as there it may not be possible to isolate the damage incubation characteristics in an experiment. However, one may be able to reconcile it in an indirect fashion. In Broedersz *et al.* [177] and Lieleg and Bausch [84] for example, it can be noted that networks subjected to lower applied shear rates start to stiffen at higher strains compared to those sheared at higher rates. This could be attributed to the fact that the damage (crosslink scission) is more severe in the former, which implies lower incubation strain while the latter shows a delayed damage initiation i.e. higher incubation strain. Another interesting observation is that irrespective of the applied rate, the damage evolution appears to converge

to a single value of $\approx 4\%$ with $\gamma \approx 0.45$, beyond which a runaway growth occurs especially for higher strain rates.
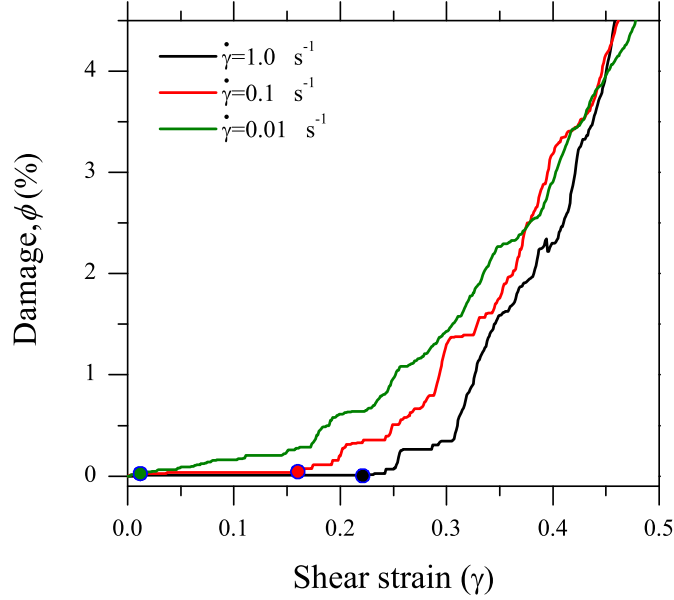
Figure 4.11: Damage evolution for three applied shear rates. Each curve is an average of 25 simulations. The solid circle on each curve indicates incubation strain γ_{in} for that particular rate.

Figures 4.12a and 4.12b show the rate-dependent γ_{in} and the critical damage for stiffness collapse, ϕ_{cr} with their corresponding variability. Whereas, the former clearly indicates a rate-dependent behavior, the same cannot be said about latter owing to a large scatter. Another important observation in the damage evolution process is that the ϕ_{cr} ranges between $\approx 0.5 - 3\%$, while the loading rate and corresponding peak stiffness vary by three orders of magnitude. This low critical damage is ascribed to the non-affine nature of the network response. It can be observed from Fig. 4.12b that the variation in ϕ_{cr} is minimum for the shear rate $\dot{\gamma} = 0.1 \text{ s}^{-1}$. For the lower rates, crosslink scission is vigorous starting at a very small strain and for higher rates the crosslink scission is very rapid after

(a) Damage incubation strain   (b) Critical damage for failure
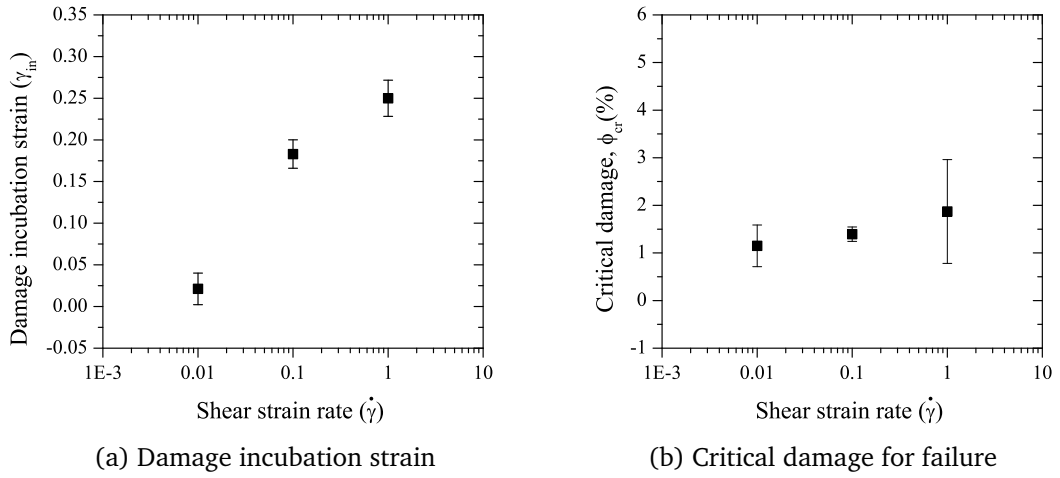
Figure 4.12: Rate effects in damage incubation strain γ_{in} and critical damage ϕ_{cr}.

incubation which brings in substantial variability in ϕ_{cr}. Given that ϕ_{cr} is relatively rate insensitive, from variability consideration one may posit that there is an optimum rate that provides a more deterministic information about critical damage irrespective of the computational window size. At the point where the network collapses, the main load carrying components are the filaments that have already aligned in the principal tensile direction. In this scenario, although there may be several intact crosslinks that connect the filaments, the effective system redundancy is governed by stress fibers. These stress fibers are like a system of springs in parallel where each of the stress fiber comprises of several filament-spring connected in series, supporting the applied deformation. When one crosslink within any of these stress fibers dissociates, it corresponds to loss of one stress fiber thereby reducing the effective stiffness dramatically (Fig. 4.13). In other words, rearrangement of filaments lowers the effective redundancy of the network, which would otherwise help maintain its structural integrity over a larger deformation.
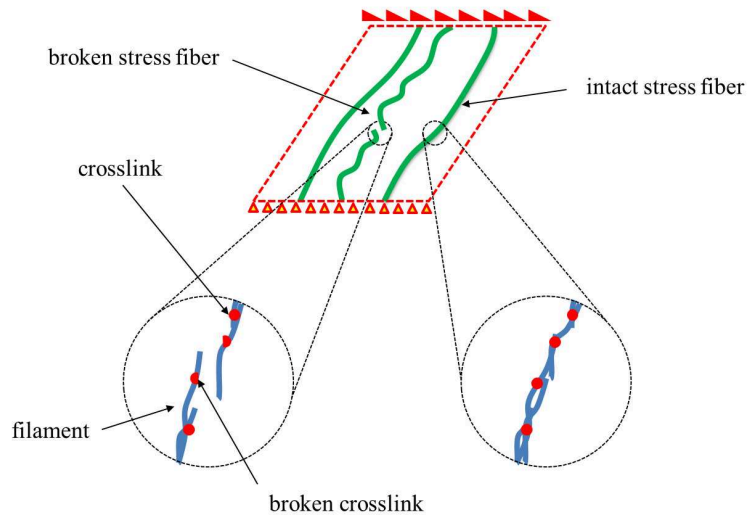
Figure 4.13: Schematic showing the formation of stress fibers at large deformation due to the preferential alignment of the filaments to the loading direction and its failure due to crosslink scission. Scission of a small fraction of crosslinks may result in the failure of stress fibers which in turn result in the network failure. The view on the left shows a broken stress fiber and the right view shows the intact one.

4.4   A Continuum Model with Damage

In this section, we present a phenomenological homogenized continuum model that incorporates the effect of non-affinity and deformation-induced damage evolution due to crosslink scission. The main objective is to show that the damage kinetics can be introduced within an existing homogenized model and demonstrate that such an enriched model qualitatively mimics the DN simulation results [178]. The model is based on the work of Planas *et al.* [179] that accounts for the filament orientation evolution in an average sense, but unlike their work that ignores non-affine effects, we approximately incorporate the influence of non-affine deformations [180].

4.4.1 Affine Deformation Model

F-actin filaments crosslinked by ABPs are assumed to be uniformly distributed in the unloaded configuration [181]. Filaments are assumed to be isotropic and homogeneous with crosslinks at the end points. The initial filament orientation θ is accounted using a distribution function. A uniform probability density function for a continuous distribution is given by [179]

$$\Gamma(\mathbf{x}) = \begin{cases} \frac{1}{b-a} & \text{if } a \leq \theta \leq b \\ 0 & \text{if } \theta < a \text{ or } \theta > b \end{cases} \tag{4.6}$$

where a and b denote the limits of θ. In the present 2D scenario with $0 \leq \theta \leq \pi$ the initial spatial distribution function is given by [179]

$$\Gamma(\mathbf{n}, \mathbf{x}) = \frac{f_f}{2\pi} \tag{4.7}$$

where f_f is the volume fraction of the filaments. In this homogenized theory, information about $\bar{\rho}$ is embedded through f_f. For the 2D case, we equivalently define it as the area fraction, i.e. $f_f \approx NLd/W^2 = 0.007$ where d is the diameter of filaments. $\mathbf{n}$ is the unit vector in the reference configuration $\mathbf{x}$, where the filament distribution is uniform

$$\mathbf{n} = \mathbf{e}_1 \cos\theta + \mathbf{e}_2 \sin\theta \tag{4.8}$$

In the deformed configuration filaments continually align with the loading direction and the overall orientation distribution deviates from its initial uniform state.

Consider a filament connected with two crosslinks in series. The stress in this

filament-crosslink system is described by

$$s_f(\lambda) = E_f^A(\lambda - 1) \tag{4.9}$$

where λ is the axial stretch in this system. E_f^A is the *effective* elastic modulus of the filament-crosslink system, ignoring the non-affine and damage effects. Note that E_f^A may itself be a function of λ depending upon the constitutive behaviors of the filament and the crosslinks. At any time t, a macroscopic simple shear $\gamma(= \dot{\gamma}t)$ applied to the network results in the following deformation gradient

$$\mathbf{F} = \begin{bmatrix} 1 & \gamma \\ 0 & 1 \end{bmatrix} \tag{4.10}$$

With affine deformation assumption, the stretch λ in an individual filament-crosslink system due to γ is [179],

$$\lambda(\theta) = |\mathbf{Fn}| = \sqrt{1 + \gamma^2 \sin^2 \theta + 2\gamma \sin \theta \cos \theta} \tag{4.11}$$

and the corresponding Cauchy stress (in 2D) is

$$\sigma = \int_0^\pi s_f(\lambda) \left[\frac{\mathbf{Fn} \otimes \mathbf{Fn}}{|\mathbf{Fn}|} - \frac{1}{2}|\mathbf{Fn}|\mathbf{I} \right] \Gamma(\mathbf{n,x})d\theta - p\mathbf{I} \tag{4.12}$$

where $\otimes$ denotes a tensor product, $\mathbf{I}$ is the identity tensor and $|\mathbf{a}|$ indicates the magnitude of a vector $\mathbf{a}$ and $\mathbf{Fn} \otimes \mathbf{Fn}$ is given by

$$\mathbf{Fn} = \begin{bmatrix} \cos \theta + \gamma \sin \theta \\ \sin \theta \end{bmatrix} \tag{4.13}$$

127

$$\mathbf{Fn} \otimes \mathbf{Fn} = \begin{bmatrix} \mathbf{Fn}_1\mathbf{Fn}_1 & \mathbf{Fn}_1\mathbf{Fn}_2 \\ \mathbf{Fn}_2\mathbf{Fn}_1 & \mathbf{Fn}_2\mathbf{Fn}_2 \end{bmatrix}$$

$$= \begin{bmatrix} (\cos\theta + \gamma\sin\theta)^2 & \sin\theta(\cos\theta + \gamma\sin\theta) \\ \sin\theta(\cos\theta + \gamma\sin\theta) & \sin^2\theta \end{bmatrix} \quad (4.14)$$

The expression is for incompressible and the factor $1/2$ is because of the 2D framework. Eq. 4.12 can be expanded as

$$\sigma = \int_0^\pi s_f \left[\frac{\mathbf{Fn} \otimes \mathbf{Fn}}{|\mathbf{Fn}|} - \frac{1}{2}|\mathbf{Fn}|\mathbf{I} \right] \Gamma(\mathbf{n,x}) - p\mathbf{I}$$

$$= \int_0^\pi E(\lambda - 1) \left[\frac{\mathbf{Fn} \otimes \mathbf{Fn}}{|\mathbf{Fn}|} - \frac{1}{2}|\mathbf{Fn}|\mathbf{I} \right] \Gamma(\mathbf{n,x}) - p\mathbf{I} \quad (4.15)$$

$$= \int_0^\pi E(|\mathbf{Fn}| - 1) \left[\frac{\mathbf{Fn} \otimes \mathbf{Fn}}{|\mathbf{Fn}|} - \frac{1}{2}|\mathbf{Fn}|\mathbf{I} \right] \Gamma(\mathbf{n,x}) - p\mathbf{I} \quad (4.16)$$

$$= \int_0^\pi E(\gamma) \left[\mathbf{Fn} \otimes \mathbf{Fn} - \frac{1}{2}|\mathbf{Fn}|^2\mathbf{I} - \frac{\mathbf{Fn} \otimes \mathbf{Fn}}{|\mathbf{Fn}|} - p\mathbf{I} \right. \quad (4.17)$$

$$\left. + \frac{1}{2}|\mathbf{Fn}|\mathbf{I} \right] \frac{f_f}{\pi} d\theta \quad (4.18)$$

For the cases considered here the stiffness E is the combined stiffness of the filament and the crosslink. We are considering two cases here, in one of them the stiffness of the crosslink is constant and in the other case, the crosslink strain hardens and the stiffness increases with deformation. The former is modeled using a linear spring while the latter is approximated using Worm Like Chain (WLC) model.

4.4.2 Crosslink with Fixed Stiffness

In order to account for the finite stiffness of the crosslinker, the crosslink is assumed to be like a linear spring with finite stiffness. As filament is connected by crosslinks at the end, a representative filaments is a system with a filament connected in series with two crosslinks. The components of stress are,

$$
\sigma_{11} = \frac{Ef_f}{\pi} \int_0^\pi \left[(\cos\theta + \gamma\sin\theta)^2 - \frac{1}{2}(1 + \gamma^2\sin^2\theta + 2\gamma\sin\theta\cos\theta) \right]
$$
$$
- \frac{Ef_f}{\pi} \int_0^\pi \left[\frac{(\cos\theta + \gamma\sin\theta)^2 - \frac{1}{2}(1 + \gamma^2\sin^2\theta + 2\gamma\sin\theta\cos\theta)}{\sqrt{1 + \gamma^2\sin^2\theta + 2\gamma\sin\theta\cos\theta}} \right] - p\mathbf{I}
$$

(4.19)

$$
\sigma_{22} = -\frac{Ef_f}{\pi} \int_0^\pi \left[\sin^2\theta - \frac{1}{2}(1 + \gamma^2\sin^2\theta + 2\gamma\sin\theta\cos\theta) \right]
$$
$$
- \frac{Ef_f}{\pi} \int_0^\pi \left[\frac{(\sin^2\theta - \frac{1}{2}(1 + \gamma^2\sin^2\theta + 2\gamma\sin\theta\cos\theta)}{\sqrt{1 + \gamma^2\sin^2\theta + 2\gamma\sin\theta\cos\theta}} \right] - p\mathbf{I}
$$

(4.20)

$$
\sigma_{12} = \sigma_{21} = -\frac{Ef_f}{\pi} \int_0^\pi \cos\theta(\cos\theta + \gamma\sin\theta)d\theta
$$
$$
- \frac{Ef_f}{\pi} \int_0^\pi \left[\frac{\cos\theta(\cos\theta + \gamma\sin\theta)}{\sqrt{1 + \gamma^2\sin^2\theta + 2\gamma\sin\theta\cos\theta}} \right] - p\mathbf{I}
$$

(4.21)

In order to solve the integrals, we take advantage of the fact that the shear strain γ is usually less than 1. The individual terms in the integral are expanded using binomial theorem, retaining terms up to order 3. All the above integrals can be

solved by considering each terms separately. Equation 4.19 becomes,

$$\sigma_{11_1} = \frac{Ef_f}{\pi} \int_0^\pi (\cos^2\theta + \gamma^2\sin^2\theta + 2\gamma\sin\theta\cos\theta - \frac{1}{2}(1 + \gamma^2\sin^2\theta + 2\gamma\sin\theta\cos\theta)d\theta$$

$$= \frac{1}{2}\frac{Ef_f}{\pi} \int_0^\pi (2\cos^2\theta + \gamma^2\sin^2\theta + 2\gamma\sin\theta\cos\theta)d\theta$$

(4.22)

The terms can be directly integrated, giving

$$\sigma_{11_1} = \frac{1}{4}Ef_f\gamma^2$$

(4.23)

The second term of the integral is

$$\sigma_{11_2} = -\frac{Ef_f}{\pi} \int_0^\pi \frac{(\cos\theta + \gamma\sin\theta)^2 - \frac{1}{2}(1 + \gamma^2\sin^2\theta + 2\gamma\sin\theta\cos\theta)}{\sqrt{1 + \gamma^2\sin^2\theta + 2\gamma\sin\theta\cos\theta}} \, d\theta$$

$$= -\frac{1}{2}\frac{Ef_f}{\pi} \int_0^\pi \frac{(2\cos^2\theta - 1 + \gamma^2\sin^2\theta + 2\gamma\sin\theta\cos\theta)}{\sqrt{1 + \gamma^2\sin^2\theta + 2\gamma\sin\theta\cos\theta}} \, d\theta$$

(4.24)

Adding and subtracting 1 to above equation

$$
\begin{aligned}
\sigma_{11_2} &= -\frac{1}{2}\frac{Ef_f}{\pi}\int_0^\pi \frac{(2\cos^2\theta - 1 - 1 + 1 + \gamma^2\sin^2\theta + 2\gamma\sin\theta\cos\theta)}{\sqrt{1 + \gamma^2\sin^2\theta + 2\gamma\sin\theta\cos\theta}}\,d\theta \\
&= -\frac{1}{2}\frac{Ef_f}{\pi}\int_0^\pi \frac{(2(\cos^2\theta - 1) + 1 + \gamma^2\sin^2\theta + 2\gamma\sin\theta\cos\theta)}{\sqrt{1 + \gamma^2\sin^2\theta + 2\gamma\sin\theta\cos\theta}}\,d\theta \\
&= -\frac{1}{2}\frac{Ef_f}{\pi}\int_0^\pi \frac{(-2\sin^2\theta + 1 + \gamma^2\sin^2\theta + 2\gamma\sin\theta\cos\theta)}{\sqrt{1 + \gamma^2\sin^2\theta + 2\gamma\sin\theta\cos\theta}}\,d\theta \\
&= -\frac{1}{2}\frac{Ef_f}{\pi}\int_0^\pi \frac{\sin^2\theta}{\sqrt{1 + \gamma^2\sin^2\theta + 2\gamma\sin\theta\cos\theta}}\,d\theta \\
&\quad - \frac{1}{2}\frac{Ef_f}{\pi}\int_0^\pi \sqrt{1 + \gamma^2\sin^2\theta + 2\gamma\sin\theta\cos\theta}\,d\theta \\
&= -\frac{1}{2}\frac{Ef_f}{\pi}I_2(\gamma) - \frac{1}{2}\frac{Ef_f}{\pi}I_1(\gamma)
\end{aligned}
\tag{4.25}
$$

Equation 4.20 can be integrated in similar fashion. First term of σ_{22} is

$$
\sigma_{22_1} = -\frac{Ef_f}{\pi}\int_0^\pi \sin^2\theta - \frac{1}{2}(1 + \gamma^2\sin^2\theta + 2\gamma\sin\theta\cos\theta)d\theta
\tag{4.26}
$$

Direct integration yields,

$$
\sigma_{22_1} = -\frac{1}{4}Ef_f\gamma^2
\tag{4.27}
$$

Second part of the integral is

131

$$\begin{aligned}
\sigma_{22_2} &= -\frac{Ef_f}{\pi} \int_0^\pi \frac{(\sin^2\theta - \frac{1}{2}(1 + \gamma^2\sin^2\theta + 2\gamma\sin\theta\cos\theta)}{\sqrt{1 + \gamma^2\sin^2\theta + 2\gamma\sin\theta\cos\theta}}\, d\theta \\
&= -\frac{Ef_f}{\pi} \int_0^\pi \frac{\sin^2\theta}{\sqrt{1 + \gamma^2\sin^2\theta + 2\gamma\sin\theta\cos\theta}}\, d\theta \\
&\quad + \frac{1}{2}\frac{Ef_f}{\pi} \int_0^\pi \sqrt{1 + \gamma^2\sin^2\theta + 2\gamma\sin\theta\cos\theta}\, d\theta \\
&= -\frac{1}{2}\frac{Ef_f}{\pi}I_2(\gamma) + \frac{1}{2}\frac{Ef_f}{\pi}I_1(\gamma)
\end{aligned} \tag{4.28}$$

First part of the shear term in the equation.4.21 becomes,

$$\begin{aligned}
\sigma_{12_1} &= -\frac{Ef_f}{\pi} \int_0^\pi \cos\theta(\cos\theta + \gamma\sin\theta)\, d\theta \\
&= \frac{1}{2}Ef_f\gamma
\end{aligned} \tag{4.29}$$

Second part of the integral is

$$\begin{aligned}
\sigma_{12_2} &= -\frac{Ef_f}{\pi} \int_0^\pi \frac{\cos\theta(\cos\theta + \gamma\sin\theta)}{\sqrt{1 + \gamma^2\sin^2\theta + 2\gamma\sin\theta\cos\theta}} \\
&= -\frac{Ef_f}{\pi}\gamma \int_0^\pi \frac{\sin^2\theta}{\sqrt{1 + \gamma^2\sin^2\theta + 2\gamma\sin\theta\cos\theta}} \\
&\quad - \frac{Ef_f}{\pi} \int_0^\pi \frac{\sin\theta\cos\theta}{\sqrt{1 + \gamma^2\sin^2\theta + 2\gamma\sin\theta\cos\theta}} \\
&= -\frac{Ef_f}{\pi}\gamma I_2(\gamma) - \frac{1}{2}\frac{Ef_f}{\pi}I_3(\gamma)
\end{aligned} \tag{4.30}$$

Expanding the terms in the above equations using binomial expansion to solve the integrals; only terms up to γ^3 are retained. Integrals I_1, I_2 and I_3 becomes,

$$I_1(\gamma) = \int_0^\pi \sqrt{1 + \gamma^2 \sin^2 \theta + 2\gamma \sin \theta \cos \theta} \; d\theta$$

$$\approx \int_0^\pi \left[1 + (\gamma^2 \sin^2 \theta + 2\gamma \sin \theta \cos \theta)\right]^{1/2} \; d\theta \qquad (4.31)$$

$$\approx \pi + \frac{3}{16}\gamma^2$$

$$I_2(\gamma) = \int_0^\pi \frac{\sin^2 \theta}{\sqrt{1 + \gamma^2 \sin^2 \theta + 2\gamma \sin \theta \cos \theta}} \; d\theta$$

$$\approx \int_0^\pi \sin^2 \theta \left[1 + (\gamma^2 \sin^2 \theta + 2\gamma \sin \theta \cos \theta)\right]^{-1/2} \; d\theta \qquad (4.32)$$

$$\approx \frac{\pi}{2} + \frac{3}{32}\gamma^2$$

$$I_2(\gamma) = \int_0^\pi \frac{\sin \theta \cos \theta}{\sqrt{1 + \gamma^2 \sin^2 \theta + 2\gamma \sin \theta \cos \theta}} \; d\theta$$

$$\approx \int_0^\pi \sin \theta \cos \theta \left[1 + (\gamma^2 \sin^2 \theta + 2\gamma \sin \theta \cos \theta)\right]^{-1/2} \; d\theta \qquad (4.33)$$

$$\approx \frac{\pi}{8}\gamma + \frac{9}{256}\gamma^3$$

Using equations 4.31,4.32 and 4.33 in equations 4.25, 4.28 and 4.30, the stress components are given by

$$\sigma_{11} = -p + \frac{Ef_f}{16}\gamma^2$$

$$\sigma_{22} = -p - \frac{Ef_f}{16}\gamma^2 \qquad (4.34)$$

$$\sigma_{12} = \frac{Ef_f}{8}\gamma + \frac{15Ef_f}{256}\gamma^3$$

σ_{12} is an odd function of γ, both linear and cubical in γ. The contribution by higher order term is very small at small strains due to the small value of the coefficient. If we neglect the higher order term in σ_{12}, Poynting effect can be observed [182]:

$$
\begin{aligned}
\sigma_{11} - \sigma_{22} &= \gamma\sigma_{12} \\
&= \frac{Ef_f}{16}\gamma^2 + \frac{Ef_f}{16}\gamma^2 \approx \gamma\sigma_{12}
\end{aligned}
\tag{4.35}
$$

4.4.3 Strain Hardening Crosslink

Crosslinkers like Filamin are flexible and shows a strain hardening type of response (ref Section. A.6 for a discussion about crosslink response). Such a response can be better approximated by WLC model. In this case the stiffness of the system is a function of deformation and the stress on the filament s_f has to be integrated over the entire orientation. Force-displacement relation for WLC model is given by

$$
F(x) = \frac{k_bT}{l_p}\left[\frac{1}{4}\left(1 - \frac{x}{L_0}\right)^{-2} + \frac{x}{L_0}\right]
\tag{4.36}
$$

Stiffness of the crosslink is

$$
F(x) = \frac{k_bT}{L_0 l_p}\left[\frac{1}{2}(1 - (\lambda - 1)^{-3}) + 1\right]
\tag{4.37}
$$

We used the expression $x/L_0 = (\lambda - 1)$ for rewriting the stiffness in terms of the stretch. When the filament is connected in series to the crosslinks at the end, the effective stiffness K_{eq} of the system is given by

134

$$K_{eq} = \frac{K_f K_x}{K_x + 2K_f}$$

$$= \frac{K_f \frac{k_b T}{L_0 l_p} \left(\frac{1}{2}(1 - (\lambda - 1)^{-3}) + 1\right)}{\frac{k_b T}{L_0 l_p} \left(\frac{1}{2}(1 - (\lambda - 1)^{-3} + 1)\right) + 2K_f} \quad (4.38)$$

The equation for shear stress obtained from Eq. 4.21

$$\sigma_{12} = \int_0^\pi \frac{K_{eq} \lambda L}{A} \frac{f_f}{\pi} (\lambda - 1) \frac{\mathbf{Fn} \otimes \mathbf{Fn}}{\lambda} \, d\theta \quad (4.39)$$

Substituting for K_{eq} from Eq. 4.38,

$$\sigma_{12} = \frac{L f_f}{A\pi} \int_0^\pi \frac{K_f \frac{k_b T}{L_0 l_p} \left(\frac{1}{2}(1 - (\lambda - 1)^{-3}) + 1\right)}{\frac{k_b T}{L_0 l_p} \left(\frac{1}{2}(1 - (\lambda - 1)^{-3}) + 1\right) + 2K_f} (\lambda - 1) \frac{\mathbf{Fn} \otimes \mathbf{Fn}}{\lambda} \, d\theta$$

$$= \frac{L f_f}{A\pi} \int_0^\pi \frac{K_f \frac{k_b T}{L_0 l_p} \left(\frac{1}{2}(1 - (\lambda - 1)^{-3}) + 1\right)}{\frac{k_b T}{L_0 l_p} \left(\frac{1}{2}(1 - (\lambda - 1)^{-3}) + 1\right) + 2K_f} \left[\mathbf{Fn} \otimes \mathbf{Fn} - \frac{\mathbf{Fn} \otimes \mathbf{Fn}}{\lambda} \right] \, d\theta$$

$$(4.40)$$

Expanding the terms, final expression for stress becomes,

$$\sigma_{12} = \frac{L f_f}{A\pi} \int_0^\pi \left[\frac{K_f \frac{1}{2}(2 - \lambda)^{-3}}{K_\lambda} \mathbf{Fn} \otimes \mathbf{Fn} + \frac{K_f}{K_\lambda} \mathbf{Fn} \otimes \mathbf{Fn} \right.$$

$$\left. - \frac{K_f \frac{1}{2}(2 - \lambda)^{-3}}{K_\lambda} \frac{\mathbf{Fn} \otimes \mathbf{Fn}}{\lambda} - \frac{K_f}{K_\lambda} \frac{\mathbf{Fn} \otimes \mathbf{Fn}}{\lambda} \right] \, d\theta \quad (4.41)$$

where K_λ is the sum of stiffness given by

$$K_\lambda = \frac{1}{2}(1 - (\lambda - 1)^{-3}) + 1 + 2\frac{K_f L_0 l_p}{k_b T} \qquad (4.42)$$

In the above expressions, λ is the stretch in the system. Replacing λ by Eq. **??** in Eq. 4.11, the resulting expression is solved numerically in MAPLE$^{\circledR}$ to obtain the stress.

4.4.4 Constitutive Response of F-actin Networks

We consider F-actin as linear elastic and crosslink behavior modeled using WLC [81, 183], the shear response in Eq. 4.41 can be rewritten as

$$\sigma_{12} = -p\mathbf{I} + \int_0^\pi \frac{E_f^A f_f}{\pi} \left\{ \mathbf{Fn} \otimes \mathbf{Fn} - \frac{1}{2}|\mathbf{Fn}|^2\mathbf{I} - \frac{\mathbf{Fn} \otimes \mathbf{Fn}}{|\mathbf{Fn}|} + \right.$$
$$\left. \frac{1}{2}|\mathbf{Fn}|\mathbf{I} \right\} d\theta \qquad (4.43)$$

where E_f^A the affine network modulus. With this, E_f^A in Eq. (4.43) becomes

$$E_f^A = \frac{\frac{K_f L}{A}\left(\frac{\hat{\lambda}^{-3}}{2} + 1\right)}{1 + \frac{\hat{\lambda}^{-3}}{2} + \frac{2K_f l_0 l_p}{k_B T}} \qquad (4.44)$$

where $\hat{\lambda} = (1 - (\lambda - 1))$, and K_f and A are the stiffness and area of the filaments, respectively.

As discussed later the initial response is determined by the crosslink behavior as it is the more compliant of the two. However, gradually, as the macroscopic strain increases the crosslink stiffens and the filament starts playing a dominant

role. This is further aided by the filament reorientation process.

4.4.5 Effect of Non-affinity

The simple springs-in-series model describing E_f^A leads to affine deformations, whereas a network may deform in a non-afffine manner triggered by filament bending [77, 126]. In this work, we do not attempt to rigorously formulate this effect. However, it is important to account for it and to that end, we refer to Zaccone and Scossa-Romano [180] who elegantly showed that in amorphous solids,

$$\mu = \mu^A - \mu^{NA} = \mu^A(1 - z^{'}) \tag{4.45}$$

where μ is the actual network shear modulus, μ^A is the modulus assuming affine deformations while μ^{NA} is the non-affine contribution that softens the overall response. In other words, the term inside the bracket describes the magnitude of non-affinity through $z^{'}$ that is related to the coordination number indicating nearest neighbor particles in contact and dimensionality of the problem. While Eq. 4.45 is only valid for central force systems, it is used here as a guidance for writing a similar form for biopolymeric networks where bending energy can stabilize the floppy (soft) modes [184, 185]. Motivated by the elegance of Eq. 4.45, we write

$$E_f = E_f^A(1 - \zeta_0) \tag{4.46}$$

where ζ_0 is a dimensionless quantity (< 1) that characterizes the network non-affinity induced by bending deformations. For a given filament density, it is expected to depend on an effective coordination number $\overline{z}$ at a crosslink (determined by whether it is an X, L or T type junction [186, 187], the effective filament length l_c between the crosslinks and a length-scale λ describing the propensity of a filament to bending [77, 188]. Although not derived here in detail, we suggest that ζ_0 would be directly proportional to l_c, but depend inversely on $\overline{z}$ and λ. Finally, using continuum damage mechanics approach, we superpose the effect of scission-induced damage and write the equivalent elastic modulus E_e of the filament-crosslink system as

$$E_e = E_f^A(1 - \zeta_0 - \zeta_1 \phi) \tag{4.47}$$

where ζ_1 is a is a phenomenological sensitivity parameter that accounts for the effect of enhancement of degradation due to reduced redundancy of the network as stress fibers form (Fig. 4.13). Equation 4.47 indicates that the softening of the network brought about by bending induced non-affinity (characterized by ζ_0) is accentuated by the damage induced from crosslink scission. The modulus E_f^A in Eq. 4.43 is substituted by Eq. 4.47. The resulting expressions for the network stress components are complicated functions of γ and are solved using MAPLE$^{\circledR}$ to obtain the overall differential shear stiffness.

4.4.6 Damage Evolution

Reiterating the characteristic features of damage evolution, we have rate-dependent incubation strain and damage growth but a rate independent strain $\gamma_e \approx 0.45$ at

Table 4.1: Value of the parameters used in damage modeling(Eq. 4.48).

$\alpha^{\gamma_{in}}$	p	$\dot{\phi}_0$ (s^{-1})	$\dot{\gamma}_0$ (s^{-1})	γ_e	n	ζ_0	ζ_1
0.25	0.4	0.067	1	0.45	0.4	0.8	50

which the runaway damage growth occurs. From these characteristics we propose the following evolution law for the crosslink scisson fraction

$$\dot{\phi} = \begin{cases} 0 & \text{if } \gamma \leq \gamma_{in} \\ \dot{\phi}_0 \left(\frac{\dot{\gamma}}{\dot{\gamma}_0}\right) \left(\frac{\gamma}{\gamma_e - \gamma}\right)^n & \text{if } \gamma > \gamma_{in} \end{cases} \tag{4.48}$$

where $\dot{\phi}_0$ is the characteristic scission rate obtained at a characteristic macroscopic deformation rate $\dot{\gamma}_0$ and n indicates its dependence on the applied and runaway strains.In the equation, the rate-dependent incubation strain $\gamma_{in} = \alpha^{\gamma_{in}} (\dot{\gamma}/\dot{\gamma}_0)^p$ is characterized by the parameters $\alpha^{\gamma_{in}}$ and p. Damage evolves only after γ_{in} is reached. These parameters are obtained form the damage evolution curves (Fig. 4.11) and the values are given in Table 4.1.

4.4.7 Network Response: Continuum Modeling Results

Figure 4.14 shows the rate-dependent stiffness and damage evolution with macroscopic shear strain obtained from the homogenized model. The result reproduces qualitative trends that were obtained in the DN results (Fig. 4.8). As both crosslink and the filament are connected in series, at small strains the response is mediated by the crosslink due to low stiffness. With continued deformation the crosslink stiffens and the filament starts contributing to the overall stiffness, because it now assumes the role of the weakest link in the filament-crosslink series system. Yet, the network stiffness increases by several orders of magnitude

owing to reasonably large stretching stiffness of the filament.
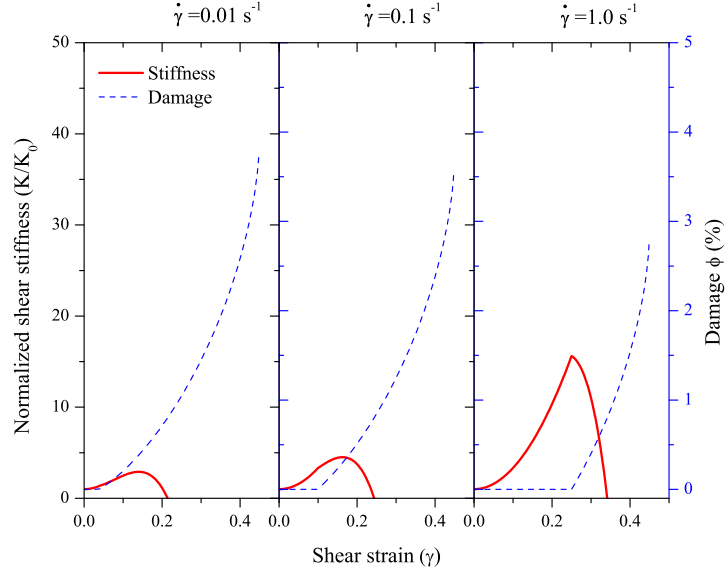
Figure 4.14: Rate-dependent stiffness response of the network the homogenized model.

Using the parameters in Table 4.1, the peak stiffness values obtained are in the same range as in the experimental observation [71] and our DN model. Importanly the underlying microstructural evolution, damage evolution and the resulting rate sensitivity of the biopolymer networks are captured using the current model in an average sense without the necessity to divulge into the specifics of a given network. The microstructural evolution of a network through filament reorientation causes stiffening of the overall response. In Planas *et al.*'s model [179] the current average network orientation without considering the damage is described by θ_p as

$$\theta_p(\mathbf{x}) = \frac{\int \gamma(\mathbf{n}, \mathbf{x})\mathbf{n}.e_1 \; dw}{\int \gamma(\mathbf{n}, x) \; dw}$$

$$= \frac{1}{f_f} \int_0^\pi \frac{\Gamma(\mathbf{n,x})\mathbf{Fn}.e1}{|\mathbf{Fn}|} d\theta \qquad (4.49)$$

$$= \frac{1}{\pi} \int_0^\pi \frac{\cos\theta + \gamma\sin\theta}{|\mathbf{Fn}|} d\theta$$

i.e. θ_p is the ratio of the projected length of filaments on the reference axis to the total length of the filaments. Evolution of θ_p depends on the type of deformation and the reference axis.
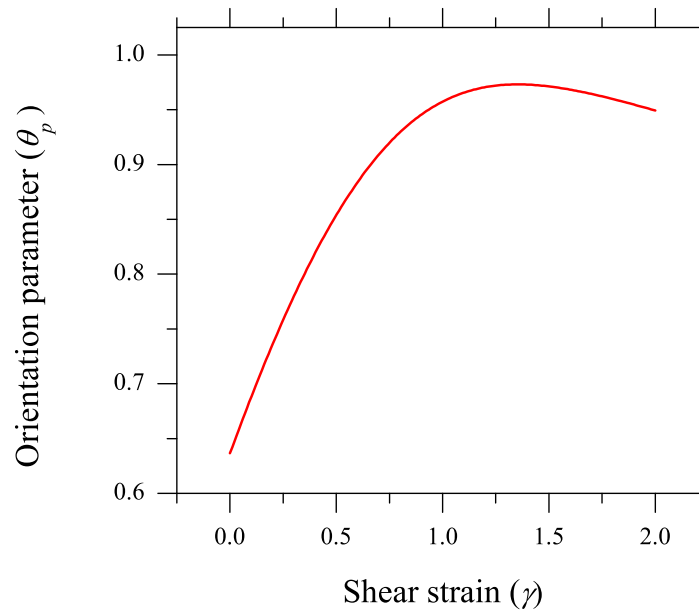
Figure 4.15: Evolution of filament orientation for shear loading with respect to 45^0 axis. At small strains principal loading direction coincides with 45^0 axis and later it deviates, evident from the initial increase and then decrease in the orientation parameter.

Figure 4.15 shows the process of filament reorientation in a network, obtained by

141

numerically integrating Eq. 4.49 for the simple shear case. For simple shear deformation, the initial principal axes are at $\approx 45^0$. During deformation, filaments get oriented towards the principal axes. The reference axis considered for the calculation of θ_p remains fixed at 45^0 while the principal axis for the simple shear case start with 45^0 and tend towards 0^0 at very large strains. For a 2D uniform distribution, the initial value of θ_p is $2/\pi$ and the limiting value when θ tends to be 0^0 is $1/\sqrt{2}$ (not shown in Fig. 4.15). For the uniform distribution, filaments are oriented in all directions in the undeformed state, but during deformation they tend to be oriented to 45^0 at small strains, reflected as initial increase in θ_p and then progressively to 0^0, reflected as the drop in θ_p.

Although not explored here, another important feature of this model is that the variability in the damage evolution that could be incorporated into the continuum model by adopting distribution functions for the parameters in Table 4.1 as those are based on the variability obtained from the DN calculations. In such a scenario, the values in Table 4.1 could be mean values.

4.5   Summary

In this work, we developed microstructurally informed models to gain insights into the rate-dependent mechanical behavior of soft, fibrous networks. F-actin network crosslinked with Filamin was chosen as a model system for this investigation. The DN approach was enriched with crosslink scission kinetics, which renders the response rate-sensitive. The stochastic nature of the scission process is embedded in the approach by integrating KMC procedure into the FE framework. We also addressed the variability of responses that arise from sampling

effects, which enables us to understand statistical aspects of the network mechanics. We also developed a homogenized damage model that was merged with an existing continuum model and phenomenologically accounted for network non-affinity. Although not explored here, an important feature of this homogenized model is that the variability in the scission-induced damage could be incorporated in a seamless manner by adopting distribution functions for the parameters in its evolution function.

In this work, the sole mechanism for rate dependent behavior is rate dependent damage evolution. Factors such as viscoelasticity, reformation of crosslinks and active rearrangement of the network architectures are not accounted for. Another mechanism which is not accounted is the strain-rate hardening of crosslinks [163]. In the case of strain-rate hardening type of crosslink, both γ_f and peak stiffness could be modulated due to the higher forces experienced by the crosslinks. It is seen that the mechanical response is inextricably linked to topological factors such as filament density, crosslink density and network architecture (see Chapter4 [187]). The dependency on the last factor is not well understood and strong connections have to be made between the topology and mechanical response to fully understand behaviors of filamentous networks. The results presented here are based on 2D filamentous networks whereas real biopolymeric networks are three-dimensional. The lower constraint effect offered by the latter [80, 128] and the resulting extended non-affinity may affect the damage evolution quantitatively, although the qualitative behavior should still hold. Finally, we have not addressed the role of the fluid medium that surrounds these networks. To the lowest order, this will result in a shear stress that varies linearly with the strain rate, solvent viscosity being the proportionality constant. This may be effectively construed as dashpots embedded within the network and this may also influence the damage evolution, especially if the viscous time-scales compare with

143

the dissociation time-scales and applied loading rate.

The research problem addressed in this chapter lies at the nexus of mechanics and chemistry. A broad class of phenomena in cellular and molecular biophysics are in this arena, including force induced unfolding or conformational change of proteins, force induced activation of ion channels, chemical to mechanical energy conversion in muscles and polymerization induced force generation in actin filaments [189]. In all these problems the effect of force on equilibria and rates of chemical reactions is treated using variants of the Bell and Eyring models at the level of single molecules or single fibers. Our treatment of the breaking of crosslinks follows along these lines but we have gone further by constructing a damage model at the continuum level that is informed by thermal activation theories at the scale of single crosslinks. As such our evolution laws are written for tensorial quantities such as stresses and strains (not just forces or extensions) even though they have their origins in one-dimensional ideas at the single molecule level. We expect that our methods that combine deterministic and stochastic elements will be applicable to a variety of filamentous network architectures where there is continuous interplay of mechanical and chemical forces.

Chapter 5

Effect of Constituent Properties on Network Response

5.1 Introduction

In Chapter 2, the overall filament length L set up the filament density and the average distance between crosslinks l_c appeared as the crosslink density[1]. We assumed the filaments to be straight line segments (Section 2.6) by invoking the persistence length (l_p) argument. We discussed the effects of network topological features on their characteristics through these three length scales. However, it is also of interest to know how the response of a given network topology is mediated by the constituent properties of the filaments and crosslinks. A fourth length scale that emerges is the characteristic filament *bending* length $l_b = \sqrt{(\kappa/\mu_s)}$, which has its origins in both, the material and the cross-sectional characteristics

---

[1]The length l_c is also sometimes correlated to the network average mesh size [156, 158].

of individual filaments [142]. The problem becomes particularly intriguing because these networks resist deformation through a combination of filament bending and stretching, which invokes myriad possibilities with regard to the degree of response nonlinearity and non-affinity as a function of their corresponding rigidities. The challenges in characterization of network response is accentuated if one considers finite stiffness of the crosslinks and their dissociation characteristics. Naturally, it becomes imperative to seek answers to the some of the basic questions that arise:

- How does the filament stretching-bending synergy affect the overall network response?

- What is the interplay between the crosslink and filament stiffnesses in determining the degree of response nonlinearity?

- For a fixed filament density, does the network response seamlessly transition from a non-affine to an affine behavior as a function of the filament and crosslink properties?

- How does crosslink dissociation affect network stiffening as a function of crosslink and filament stiffness?

- Is it possible to provide a simple, predictive model for network response that accounts for topological effect, non-affinity and failure?

In the literature on fibrous networks, especially pertaining to biopolymeric systems, some of the aspects, e.g., bending-stretching nexus, degree of non-affinity, and so forth, have been discussed [117, 130, 158, 184]. However, most of these works have focused on addressing aspects related to the network behaviors as a function of the filament density, filament length etc. For example, Onck *et al.* [78] attributed the nonlinear stiffening in fibrous networks mimicking F-actin

architectures to the non-affine deformations induced by filament bending that is strongly influenced by the filament density. Head *et al.* [142] delineated the network deformation into affine and non-affine and developed scaling laws based on the filament properties. Missel *et al.* [190] studied the affine/non-affine transition in topologically anisotropic networks and found that the stress-strain relation ship at both small and finite strains are different from affine predictions of orthotropic continuum linear elasticity. Bai *et al.* [188] investigated the role of filament length polydispersity (having filaments of multiple length) in the affine/non-affine transition and observed the shift of transition to lower filament densities. Frey and coworkers [130, 184] developed self-consistent effective medium models describing non-affine deformations. Using a DN model Wilhelm and Frey [191] obtained different scaling regimes in stiff random fibrous networks that includes the bending dominated regime. However, the role of crosslink response was not probed in any of the above mentioned works. From the perspective of biopolymers having a finite crosslink stiffness, it is important to understand the role of crosslink response.

In this chapter, we seek answers to the above-mentioned questions using our model problem comprising simple shear of a network with fixed filament density ($\bar{\rho} = 10$) and network topology (Fig. 5.6), but varying the filament and crosslink rigidities over a wide range [2]. Starting with typical rigidity parameters that resemble F-actin filaments, the investigation extends over nearly three decades of filament stiffnesses. In the following sections, we first describe the results pertaining to the role of filament properties assuming the crosslinks to be rigid. We

---

[2]Though we present the results of a single topological realization, different topologies were with nominally similar topological parameters were investigated and they demonstrated same trend in the response with a variation of $< 10\%$. Note that Chapter 3 discusses the aspects of topological variability.

then elucidate the role of the crosslink properties including the effect of their dissociation characteristics on the network behavior over the range of rigidities. One can imagine that building a general predictive model would be a complicated agenda, but we take a step toward addressing the complexity of the problem. The highlight of this investigation is the resulting response map that fully describes the overall network response for a wide range of filament properties and a fixed $\bar{\rho}$. We discuss the significance of such a predictive map and its implications on the design of fibrous networks.

5.2   Role of Filament Properties

As mentioned in the introductory statements of this chapter, the role of the filament properties in the overall network response may be ascribed through the characteristic bending length scale l_b, which is simply the square root of the ratio of the bending rigidity $\kappa = EI$ and the stretching rigidity $\mu_s = EA$, where E, I and A are respectively the elastic modulus, second moment of area and the cross-sectional area of the filament. For purposes of illustration, let the elastic modulus be constant; then, $l_b = \sqrt{I/A}$, which is the definition of the radius of gyration of a column that plays an important role in bending and buckling of slender structures. It is important to find out if it is the ratio (i.e., l_b only) that matters in the overall response, or the individual components of l_b also play a role. For example, it may so happen that two topologically identical networks may comprise filaments that also possess identical l_b, but the individual terms (i.e., I and A) may be vary, albeit proportionately (Case I). Alternatively, they may vary disproportionately so that filaments the two topologically identical networks have different l_b (Case II). We discuss the constant l_b case first followed by the variable l_b case. In both the cases the filaments obey linear elasticity and the

crosslinks are rigid.

5.2.1 Case I: Constant l_b

Fig. 5.1a shows the $K - \gamma$ response of the network topology in Fig. 5.6. Note that the nonlinear behavior is a direct result of the non-affine nature of network deformation (see Chapter 3, Section 3.4 for a discussion about the non-affine response). With this in mind, the Fig. 5.1a shows that for a constant $l_b = 2$ nm, larger the I and A, stiffer is the actual $K - \gamma$ response. This is expected because the overall network tends to be stiffer. However, the evolution of the normalized stiffness $\hat{K}(= K/K_0)$ collapse onto a single curve (Fig. 5.1b). That is, the rate of stiffening (characterizing the non-affine nature) of these networks is identical, indicating that it is the ratio rather than the individual components of l_b that matters in describing the non-affine characteristics of a rigidly crosslinked network (Fig. 5.1a). Therefore, at least for the limited scenario of rigidly crosslinked networks with no failure, it would be appropriate to simply prescribe an l_b parameter to obtain a desired network response without being concerned about the choice of individual constituent parameters for the filaments. Given that in all the cases, the l_b/l_c ratio is constant, K_0 is expected to adhere to the following scaling law,

$$ K_0 \propto \left(\frac{\kappa}{l_c^4} \right) \left(\frac{l_c}{\xi} \right)^q \tag{5.1} $$

where q has a value of 3 in ref. [156] and 2 in ref. [129] depending upon whether the effect of network topology is accounted for in the scaling or ignored. This scaling together with a fitting function for the $\tilde{K} - \gamma$ curves provides a complete description for any network with a given l_b.

<div align="center">(a) Stiffness   (b) Normalized Stiffness</div>
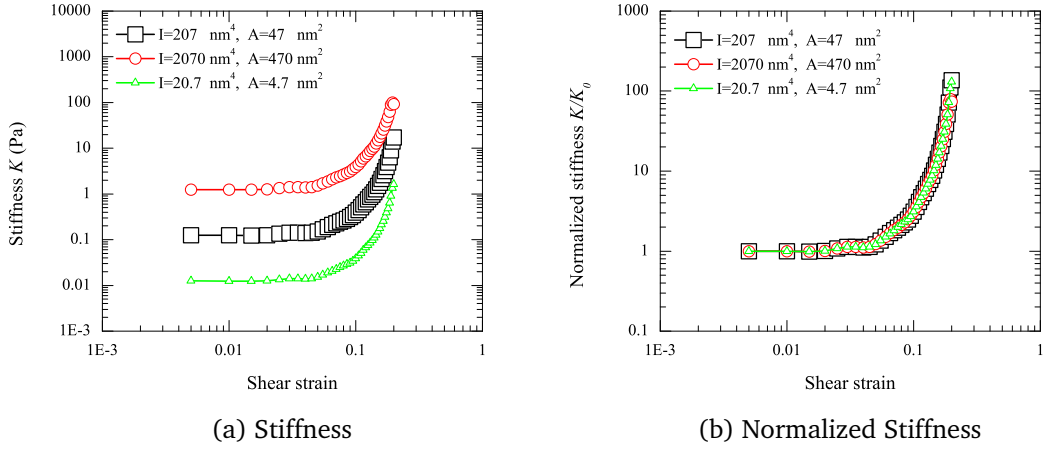
Figure 5.1: Stiffness evolution of topologically identical networks with different combination of bending and stretching stiffness producing fixed $l_b \approx 2$ nm. (a) Network stiffness scales with the absolute value of filament stiffness (the stiffness parameters are shown in the legend). (b) The normalized response superposes into a single curve.

5.2.2 Case II: Variable l_b

Figure 5.2a shows that the situation in the case of variable l_b is rather different from its predecessor in Section 5.2.1. It can be immediately noted that the initial stiffness K_0 scales with l_b, but unlike in Case I, this scaling is not maintained throughout the entire deformation regime. Consequently, the responses are not amenable to degeneration into a single master curve (Fig. 5.2b). Note that for a fixed topology a higher l_b indicates a network that is more resistant to bending. As mentioned earlier, it is the propensity of the filaments to undergo bending that renders non-affinity in the network response (see Section 3.4). Naturally, with increasing l_b the filament stretching becomes increasingly preferred mode and the nonlinearity in the $K - \gamma$ response diminishes. This is further clarified in the normalized stiffness response in Fig. 5.2b where the degree of nonlinearity

<div align="center">150</div>

decreases with increasing l_b to the extent that for $l_b = 2000$ nm and the response is affine over a large strain range.

(a) Stiffness (b) Normalized Stiffness
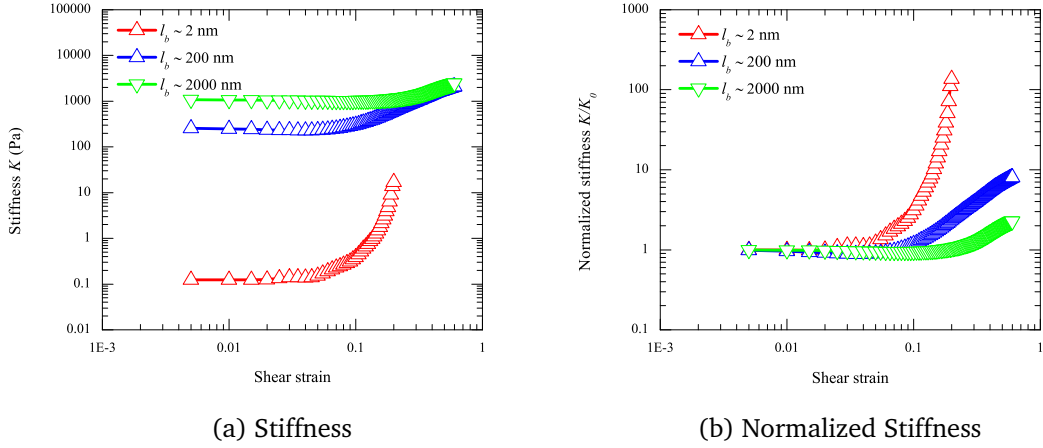
Figure 5.2: Stiffness evolution of networks with increasing bending length $l_b \approx 2, 200$ and 2000 nm. Network stiffness varies with l_b and considerable difference is seen in the hardening response. (a) The initial network stiffness increases with the bending stiffness of the filaments but the stiffness attained at 10% strain do not follow the same trend. (b) Curves cannot be superposed to a single curve when scaled with the initial stiffness.

It is useful to compare this with the case of changing l_c keeping l_b fixed (Chapter 3). It was ascertained in Section 3.4.2 that in the former situation the normalized stiffness curves collapses on to a single master curve that follows $\hat{K} \propto \hat{\tau}^{3/2}$ scaling with the normalized stress $\hat{\tau}$ [156]. Performing a similar normalization for the cases in Fig. 5.2 and re-plotting the curves alongside the case of varying l_c at fixed l_b (Fig. 5.3), we observe that the latter do not readily degenerate to a master curve indicating the failure of the scaling law. The reason for this failure lies in the fact that with increasing l_b, the entire deformation process is dominated by filament stretching, whereas the scaling law works well only for the cases where there is a stark transition from bending to stretching, as was the case in [156].

(a) Fixed l_b and varying l_c (b) Varying l_b and fixed l_c
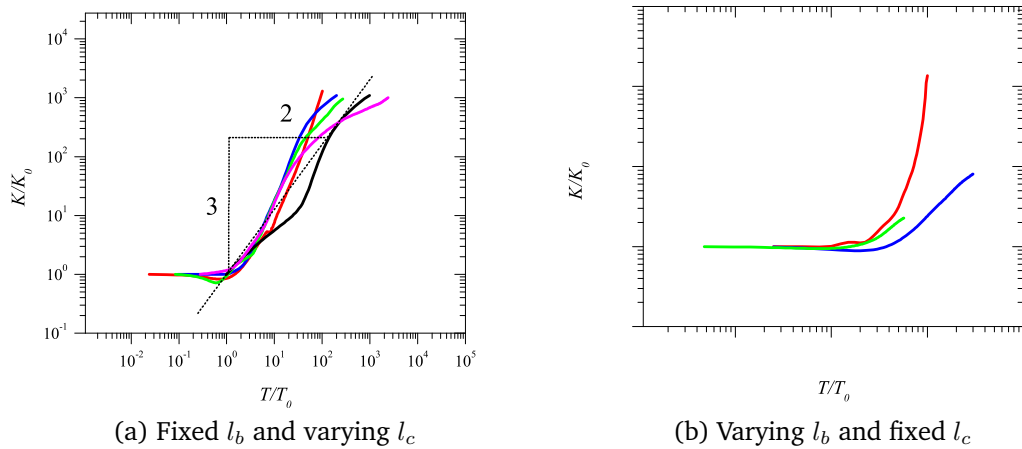
Figure 5.3: Role of l_b and l_c in the stiffness evolution of networks. (a) With fixed l_b and varying l_c, curves collapses when the stiffness is scaled and plotted as a function of scaled stress as shown by Žagar *et al.* [156]. (b) With varying l_b and fixed l_c, such a scaling response is not observed.

5.3 Role of Crosslink Stiffness

Crosslinks may be broadly classified as rigid or compliant depending on their ability to extend under applied tension in consonance with the filaments they connect. For example, *Scruin*, an Actin Binding Protein (ABP) in F-actin networks is relatively rigid compared to the filaments. On the other hand, the stiffness of *Filamin* is lower than the F-actin filaments and may be classified as compliant [157,192]. Apart from rigidly crosslinked biopolymeric networks, synthetic fibrous architectures such as electrospun networks may also be classified under this category owing to the fusion bonding between filaments [115,193]. The response of such networks is governed by the filament properties and are often adopted as model systems to investigate the topological effects (e.g., [80,110,112]). For networks with compliant crosslinks, the effect of the crosslink stiffness on the overall

network response becomes an important question to address as the load transfer paths could be significantly altered owing to additional kinematic degrees of freedom and may have important implications on the degree of non-affinity, stiffening and ultimately rupture of networks.

(a) Crosslink response   (b) Network response
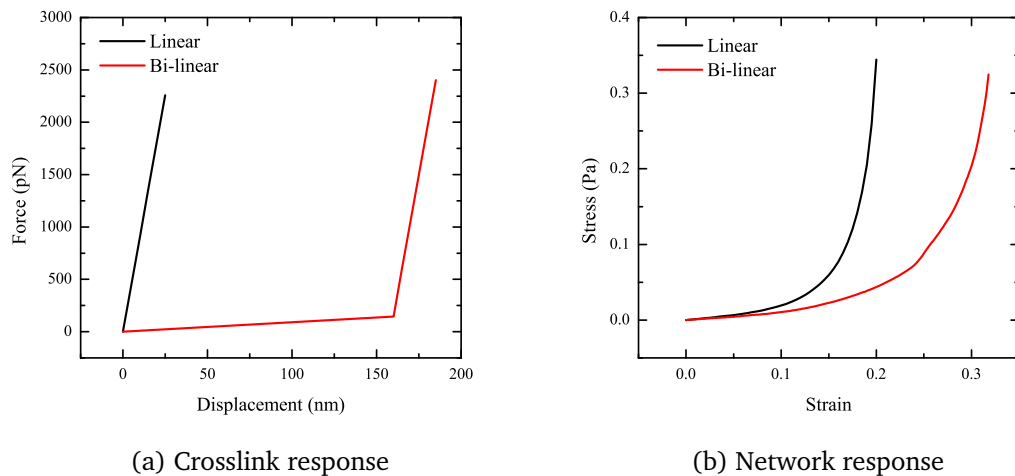
Figure 5.4: Crosslink response and corresponding network response. (a) Linear and bi-linear crosslink response. (b) Response of networks with crosslinks shown in (a). Network with linear crosslinks shows early stiffening.

As an illustration of networks with flexible crosslinks, consider two canonical crosslink elastic behaviors - linear and bilinear (Fig. 5.4a); the latter may be construed as a simplification of a more realistic nonlinear constitutive characteristic of some crosslinkers [192]. Further, let the stiffness of the linear elastic crosslink be the same as the second leg of the bilinear crosslink. Figure 5.4b shows the shear responses of two identical network topologies, one comprising the linear elastic crosslinks and the other comprising the bilinear crosslinks. While both the networks result in an overall nonlinear stress-stain response, the network with *nonlinear* crosslinks is more compliant than its linear counterpart. The enhanced flexibility of the nonlinear crosslinks allows the network to deform more easily

over an extended strain regime and the overall response stiffens only after the crosslinks stretch out their initial flimsy behavior.
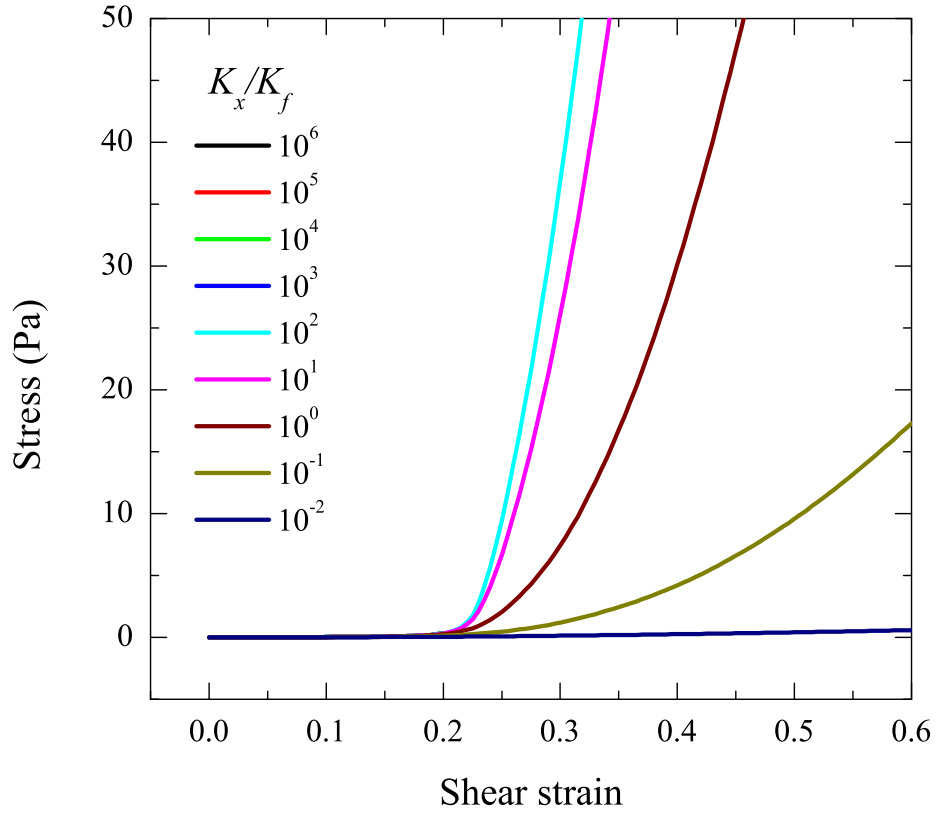
Figure 5.5: Variation of the average $\tau - \gamma$ response of network with $\bar{\rho} = 10$ as a function of crosslink stretching stiffness K_x. Beyond $K_x/K_f \approx 10^2$, crosslinks act as if rigid and the network response becomes independent of K_x.

Motivated by this example, we delineate the role of crosslink stiffness on the stiffening characteristics of networks. For simplicity, we assume the crosslinks (and the filaments also) to be linearly elastic as key network features observed in the nonlinear crosslinks are qualitatively retained. Figure 5.5 shows the overall $\tau - \gamma$ responses for the crosslink stretching stiffness K_x ranging from $10^{-2}K_f -$

$10^6 K_f$, where $K_f = 2 \, \text{pN} \, \text{nm}$ is the filament stretching stiffness. Given that the network topologies are identical the difference in responses are directly linked to the interplay between the filament and crosslink stiffnesses. This interplay is brought about by the different ways in which the crosslink stiffness leads to the deformations in the filaments.

For the most compliant crosslink considered here, the network deforms profusely driven dominantly by the crosslink stretching (Fig. 5.6a). The filaments play second fiddle accommodating the crosslink stretching by themselves bending (given their low bending rigidity), both of which result in very low stresses. As a result, the overall network response does not stiffen at all even when sheared to large strains ($\gamma > 1$). An order of increase in $K_x/K_f = 10^{-1}$ appreciably changes the network dynamics, although still $K_x < K_f$. The network stiffening occurs at a much lower strain than the preceding case and indicates that the initial filament bending (plateau region) causes them to reorient along the principal tensile (and compressive) axes (Fig. 5.6b). The crosslinks too tend to align along these axes and the overall behavior is then a manifestation of springs-in-series like scenario, where the response is dictated by the weaker crosslinks, but modulated by the stiffer filaments. The trend remains the same for the cases $K_x/K_f = 1$ and 10, with the filaments playing an increasingly important role while the crosslinks becoming the source of transferring loads between their connecting filaments. Finally, beyond $K_x/K_f \approx 100$ the crosslinks are so stiff compared to the filaments that the network effectively acts as if rigidly crosslinked and the response is independent of K_x (Fig. 5.6c). This also suggests that from a modeling viewpoint, $K_x/K_f \approx 100$ seems to be a reasonable assumption for rigid crosslinks.

(a) $K_x/K_f \approx 10^{-2}$
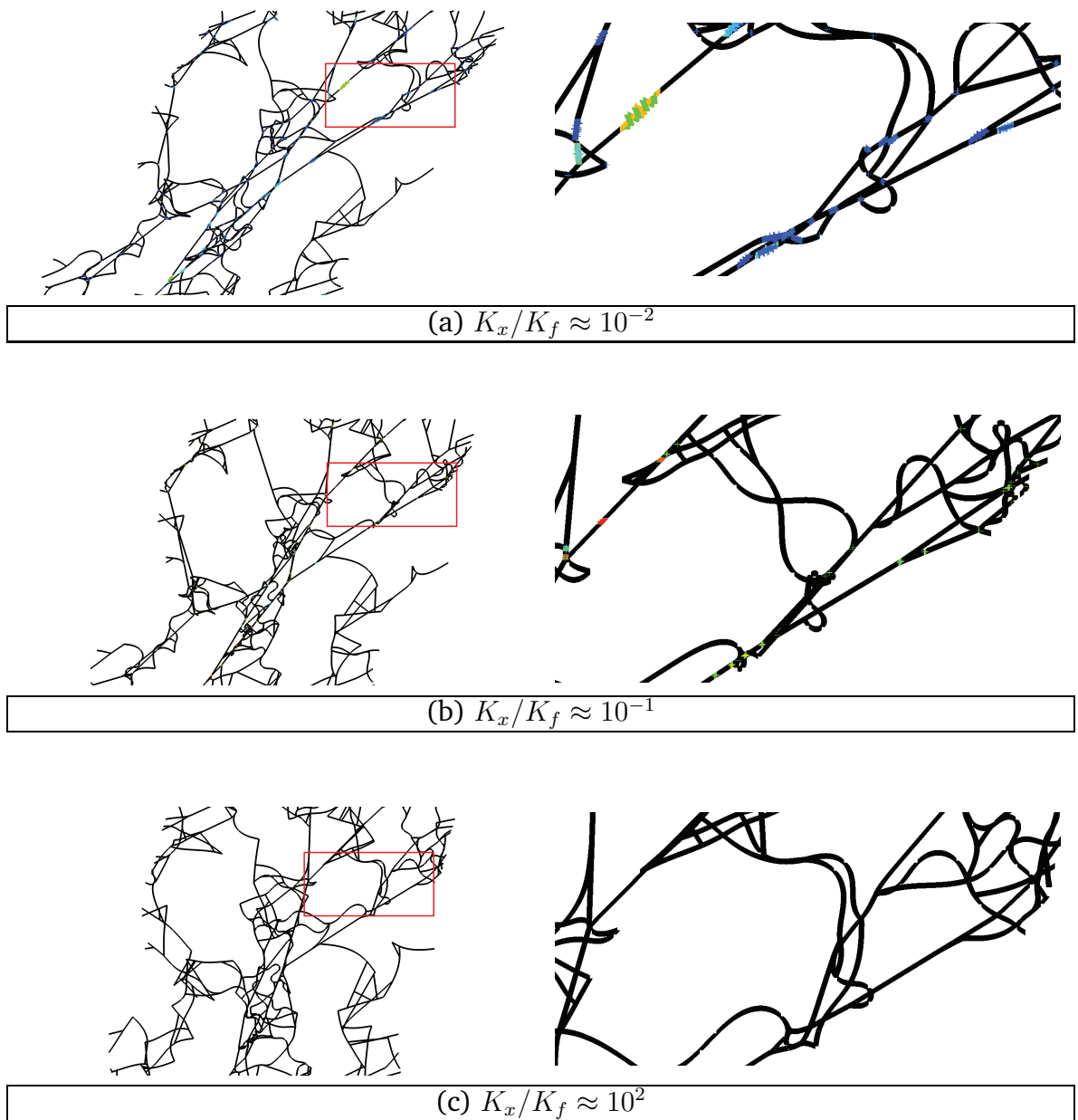
(b) $K_x/K_f \approx 10^{-1}$

(c) $K_x/K_f \approx 10^2$

Figure 5.6: Snapshots of the deformed networks at $\tau \approx 0.5$ Pa for (a) $K_x/K_f = 10^{-2}$, (b) $K_x/K_f = 10^{-1}$, and (c) $K_x/K_f = 10^2$. Figures on the right are enlarged view of the region highlighted by red rectangles. Higher resistance to deformation offered by the crosslinks with increasing K_x/K_f is indicated by the reduced expansion of crosslinks (colored springs represent deformed crosslinks).

A similar saturation characteristic is also observed for K_0 (Fig. 5.7), although the

range over which K_0 varies is small (between 0.11 Pa for $K_x/K_f \approx 10^{-2}$ and 0.125 Pa for $K_x/K_f \approx 10^6$). Interestingly, for $K_x/K_f > 0.1$, the transition strain γ_T is nearly independent of K_x, which means that γ_T is governed by the collective behavior of the filaments and the crosslink flexibility does not play any major role. Consequently, for a network with given constituent parameters, the stiffening initiation depends only on the topological arrangements of the filaments.
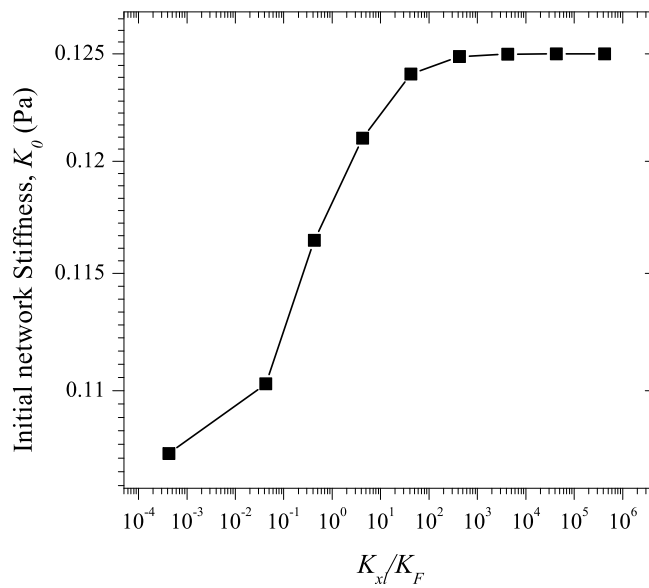
Figure 5.7: Variation of initial stiffness with increasing crosslink stiffness.

5.4 Network Response with Failure of Crosslinks

In Chapter 4, we interrogated the stochastic failure of fibrous networks driven by crosslink scission. However, there we focused on the rate effects in network stiffening and softening mediated by stochastic nature of crosslinks and topological variability. In this section, we re-invoke the crosslink scission mechanics, but ask a different question: how does the filament-crosslink stiffness synergy affect

the network response characteristics, i.e., K_0, γ_T, peak stress and critical damage (fraction crosslinks broken, ϕ)? To answer this and allied questions, we use the same network topology as in the preceding sections together with a range of K_x/K_f. The networks are sheared at $\dot{\gamma} = 1 \text{ s}^{-1}$, but unlike in Chapter 4 here we do not discuss the rate-dependent behavior as main features are unaffected by the applied rate. For simplicity, we also suppress the stochastic nature of scission process (these are briefly discussed later in Section 5.5.4).
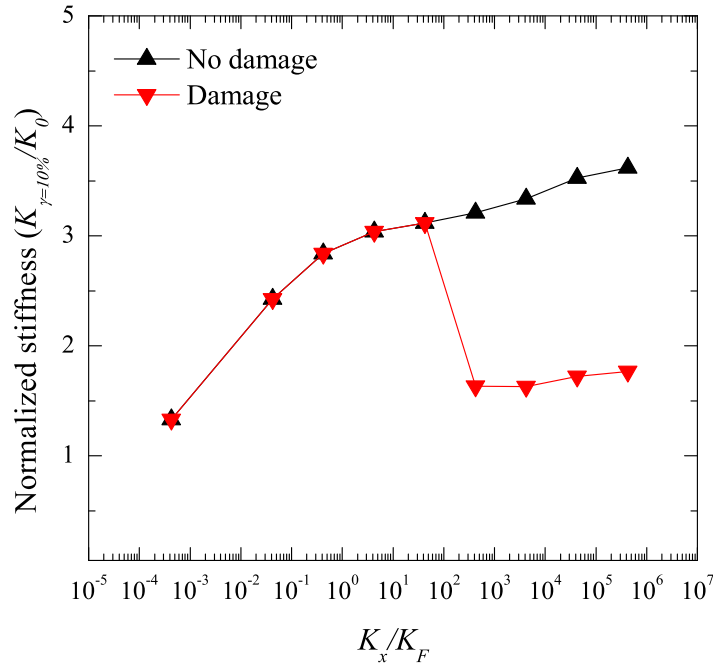
Figure 5.8: Variation of normalized network stiffness $\hat{K}$ at $\gamma = 10\%$ as a function of increasing crosslink stiffness. For rigid crosslinks without failure (black curve), when the crosslink stiffness is ≈ 10 times the filament stiffness, network stiffness saturates as the crosslinks acts as rigid ones. When damage is incorporated (red curve), overall network stiffness drops when the crosslink stiffness is increased beyond certain value due to the crosslink scission.

Note that for the pristine crosslinks case (Fig. 5.5 and 5.7) both, small strain

K_0 and large strain responses $K(\gamma)$ become stiffer with the increasing K_x, but saturate beyond a critical K_x/K_f. With increasing K_x the forces induced on individual crosslinks increase. This leads to an escalation of the crosslink scission rate (Eq. 4.1) thereby enhancing the probability of satisfying the scission criterion (Eq. 4.3). Therefore, it can be expected that for nearly all the K_x/K_f ratios considered here weakening of the network stiffness is expected at some strain. Indeed, the situation dramatically changes with the inclusion of crosslink scission. Figure 5.8 inspects the effect of crosslink scission on the normalized network stiffness $\hat{K}$ at $\gamma = 10\%$. While the trend for $\hat{K}$ follows that of the pristine crosslink case up to $K_x/K_f \approx 10^2$, beyond that the networks exhibit high compliance. This reduction in $\hat{K}$ suggests that for *rigidly* crosslinked networks the scission process may initiate at small strains, possibly even concurrently with the commencement of loading.

Figure 5.9 illustrates this behavior discussion quantitatively where solid lines with symbols (bottom figure) indicate the network tangent stiffness and the lines (top figure) show the damage (defined in Chapter 4). Relatively compliant crosslinks ($K_x/K_f \ll 100$) tend to dictate the overall load sharing and the overall stiffness is low (e.g., solid green line in Fig. 5.9). Indeed, the stiffness in this particular case is so low that no scission occurs over the strain range noted from the absence of the corresponding damage evolution curve (there is no green line in the damage plot as no crosslinks are broken). With increasing crosslink stiffness the network stiffness increases, resulting in some crosslink scission that occurs at intermediate to large strains (e.g., $\gamma \approx 0.2$ for $K_x/K_f = 1$). For rigidly crosslinked networks, instead of high initial and finite strain stiffnesses, one observes a weaker response (black curve). These networks, weakened by the scission process initiated at small strain (≈ 0.02), exhibit an initial stiffness comparable to their counterpart with $K_x/K_f \approx 1$ that does not sustain damage

over a large strain range. Note that this feature is also clear in Fig. 5.8. The crosslink scission induced softening with increasing K_x indicates that for a given set of scission characteristics, there could be an optimum value of the K_x at which the maximum network stiffness can be achieved. Increasing the stiffness of the crosslink beyond this value will result in precipitous softening rather than stiffening.
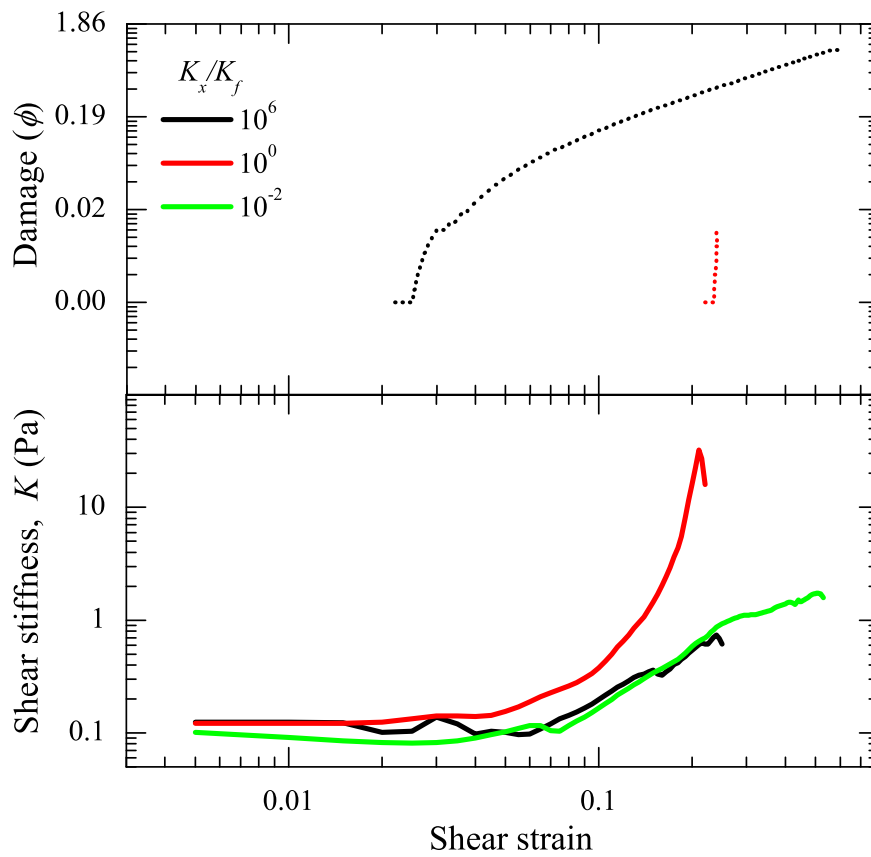
Figure 5.9: Stiffness and damage evolution for three crosslink stiffness. Solid lines shows the stiffness and dotted lines show corresponding damage.

5.5 Toward Constructing a Predictive Response Map

In Sections 5.2.1 and 5.2.2, we observed that the nonlinear stiffening varies significantly with l_b. An interesting query that arises is whether these observations can be integrated into a response surface that provides a minimalist approach to predicting the response of any network with a given set of parameters. This section describes an approach toward constructing such a *map* for a fixed $\bar{\rho}$. To do so, the first step is to perform a comprehensive parametric study over a wide range of stretching and bending stiffnesses for both, fixed and varying l_b [3]. Here we assume the crosslinks to be rigid and therefore, the effect of crosslink stiffness is not interrogated. It has been seen that both initial stiffness and the overall response varies considerably with l_b and cannot be predicted from l_b alone. In this section we probe the initial stiffness and the nonlinear response of networks up to a strain of 15% [4]. For a rigidly crosslinked network, it is l_c that affects the overall network response rather than actual filament length L. We define normalized parameters by scaling stiffnesses with E and l_c. Such a scaling helps to incorporate the role of l_c or $\bar{\rho}$ as increasing $\bar{\rho}$ leads to a decrease in l_c.

5.5.1 Initial Stiffness

Figure 5.10 shows the surface plot of $\tilde{K}_0 = K_0/El_c$ as a function of $\tilde{K}_s = K_s/El_c$ and $\tilde{K}_b = K_b/El_c$ that is interpolated from the results obtained for the simulated cases. Traversing along increasing abscissa (at any fixed $\tilde{K}_s$) indicates an increased energy cost for a network to deform through filament bending, while

---

[3] A total of 49 simulations were performed (indicated by circles in Fig. 5.10) keeping the network topology the same.

[4] For the $\bar{\rho}$ considered here, the nonlinearity/no-affinity settles down and the network response becomes stretching dominated at $\gamma \approx 15\%$, beyond which the response is similar. Also, for the range of stiffnesses probed here numerical solutions are possible up to this strain, beyond which some cases give convergence problems.

traversing along increasing ordinate at a fixed $\tilde{K}_b$ indicates increasing effort to stretch the filaments. On this backdrop, the contour variation shows some interesting features.
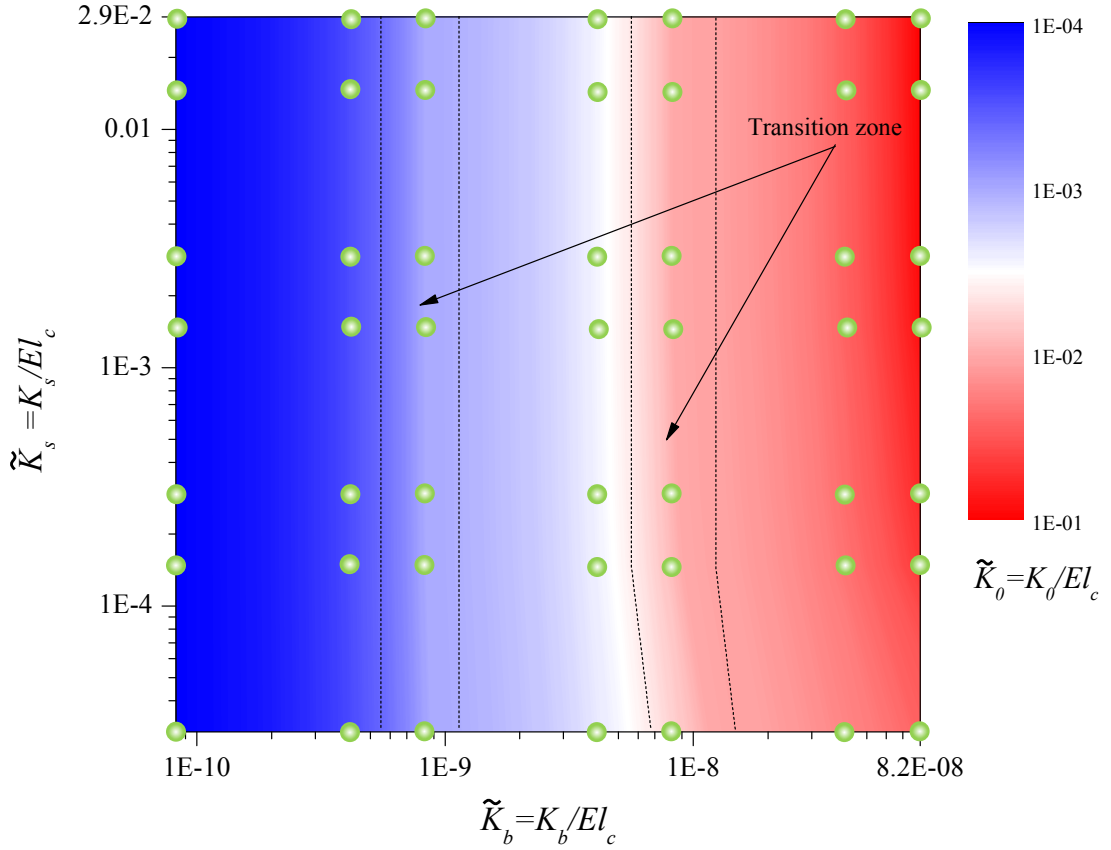
Figure 5.10: Contour plot showing the variation of scaled initial network stiffness ($\tilde{K}_0$) with normalized filament stiffnesses $\tilde{K}_s$ and $\tilde{K}_b$. Superposed circles indicate the simulated cases used in constructing the contour plot.

Note that $l_b = \sqrt{(K_b/K_s)}$ varies in both the scenarios. However, the effect of this variation is significantly different along the paths of constant $\tilde{K}_b$ and $\tilde{K}_s$. For a fixed $\tilde{K}_s$, $\tilde{K}_0$ increases with increasing $\tilde{K}_b$. However, for a fixed $\tilde{K}_b$, $\tilde{K}_0$ is nearly constant. There are thick vertical bands in Fig. 5.10 delineating regions with constant $\tilde{K}_0$ where networks with a range of $l_b's$ essentially exhibit identical initial stiffness. Note however, that this does not necessarily mean the entire

$\tilde{K} - \gamma$ evolution for these networks is the same (discussed *et seq*).

5.5.2 Stiffening Evolution
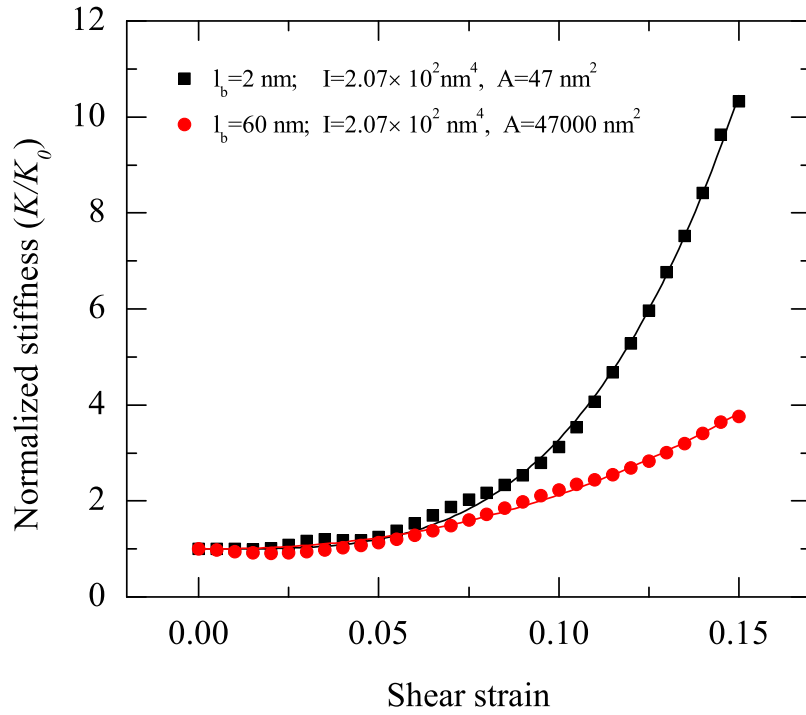
Figure 5.11: Illustrative plot showing the stiffening evolution for same the network topology with different l_b. (black, $l_b = 2$ nm and red, $l_b = 60$ nm). Symbols show the actual responses and the lines are the fits.

To characterize the stiffening evolution, the $K - \gamma$ responses (up to $\gamma_{max} = 15\%$) obtained from each $\tau - \gamma$ are normalized ($\hat{K} = K/K_0$) so that all the curves can be superposed on to one plot. These normalized responses are well-described by power-law functions of the form $\hat{K} = 1 + \alpha^{NA}\gamma^{nNA}$ (e.g., Fig. 5.11), where

$\alpha^{NA} = \alpha^{NA}(l_b, l_c, \gamma_{max})$ and $n^{NA} = n^{NA}(l_b, l_c, \gamma_{max})$[5]. Note that α^{NA} and n^{NA} together provide the measure of the overall network non-affinity, because the material properties are linear elastic and the crosslinks are rigid. In the limiting case, $n^{NA} = 0$ or $\alpha^{NA} = 0$ indicates affine deformation.
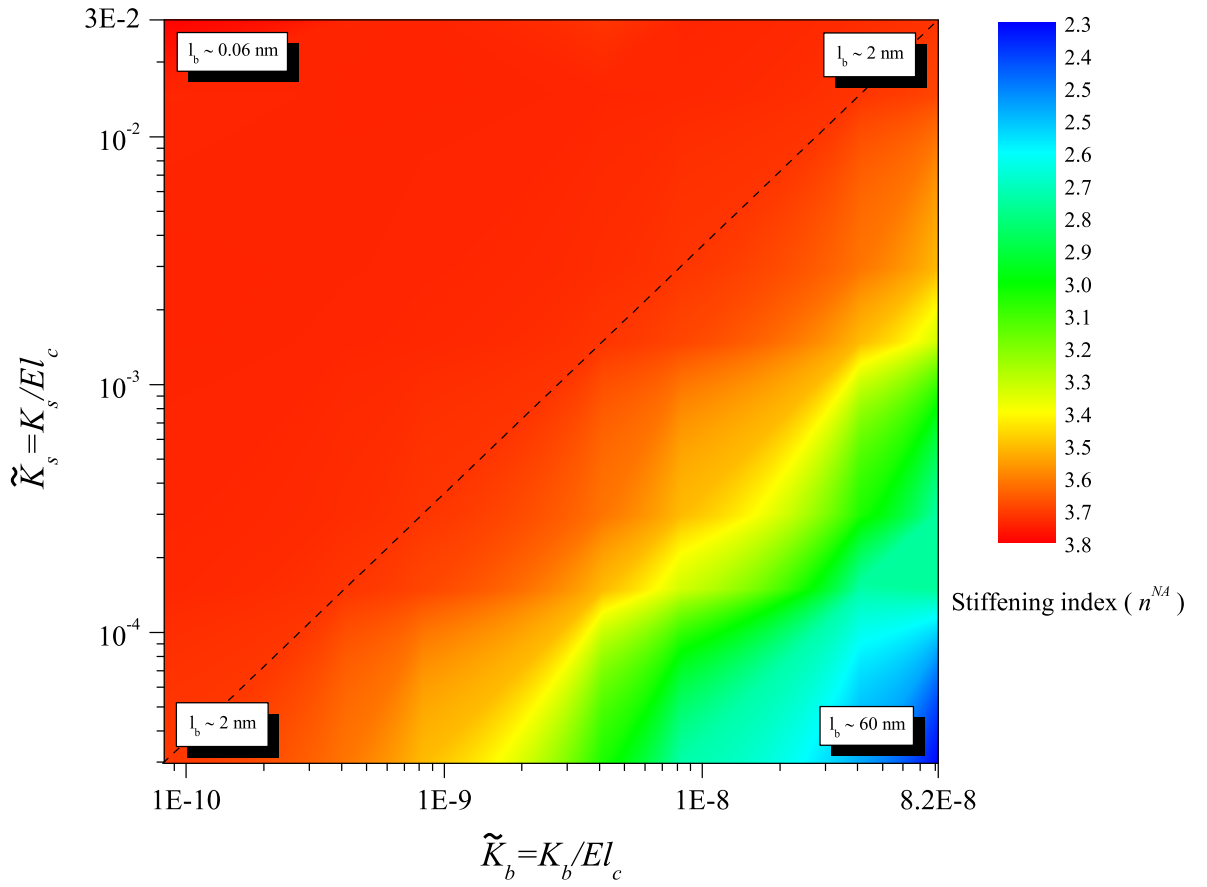
Figure 5.12: Variation of stiffening index n^{NA} with normalized filament stiffnesses $\tilde{K}_s$ and $\tilde{K}_b$.

---

[5]In general, the magnitudes of α^{NA} and n^{NA} are expected to depend on the level of strain (i.e., γ_{max}); however, as is shown later there is a $\tilde{K}_s - \tilde{K}_b$ domain where these are independent of this strain.

Figure 5.12 collates the response of all the simulated cases and shows the variation of n^{NA} with $\tilde{K}_s$ and $\tilde{K}_b$. For further discussion, we refer the line of constant $l_b = 2$ nm as the *main* diagonal. Any line parallel to it represents a constant l_b line. It was observed in Section 5.2.1 that the network stiffening response is governed by the bending nature of the filaments and the results consolidated in this map corroborates with this observation. Along any given constant l_b line the network stiffening rate is identical. For example, if we consider two networks with identical topologies, one at the lower left corner of $l_b = 2$ nm and other at its top right corner, both exhibit identical stiffening rate although their filament stiffnesses are three orders of magnitude apart. The role of filament stiffnesses is to simply translate the curves proportionately (Fig. 5.1).

The region above the main diagonal from the lower left corner to the top right corner may be viewed as the domain of *constant stiffening rate* as the magnitude of n^{NA} is the same irrespective of the filament stiffnesses. The region below this diagonal may be referred to as the domain of *variable stiffening rate* as n^{NA} explicitly depends on the filament stiffnesses. If we traverse along the increasing $\tilde{K}_b$, in the lower region of the map n^{NA} decreases from ≈ 3.6 to ≈ 2.2 as l_b increases from 2 nm to 60 nm. As l_b increases, bending costs more energy and the process of filament realignment and the bending-stretching transition is delayed. At the same time if we traverse along the increasing the bending stiffness at the upper regions of the contour where l_b increases from ≈ 0.06 to ≈ 2, the stiffening index remains constant. This is attributed to the interplay between the bending-stretching nature of the filament deformation. The network response is governed by the lower of the two stiffnesses. At $l_b \approx 2$ nm the network response is governed by the bending of the filaments, leading to an initially highly flimsy behavior that appreciably stiffens only after significant filament reorientation occurs so that stretching mode kicks in. Lowering l_b below this value does not change this

165

mode much, as highlighted by the constant n^{NA} domain. On the other hand, as l_b increases from 2 nm to 60 nm (either traversing along the increasing $\tilde{K}_b$ at $\tilde{K}_s = 3 \times 10^{-5}$ or along decreasing $\tilde{K}_s$ at $\tilde{K}_b = 8 \times 10^{-8}$) the network response increasingly renders through a stretching dominated behavior as evident from decreasing n^{NA}. It shows that a l_b of 2 nm or lower makes the network response bending dominated and facilitates the reorientation of the filaments leading to bending to stretching transition and the resulting stiffening.

5.5.3 Mapping the Scission-induced Damage

The observations on the network responses as a function of filament stiffnesses provide a way to predict the entire stress-strain response of pristine networks that lie within the ranges investigated, albeit for a given $\bar{\rho}$. Given the filament stiffness of a network, its full response curve up to $\gamma_{max} = 15\%$ can be predicted from the maps of $\tilde{K}_0$, α^{NA} and n^{NA}. Fig. 5.13 shows the combined contour of $\tilde{K}_0$ and α^{NA}. The variation of α^{NA} is similar to the variation of the n^{NA} and these two parameters helps to determine the response at finite strains once the initial stiffness is known. One may take a step further and ask if it would be possible to map out the failure accrued by a network in a similar manner given its stiffening characteristics. For example, for networks in the domains of constant $\tilde{K}_0$ and α^{NA} (Fig. 5.13), one may conjecture that the damage evolution through scission would also be the same for the networks in these regions. We probe this important aspect by characterizing the damage responses of selected networks marked by yellow circles in Fig. 5.13.
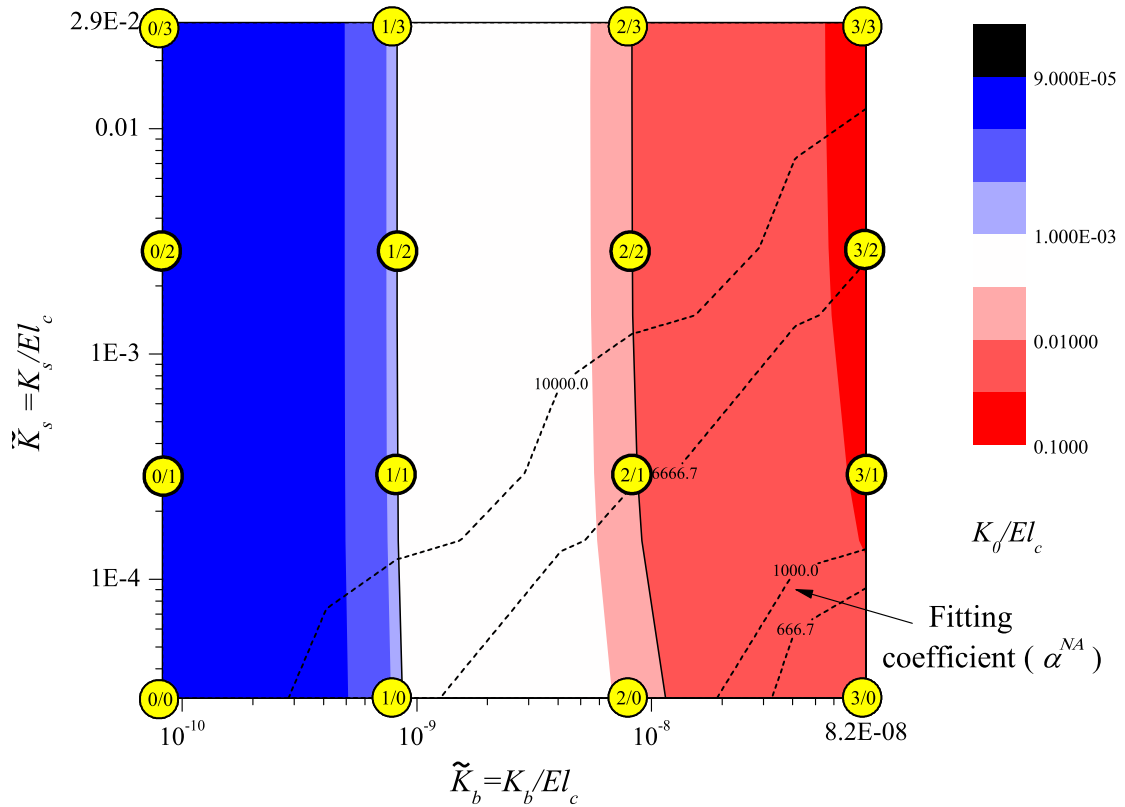
Figure 5.13: Variation of the normalized initial stiffness $\tilde{K}_0$ (colored contours) and the coefficient of the power law fit α^{NA} (dashed lines) with $\tilde{K}_s$ and $\tilde{K}_b$.

Before discussing the results, one may ask: how is such a characterization useful? We believe that such an investigation may be useful in providing important guidelines from the viewpoint of designing fibrous architectures for various engineering purposes (e.g., scaffolds in tissue engineering [115, 155]). For instance, the networks at the extremes of the main diagonal (Fig. 5.12) possess identical stiffening rates (because l_b is the same). However, the overall levels of stress in these two cases are significantly different. Furthermore, if we probe the characteristics along the diagonal of increasing l_b, i.e., moving down from top left to

167

bottom right corner, the response changes from hardening to linear ones. Based on the stiffness values, one may postulate that the networks at different points on the contour may represent different materials but to make such connections, exhaustive investigations have to be done.

In this section we are focusing on the role of stiffness in the damage response of networks. We consider two types of crosslinks; rigid and flexible ones and the variation in damage evolution for these two types of networks are discussed in the the next two sections.

Rigid Crosslinks

In this section, we examine the damage response of the networks with rigid crosslinks (same networks used to create the response contours in Fig. 5.10, 5.12 and 5.13). We also assume that across the entire range of $\tilde{K}_s$ and $\tilde{K}_b$, the kinetics of scission process follow the Bell model, as discussed in Chapter 4 [166, 168, 169]. Across different stiffnesses, same parameters is used in the Bell model so that the results for various simulations can be compared. The numerals in the yellow circles superposed on Fig. 5.13 is coded as **b/s**, where **b** indicates a particular level of $\tilde{K}_b$ and **s** indicates a level of $\tilde{K}_s$ (also see Table 5.1). For the cases simulated, both **s** and **b** takes the values 0 and 3, i.e., the stiffnesses ranges by three orders of magnitude.
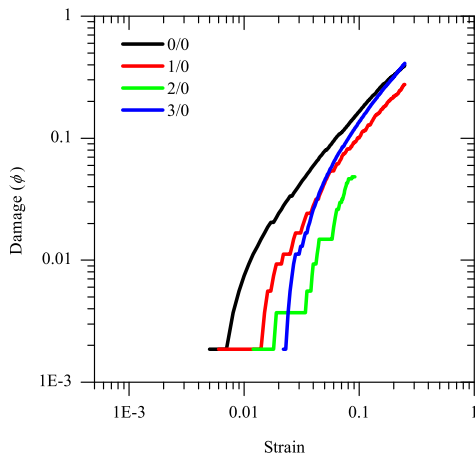
(a) $\tilde{K}_s = 2.9 \times 10^{-5}$
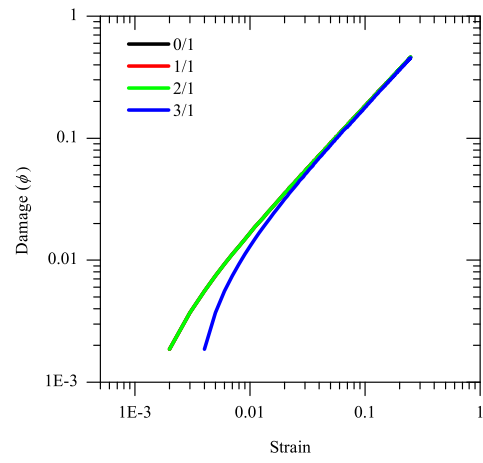
(b) $\tilde{K}_s = 2.9 \times 10^{-4}$
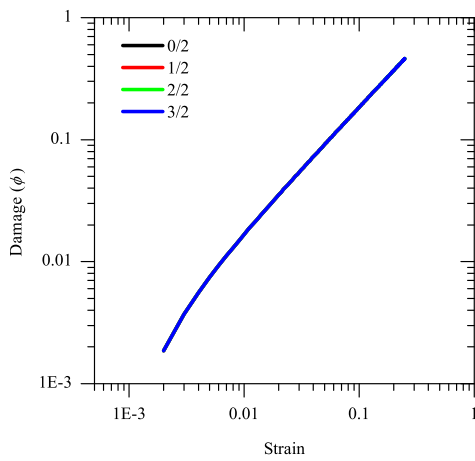
(c) $\tilde{K}_s = 2.9 \times 10^{-3}$
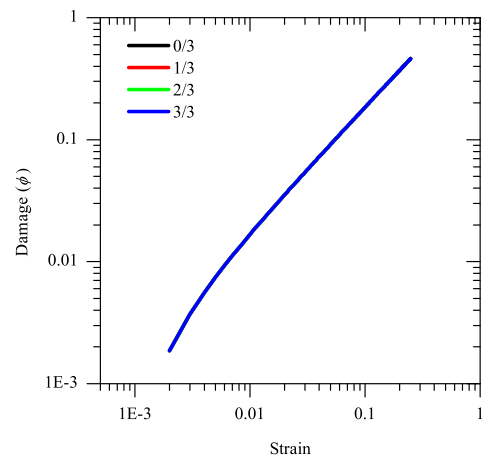
(d) $\tilde{K}_s = 2.9 \times 10^{-2}$

Figure 5.14: Damage evolution of the networks marked in Fig. 5.13. Each figure shows the damage evolution for varying $\tilde{K}_b$ at a fixed $\tilde{K}_s$. As can be seen from Fig. (a) to (d), damage evolution becomes independent of $\tilde{K}_b$. Scale in all figures is the same.

Table 5.1: Filament characteristics for the networks marked in Fig. 5.13. K_b^A and K_s^A indicate F-actin bending and stretching stiffness respectively.

Network Designation	Bending stiffness K_b/K_b^A	Stretching stiffness K_s/K_s^A
0/0	10^0	10^0
1/0	10^1	10^0
2/0	10^2	10^0
3/0	10^3	10^0
0/1	10^0	10^1
1/1	10^1	10^1
2/1	10^2	10^1
3/1	10^3	10^1
0/2	10^0	10^2
1/2	10^1	10^2
2/2	10^2	10^2
3/2	10^3	10^2
0/3	10^0	10^3
1/3	10^1	10^3
2/3	10^2	10^3
3/3	10^3	10^3

Fig. 5.14 show the damage responses, grouped by each $\tilde{K}_s$. Fig. 5.14a shows the response at a fixed $\tilde{K}_s = 2.9 \times 10^{-5}$ and increasing $\tilde{K}_b$. Recalling the discussion of damage in Chapter 4, Section 4.4.6, damage is defined as the fraction of crosslinks broken and is characterized by two parameters; initiation strain (γ_{in}) and growth rate once the damage initiates. For a fixed filament stiffness, γ_{in} shows a rate dependent response and is given by $\gamma_{in} = \alpha^{\gamma_{in}} (\dot{\gamma}/\dot{\gamma}_0)^p$. The key observations from the damage curves in Fig. 5.14 are:

- For a limited range of $\tilde{K}_s$, γ_{in} decreases with increasing $\tilde{K}_b$

- Delayed initiation of damage results in a steeper damage growth

- At higher $\tilde{K}_s$, damage evolution is independent of $\tilde{K}_b$

Extending the observation from Chapter 4, γ_{in} is a function of the filament properties and the network topology; i.e., $\gamma_{in} = f(l_b, l_c, \gamma_{max})$. Fig. 5.14b shows that the trend changes with increasing $\tilde{K}_s$, the sensitivity of γ_{in} to $\tilde{K}_b$ decreases. As we move on to Fig. 5.14c and Fig. 5.14d, irrespective of the value of $\tilde{K}_0$ and α^{NA}, damage becomes insensitive to $\tilde{K}_b$ for a fixed $\tilde{K}_s$.
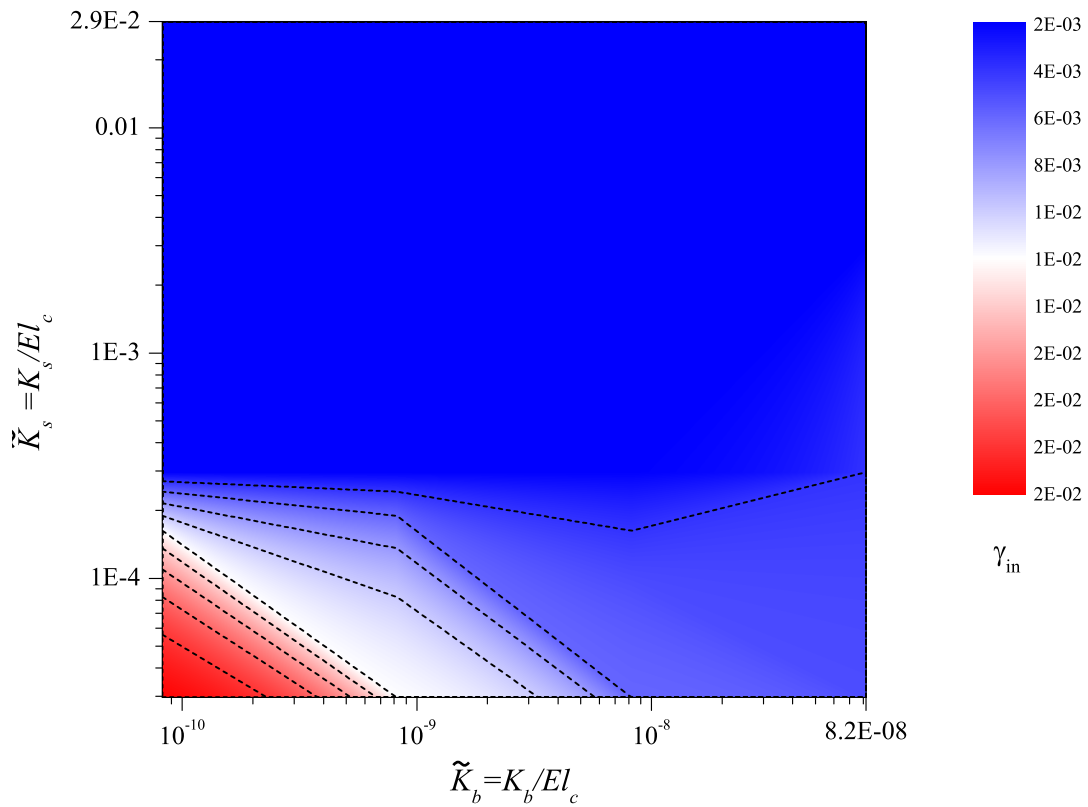
Figure 5.15: Variation of γ_{in} with normalized filament stiffnesses $\tilde{K}_s$ and $\tilde{K}_b$. γ_{in} depends on the filament stiffness only for a sort range and above this value, damage is independent of the underlying filament stiffness (blue region above the upper contour line).

171

To better understand the variation of damage response with $\tilde{K}_b$ and $\tilde{K}_s$, we collate the information in Fig. 5.14 to a contour plot. The plot along with the contours is shown in Fig. 5.15. Variations in γ_{in} ceases at about $\tilde{K}_s = 3 \times 10^{-4}$ and it remains the same with further increase in $\tilde{K}_s$ and $\tilde{K}_b$. Only in a short range, γ_{in} depends on the filament stiffness, then it is independent of the filament properties. Increase in $\tilde{K}_b$ results in lower values of γ_{in} and this may be due to the increase in the overall stress level that leads to early damage (see different regimes in Fig. 5.13). This early initiation leads to merciful collapse of the network as the subsequent damage growth rate is modest and the failure will be gradual (see the difference in the slopes of green and blue curves in Fig. 5.14b).

Predicting the damage from the stiffnesses calls for in-depth understanding the complex damage evolution process; the nexus between the filament-crosslink stiffness, dependence on Bell model parameters, deformation rate etc. In Chapter 4, we explored the rate effects and found that the rate dependency of the damage evolution makes the overall response rate dependent. In the next section, we consider the same examples from Chapter 4 and vary the filament stiffness but at a fixed loading rate.

Flexible Crosslinks

In order to understand the interplay of the filament-crosslink stiffness, we used crosslinks with stiffness corresponding to ABP filamin. For the cases considered, the crosslink is compliant compared to filaments. Mechanical response and damage of eight selected networks marked in Fig. 5.13 (two central rows with thick outlines) is discussed in this section. For the cases simulated, **s** takes the values 1 and 2, while **b** ranges from 0-3.
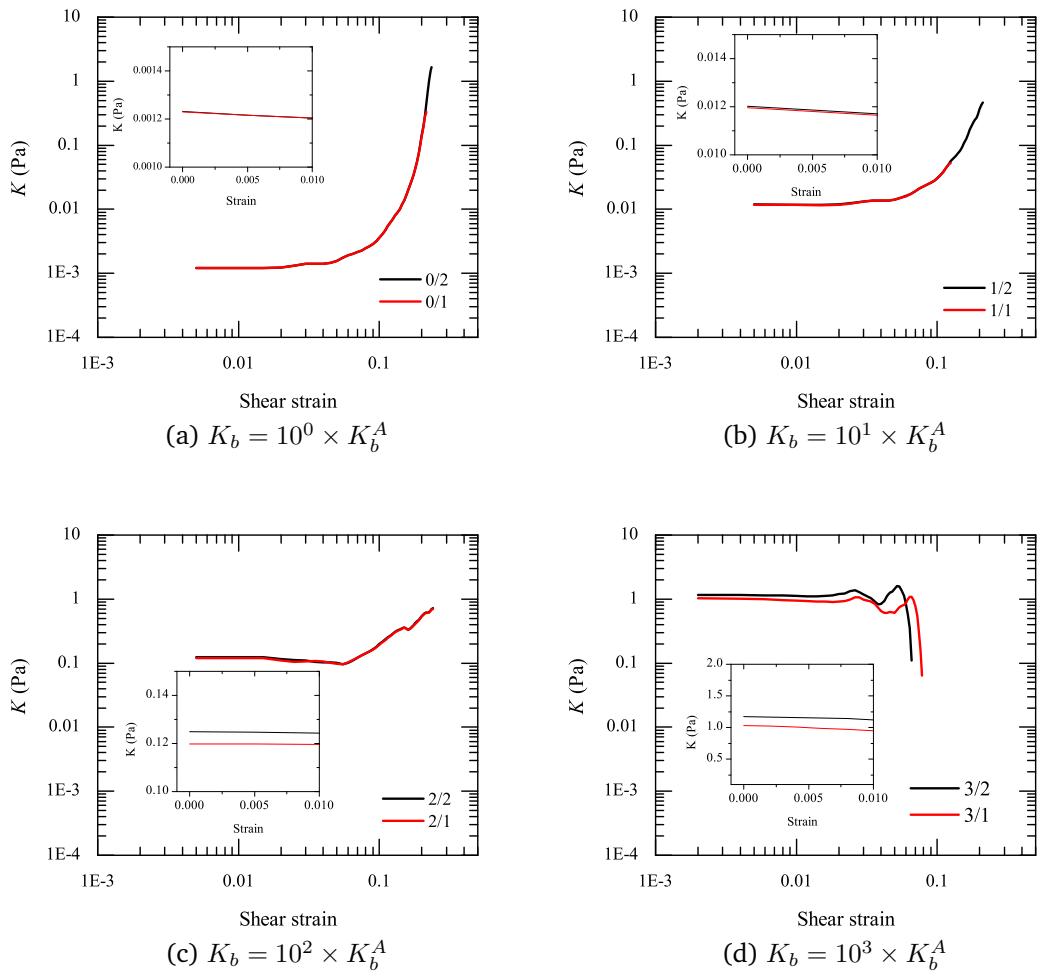
Figure 5.16: Evolution of K with strain for the eight networks marked in Fig. 5.13 in the presence of crosslink scission. K_s is 10 times and 100 times of F-actin for each K_b. Scale in all figures is the same.

Figure 5.16 shows the mechanical response of the selected networks and Fig. 5.17 shows their corresponding damage evolution. The insets in Figs. 5.16 are enlarged views of the small strain network stiffness, which scale with the filament bending stiffness. The stiffness and damage evolution curves exhibit some interesting features. Note that although the initial stiffness and the subsequent plateau (before stiffening commences) varies by orders of magnitude in the four

173

sets of cases, the finite strain ($\approx \gamma \, 0.1 - 0.2$) stiffness is nearly the same in all the cases ($\approx 1 \, \mathrm{Pa}$). Likewise, the ultimate damage at this finite strain is also nearly the same in all the cases (≈ 0.2).

With these broad observations, let us compare the results further. As expected, the $K - \gamma$ responses for cases 0/1 and 0/2 are identical (Fig. 5.16a) given their identical $\tilde{K}_0$ and α^{NA}. Importantly, both the cases also exhibit identical damage evolution (Fig. 5.17a and b). Likewise, the stiffness and damage evolution with strain for the 1/1 and 1/2 cases also superpose. What is interesting between the "0/**s**" family and "1/**s**" family is that the stiffness plateau set by K_0 is an order of magnitude higher in the latter compared to the former (cf. Fig. 5.16a and b), yet their damage evolution curves are identical (cf. Fig. 5.17a and b). This indicates that (at least in the case of rigidly crosslinked networks) the underlying crosslink scission process is unaffected below a certain threshold filament bending stiffness K_b. This statement is reinforced by the damage evolution for the 2/**s** and 3/**s** cases (Fig. 5.17c and d) that despite possessing nearly the same finite strain stiffness ($\approx 1 \, \mathrm{Pa}$) exhibit distinctly different damage evolutions amongst compared to the preceding cases on two counts. First, in the 2/**s** and 3/**s** families the damage initiates at a much later strain (nearly an order of magnitude larger) compared to 0/**s** and 1/**s** families. Second, given that the final dissociated crosslinks is the same in all the cases, the rate of damage growth is much higher in the 2/**s** and 3/**s**. In other words, all the topological parameters (e.g., $\bar{\rho}$, filament distribution, standard deviation) held constant, the nucleation and rate of damage growth is set by the K_b. This aspect of K_b mediated damage evolution may be construed as the flexurally stiff networks degrading rather catastrophically compared to more graceful softening in the flexurally compliant networks.
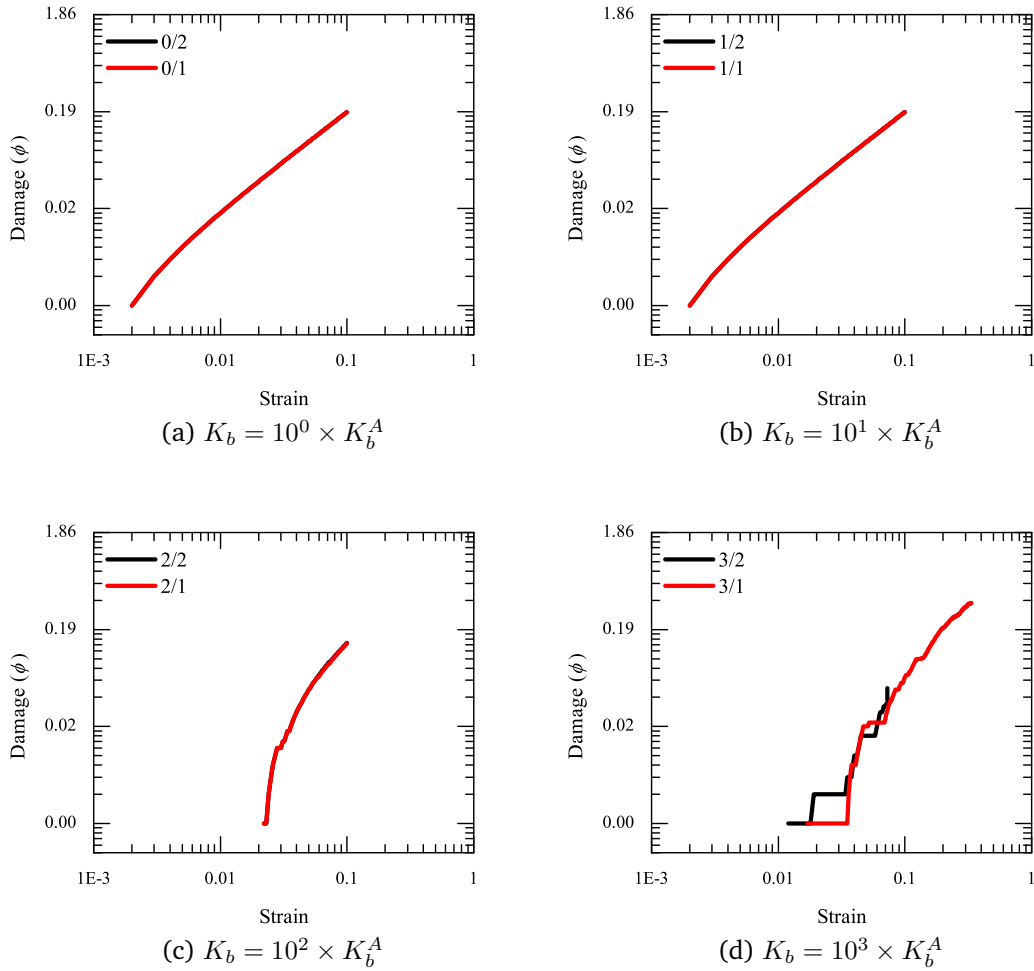
Figure 5.17: Damage evolution of the eight selected networks marked in Fig. 5.13. Scale in all figures is the same.

Focusing on the specific cases, note further that for the 2/1 and 2/2 cases the damage evolution follows identical trends although they are sampled from somewhat different stiffening regimes (see Fig. 5.13). This observation suggests that the evolution may have a threshold sensitivity resolution with regard to α^{NA} and n^{NA}. Finally, there does exist some difference in the damage evolution for cases 3/1 ($\alpha^{NA} \approx 1000$) and 3/2 ($\alpha^{NA} \approx 7000$, but seem to quickly overlap as deformation progresses. Although this may seem to be a minor difference or

175

possibly even an artifact of the numerical simulation, it is worthwhile to note that except for the different filament properties all the other characteristics are identical. Further, we do not observe such "artifact" in any of its predecessors and the observations in this section is similar to the damage characteristics observed for networks with rigid crosslinks and this corroborates the dependence of damage on stiffnesses. With this, we believe that the (initial) difference in the damage evolution may largely be a physical effect rather than artificial. One may expect the difference in the evolution to be more discernable for the cases with significantly different values of α^{NA} and n^{NA}.

5.5.4   Role of Stochasticity
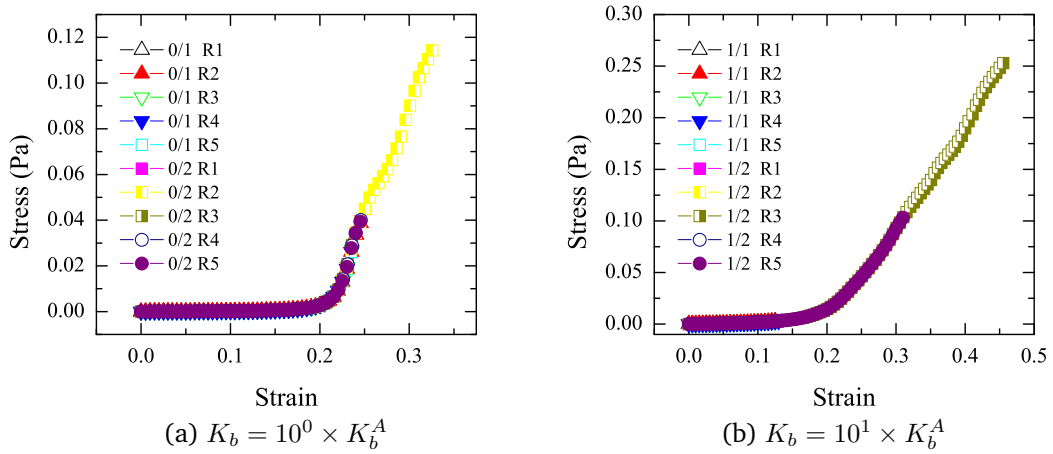
Figure 5.18: Stress-strain responses for two K_b values and each having five stochastic simulations for two different K_s.

The results presented previous section are with deterministic crosslink scission criterion. Here, we relax that assumption by re-invoking the KMC step (Section

4.2.1, Chapter 4). Keeping the basic approach the same as in the preceding sections, we consider two different values for K_b and for each of them, we consider two K_s values. For each combination, we perform five simulations (i.e., total 20 simulations) in order to interrogate the stochastic nature of the scission process. Figures 5.18a and 5.18b collate all the $\tau - \gamma$ responses, and for each K_b the responses are nearly identical. The effect of bending stiffness on overall response can be easily noted from the two figures in Fig. 5.18. For $K_b = K_b^A$, the stress is nearly zero till a strain of $\approx 20\%$ where as $K_b = 10^1 \times K_b^A$ shows more linear response and networks start to stiffen at strains as alow as $\approx 10\%$.

5.5.5 Non-affine Response

The variation in stiffening response seen in Section 5.5.2 is tightly couple to the affine/non-affine nature of the deformation. It is postulated that the crossover of response from affine to non-affine depends on the the filament density (it has been incorporated by the length scale l_c which is defined as the distance between crosslinks) and the material length scale l_b. These two information is incorporated into a new length scale λ_{na} which is defined as $\lambda_{na}(l_c, l_b) = l_c(l_c/l_b)^{1/3}$ [126]. Based on this definition, Head *et al.* classified the deformation to be affine if a non dimensional number $L/\lambda_{na} >> 1$ (≈ 10 or higher) and non-affine if $L/\lambda_{na} < 1$ [142].

For highly anisotropic networks, L/λ_{na} is not the only measure of non-affinity. These networks behaves different from an orthotropic solids and this strong non-linearity is attributed to the cooperative bending and Euler buckling related to the *floppy modes* of the filament networks. Spatial heterogeneity in strain field is used as a measure of non-affinity. This measure does not depend on the net

filament orientation of the network or on the loading direction. Bending of a filament encourages the cooperative bending in the filaments which it is connected to it until the filament length is too small enough to be incompliant for bending.
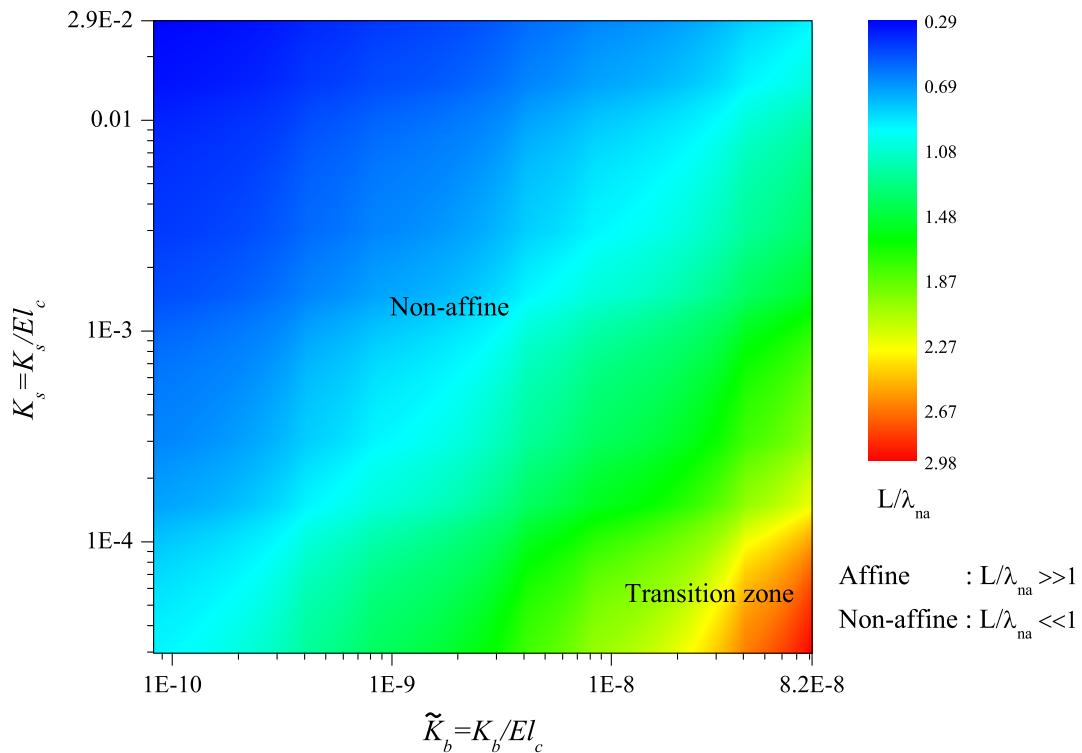
Figure 5.19: Deformation mapping with the variation in filament stiffness. Based the L/λ_{na} criterion, the entire regime is non-affine deformation.

For lower L/λ_{na} values, networks shows more non-affine response due to the Euler buckling of filaments which results in nonlinear softening and more energy will be stored in bending than stretching. In the case of networks having a fixed L/λ_{na} and loading direction, one which the highest anisotropy shows the highest nonlinearity. This is due to the pronounced buckling of the highly oriented filaments under compression. Figure 5.19 shows the measure of non-affine response

(L/λ_{na}) of the networks with varying stiffness. For the networks considered here, L/λ_{na} varies from ≈ 0.29 to 2.9 and based on the description of Head *et al.* [142] it falls in the transition regime. As in Fig. 5.12, deformation is similar along the constant l_b lines. This is due to the fact that the bending depends on the value of l_b and at a fixed l_b, the bending response of the filaments are identical. When the $l_b \approx 0.06$ nm network shows higher bending and the response is highly non-affine but the stiffening response was insensitive to a value of l_b less than 2 nm. As the l_b increases, bending energy increases and the response becomes more affine due to the stretching dominated response. This transition can be observed at l_b of 60 nm. Increasing l_b beyond this value may make the response more affine (region pointed by the arrow in Fig. 5.19). This corroborates that increasing the bending stiffness alone could make the non-affine to affine transition without increasing the filament density [126].

5.6   Summary

The role of filament properties on the mechanical response and damage are shown using 2D filament networks in a finite element framework. Key aspects of the mechanical response like initial stiffness, finite strain stiffness, stiffening, damage etc. are discussed in the context of the material length scale l_b and topological length scale l_c. A parametric study of the network response over three decades of the filament stiffness is done and the results are presented as contour plots. The correlation between the mechanical response and damage over a wide parametric space provides insights to develop a predictive map for the network response. Affine/non-affine transition in the same parametric space is also briefly discussed.

Chapter 6

Micromechanics of diffusion-induced damage evolution in reinforced polymers

6.1 Introduction

One of the manifestations of random architectures relevant to mechanics community is composites where randomly arranged reinforcement inside a matrix that makes the composite stronger. The reinforcement could be of different size, shape and volume fractions. This chapter focuses the random architectures of fibers which forms the microstructure of the fiber reinforced composites. Previous chapters focused in the mechanics and characterization discrete random architectures of filamentous networks. Mechanics of networks is explained in terms of filament/crosslink property and crosslink failure was accounted as damage. As in the fiber networks, topology is characterized in terms of statistical parameters and its correlation with damage is shown. Damage is quantified as

180

the debonding of the interfaces which is an integral part that transfers the load from the fibers to the matrix.

Polymers, natural or synthetic are often reinforced with stiffer inclusions in the form of fibers or particles to create heterogeneous composites that are attractive for applications where mechanical strength and stability are of primary interest. The choice of the polymer (matrix) and inclusion (reinforcement) is dictated by the requirements of the end application. Many large-scale structural applications such as automotive, aerospace, turbine blades etc. typically employ epoxy-based polymeric matrices reinforced with high strength synthetic fibers such as glass or carbon. Often, the differences in the physical, mechanical and chemical properties of these two constituents create a large property mismatch in the interfacial regions of the composite. Under external stimuli, high stresses tend to concentrate around these interfacial regions and this may potentially lead to overall composite degradation through a variety of microstructural instabilities including interface debonding, fiber breaking, void nucleation and shear localization in the matrix that are precursors to the macro-structural failure. It has been long recognized that while polymer composites possess exceptional potential in designing light and strong applications, their use may be limited by the fact that their response to environmental conditions during their functional life is not well understood. This is especially critical when one recognizes that they are deployed in protean service environments and are expected to perform over long periods of time. Residual stresses occur in a composite subjected to varying temperature or moisture conditions, due to the difference in the thermal or moisture expansion coefficients between the fiber and the matrix. In particular, moisture ingress may assist the degradation of composites, possibly further amplified by temperature, that may be detrimental, for example, wind energy or marine structures that experience a range of changes in temperature and moisture (salinity may

have additional effects) in addition to the regular mechanical loads [194, 195]. Composites used for dental restoration purposes may experience aqueous service environments that range between strongly acidic to strongly alkaline [196]. Further, the moisture diffusivity itself may be a function of the applied stress, which in turn may affect the stress distribution in the composite [197–199]. The absorbed moisture may lead to matrix cracking [200–204] or plasticize the matrix thereby reducing effective stiffness and strength of polymers [200] and their composites [194, 195, 205]. An efficient design of a composite for specific functions relies heavily on the ability to predict the possible mechanisms of failure at multiple length and time-scales when subjected to such synergistic environments [206, 207]. These effects may be further complicated by the fact the most composite micro-architectures exhibit random inclusion topologies.

The aforementioned scenarios pose challenges for engineers and necessitate a better understanding of the mechanical behavior of such heterogeneous micro-architectures in hostile environments (moisture) as a function of microstructural details.In this work, we focus on the moisture induced damage in composites. The randomness in the microstructure not just affect the load transfer but also the diffusion pathways. The moisture transport can be better understood by considering the tortuosity of the microstructure. Accounting for the discreteness of the microstructure is important as the moisture transport is a highly direction dependent phenomenon. Presence of externally applied forces makes it a coupled problem and we study this using a micromechanical model which accounts for the spatial heterogeneities of the microstructure. The following sections give a brief background about how moisture degrades composites.

6.1.1 Moisture Induced Damage of Epoxies

Epoxies have an affinity to water as it has polar sites which react with water and it may lead to plasticization. Water enters the epoxy by diffusion and the absorbed water has to components; water which resides in the free volume in the polymer called *free water* as it can further diffuse to other locations and another component which react with the polymer called *bound water* [208–210]. Usually the water molecule inside the epoxy breaks the existing hydrogen bonds and reacts which the amine groups resulting in chain scission [211–213]. These two interactions leads to plasticization and failure strain may increase [214].

One of the best ways to shed light into the moisture induced damage in polymers is to utilize the spectroscopic information [215]. Experiments like Fourier transformed infrared spectroscopy (FT-IR), FT-IR microscopy and Raman chemical imaging are used to study the extend of degradation like hydroxyl reactions, chain scission etc [216]. Damage depends on the stoichiometry of epoxies, sometimes a strengthening response is observed if the water molecules aids in the epoxide reaction. Polyester based composites shows an increase in strength after subjected to moisture [215].

6.1.2 Moisture Induced Damage of Glass Fibers

Glass fibers reacts with water leading to loss of strength and the reaction by-products could lead to weakening of the interface and further undesirable effects. This effect is more dominant if some coupling agents are applied to the glass fibers [215]. Liao and Tan found that the moisture induced stress alone is sufficient to cause stress corrosion in E-glass fibers even in the absence of externally applied load [217]. Their experiments concluded that the glass fibers in

epoxy matrix composite degraded at a faster rate than the stress free aging of glass fibers. A review by DiBenedetto discusses about the various mechanisms by which the polymer-siloxane-glass interfaces are formed and the interface thickness is identified as 100-500 nm [218]. The nature of water on the glass surface of epoxy/glass composites were studied using fluorescence methods [219]. Fibers with different silane coating revealed that the diffusivity around the interfaces differs with the coating resulting in low absorption of water but the gross sorption of the composite remained the same.

6.1.3   Moisture Induced Damage of Interfaces

Depending on the fiber/matrix composition, the interface may be the weakest region where the damage could initiate even without considering the moisture induced degradation [215]. Presence of environmental stimuli along with the external load may lead to the interface debonding. Once the interface is debonded, it may act as channels for the transportation of moisture and further exacerbate the damage (Fig. 1.10). Chateauminois *et al.* studied the effect of hygro-thermal loading on epoxy reinforced with unidirectional fibers and observed that the diffusion follows Fick's law at temperatures below 70^0C but deviates from Fick's law at prolonged exposures which coincides with the interface debonding. They attributed the irreversible damage of the interface only at the non-fickian diffusion which takes place after the epoxy has saturated with moisture [220]. Interface strength of composites can be varied by different chemical treatments to the fiber surfaces. The effect of interface strength and the debonded interface on diffusion characteristics was studied by Tsenoglou *et al.* by considering fibers with various surface treatments [221].

184

6.1.4 Characterization of Interfaces

In the micromechanics model, we are explicitly looking at the interface behavior. One should have thorough understanding about the interface behavior and its damage response to develop such models. Extensive work has been done to characterize the interfaces of various fiber/matrix combinations and the interface shear strength and fracture energies have been identified. The presence of covalent bonds at the interface is still debated but the major consensus is for it, at least in the presence of coupling agents [215]. Few experiments which shed light into the interface response are microbond/micro droplet experiments (Fig. 6.1), fiber push out (Fig. 6.2) and fiber fragmentation tests [222, 223]. Apart from these, visual observation of the scanning electron microscopy images of the interfaces gives information about the condition of the interface like debonding, presence of chemical species etc (Fig. 1.10). We need the information about the role of moisture in weakening of the interface to account for the moisture induced degradation.

Fracture mechanics approach has been used for the damage modeling of composites at both ply and micromechanics level. A review paper by Tay discusses the major developments in this field over last one decade [105]. We use a similar approach and model the interface using cohesive elements that follows the traction separation rule [224, 225].

Microbond experiment is used to measure the interface strength by depositing a drop of the polymer on a single fiber and the shear strength is calculated by pulling out the fiber from the epoxy droplet after it has hardened. It is highly dependent on factors like the uniformity of the fiber diameter and out of roundness of fiber diameters. Miller and coworkers discusses about the variability of interface strength obtained using the micro bond experiments accounting for above

185
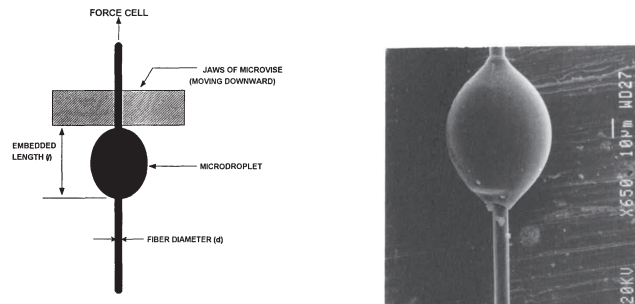
(a) Schematic diagram [226]   (b)Experiment [227]

Figure 6.1: Microbond test to find out the interface shear strength.

factors and the analysis of the droplet configuration [226, 228]. Kang *et al.* conducted microbond experiments with carbon fiber epoxy composite to find out the interface strength. They found the interface strength depends on the range of the embedded length of the fiber and further probed the stress distribution in the epoxy droplet using finite element studies [229]. In a subsequent work by the same group, Choi and park used a quasi-disk type droplet and found more reliable information about the interface strength [222]. Zhou *et al.* used fiber push out and fragmentation experiments to find out find the interface strength and energy of composites. Their experiments with E-glass/epoxy system with and without chemical treatments of the fiber revealed that the former shows higher interface strength and energy [223].

In order to understand the interface response under the influence of moisture, Gaur *et al.* conducted the microbond experiments for various fiber/matrix combinations [231]. An interesting observation in this work is that the interface strength of all fibers in the epoxy matrix decreased after aging in water at 88^0 C while the same fibers in polyethylene matrix showed an increase in strength. Hodzic *et al.* studied about the interface strength of composites with glass fibers
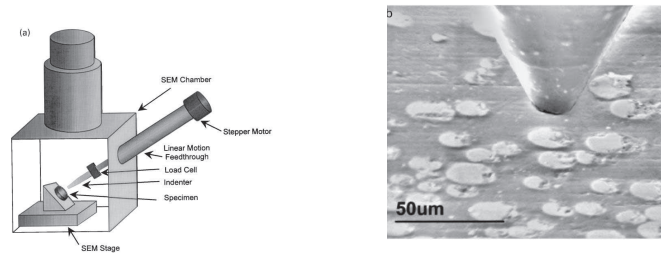
(a) Schematic diagram [230]   (b) Experiment [230]

Figure 6.2: The interface strength can be determined by fiber push out test. Individual fibers are pushed out from a cross-section of the composite using a nano-indentor.

and various matrix materials including the effect of moisture [232]. They identified interphase region and observed the debonding of interface even in the case specimens subjected to only hygrothermal loads [233]. Their work showed that polyester based composites showed excellent resistance to moisture induced degradation of the interface and remained intact even after 6 weeks of aging in water [234]. Microbond experiments by Biro and coworkers on epoxy/carbon fiber composites revealed $20 - 40\%$ drop in the interface strength after 6 hours of exposure to hot water [227]. X-ray photo electron microscopy did not reveal much variation in the surface chemistry of the fibers and the loss of strength was attributed to the plasticization of the epoxy and mismatch strains. These experiments provided valuable information about the interface response of the composites that can be used in micromechanics based models.
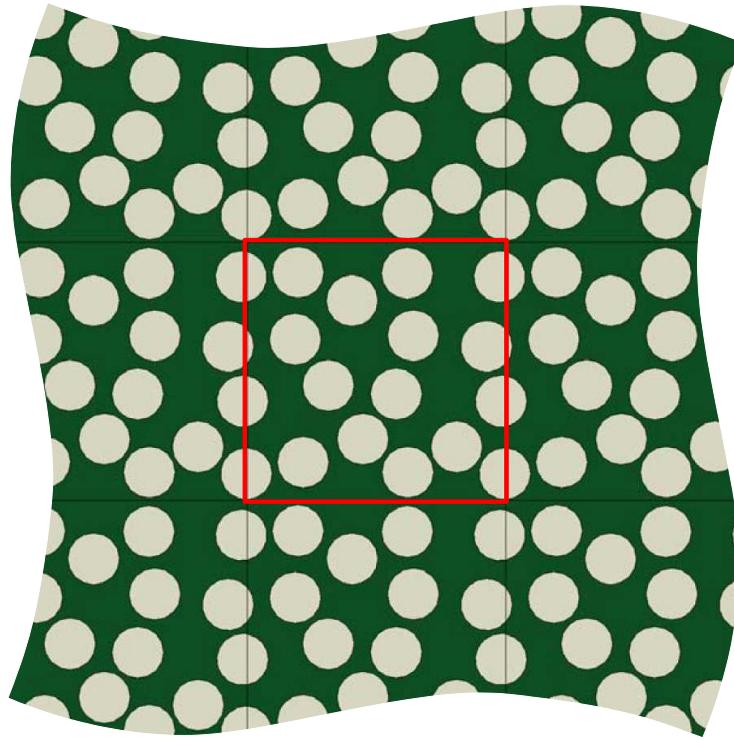
Figure 6.3: A transverse section of a unidirectionally reinforced composite with random fiber arrangement. The random architecture can be approximated by a periodically repeating domain, shown by the red square.

6.2 Computational Modeling

In this work, we numerically investigate the response of reinforced glassy polymers under transient hygro-mechanical conditions at the microstructural length-scale. We focus on modeling the nucleation and evolution of damage at the micromechanical scale in a model glass-reinforced epoxy polymer composite subjected to moisture and mechanical loads under isothermal conditions. Of the above-mentioned possible micro-structural modes of failure, we explicitly model the experimentally observed debonding at the matrix-inclusion interfaces due to moisture-induced stresses [195, 235, 236]. Such debonded interfaces may act

as channels causing accelerated diffusion especially if it is in the exposed surface [237]. Further, some experiments on glass fiber-epoxy matrix composites have revealed that both the strength and toughness of the fiber-matrix interfaces may degrade significantly in moist environments exacerbating the severity of damage [195, 238]. Motivated by these experimental observations (see also [239]), we incorporate the possibility of the interface behavior that continuously degrades with the evolution of local moisture concentration. While the moisture diffusion and stress build-up phenomena in composites have been modeled by researchers (e.g., [240, 241]), there are relatively few works that model the evolution of hygro-mechanically induced damage, in general (e.g., [199, 242]) and interface failure, in particular (e.g., [243]). Some works that do model interfacial effects under hygral or thermal excursions resort to the restrictive assumption of unit cells with regularly arranged fibers (e.g., [244]), which is seldom the case in real materials [245]. In fact, the effective diffusivities may strongly be affected by the tortuosity of the microstructure, which may have direct implications on the build-up of differential stresses [241, 245, 246]. In this work, we relax this restriction by choosing representative volume elements (RVEs) with random arrangements alongside the regularly arranged RVEs. Fig. 6.3 shows a section of unidirectionally reinforced composite with infinite dimension along both x and y axis. Fibers are randomly placed in the matrix and one of the simplifications to such an arrangement is periodicity. The red square box is a periodic unit cell, representative of the entire microstructure and is considered as the RVE for modeling. The enitre microstructure can be generated by translating the RVE along both axis.

In précis, the objective of this work is to develop a predictive approach to characterize moisture diffusion-induced damage incurred through interfacial failure

in reinforced polymers as a function of microstructural randomness and its effect on the subsequent response when loaded mechanically. In the next section, we describe the computational setup and the details of the finite element (FE) models used in the investigation.
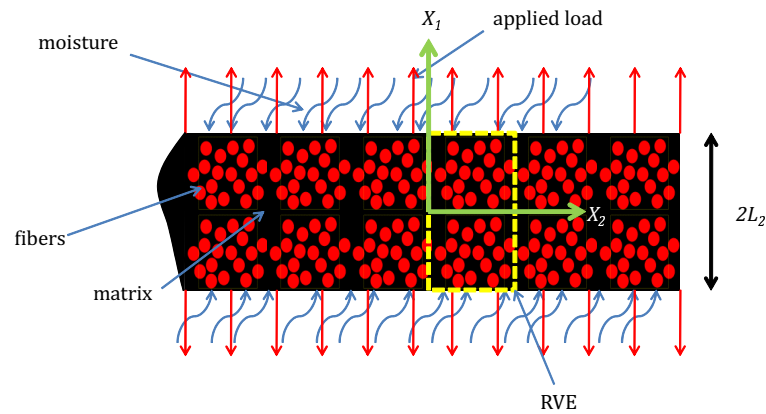
Figure 6.4: A unidirectionally reinforced composite lamina subjected to mechanical and moisture boundary conditions. The lamina is periodic in the X_1 - direction. A typical RVE considered in the computational modeling is shown by the dashed boundary.

Figure 6.4 shows a typical section of a unidirectionally reinforced lamina of thickness $2L_2 = 100 \ \mu$m [206] in the X_2 direction considered in the present work. We consider the lamina to be infinitely long in the X_1 direction, comprising repeating unit cells giving a periodic RVE in that direction (shown in the Fig. 6.4 by the dashed box). Further, we assume that the lamina is symmetric about $X_2 = 0$ and satisfies the plane-strain condition in the X_3 direction. Within an RVE the fibers may be arranged in a regular or random manner. The top and bottom surfaces of the lamina may be subjected to mechanical and/or moisture boundary conditions (b.c.'s).

6.2.1 RVE generation and characterization of micro-architectures

Microstructural characterizations of real composites unequivocally reveal the random topological arrangements of fibers (e.g., [107, 247]). While one may use digitized versions of such real microstructures, we adopt a more computational approach in that we generate artificial microstructural arrangements mimicking real composites [248]. Such a strategy enables comparing a wide range of microstructures with different fiber volume fractions (v_f), arrangements and fiber diameters.
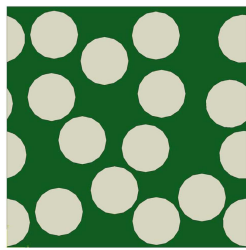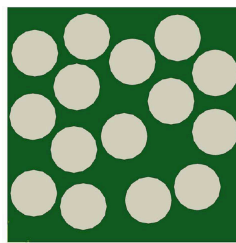
(a) Random 1 (R1)   (c) Random 2 (R2)   (b) Random 3 (R3)
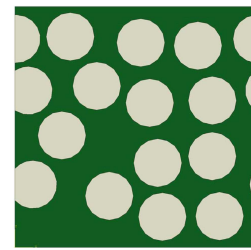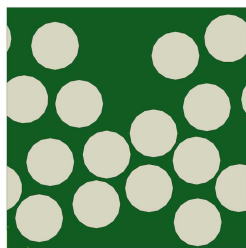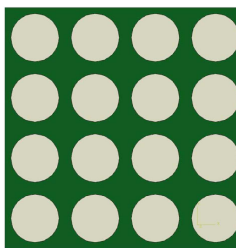
(d) Random Cluster (RC)   (e) Square Regular (SR)   (f) Square Cluster (SC)
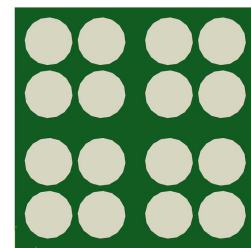
Figure 6.5: RVEs with different fiber arrangements having $v_f = 0.5$ and $d = 10$ μm .

As an example, Fig. 6.5 a-f shows six of the nearly fifty[1] different RVEs considered in this work that are generated using an in-house code for two-dimensional (2D) heterogeneous composite micro-architectures with desired fiber arrangements (regular/ random and uniform/ clustered), for a given fiber diameter d and v_f

---

[1]These include RVEs for different v_f ($v_f = 0.30, 0.40, 0.50, 0.60$) and diameters ($d = 9, 10, 11$ μm).

. Specifically, these RVEs are constructed for fixed $v_f = 0.47$ for all the random arrangements and equal to 0.50 for the two regular arrangements to investigate the effects of fiber distribution. These volume fractions are represented by fifteen (sixteen in the case of the regular arrangements) $10~\mu\mathrm{m}$ diameter fibers [230], which also sets up the size of the RVE. The RVEs in Fig. 6.5a to c are three different random (R1, R2, R3) arrangements. Note that amongst these three the R2 arrangement has all the fibers completely inside the RVE, which means that there exists a thin matrix-rich layer at the edges of the RVE [245]. Figure 6.5d shows a random arrangement but with a clustering (RC) of fibers leaving what appears to be a big region in the microstructure that is matrix-rich. Fig. 6.5e shows the regular square (SR) arrangement, used as benchmark. Finally, Fig. 6.5f shows the square clustered (SC) arrangement where a set of four fibers are placed close together and this arrangement is repeated within the RVE. This description of the RVEs with random fiber arrangements is qualitative.

In literature, different approaches have been formulated to characterize the topological disorder in composite microstructures. Pyrz *et al.* [249] defined topological entropy based on the Dirichlet tessellation method and correlated it with the microstructural stress field in fiber composites. Chen and Papathanasiou [247] used a second-order intensity function based on a cut-off radius and the number of fibers within that zone to characterize different fiber arrangements. Based on an exclusion probability defined by Torquato [250] few others [251, 252] used the nearest neighbor distance. In this work, we quantify the heterogeneity of fiber distribution (i.e., clustering) in different RVEs using the center-to-center (c-c) distance between the neighboring fibers. The neighbors of a fiber are defined such that the lines joining the centers of two fibers do not trespass other fibers. Then, the coefficient of variation C_v ($=\Sigma/\xi$, Σ = standard deviation and ξ= mean) of the c-c distance can be used as a metric to quantify clustering. Figure

6.6 shows an example for a random arrangement with $d = 10$ μm and $v_f = 0.47$. Green circles are the fibers, the magenta outline represents the periodicity of the RVE, and the blue and red lines connect the centers of fibers such that none of the lines pass through an intermediate fiber. Note that the red lines connect fibers that are significantly apart from each other even though they may not necessarily communicate with each other through their stress fields, yet they can be connected topologically as far as the definition of c-c connectivity is concerned. From a topological perspective, this situation may not be uncommon in random microstructures; however, from the physical viewpoint it may not be relevant to include such remote influences. An important question then arises: for a given fiber, how many surrounding fibers influence its failure? In other words, is there a cut-off radius r_c that can be used in determining C_v? From a stress concentration argument, one may consider that fibers that are more than $\approx 1 - 2$ fiber diameters away from the fiber edge may not significantly influence its failure. Referring back to our example in Fig. 6.6, for a fiber at the center, the neighborhood of influence with $r_c = 4r$ ($r = d/2$) and the c-c lines falling within this cut-off are shown by blue lines and are used to calculate a C_v; the red lines exceed this distance and are ignored in the calculation of C_v. As such, the C_v for a given RVE then depends on the chosen r_c. Therefore, to evaluate its influence we chose three different r_c's to calculate the relevant c-c distances, namely, $4r$, $4.5r$ and $5r$ (so that the edge-edge distance between any two interacting fibers are $= 2r$, $2.5r$ and $3r$, respectively). This also partly accounts for the next nearest neighbor interactions. In section 6.3.3, we discuss the correlation between C_v's defined this way and the overall damage. We demonstrate that the degree of overall damage correlates well with the C_v across protean RVEs with different distributions, v_f and diameters.

193
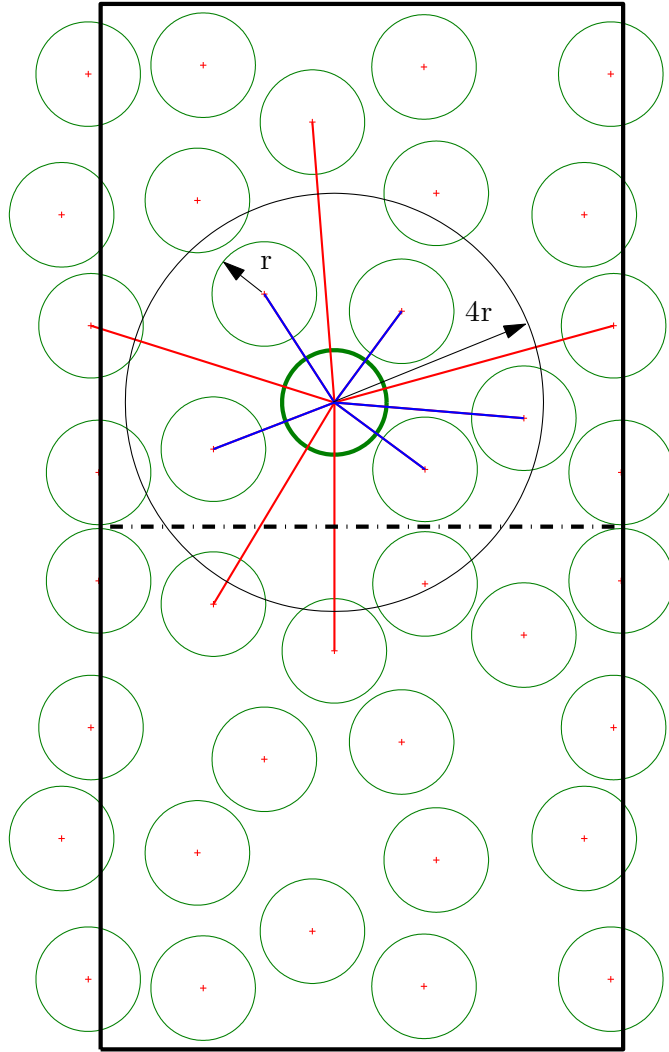
Figure 6.6: Illustration showing the calculation of C_v based on cut-off radius r_c for a RVE (see section 6.2.1 for details).

In order to ensure proper modeling of the fiber-matrix interfaces we do not allow a fiber touching another. The topological periodicity of the fiber arrangement is ensured at the left and right edges of the RVE and is also specified in terms of the coupling between the kinematic boundary conditions (b.c.'s) at these edges as discussed in the next section.

6.2.2 Finite Element Model

An important aspect of this work is to model the transient moisture diffusion, which is assumed to obey Fick's law. The Fick's law is analogous to the Fourier's heat conduction law [240], which is available in ABAQUS/ STANDARD$^{\textregistered}$ FE program [141] as a coupled temperature-displacement analysis procedure. We exploit this analogy to model the transient, coupled moisture-displacement problem. The moisture diffusivity (D_m) is specified in terms of the equivalent thermal diffusivity (D_t) in ABAQUS/ CAE$^{\textregistered}$ [2]. The temperature evolution in the RVE then resembles the moisture diffusion. Likewise, the moisture B.C. is specified in terms of an equivalent temperature. Note that the thermal-moisture direct analogy [253] adopted here is valid only as long as only one of the phases is capable of moisture diffusion[3], which is true in the present work. The micro-architectures generated by the code are imported into ABAQUS and meshed using the plane strain, linear quadrilateral finite elements with displacement and moisture degrees of freedom (CPE4T). In our calculations, a typical RVE comprises of ≈ 30000 finite elements after conducting mesh convergence with different mesh densities for a few cases. The periodic kinematic b.c.'s applied to the left

---

[2]In ABAQUS$^{\textregistered}$, $D_t = k/(\rho c_p)$, where k is the thermal conductivity, ρ the mass density and c_p the specific heat. However, it is the ratio that is important rather than the values of the individual parameters.

[3]Alternatively, one may adopt a normalized analogy [253], which can be used under a generalized case of a bi-material system where both the phases are pervious.

and right edges may be expressed in terms of the displacement vector $\overrightarrow{U_1}$ which relates the displacement between the opposite edges of the RVE, $X_1 = 0$ and $X_1 = L_1$ [106],

$$\overrightarrow{u}\,(0, X_2) - \overrightarrow{u}\,(L_1, X_2) = \overrightarrow{U_1} \tag{6.1}$$

where u_1 is the displacement in the X_1-direction and L_1 sets the wavelength of the periodicity. The vector $\overrightarrow{U_1} = (u_1, 0)$ is computed from the condition that the average stress perpendicular to the loading axis should be zero, therefore

$$\int_0^{L_2} \overrightarrow{t}\, dX_2 = 0 \qquad on\ X_1 = 0\ \ and\ \ X_1 = L_1 \tag{6.2}$$

where t is the traction vector. On the top and bottom edges both displacement and moisture b.c.'s may be present. The average strain due to an applied velocity v in the X_2 direction is

$$\dot{\overline{\varepsilon}}_{22} = \frac{v}{L_2} \tag{6.3}$$

The corresponding average stress and strain is then (at time t) given by

$$\overline{\sigma}_{22} = \frac{1}{L_1}\int_0^{L_1} \sigma_{22}\,(X_1, L_2)\, dX_1 \quad \text{and} \quad \overline{\varepsilon}_{22} = \int_0^t \dot{\overline{\varepsilon}}_{22}\, dt \tag{6.4}$$

196

6.2.3 Constitutive Laws

In the present case, a linear, hygro-elastic constitutive law[4] is adopted for the matrix phase

$$\sigma = \mathbf{E} : [\varepsilon - \beta \left(c - c_0\right)\mathbf{I}] \tag{6.5}$$

where σ is the stress tensor, $\mathbf{E}$ is the fourth-order elasticity tensor, ε is the total strain tensor. β is the isotropic coefficient of moisture expansion defined for the percentage by weight of the moisture absorbed by the matrix is given by $c = \int_0^t \dot{c}(t')dt'$ is the moisture concentration at time t, c_0 is the reference moisture concentration and $\mathbf{I}$ is the identity tensor. The moisture evolution follows Fick's law

$$\dot{c} = D_m \nabla^2 c \tag{6.6}$$

where D_m is the matrix moisture diffusivity and ∇^2 is the Laplacian. Like the matrix, the fibers are also assumed to be linearly elastic and isotropic, but impermeable. Table 6.1 lists the material properties that are representative of an epoxy resin and E-glass fiber [230, 241], where the elastic properties of the epoxy correspond to the glassy regime. While it has been observed that moisture may degrade the elastic properties of some epoxies [200, 204, 254], the effect is much more severe and irreversible in the transition and rubbery regimes (attributed to chain scission processes) than in the glassy regime where it can at times be largely reversible [255, 256]. While recent atomistic simulations attempt to address the deterioration of the glassy elastic modulus the underlying mechanisms

---

[4]The operation $\mathbf{A}{:}\mathbf{B}$ denotes a contracted product between two tensors or between a tensor and a vector.

Table 6.1: Material properties for the fibers and matrix used in simulations.

	Elastic modulus, E (GPa)	Poisson's ratio, v	Diffusion coefficient, D (mm^{2}s^{-1})	Moisture expansion coefficient, β(mm/mm %H$_2$O)
Fiber	75	0.28	0	0
Matrix	4	0.38	$54{\times}10^{-8}$	$3.24{\times}10^{-4}$

are not fully unraveled [254, 257]. In this work, we do not consider the elastic degradation of polymer. Further, we also ignore plasticization (i.e., lowering of glass transition temperature) given that the simulation time-scales are much shorter than the typical viscoelastic time-scales for epoxies.

6.2.4 Interface Cohesive Behavior

Fiber-matrix interfaces are considered as a cohesive surface and its constitutive description is provided by a traction-separation law [141]. A linear, elastic traction-separation law $\left\{ \vec{t} \right\} = [\mathbf{K}] \left\{ \vec{\delta} \right\}$ is adopted, where $\left\{ \vec{t} \right\}$ is the nominal interface traction vector with component t_n in the normal direction and t_s in the shear direction, $\left\{ \vec{\delta} \right\}$ is the vector of displacement jumps across the interface having components δ_n and δ_s and $[\mathbf{K}]$ is the interfacial stiffness matrix. The interface softening initiates when the magnitude of the nominal stress in the normal (n) or tangential (s) directions reach their critical values, N or S , respectively (Fig. 6.7) given by

$$\max \left\{ \frac{\langle t_n \rangle}{N}, \frac{t_s}{S} \right\} = 1 \qquad (6.7)$$

The subsequent softening behavior at an interface node is governed by the damage variable

$$\phi_{int} = \frac{\overline{\delta}^f \left(\overline{\delta}^{max} - \overline{\delta}^0\right)}{\overline{\delta}^{max} \left(\overline{\delta}^f - \overline{\delta}^0\right)} \tag{6.8}$$

where $\overline{\delta} = \sqrt{<\delta_n>^2 + \delta_s^2}$. The value of $\overline{\delta}$ when the failure begins is given by $\overline{\delta}^0$ and the interface fails completely when reaches $\overline{\delta}$ reaches the value $\overline{\delta}^f$. $\overline{\delta}^{max}$ is the maximum value of $\overline{\delta}$ at any given instant of time. Note that at a given interface node, $0 \leq \phi_{int} \leq 1$ where the lower limit denotes that the interface is intact at that node and the upper limit denotes complete separation at that node. We assume that both the normal and tangential displacement jumps contribute to the failure which is modeled via a mixed mode based failure criterion

$$\frac{G_n}{G_n^c} + \frac{G_t}{G_t^c} = 1 \tag{6.9}$$

where G_n^c and G_t^c are the mode-I and mode-II energy release rates. Debonding initiates when Eq. 6.9 is satisfied at a point on an interface. As both fracture modes contribute towards failure (Eq. 6.7), an interface may fail before the failure energy reaches the critical value in any of the directions.

As noted earlier, some experiments indicate that the interface strength and toughness may be affected by moisture [195, 239]. We account for this possibility by allowing the normal and shear tractions to degrade with moisture (Fig. 6.7). Note that in both the *moisture-resistant* (i.e., interface strength unaffected by moisture) and *moisture-affected* scenarios the interfaces may still debond, but the later will be much softer than the former. Irrespective of the nature of the interfaces we assume the final failure to occur at the same displacement $\overline{\delta}^f$; consequently, the fracture energy (i.e., the area under the traction-separation curve) is also smaller for a moisture-affected interface. For calculation purposes, we

assume that the critical fracture energies linearly degrade to half their original values as the local moisture concentration reaches the ambient value.
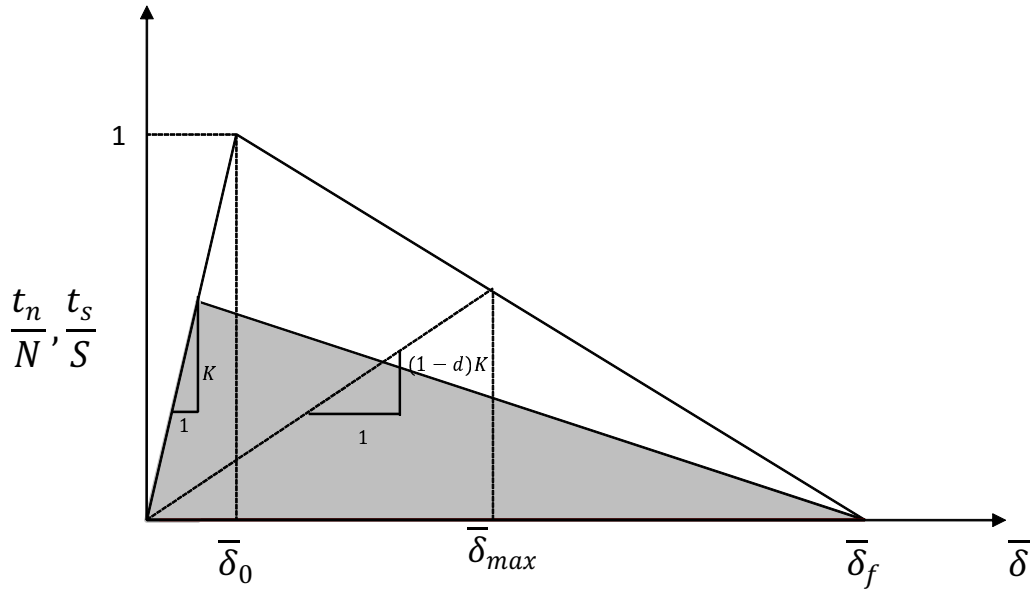
Figure 6.7: The traction-separation law used for modeling fiber-matrix interface. The shaded triangle shows the degraded traction-separation rule when the moisture concentration at an interface reaches a critical value.

6.3 Damage Response of Epoxy-Glass Composites

In this section, we consider different scenarios that involve moisture and mechanical b.c.'s. In Sections 6.3.1 and 6.3.2 we discuss all the results pertaining to the six RVEs shown in Fig. 6.5 that constitute a fixed fiber diameter $d = 10 \ \mu m$ and nearly the same $v_f \approx 0.47 - 0.5$. Section 6.3.3 expands the discussion to a range of v_f and d .

In Section 6.3.1, we consider the RVEs subjected only to the moisture b.c. In this case, we investigate the evolution of damage due to debonding as a function

of the fiber arrangements for moisture-resistant and moisture-affected interface strengths. We choose the moisture b.c. that represents the typical weight gain at saturation in reinforced polymers exposed to moisture. For example, the saturation weight gain in glass reinforced epoxy composites at 85% relative humidity and 85^0C is approximately 1.5% of the initial weight. These values mimic the accelerated conditions that are typically resorted to in laboratory-scale experiments [240] and we apply this moisture b.c. ($c_\infty = 1.5\%$). Later, in Section 6.3.2, we consider the cases where the moisture and mechanical b.c.'s are applied sequentially.

6.3.1 Moisture induced debonding

RVEs in Fig. 6.5 are subjected to the moisture b.c. on the top edge. As the moisture diffuses through the matrix, differential expansion between the matrix and fibers induce interfacial stresses that may nucleate debonding and lead to progressive damage evolution. We quantify the overall damage sustained by an RVE at time t by an aggregate damage parameter $\psi(t) = \frac{1}{n}\sum_{i=1}^{n}\phi_{int_i}(t)$, $(0 < \psi < 1)$, where ϕ_{int_i} is given in Eq. 6.8 and n is the total number of nodes at all the interfaces in a RVE. Here, the physical time considered is long enough for the moisture to equilibrate throughout in the RVEs.

Damage Evolution: Moisture-resistant Interfaces

To begin with, we consider moisture-resistant interfaces so that the interfacial strengths $N = S = 25$ MPa and fracture energies ($G_n^c = G_t^c = 50$ Jm^{-2}) are unaltered even in the presence of moisture [230, 258]. Figure 6.8 a and b show the temporal evolution of ψ in the six RVEs and its dependence on the their

topological descriptor, C_v , respectively. For fixed v_f the damage evolution is significantly different depending upon the micro-architecture and for the applied b.c. the RC-RVE (largest C_v) sustains the maximum overall damage while the SR arrangement (lowest C_v) experiences no damage at all. Note that for different $v_f's$ and fiber size d , it is possible that even an SR-RVE may exhibit damage; however, it is almost always the case that an SR-RVE sustains the least overall damage. This emphasizes the strong influence of the fiber arrangement on the damage evolution under moisture ingress. For the specific cases considered in this section, the SR-RVE is the least clustered arrangement (as expected) and sustains least (no) damage, whereas the RC-RVE is the most clustered (highest C_v) and sustains most damage. Indeed, for the six RVEs shown here, the $C_v - \psi$ follows a simple linear relation (Fig. 6.8 b). As will be shown in section 6.3.3, for different $v_f's$ and $d's$, the clustering effect quantified by C_v correlates linearly with the overall damage ψ sustained due to moisture ingress by the RVEs.

(a)   (b)
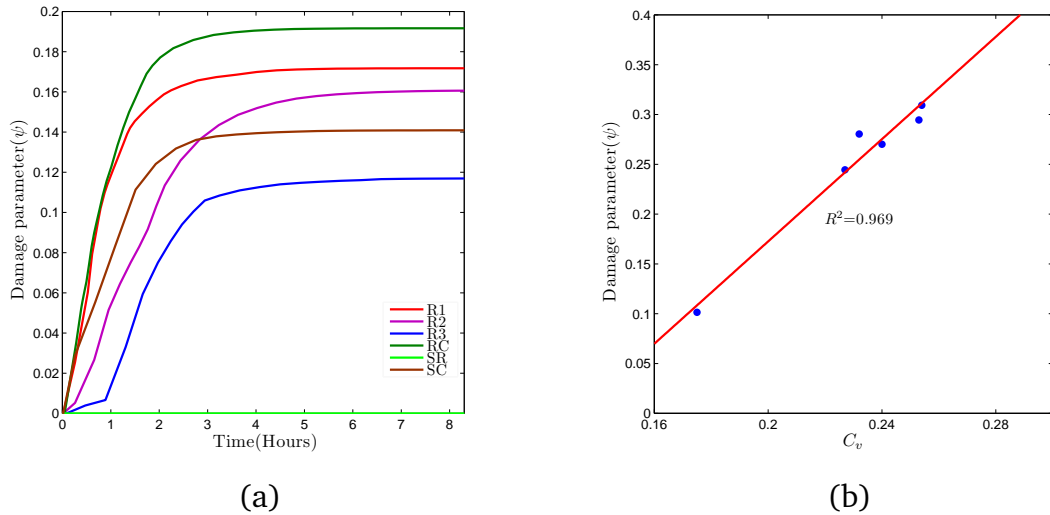
Figure 6.8: Evolution of the overall interface damage ψ (a), and $\psi - C_v$ correlation between damage for $v_f = 0.50$ and $d = 10 \ \mu$m with for $r_c = 4r$ (b) when the interface is moisture-resistant.

A common feature between all arrangements except the SR arrangement is that

there are matrix-rich pockets present due to some amount of fiber clustering. It is interesting to note the pattern of evolution of damage between the SC, R1 and RC arrangements. The overall damage evolution is nearly the same in three arrangements up to about 20 minutes after which the rate of growth in SC falls appreciably. However, the aggregate damage in RC and R1 RVEs continue to grow almost identically much further ($t \approx 60$ minutes). By this time the moisture has diffused through almost half the thickness of the RVEs. If we consider the top half of all the RVEs, R1 and RC arrangements have more matrix-rich regions compared to the other RVEs, which results in the similar response of R1 and RC arrangements.

(a) SR   (b) R3   (c) RC
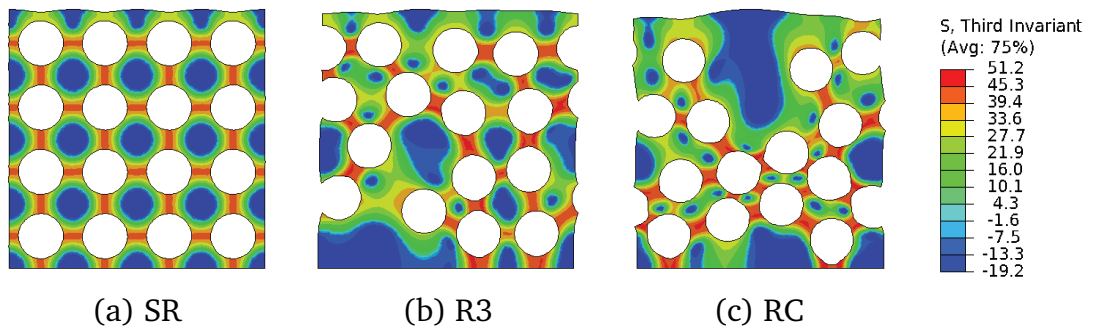
Figure 6.9: Distribution of third invariant of the deviatoric stress tensor in (a) SR, (b) R3 and (c) RC arrangements corresponding to the time at which the RVE attains equilibrium concentration in the entire domain (moisture-resistant interfaces). Deformed profiles are scaled fifty times and fibers are removed for clarity.

Figure 6.9 compares the distribution of the third invariant $J_3 = \frac{9}{2}[S \bigotimes S]^{\frac{1}{3}}$ of the deviatoric stress tensor S, for SR, R3 and RC arrangements when the steady-state condition is reached ($\dot{C} = 0$). The J_3 invariant combines the influence of all stress components, but also distinguishes between the tensile and compression regions (unlike the von-Mises invariant) and therefore, provides an indication of the hot-spots that are susceptible to interfacial damage. The SR-RVE deforms uniformly except at the top edge, which deforms freely to satisfy the traction b.c.

In comparison, the R3 and RC arrangements experience a non-uniform distribution of highly stressed regions that also sustain severe deformation than the other parts within the RVE resulting in heavy debonding. The debonding in the RC arrangement is much more severe than the other two arrangements. Further, we observe that in the RC arrangement debonding is nearly aligned with the X_1 - direction unlike the SR and R3 that tend to debond along the X_2 - direction.

6.3.2 Damage Evolution: Moisture-affected Interfaces

To investigate the effect of degrading interfaces on the damage evolution we allow the cohesive strength to weaken with the local moisture concentration keeping all other parameters the same as in the previous case. A key question we ask is: what is the influence of degrading interfaces on the damage evolution with reference to the trends observed in the preceding sub-section? To answer this question the initial values (at $c = 0$) of interfacial strengths ($N = S = 25$ MPa) and energies ($G_c = 50$ Jm^{-2}) are now assumed to linearly degrade to 50% (shaded area in Fig. 6.7) as the local moisture concentration reaches the its maximum value [239]. Figure 6.10 shows the evolution of ψ for the six RVEs under the applied moisture b.c. of $c_\infty = 1.5\%$ at the top edge. As expected the overall damage in each of the RVEs is more severe than their preceding moisture-resistant counterparts, because the interfaces become progressively weaker with the evolution of the local moisture concentration. The severity of damage is emphasized from the fact the SR arrangement, which showed no damage in the preceding case too exhibits some damage, although it is still the lowest amongst all the six RVEs. These observations suggest that it is important to rigorously characterize the effect of moisture on the interface behavior and is vital to predicting the overall composite response. The overall trends of damage evolution for other RVEs are

qualitatively similar to those in Fig. 6.8.a although there are a few differences especially at later stages. The damage evolution in the R2 and R3 arrangements is initially slow in comparison to the SC arrangement, but evolves faster beyond $t \approx 1.6$ hours.
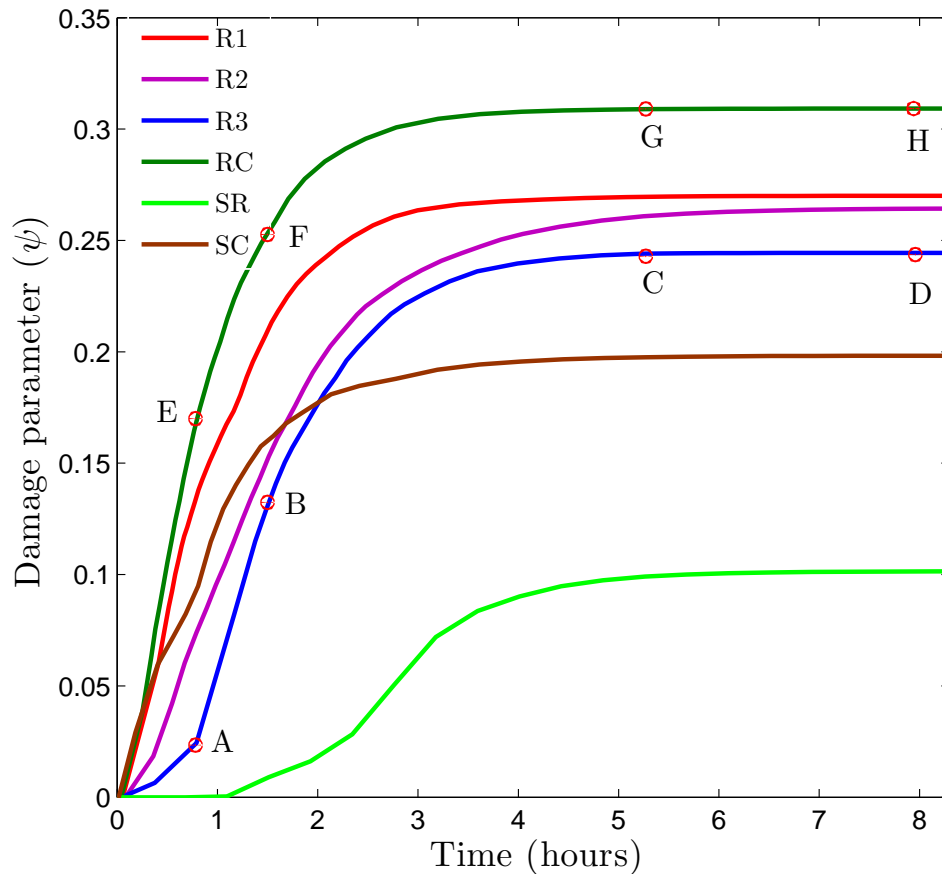
Figure 6.10: Diffusion-induced evolution of interface damage ψ for moisture-affected interfaces. The open circles indicate the location of the snapshots shown in Fig. 6.11.

In determining the influence of a microstructure on the diffusion-induced damage one has to consider two microstructural aspects: (a) the degree of fiber clustering, and (b) tortuosity [259]. In the present context, while the former is described here by C_v, the later may be described by the time it takes for moisture

205

to fully equilibrate in an RVE. The longer the time taken the more tortuous a microstructure is and smaller is its apparent diffusivity. As an example, we compare the tortuosities vis-á-vis the overall damage sustained in the SR (lowest C_v, lowest damage), R3 (least overall damage amongst all random arrangements with $v_f = 0.47, d = 10 \ \mu m$) and RC (most severe overall damage) RVEs. Figure 6.11 shows the snapshots of the moisture concentration contour for the RC and R3 arrangements at different times. In the present context of diffusion-induced damage, we define a normalized tortuosity, $\zeta = t_c/t_m$, where t_c is the time required for moisture saturation in an RVE with a given v_f and characteristic dimension (in the diffusion direction) L_2, and t_m is the corresponding time required for moisture saturation in bare matrix with the same characteristic dimension .
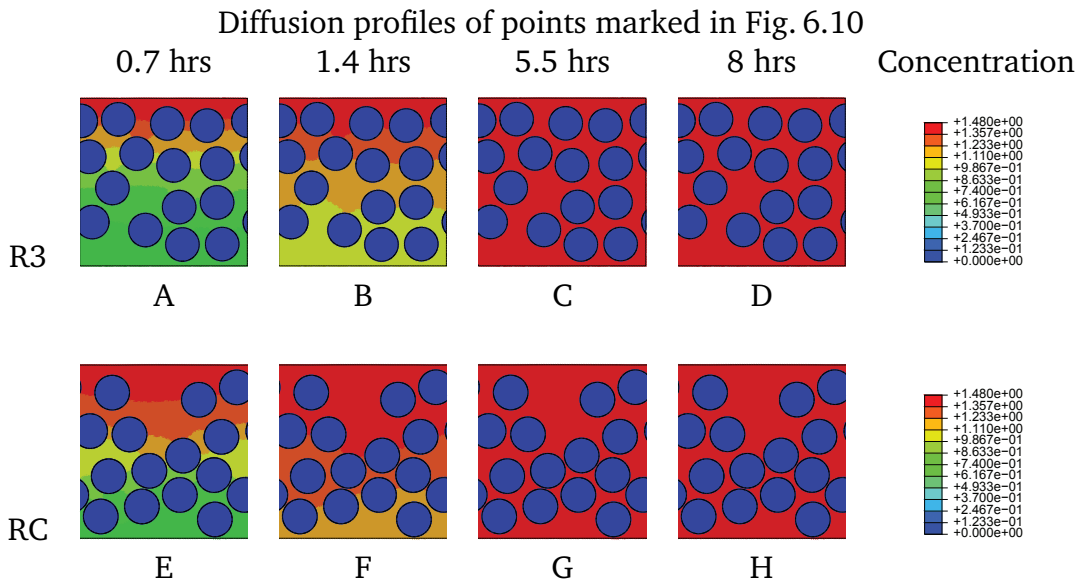
Figure 6.11: Snapshots of moisture diffusion profiles for the R3 and RC arrangements at $t = 0.7, 1.4, 5.5$ and 8 hours. Note the higher rate of diffusion in the RC-RVE.

As per this definition, although the SR-RVE is less clustered (C_v of ≈ 0.17) than the RC-RVE (C_v of ≈ 0.25), they exhibit similar tortuosities (ζ of SR ≈ 9.1 ζ of RC ≈ 9.0). However, the RC-RVE experiences significantly higher damage (ψ

of RC ≈ 0.31) than the SR-RVE (ψ of SR ≈ 0.1) (Fig. 6.10). Between the two random arrangements, the R3-RVE is less clustered (C_v of R3 ≈ 0.227), more tortuous (ζ of R3 ≈ 11), but sustains lesser damage (ψ of R3 ≈ 0.24) than the RC-RVE. That is, unlike C_v, ψ does not show a consistent correlation with damage. In other words, this suggests the C_v and ψ do not necessarily correlate in a simple (monotonic, linear) manner like the $\psi - C_v$ relation (section 6.3.3). This is because, while C_v compares different RVEs purely from the topological viewpoint, ζ involves a spatio-temporal description that depends on the resistance to moisture ingress along the direction of moisture ingress. This can be most easily illustrated by considering an RVE, say RC, and switching the plane of symmetry with the direction of moisture ingress. Although not shown here, in this scenario the C_v of the flipped RC-RVE is the same as its original version, but is more tortuous. In summary, clustering is a topological descriptor that can be used to describe the severity of damage vis-á-vis microstructural spatial heterogeneity, whereas tortuosity has to be determined with reference to the direction of diffusion and may not give a systematic correlation with damage, although it may have an influence on the damage.

Mechanical Loading of Initially Damaged Microstructures

While composite microstructures that have sustained initial damage such as that induced due to moisture ingress are expected to demonstrate a compromised response compared to their pristine counterparts when subsequently subjected to mechanical stimuli. A natural question that then arises is: how does this initial diffusion-induced damage incurred in the microstructures affect the performance when subjected to mechanical stimuli? Does microstructural disorder still dictate the further evolution of damage and affect its stiffness and the aggregate (stress-strain) response? If so, what degree does it affect? To answer these questions, we

207

examine the response of the initially damaged (due to moisture) microstructures in the presence of applied mechanical load. A displacement b.c. (resulting in the macroscopic final strain of $\bar{\varepsilon} = 3\%$) is applied on the top face of each of the six RVEs considered in the preceding section after the moisture has completely equilibrated and the diffusion-induced damaged has saturated. We simulate this as a two-step loading case in ABAQUS$^{\circledR}$, where in the first step the moisture b.c. is applied and when moisture fully saturates, the second step corresponding to the mechanical b.c. is invoked. Figure 6.12 shows the average stress ($\bar{\sigma}_{22}$) -strain ($\bar{\varepsilon}$) response of the six RVEs. For brevity, we show only the results for the moisture-affected interfaces as the results for the moisture-resistant interfaces are qualitatively similar. In Fig. 6.12 the initial stress-free strain corresponds to the first step that evolves due to the constrained moisture expansion of the RVEs. The stresses due to the constraint from the fibers are locked in the matrix and fibers as residual stresses, but do not manifest themselves in the stress-strain response as they self-equilibrate. However, these stresses play a vital role in determining the response of the RVEs in the subsequent mechanical loading step. As noted in the preceding section the interface debonding initiates due to moisture ingress. In the two-step loading, this initial diffusion-induced interfacial damage leads to an overall softer average stress-strain response in all the RVEs compared to the cases where the interfaces do not encounter moisture induced stresses. This is clearly reflected in Table 6.2 that shows the initial tangent moduli (calculated at small times in the second step). The moduli of the initially damaged RVEs (in both, the moisture-resistant and moisture-affected cases) are $\approx 10 - 30\%$ lower than their corresponding pristine interface counterparts. As the loading progresses the stress-strain response becomes nonlinear due to the rapid evolution of damage.

An interesting aspect comes to the fore when one observes the modulus degradation for the SR arrangement with moisture-resistant interfaces (Table 6.2). Note

Table 6.2: Initial tangent moduli during the mechanical loading step of the sequential loading case.

RVE	Perfect interface	Moisture-resistant		Moisture-affected	
	E	E	Δ E	E	Δ E
	(GPa)	(GPa)		(GPa)	
R1	11.5	9.6	17%	8.8	23%
R2	10.9	9.9	10%	8.9	19%
R3	11.7	8.8	25%	7.8	33%
RC	11.2	9.9	12%	9.1	19%
SR	13.6	10.9	20%	9.8	28%
SC	14.0	10.6	24%	9.6	32%

that in case of the moisture-only b.c. (with $c_\infty = 1.5\%$) this arrangement does not exhibit any damage (Fig. 6.9.a); however, post-equilibration it shows a substantial drop in the initial tangent modulus of nearly 20% upon application of a small mechanical load. This indicates that the debonding commences as soon as the SR composite is loaded mechanically. The reason for such a sudden decrease in the stiffness is explained as follows: During the moisture diffusion step the ligaments connecting a column of fibers experience tensile stress in the X_2 -direction. This also induces a tensile stress at the interfacial regions near the top and bottom (the poles) of each fiber (Fig. 6.9.a). In the subsequent step, when a mechanical load is applied in the same direction the normal stresses in the ligaments along the loading direction superpose with the initial residual stresses causing the interfaces to instantaneously debond as the total stress exceeds the critical value. As the SR-RVE comprises regular fiber arrangement the stress state is identical at all the poles (except those near the top edge due to boundary effects) causing simultaneous failure of all the interfaces near the poles. A similar characteristic is also observed in the R3 arrangement (Fig. 6.9.b), which has two columns of fibers that are nearly aligned.

It is interesting to note that although the RC arrangement sustains the maximum

overall damage at the end of the moisture step (Fig. 6.10 and Fig. 6.9.c) it is the R3, SC and SR arrangements that show the largest drops in their tangent moduli in both the moisture-resistant and moisture-affected scenarios (Table 6.2). This phenomenon is ascribed again to the location of the debonding with respect to the loading axis. For the SR, SC and R3 arrangements it is the interfacial regions near the fiber poles that debond as these architectures resemble columnar fiber arrangements. In contrast, in the RC arrangement that does not show the tendency of columnar fiber arrangement the debonding is profuse at the fiber equatorial regions (90^0 to the poles) while the poles of the fibers remain connected to the matrix. Naturally, when loaded along the direction of the poles (X_2 -direction) the RC arrangement is capable of carrying more stress by sharing it with the fibers than the SR, SC and R3, at least initially. The same argument holds true for the R1 and R2 arrangements too. At later stages though, debonding also evolves at the poles in the RC-RVE, but correspondingly the equators in the SR, SC and to some extent R3 don't, because at the equators the state of stress is predominantly compressive for the aligned fibers arrangements. Consequently, the RC topology (also, R1 and R2) suffers from a more severe overall softening elastic behavior compared to the SR, SC and R3 topologies (Fig. 6.13).
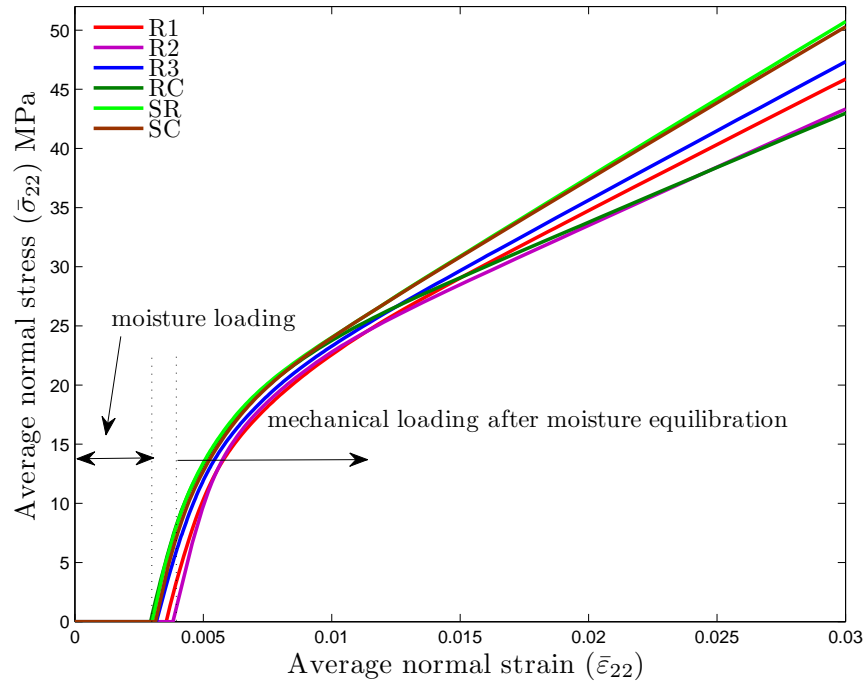
Figure 6.12: Average normal stress $\bar{\sigma}_{22}$ - normal strain $\bar{\varepsilon}_{22}$ of the RVEs subjected to mechanical loading after moisture has equilibrated (moisture-affected interfaces). Moisture-resistant interfaces show a similar, but stronger response.

From these observations, we summarize that the overall stress-strain behaviors of the initially damaged microstructures exhibit similar qualitative trends irrespective of the RVE randomness. The lesser the initial damage in an RVE the better is its load carrying capacity. In addition, if the fiber arrangements are favorably aligned with the loading direction the damage accrues much more rapidly even if the initial (moisture-induced) damage is small (e.g., the SR-RVE). Taking this observation further, we posit that for the loading conditions simulating biaxial (tensile) stress states (as in the moisture diffusion scenario) it is the degree of clustering that decides the severity of damage; on the other hand, for uniaxial (or, significantly directionally biased) loading cases (e.g., the applied mechanical load scenario in this work) it is the alignment with reference to the primary

211

loading direction that matters.

6.3.3 Effect of Volume Fraction and Fiber Diameter

We now generalize the damage characterization for RVEs with different v_f and diameter d . For consistent comparison, we restrict our attention to the damage sustained by different RVEs with moisture-affected interfaces at the end of the moisture loading step. As mentioned in Section 6.2.1, we calculate the coefficient of variation C_v for each RVE with three different r_c .
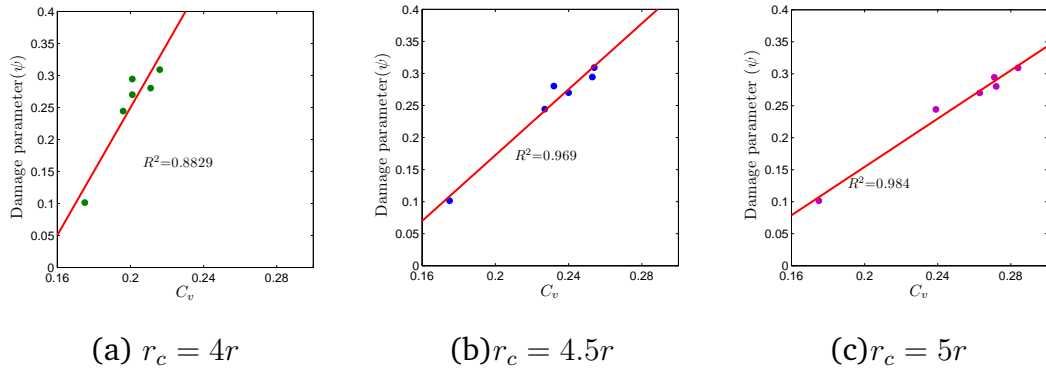
(a) $r_c = 4r$ (b)$r_c = 4.5r$ (c)$r_c = 5r$

Figure 6.13: $\psi - C_v$ correlation for $v_f = 0.50$ with (a) $r_c = 4r$, (b) $r_c = 4.5r$, and (c) $r_c = 5r$ for moisture-affected interface.

As an illustration of the procedure used to correlate damage with C_v , Fig. 6.13 a-c shows the correlation between ψ and C_v computed using different r_c (section 6.2.1), for a fixed $v_f = 0.50$ and $d = 10 \ \mu$m. The plots also indicate a linear fit along with the R^2 values. It can be seen that for these cases, the correlation is quite high. The same approach is adopted for a range of v_f ($v_f = 0.30, 0.40$ and 0.60) in addition to $v_f = 0.50$. For each v_f we considered an SR-RVE and five random arrangements. To incorporate the influence of d, we considered RVEs with $d = 9, 10$ and $11 \ \mu$m in these simulations. For each RVE, ψ due to moisture diffusion was obtained from the FE simulations. Each ψ was then plotted separately

212

against the C_v of their corresponding RVEs based on the r_c defined earlier and a linear regression was performed for each case (similar to Fig. 6.3.1b). Figure6.13 consolidates all these data where the R^2 values emerging from the linear regression analysis are plotted against v_f. It can be observed that high correlations between ψ and C_v are obtained for different r_c values across a range of v_f. While $r_c = 4.5r$ and $r_c = 5r$ provided good correlations across all v_f, the only reason for a relatively weaker correlation in the case of $r_c = 4r$ and $v_f = 0.40$ (Fig. 6.14) is due to one outlier in the random arrangement that had a C_v smaller than the SR-RVE (for $r_c = 4r$), but exhibited damage that was more severe than the SR-RVE for the same v_f.
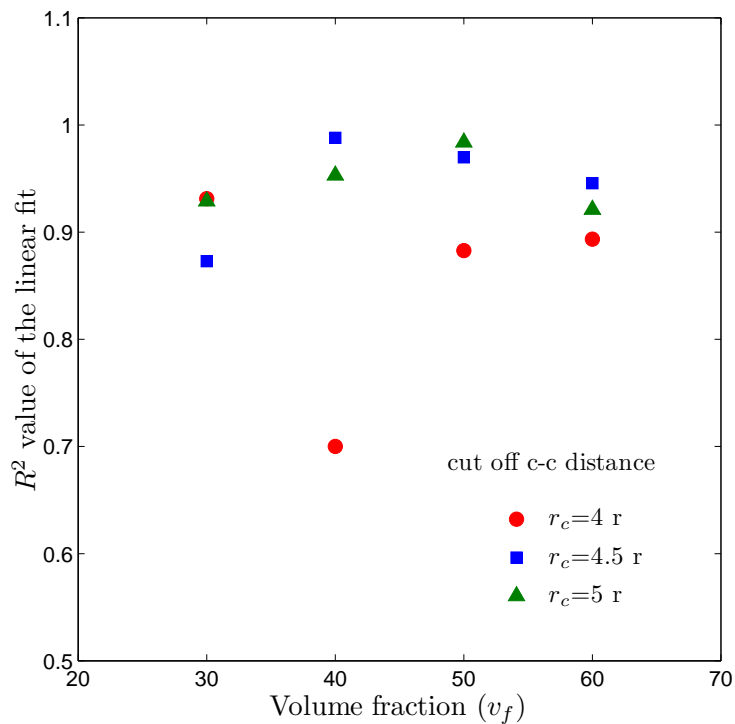
Figure 6.14: Comparison of $C_v - \psi$ correlation for different fiber v_f determined from the linear regression (R^2) for different cut-off radii (moisture-affected interfaces).

213

6.4 Summary

In this chapter, we modeled the transient damage response of reinforced poly-
mers subjected to the stresses induced due to moisture diffusion and mechanical
loading. The study reveals that fiber distribution plays a significant role in the
diffusion induced residual stresses in a composite. This in turn determines the
hotspots for debonding, which may adversely affect the initial stiffness (e.g., in
columnar fiber arrangement) or the overall stress (clustered arrangement). A
trend that emerges from the results presented here is that the fiber clustering
tends to hurt the performance of a composite over a period of time compared
to the more regularly spaced arrangements [240]. The topological descriptor C_v
characterizing the spatial inhomogeneity of fiber distribution is identified using
the concept of cut-off radius that is motivated based on the mechanistic and ge-
ometric basis. The C_v correlates linearly with the overall diffusion-induced dam-
age sustained for different RVEs over a range of fiber v_f and diameters; however,
it does not enjoy a simple relationship with the tortuosity of RVE owing to the
highly directional nature of the later. An investigation of the synergistic effects
of the moisture and mechanical loads indicates that moisture ingress assists the
runaway microstructural failure that is dominated by the mechanical loading in
the later stages. It is important to characterize the strength and toughness of in-
terfaces in the presence of moisture as moisture-affected interfaces may not only
cause significant degradation, but also accelerate the permeability through the
channels that may form near the fibers. The degradation of the transverse stiff-
ness of an RVE induced by initial moisture ingress also does not show a simple
relation with C_v , again due to the directionality-induced complex interaction-
s between the interfaces and the dominant loading direction. While this study
uses the glass-fiber reinforced epoxy composite as a model system, some of the

observations may be applicable in a variety of composites such as those used in dental restoration purposes or in pharmaceuticals. Our future work will focus on incorporating the mechanistic representation of the polymer degradation due to diffusion in to its continuum constitutive description, viscoelastic relaxation mechanisms and investigating their impact on the composite microstructural response.

Chapter 7

Summary and Future Directions

The work compiled in this dissertation is a basis for the discrete modeling approaches for random microtructures. It can be further extended to model a variety of materials having similar microstructure. Necessary software tools for the random microstructure generation, a stochastic simulation methodology for random fibrous networks and a micromechanical model for the interface damage in FRCs are developed. A summary of the key contributions of the thesis and an outlook for the further extension of the current work is discussed in this chapter.

7.1 Summary

Understanding various deformation mechanisms of materials requires modeling at the smallest possible length scale. Molecular models are computationally expensive and time scales achieved are physically unrealistic. Meso-scale modeling is one of the approaches that addresses some of these issues at a reasonable computational cost. In this work, two such models are developed. First, a discrete network (DN) model is developed for random fibrous networks and the response

216

of a model system is studied in details. Next, fiber reinforced composite (FRC) having a random microstructure is chosen and a discrete micromechanical model is developed. We begin with the generation of random microstructures, implemented the discrete models in a finite element(FE) framework and then checked correlation between the topological parameters and the response.

Discrete microstructures (DM) are numerically recreated and characterized using computational algorithms. A MATLAB$^{\circledR}$ based toolkit, **NetGen** is developed for the topology generation and characterization of random fiber networks. **NetGen** is a generic FE preprocessing software for random filamentous network that generates network with required topological parameters and characterize the networks using statistical descriptors. The output of **NetGen** is an input file that can be seamlessly read by commercial FE software ABAQUS$^{\circledR}$. Statistical parameters which account for the density and orientation of the filaments in a network are identified. For instance, a parameter *fabric factor* can be used to characterize networks with uniform/preferred filament orientation. Algorithms are developed in C++ for the generation and characterization of periodic microstructure of fiber reinforced composites. These microstructures are characterized using *center-to-center distance* of fibers.

The mechanical response and damage characteristics are examined by implementing models in commercial FE package ABAQUS$^{\circledR}$ using its subroutine capabilities. The DN model for filamentous networks explicitly model random topologies. F-actin networks crosslinked with actin binding protein filamin is used as a model system to study the mechanical response of filamentous networks. The study is further extended to examine the network response over three decades of filament stiffnesses. Contour plots generated from these simulations are precursors to a general predictive response model for filamentous networks. The nexus between the filament/crosslink stiffness and the damage is examined for

217

the entire range of stiffness considered. Fibrous biopolymeric networks exhibit rate-dependent stiffening, identification of peak stiffness and softening followed by failure. This failure is attributed to the failure of crosslinking proteins which is often a stochastic process. The stochastic crosslink scission is incorporated into the DN model using Kinetic Monte Carlo algorithm. The micromechanical model for the interface damage in FRCs handles both mechanical and environmental stimuli. An epoxy-glass composite is taken as a model system to investigate the microstructural role in transient degradation of such architectures induced by the moisture-induced interface debonding. The interplay of the randomness in fiber arrangement and the overall damage is elucidated through its correlation with the coefficient of variation of the center-to-center distance of fibers that characterizes fiber clustering.

7.2 Future Directions

7.2.1 Discrete Network Modeling

The discrete network model for soft fibrous networks is a 2-Dimensional (2D) model with few simplifying assumptions such as, straight filaments, no fluid media, no relinking of crosslinks etc. As an immediate expansion of the current work is to relax some of these assumptions. It has been shown by Van der Giessen and co-workers [78, 79] that the 3-Dimensional (3D) models are less confined compared to 2D and may result in more non-affine deformations and compliant responses. However these simulations were with rigid crosslinks and the effect on crosslink scission on damage is not known. In order to have a better understanding of the damage response in actual networks, a 3D modeling approach with stochastic crosslink scission has to be developed. The major steps towards

3D modeling are

- Developing the 3D version of the networks generation software.

- Performing 3D network simulations over a range of constituent properties.

- Highlighting key differences between the local and global response characteristics among 2D and 3D, while providing an average measures for the same.

Some of these networks may be influenced by the ambience they reside in. For example, F-actin networks are usually surrounded by a fluid medium that represents highly damped system. This and many existing works ignore such advanced complicating features. However for the realistic representation, one must account for them. In our networks, the first order effect of accounting fluid would be the additional stress generated due to the viscosity.

Another simplifying assumption in this work is the permanent failure of crosslinks. In reality, rebinding is possible and may be an important process for network stability. Crosslink relinking mechanism is very important especially when the formation of stress fibers, filapodia etc. are to be modeled. Sunil Kumar and co-workers [171] have modeled semi-flexible filaments with crosslink reformation. For the *in vivo* cells, the relinking may depend on several factors such as the proximity to the filaments, chemical and mechanical signals etc. One of the ways it could be implemented in the current model is by specifying a geometric threshold for filament proximity and combining it into a contact algorithm via a kinetic expression based on relevant parameters (mechanical, chemical, physical etc.). The competition between dissociation and relinking may provide interesting load transfer pathways.

The current work is well suited for studying the damage in polymers and can be extended for the multi-scale modeling of polymers. Such a model can deliver highly enriched and accurate approximation of the mechanisms taking place during the deformation and damage of polymers. The information obtained from these models can be further used to develop simplified continuum models. A schematic representation of one such approach is explained below.
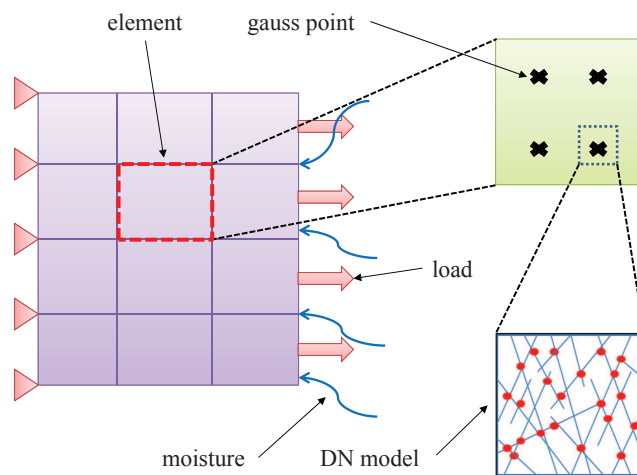
Figure 7.1: A schematic representation of multi-scale modeling approach for polymers.

For a finer representation of the physics at a better spatial resolution, multi-scale finite element modeling approach has to be used. In this approach, the material can be resolved into DN models at each gauss point and the property definition for the material comes from the discrete network which is a representative of that point (Fig.7.1). As the damage of the discrete material takes place due to the crosslink scission, it leads to the degradation of the material at the larger length scales. The advantage of this approach is that the material parameters like elastic modulus, poisson's ratio and even the damage parameters are derived from the

DN models rather than using any assumptions. This approach can be used for both biopolymer as well as synthetic polymers. These multi-scale calculations are computationally intensive compared to the conventional FE methods. However, once the right physics is modeled and parameters are extracted out, governing laws can be derived out of these discrete calculations which can be generalized to develop enriched continuum models.

In the current work, the discrete network model is a non-affine model while the continuum model has incorporated the non-affine behavior in a phenomenological manner without much physical underpinnings. This model has to be enriched by incorporating the non-affine behavior which brings in the effect of filament bending stiffness and the filament density. It is observed in experiments that the initial network stiffness increases with increase in the bending length l_b and decrease in l_c which is a consequence of the increase in $\bar{\rho}$ [77]. It is known that at these sub-micron length scales, non-bonding interactions become dominant. They play an increasingly important role as the length scale becomes small. These effects have to be incorporated and the model can be further enriched by incorporating couple stress theory, non-local theories etc.

In the continuum model, we used a damage sensitivity parameter ζ to capture the network collapse at a low critical damage that is attributed to the loss of percolation. This is a simplistic assumption and we used this parameter with the qualitative understanding of the physics of the problem. We have to develop rigorous mathematical models to find out the actual value of this parameter accounting for the underlying physics of the loss of percolation, formation of stress fiber etc.

7.2.2 Micromechanics Modeling

In the micromechanical model for FRCs, we accounted for the degradation of interface with moisture and debonding under the applied load. It is known that epoxies degrade with moisture and leads to significant reduction in strength. And so is the case with glass fibers. A comprehensive model should account for all these types of damages.

Most of the polymers, at least in long time scales acts as a viscoelastic material. In the current work, epoxy is assumed to be a linearly elastic material. There are three time scales involved in the problem studied; (a) relaxation time scales of the polymer, (b) moisture diffusion time scales and (c) the loading rate. A careful treatment of all the three time scales has to be done for incorporating the right physics.

Based on the work of Xiao and Shanahan [202, 211–214], we have partially developed a probabilistic model for the degradation of the epoxies with moisture. The model has been tested for the polymer alone cases (Appendix B). It has to be implemented along with the interface degradation for a more accurate modeling of moisture induced degradation of FRCs. Further to it, the debonded interfaces could acts as channels for diffusion and current model does not account for these secondary effects. These may have a significant contribution to the overall damage especially when the structure is exposed to the environment.

Another important consideration is the influence of temperature in the overall response. It is well known that the strength of polymers is a function of temperature and it may also affect the transport properties of moisture. In the current work, we used a temperature analogy to model the transport of moisture and hence the model could handle only isothermal loading conditions. Further

to it, we assumed that the glass fibers are impermeable. A normalized analogy [253] can better handle the transport of moisture for a bi-materials system and accounts for the temperature effects. In a nutshell, the future model should include the following details:

- Viscoelasticity for the polymer constitutive response.

- Damage of the polymeric matrix.

- Normalized analogy for moisture transport.

- Channeling effects after the initiation of interface debonding.

Bibliography

[1] S. Hyun and S. Torquato, "Designing composite microstructures with targeted properties," *Journal of Materials Research*, vol. 16, no. 1, pp. 280–285, 2001.

[2] S. Zhou and Q. Li, "A microstructure diagram for known bounds in conductivity," *Journal of Materials Research*, vol. 23, no. 03, pp. 798–811, 2008.

[3] H. Espinosa, A. Juster, F. Latourte, O. Loh, D. Gregoire, and P. Zavattieri, "Tablet-level origin of toughening in abalone shells and translation to synthetic composite materials," *Nature communications*, vol. 2, p. 173, 2011.

[4] M. Rousseau, E. Lopez, P. Stempflé, M. Brendlé, L. Franke, A. Guette, R. Naslain, and X. Bourrat, "Multiscale structure of sheet nacre," *Biomaterials*, vol. 26, no. 31, pp. 6254–6262, 2005.

[5] B. Bhushan, "Biomimetics: lessons from nature–an overview," *Philosophical Transactions of the Royal Society A: Mathematical, Physical and Engineering Sciences*, vol. 367, no. 1893, pp. 1445–1486, 2009.

[6] M. Meyers, P. Chen, A. Lin, and Y. Seki, "Biological materials: structure and mechanical properties," *Progress in Materials Science*, vol. 53, no. 1, pp. 1–206, 2008.

[7] P. Fratzl and R. Weinkamer, "Natures hierarchical materials," *Progress in Materials Science*, vol. 52, no. 8, pp. 1263 – 1334, 2007. [Online]. Available: http://www.sciencedirect.com/science/article/pii/S007964250700045X

[8] R. Lakes, "Materials with structural hierarchy," *Nature*, vol. 361, no. 6412, pp. 511–515, 1993.

[9] A. Jackson, J. Vincent, and R. Turner, "The mechanical design of nacre," *Proceedings of the Royal society of London. Series B. Biological sciences*, vol. 234, no. 1277, pp. 415–440, 1988.

[10] H. Fabritius, C. Sachs, D. Raabe, S. Nikolov, M. Frik, and J. Neugebauer, "Chitin in the exoskeletons of arthropoda: From ancient design to novel materials science," in *Chitin*, ser. Topics in Geobiology, N. S. Gupta, Ed. Springer Netherlands, 2011, vol. 34, pp. 35–60.

[11] H. Gao, B. Ji, I. Jäger, E. Arzt, and P. Fratzl, "Materials become insensitive to flaws at nanoscale: lessons from nature," *Proceedings of the National Academy of Sciences of the United States of America*, vol. 100, no. 10, p. 5597, 2003.

[12] P. LeDuc and D. Robinson, "Using lessons from cellular and molecular structures for future materials," *Advanced Materials*, vol. 19, no. 22, pp. 3761–3770, 2007. [Online]. Available: http://dx.doi.org/10.1002/adma.200701286

[13] T. Tsotsis, "Continuous carbon-nanotube-reinforced polymer precursors and carbon fibers," Jun. 10 2011, uS Patent App. 13/157,587.

[14] H. Qian, E. Greenhalgh, M. Shaffer, and A. Bismarck, "Carbon nanotube-based hierarchical composites: a review," *J. Mater. Chem.*, vol. 20, no. 23,

pp. 4751–4762, 2010.

[15] H. Qian, A. Bismarck, E. Greenhalgh, G. Kalinka, and M. Shaffer, "Hierarchical composites reinforced with carbon nanotube grafted fibers: the potential assessed at the single fiber level," *Chemistry of Materials*, vol. 20, no. 5, pp. 1862–1869, 2008.

[16] E. Munch, M. Launey, D. Alsem, E. Saiz, A. Tomsia, and R. Ritchie, "Tough, bio-inspired hybrid materials," *Science*, vol. 322, no. 5907, pp. 1516–1520, 2008.

[17] Z. Tang, N. Kotov, S. Magonov, B. Ozturk *et al.*, "Nanostructured artificial nacre," *Nature materials*, vol. 2, no. 6, pp. 413–418, 2003.

[18] S. Bal and S. Samal, "Carbon nanotube reinforced polymer compositesa state of the art," *Bulletin of Materials Science*, vol. 30, no. 4, pp. 379–386, 2007.

[19] W. Ma, L. Liu, Z. Zhang, R. Yang, G. Liu, T. Zhang, X. An, X. Yi, Y. Ren, Z. Niu *et al.*, "High-strength composite fibers: realizing true potential of carbon nanotubes in polymer matrix through continuous reticulate architecture and molecular level couplings," *Nano letters*, vol. 9, no. 8, pp. 2855–2861, 2009.

[20] G. Bao, S. Suresh *et al.*, "Cell and molecular mechanics of biological materials," *Nature materials*, vol. 2, no. 11, pp. 715–725, 2003.

[21] A. Bledzki, A. Kessler, R. Rikards, and A. Chate, "Determination of elastic constants of glass/epoxy unidirectional laminates by the vibration testing of plates," *Composites science and technology*, vol. 59, no. 13, pp. 2015–2024, 1999.

[22] A. Cohen, X. Liu, E. Stein, D. McMahon, H. Rogers, J. LeMaster, R. Recker, J. Lappe, X. Guo, and E. Shane, "Bone microarchitecture and stiffness in premenopausal women with idiopathic osteoporosis," *Journal of Clinical Endocrinology & Metabolism*, vol. 94, no. 11, pp. 4351–4360, 2009.

[23] L. Mishnaevsky and H. Qing, "Micromechanical modelling of mechanical behaviour and strength of wood: State-of-the-art review," *Computational Materials Science*, vol. 44, no. 2, pp. 363–370, 2008.

[24] S. Weiner, W. Traub, and H. Wagner, "Lamellar bone: structure-function relations," *Journal of structural biology*, vol. 126, no. 3, pp. 241–255, 1999.

[25] C. Wu and W. Xu, "Atomistic molecular modelling of crosslinked epoxy resin," *Polymer*, vol. 47, no. 16, pp. 6004–6009, 2006.

[26] D. Vignjevic, D. Yarar, M. Welch, J. Peloquin, T. Svitkina, and G. Borisy, "Formation of filopodia-like bundles in vitro from a dendritic network," *The Journal of cell biology*, vol. 160, no. 6, pp. 951–962, 2003.

[27] C. Bronkhorst, "Modelling paper as a two-dimensional elastic–plastic stochastic network," *International journal of solids and structures*, vol. 40, no. 20, pp. 5441–5454, 2003.

[28] L. Ghasemi-Mobarakeh, M. Prabhakaran, M. Morshed, M. Nasr-Esfahani, and S. Ramakrishna, "Electrospun poly-caprolactone/gelatin nanofibrous scaffolds for nerve tissue engineering," *Biomaterials*, vol. 29, no. 34, pp. 4532–4539, 2008.

[29] "ELECTRONICS, transparent conductive films," http://www.unidym.com/technology/cnt_application_electronics.html, accessed: 03/05/2012.

227

[30] C. Chan, R. Ruffo, S. Hong, R. Huggins, and Y. Cui, "Structural and electro-chemical study of the reaction of lithium with silicon nanowires," *Journal of power sources*, vol. 189, no. 1, pp. 34–39, 2009.

[31] M. Malkoch, R. Vestberg, N. Gupta, L. Mespouille, P. Dubois, A. Mason, J. Hedrick, Q. Liao, C. Frank, and K. Kingsbury, "Synthesis of well-defined hydrogel networks using click chemistry," *Chemical Communications*, no. 26, pp. 2774–2776, 2006.

[32] L. Hu, D. Hecht, and G. Grner, "Percolation in transparent and conducting carbon nanotube networks," *Nano Letters*, vol. 4, no. 12, pp. 2513–2517, 2004.

[33] M. Gardel, J. Shin, F. MacKintosh, L. Mahadevan, P. Matsudaira, and D. Weitz, "Elastic behavior of cross-linked and bundled actin networks," *Science*, vol. 304, no. 5675, p. 1301, 2004.

[34] L. Treloar, *The Physics of Rubber Elasticity*. Oxford University Press, USA, 2005.

[35] R. HAgglund and P. Isaksson, "On the coupling between macroscopic material degradation and interfiber bond fracture in an idealized fiber network," *International Journal of Solids and Structures*, vol. 45, no. 3-4, pp. 868–878, 2008.

[36] D. Klosterman, R. Chartoff, G. Graves, N. Osborne, and B. Priore, "Interfacial characteristics of composites fabricated by laminated object manufacturing," *Composites Part A: Applied Science and Manufacturing*, vol. 29, no. 9-10, pp. 1165–1174, 1998.

[37] I. CERNY and R. Mayer, "Fatigue of selected grp composite components and joints with damage evaluation," *Composite structures*, vol. 94, no. 2,

pp. 664–670, 2012.

[38] S. Cranford and M. Buehler, "Materiomics: biological protein materials, from nano to macro," *Nanotechnology, Science and Applications*, vol. 3, pp. 127–148, 2010.

[39] H. Hatami-Marbini, A. Shahsavari, and R. Picu, "Multiscale modeling of semiflexible random fibrous structures," *Computer-Aided Design*, 2011.

[40] L. Mishnaevsky and S. Schumacher, "Continuum mesomechanical finite element modeling in materials development: A state-of-the-art review," *Applied Mechanics Reviews*, vol. 54, no. 1, pp. 49–68, 2001.

[41] S. Glotzer and W. Paul, "Molecular and mesoscale simulation methods for polymer materials," *Annual Review of Materials Research*, vol. 32, no. 1, pp. 401–436, 2002.

[42] T. Gates, G. Odegard, S. Frankland, and T. Clancy, "Computational materials: multi-scale modeling and simulation of nanostructured materials," *Composites Science and Technology*, vol. 65, no. 15, pp. 2416–2434, 2005.

[43] F. Vernerey, W. K. Liu, and B. Moran, "Multi-scale micromorphic theory for hierarchical materials," *Journal of the Mechanics and Physics of Solids*, vol. 55, no. 12, pp. 2603 – 2651, 2007. [Online]. Available: http://www.sciencedirect.com/science/article/pii/S0022509607000877

[44] J. Bouvard, D. Ward, D. Hossain, S. Nouranian, E. Marin, and M. Horstemeyer, "Review of hierarchical multiscale modeling to describe the mechanical behavior of amorphous polymers," *Journal of Engineering Materials and Technology*, vol. 131, p. 041206, 2009.

[45] H. Yao and H. Gao, "Multi-scale cohesive laws in hierarchical materials," *International Journal of Solids and Structures*, vol. 44,

no. 2526, pp. 8177 – 8193, 2007. [Online]. Available: http://www.sciencedirect.com/science/article/pii/S0020768307002454

[46] P. Valavala, T. Clancy, G. Odegard, and T. Gates, "Nonlinear multiscale modeling of polymer materials," *International journal of solids and structures*, vol. 44, no. 3, pp. 1161–1179, 2007.

[47] P. Valavala, G. Odegard, and E. Aifantis, "Influence of representative volume element size on predicted elastic properties of polymer materials," *Modelling and Simulation in Materials Science and Engineering*, vol. 17, p. 045004, 2009.

[48] G. Odegard, T. Gates, L. Nicholson, and K. Wise, "Equivalent-continuum modeling of nano-structured materials," *Composites Science and Technology*, vol. 62, no. 14, pp. 1869–1880, 2002.

[49] J. Baschnagel, K. Binder, P. Doruker, A. Gusev, O. Hahn, K. Kremer, W. Mattice, F. Müller-Plathe, M. Murat, W. Paul *et al.*, "Bridging the gap between atomistic and coarse-grained models of polymers: Status and perspectives," *Viscoelasticity, atomistic models, statistical chemistry*, pp. 41–156, 2000.

[50] D. Reith, H. Meyer, and F. Müller-Plathe, "Mapping atomistic to coarse-grained polymer models using automatic simplex optimization to fit structural properties," *Macromolecules*, vol. 34, no. 7, pp. 2335–2345, 2001.

[51] P. Chandran and V. Barocas, "Deterministic material-based averaging theory model of collagen gel micromechanics," *Journal of biomechanical engineering*, vol. 129, p. 137, 2007.

[52] T. Stylianopoulos and V. Barocas, "Volume-averaging theory for the study

of the mechanics of collagen networks," *Computer methods in applied mechanics and engineering*, vol. 196, no. 31, pp. 2981–2990, 2007.

[53] R. Breuls, B. Sengers, C. Oomens, C. Bouten, and F. Baaijens, "Predicting local cell deformations in engineered tissue constructs: a multilevel finite element approach," *Journal of biomechanical engineering*, vol. 124, p. 198, 2002.

[54] R. Smit, W. Brekelmans, and H. Meijer, "Prediction of the mechanical behavior of nonlinear heterogeneous systems by multi-level finite element modeling," *Computer Methods in Applied Mechanics and Engineering*, vol. 155, no. 1, pp. 181–192, 1998.

[55] "Wikipedia, actin," http://en.wikipedia.org/wiki/Actin, accessed: 16/06/2012.

[56] "Science images, skin," //http://www.sciencephoto.com, accessed: 17/06/2012.

[57] "Galleries, fluorescence microscopy digital image gallery," http://www.microscopyu.com, accessed: 17/06/2012.

[58] "Clipart for free," http://clipart-for-free.blogspot.sg, accessed: 17/06/2012.

[59] "Wikipedia, cytoskeleton," http://en.wikipedia.org/wiki/Cytoskeleton, accessed: 16/06/2012.

[60] D. Boal, *Mechanics of the Cell*. Cambridge Univiversity Press, 2002.

[61] J. Stricker, T. Falzone, and M. Gardel, "Mechanics of the f-actin cytoskeleton," *Journal of biomechanics*, vol. 43, no. 1, pp. 9–14, 2010.

[62] E. Chhabra and H. Higgs, "The many faces of actin: matching assembly factors with cellular structures," *Nature Cell Biology*, vol. 9, no. 10, pp. 1110–1121, 2007.

[63] T. Stossel, J. Condeelis, L. Cooley, J. Hartwig, A. Noegel, M. Schleicher, and S. Shapiro, "Filamins as integrators of cell mechanics and signalling," *Nature Reviews Molecular Cell Biology*, vol. 2, no. 2, pp. 138–145, 2001.

[64] S. Suresh, "Biomechanics and biophysics of cancer cells," *Acta Materialia*, vol. 55, no. 12, pp. 3989–4014, 2007.

[65] A. Clark and E. Paluch, "Mechanics and regulation of cell shape during the cell cycle," *Cell Cycle in Development*, pp. 31–73, 2011.

[66] J. Sanger, "Changing patterns of actin localization during cell division," *Proceedings of the National Academy of Sciences*, vol. 72, no. 5, p. 1913, 1975.

[67] J. Theriot and T. Mitchison, "Actin microfilament dynamics in locomoting cells," *Nature*, vol. 352, no. 6331, pp. 126–131, 1991.

[68] S. Cranford and M. Buehler, "Materiomics: biological protein materials, from nano to macro," *Nanotechnology, Science and Applications*, vol. 3, pp. 127–148, 2010.

[69] B. Schnurr, F. Gittes, F. MacKintosh, and C. Schmidt, "Determining microscopic viscoelasticity in flexible and semiflexible polymer networks from thermal fluctuations," *Macromolecules*, vol. 30, no. 25, pp. 7781–7792, 1997.

[70] M. Gardel, F. Nakamura, J. Hartwig, J. Crocker, T. Stossel, and D. Weitz, "Stress-dependent elasticity of composite actin networks as a model for cell behavior," *Physical Review Letters*, vol. 96, no. 8, p. 88102, 2006.

[71] C. Broedersz, K. Kasza, L. Jawerth, S. Mnster, D. Weitz, and F. MacKintosh, "Measurement of nonlinear rheology of cross-linked biopolymer gels," *Soft Matter*, vol. 6, no. 17, pp. 4120–4127, 2010.

[72] K. Schmoller, O. Lieleg, and A. Bausch, "Structural and viscoelastic properties of actin/filamin networks: cross-linked versus bundled networks," *Biophysical Journal*, vol. 97, no. 1, pp. 83–89, 2009.

[73] Y. Termonia, "Computer model for the mechanical properties of synthetic and biological polymer fibers," *Pergamon Materials Series*, vol. 4, pp. 271–291, 2000.

[74] F. MacKintosh, J. Ks, and P. Janmey, "Elasticity of semiflexible biopolymer networks," *Physical Review Letters*, vol. 75, no. 24, pp. 4425–4428, 1995.

[75] F. Gittes and F. MacKintosh, "Dynamic shear modulus of a semiflexible polymer network," *Physical Review E*, vol. 58, no. 2, pp. 1241–1244, 1998.

[76] K. Kasza, G. Koenderink, Y. Lin, C. Broedersz, W. Messner, F. Nakamura, T. Stossel, F. MacKintosh, and D. Weitz, "Nonlinear elasticity of stiff biopolymers connected by flexible linkers," *Physical Review E*, vol. 79, no. 4, p. 041928, 2009.

[77] D. Head, A. Levine, and F. MacKintosh, "Distinct regimes of elastic response and deformation modes of cross-linked cytoskeletal and semiflexible polymer networks," *Physical Review E*, vol. 68, no. 6, p. 061907, 2003.

[78] P. Onck, T. Koeman, T. Van Dillen, and E. Van Der Giessen, "Alternative explanation of stiffening in cross-linked semiflexible networks," *Physical Review Letters*, vol. 95, no. 17, p. 178102, 2005.

[79] E. Huisman, T. Van Dillen, P. Onck, and E. Van der Giessen, "Three-dimensional cross-linked f-actin networks: relation between network architecture and mechanical behavior," *Physical Review Letters*, vol. 99, no. 20, p. 208103, 2007.

[80] T. Van Dillen, P. Onck, and E. Van der Giessen, "Models for stiffening in cross-linked biopolymer networks: A comparative study," *Journal of the Mechanics and Physics of Solids*, vol. 56, no. 6, pp. 2240–2264, 2008.

[81] C. Broedersz, C. Storm, and F. MacKintosh, "Nonlinear elasticity of composite networks of stiff biopolymers with flexible linkers," *Physical Review Letters*, vol. 101, no. 11, p. 118103, 2008.

[82] P. Chen and V. Shenoy, "Strain stiffening induced by molecular motors in active crosslinked biopolymer networks," *Soft Matter*, vol. 7, no. 2, pp. 355–358, 2010.

[83] Y. Tseng, K. An, O. Esue, and D. Wirtz, "The bimodal role of filamin in controlling the architecture and mechanics of f-actin networks," *Journal of Biological Chemistry*, vol. 279, no. 3, p. 1819, 2004.

[84] O. Lieleg and A. Bausch, "Cross-linker unbinding and self-similarity in bundled cytoskeletal networks," *Physical Review Letters*, vol. 99, no. 15, p. 158105, 2007.

[85] J. Xu, Y. Tseng, and D. Wirtz, "Strain hardening of actin filament networks regulation by the dynamic cross-linking protein α-actinin," *Journal of Biological Chemistry*, vol. 275, no. 46, pp. 35 886–35 892, 2000.

[86] C. Semmrich, A. Bausch *et al.*, "Nonlinear mechanics of entangled f-actin solutions," *Soft Matter*, vol. 4, no. 8, pp. 1675–1680, 2008.

[87] O. Chaudhuri, S. Parekh, and D. Fletcher, "Reversible stress softening of actin networks," *Nature*, vol. 445, no. 7125, p. 295, 2007.

[88] S. Tianxiang and P. Prashant K, "Semiflexible filament networks viewed as fluctuating beam-frames," *Accepted in Soft Matter*.

[89] B. DiDonna and A. Levine, "Unfolding cross-linkers as rheology regulators in f-actin networks," *Physical Review E*, vol. 75, no. 4, p. 041909, 2007.

[90] O. Lieleg, M. Claessens, and A. Bausch, "Structure and dynamics of cross-linked actin networks," *Soft Matter*, vol. 6, no. 2, pp. 218–225, 2009.

[91] S. Suresh, J. Spatz, J. Mills, A. Micoulet, M. Dao, C. Lim, M. Beil, and T. Seufferlein, "Connections between single-cell biomechanics and human disease states: gastrointestinal cancer and malaria," *Acta Biomaterialia*, vol. 1, no. 1, pp. 15–30, 2005.

[92] Q. Li, G. Lee, C. Ong, and C. Lim, "Afm indentation study of breast cancer cells," *Biochemical and biophysical research communications*, vol. 374, no. 4, pp. 609–613, 2008.

[93] D. Butler, S. Goldstein, and F. Guilak, "Functional tissue engineering: the role of biomechanics," *Journal of biomechanical engineering*, vol. 122, p. 570, 2000.

[94] D. Lee, M. Knight, J. Campbell, and D. Bader, "Stem cell mechanobiology," *Journal of cellular biochemistry*, vol. 112, no. 1, pp. 1–9, 2011.

[95] "Ge wind energy," http://www.ge-energy.com, accessed: 26/06/2012.

[96] "Epoxy curing agent," http://www.reinforcedplastics.com/, accessed: 25/06/2012.

[97] H. Ghasemnejad, L. Occhineri, and D. Swift-Hook, "Post-buckling failure in multi-delaminated composite wind turbine blade materials," *Materials & Design*, vol. 32, no. 10, pp. 5106 – 5112, 2011.

[98] W. Morais, J. d'Almeida, and L. Godefroid, "Effect of the fiber reinforcement on the low energy impact behavior of fabric reinforced resin matrix composite materials," *Journal of the Brazilian Society of Mechanical Sciences and Engineering*, vol. 25, no. 4, pp. 325–328, 2003.

[99] L. Gautier, B. Mortaigne, and V. Bellenger, "Interface damage study of hydrothermally aged glass-fibre-reinforced polyester composites," *Composites science and technology*, vol. 59, no. 16, pp. 2329–2337, 1999.

[100] D. Boksman, A. Hepburn, E. Kogan, M. Friedman, and W. de Rijk, "Fiber post techniques for anatomical root variations." *Dentistry today*, vol. 30, no. 5, pp. 104–106, 2011.

[101] L. Mishnaevsky Jr, *Computational mesomechanics of composites*. Wiley Online Library, 2007.

[102] H. Böhm, "A short introduction to basic aspects of continuum micromechanics," *CDL-FMD Report*, vol. 3, 1998.

[103] G. Tandon and N. Pagano, "Micromechanical analysis of the fiber push-out and re-push test," *Composites science and technology*, vol. 58, no. 11, pp. 1709–1725, 1998.

[104] M. Romanowicz, "Effect of interfacial debonding on the failure behavior in a fiber-reinforced composite subjected to transverse tension," *Computational Materials Science*, vol. 47, no. 1, pp. 225–231, 2009.

[105] T. Tay, "Characterization and analysis of delamination fracture in composites: an overview of developments from 1990 to 2001," *Applied Mechanics*

Reviews, vol. 56, p. 1, 2003.

[106] C. Gonzlez and J. LLorca, "Mechanical behavior of unidirectional fiber-reinforced polymers under transverse compression: microscopic mechanisms and modeling," *Composites Science and Technology*, vol. 67, no. 13, pp. 2795–2806, 2007.

[107] L. Mishnaevsky Jr and P. Brndsted, "Statistical modelling of compression and fatigue damage of unidirectional fiber reinforced composites," *Composites Science and Technology*, vol. 69, no. 3-4, pp. 477–484, 2009.

[108] E. Frey, K. Kroy, and J. Wilhelm, "Viscoelasticity of biopolymer networks and statistical mechanics of semiflexible polymers," *Advances in Structural Biology*, vol. 5, pp. 135–168, 1999.

[109] A. S. Abhilash, P. K. Purohit, and S. P. Joshi, "Stochastic rate-dependent elasticity and failure of soft fibrous networks," *Soft Matter*, vol. 8, pp. 7004–7016, 2012. [Online]. Available: http://dx.doi.org/10.1039/C2SM25450F

[110] S. Heyden, *Network modelling for the evaluation of mechanical properties of cellulose fibre fluff*. Lund Univiversity, 2000.

[111] R. Hägglund and P. Isaksson, "On the coupling between macroscopic material degradation and interfiber bond fracture in an idealized fiber network," *International Journal of Solids and Structures*, vol. 45, no. 3-4, pp. 868–878, 2008.

[112] P. Isaksson and R. Hägglund, "Evolution of bond fractures in a randomly distributed fiber network," *International journal of solids and structures*, vol. 44, no. 18, pp. 6135–6147, 2007.

[113] J. Astrom, S. Saarinen, K. Niskanen, and J. Kurkijarvi, "Microscopic mechanics of fiber networks," *Journal of applied physics*, vol. 75, no. 5, pp. 2383–2392, 1994.

[114] X. Wu and Y. Dzenis, "Elasticity of planar fiber networks," *Journal of applied physics*, vol. 98, p. 093501, 2005.

[115] X. Wei, Z. Xia, S. Wong, and A. Baji, "Modelling of mechanical properties of electrospun nanofibre network," *International Journal of Experimental and Computational Biomechanics*, vol. 1, no. 1, pp. 45–57, 2009.

[116] A. Agic and B. Mijovic, "Mechanical properties of electrospun carbon nanotube composites," *Journal of the Textile Institute*, vol. 97, no. 5, pp. 419–427, 2006.

[117] F. Chen, D. Porter, and F. Vollrath, "Silkworm cocoons inspire models for random fiber and particulate composites," *Physical Review E*, vol. 82, no. 4, p. 041911, 2010.

[118] Y. Termonia, P. Meakin, and P. Smith, "Theoretical study of the influence of the molecular weight on the maximum tensile strength of polymer fibers," *Macromolecules*, vol. 18, no. 11, pp. 2246–2252, 1985.

[119] Y. Termonia and P. Smith, "Kinetic model for tensile deformation of polymers," *Macromolecules*, vol. 20, no. 4, pp. 835–838, 1987.

[120] Y. Termoni a and P. Smith, "Kinetic model for tensile deformation of polymers. 2. effect of entanglement spacing," *Macromolecules*, vol. 21, no. 7, pp. 2184–2189, 1988.

[121] Y. Termonia, S. Allen, and P. Smith, "Kinetic model for tensile deformation of polymers. 3. effects of deformation rate and temperature," *Macromolecules*, vol. 21, no. 12, pp. 3485–3489, 1988.

[122] S. Zhurkov, "Kinetic concept of the strength of solids," *International Journal of Fracture*, vol. 26, no. 4, pp. 295–307, 1984.

[123] G. Bell, "Models for the specific adhesion of cells to cells," *Science*, vol. 200, no. 4342, pp. 618–627, 1978.

[124] Y. Termonia, "Molecular modeling of spider silk elasticity," *Macromolecules*, vol. 27, no. 25, pp. 7378–7381, 1994.

[125] Y. Jin and T. Wang, "Three-dimensional numerical modeling of the damage mechanism of amorphous polymer network," *Computational Materials Science*, vol. 46, no. 3, pp. 632–638, 2009.

[126] D. A. Head, A. J. Levine, and F. C. MacKintosh, "Deformation of cross-linked semiflexible polymer networks," *Phys. Rev. Lett.*, vol. 91, p. 108102, Sep 2003. [Online]. Available: http://link.aps.org/doi/10.1103/PhysRevLett.91.108102

[127] H. Hatami-Marbini and R. Picu, "Effect of fiber orientation on the non-affine deformation of random fiber networks," *Acta Mechanica*, vol. 205, no. 1, pp. 77–84, 2009.

[128] E. Huisman, T. Van Dillen, P. Onck, and E. Van der Giessen, "Three-dimensional cross-linked f-actin networks: relation between network architecture and mechanical behavior," *Physical review letters*, vol. 99, no. 20, p. 208103, 2007.

[129] F. MacKintosh, J. Käs, and P. Janmey, "Elasticity of semiflexible biopolymer networks," *Physical review letters*, vol. 75, no. 24, pp. 4425–4428, 1995.

[130] C. Heussinger and E. Frey, "Floppy modes and nonaffine deformations in random fiber networks," *Physical review letters*, vol. 97, no. 10, p. 105501,

2006.

[131] C. "Heussinger and E. Frey, "Role of architecture in the elastic response of semiflexible polymer and fiber networks," *Physical Review E*, vol. 75, no. 1, p. 011917, 2007.

[132] P. Boolchand, X. Feng, D. Selvanathan, W. Bresser, M. Thorpe, and P. Duxbury, "Rigidity theory and applications," 1999.

[133] G. E. Pike and C. H. Seager, "Percolation and conductivity: A computer study. i," *Phys. Rev. B*, vol. 10, pp. 1421–1434, Aug 1974. [Online]. Available: http://link.aps.org/doi/10.1103/PhysRevB.10.1421

[134] "Wikipedia, line-line intersection," http://en.wikipedia.org/wiki/ Line-line_intersection, accessed: 10/06/2012.

[135] S. Kähkönen, *Elasticity and Stiffness Evolution in Random Fibre Networks*. University of Jyväskylä, 2003.

[136] B. Ripley, "Tests of randomness' for spatial point patterns," *Journal of the Royal Statistical Society. Series B (Methodological)*, pp. 368–374, 1979.

[137] S. Torquato, "Nearest-neighbor statistics for packings of hard spheres and disks," *Physical Review E*, vol. 51, no. 4, p. 3170, 1995.

[138] Y. Wu, W. Zhou, B. Wang, and F. Yang, "Modeling and characterization of two-phase composites by voronoi diagram in the laguerre geometry based on random close packing of spheres," *Computational Materials Science*, vol. 47, no. 4, pp. 951 – 961, 2010. [Online]. Available: http://www.sciencedirect.com/science/article/pii/S092702560900439X

[139] V. Kushch, S. Shmegera, and L. Mishnaevsky Jr, "Statistics of microstructure, peak stress and interface damage in fiber reinforced composites,"

Journal of the Mechanics of Materials and Structures, vol. 4, no. 6, pp. 1089–1107, 2009.

[140] A. Abhilash, S. Joshi, A. Mukherjee, and L. Mishnaevsky, "Micromechanics of diffusion-induced damage evolution in reinforced polymers," *Composites Science and Technology*, vol. 71, no. 3, pp. 333–342, 2011.

[141] S. Inc., *ABAQUS Version 6.9 Online Documentation*, p. 2010.

[142] D. Head, A. Levine, and F. MacKintosh, "Distinct regimes of elastic response and deformation modes of cross-linked cytoskeletal and semiflexible polymer networks," *Physical Review E*, vol. 68, no. 6, p. 061907, 2003.

[143] I. Salib, G. Kolmakov, C. Gnegy, K. Matyjaszewski, and A. Balazs, "Role of parallel reformable bonds in the self-healing of cross-linked nanogel particles," *Langmuir*, 2011.

[144] S. Baxter, M. Hossain, and L. Graham, "Micromechanics based random material property fields for particulate reinforced composites," *International journal of solids and structures*, vol. 38, no. 50, pp. 9209–9220, 2001.

[145] L. Graham-Brady, "Statistical characterization of meso-scale uniaxial compressive strength in brittle materials with randomly occurring flaws," *International Journal of Solids and Structures*, vol. 47, no. 18, pp. 2398–2413, 2010.

[146] S. Baxter and L. Graham, "Characterization of random composites using moving-window technique," *Journal of engineering mechanics*, vol. 126, p. 389, 2000.

[147] G. Lilliu and J. van Mier, "3d lattice type fracture model for concrete," *Engineering Fracture Mechanics*, vol. 70, no. 7-8, pp. 927–941, 2003.

[148] R. Ince, A. Arslan, and B. Karihaloo, "Lattice modelling of size effect in concrete strength," *Engineering fracture mechanics*, vol. 70, no. 16, pp. 2307–2320, 2003.

[149] H. Zhu, J. Hobdell, and A. Windle, "Effects of cell irregularity on the elastic properties of 2d voronoi honeycombs," *Journal of the Mechanics and Physics of Solids*, vol. 49, no. 4, pp. 857–870, 2001.

[150] A. Fazekas, R. Dendievel, L. Salvo, and Y. Bréchet, "Effect of microstructural topology upon the stiffness and strength of 2d cellular structures," *International journal of mechanical sciences*, vol. 44, no. 10, pp. 2047–2066, 2002.

[151] G. Žagar, P. Onck, and E. Giessen, "Small strain topological effects of biopolymer networks with rigid cross-links," in *IUTAM Symposium on Cellular, Molecular and Tissue Mechanics*. Springer, 2010, pp. 161–169.

[152] J. Goffin, P. Pittet, G. Csucs, J. Lussi, J. Meister, and B. Hinz, "Focal adhesion size controls tension-dependent recruitment of α-smooth muscle actin to stress fibers," *The Journal of cell biology*, vol. 172, no. 2, pp. 259–268, 2006.

[153] S. Pellegrin and H. Mellor, "Actin stress fibres," *Journal of cell science*, vol. 120, no. 20, pp. 3491–3499, 2007.

[154] P. Hotulainen and P. Lappalainen, "Stress fibers are generated by two distinct actin assembly mechanisms in motile cells," *The Journal of cell biology*, vol. 173, no. 3, pp. 383–394, 2006.

[155] M. Prabhakaran, J. Venugopal, and S. Ramakrishna, "Electrospun nanostructured scaffolds for bone tissue engineering," *Acta biomaterialia*, vol. 5, no. 8, pp. 2884–2893, 2009.

[156] G. Žagar, P. Onck, and E. Van der Giessen, "Elasticity of rigidly cross-linked networks of athermal filaments," *Macromolecules*, 2011.

[157] M. Gardel, J. Shin, F. MacKintosh, L. Mahadevan, P. Matsudaira, and D. Weitz, "Elastic behavior of cross-linked and bundled actin networks," *Science*, vol. 304, no. 5675, pp. 1301–1305, 2004.

[158] R. Picu, "Mechanics of random fiber networksa review," *Soft Matter*, vol. 7, no. 15, pp. 6768–6785, 2011.

[159] M. Nunnally, L. Powell, and S. Craig, "Reconstitution and regulation of actin gel-sol transformation with purified filamin and villin." *Journal of Biological Chemistry*, vol. 256, no. 5, p. 2083, 1981.

[160] A. Ott, M. Magnasco, A. Simon, and A. Libchaber, "Measurement of the persistence length of polymerized actin using fluorescence microscopy," *Physical Review E*, vol. 48, no. 3, pp. 1642–1645, 1993.

[161] J. Condeelis, M. Vahey, J. Carboni, J. DeMey, and S. Ogihara, "Properties of the 120,000-and 95,000-dalton actin-binding proteins from dictyostelium discoideum and their possible functions in assembling the cytoplasmic matrix," *The Journal of cell biology*, vol. 99, no. 1, p. 119s, 1984.

[162] M. Jhon and D. Chrzan, "Statistical approach to the unfolding of mechanically stressed biopolymers," *Journal of the Mechanical Behavior of Biomedical Materials*, vol. 2, no. 6, pp. 603–606, 2009.

[163] M. Li and M. Kouza, "Dependence of protein mechanical unfolding pathways on pulling speeds," *The Journal of Chemical Physics*, vol. 130, p. 145102, 2009.

[164] M. Schlierf and M. Rief, "Single-molecule unfolding force distributions reveal a funnel-shaped energy landscape," *Biophysical Journal*, vol. 90,

no. 4, pp. L33–L35, 2006.

[165] J. Ferrer, H. Lee, J. Chen, B. Pelz, F. Nakamura, R. Kamm, and M. Lang, "Measuring molecular rupture forces between single actin filaments and actin-binding proteins," *Proceedings of the National Academy of Sciences*, vol. 105, no. 27, p. 9221, 2008.

[166] G. Bell, "Models for the specific adhesion of cells to cells," *Science*, vol. 200, no. 4342, p. 618, 1978.

[167] A. Voter, "Introduction to the kinetic monte carlo method," *Radiation Effects in Solids*, pp. 1–23, 2007.

[168] T. Nishizaka, R. Seo, H. Tadakuma, K. Kinosita Jr, and S. Ishiwata, "Characterization of single actomyosin rigor bonds: load dependence of lifetime and mechanical properties," *Biophysical journal*, vol. 79, no. 2, pp. 962–974, 2000.

[169] H. Lee, B. Pelz, J. Ferrer, T. Kim, M. Lang, and R. Kamm, "Cytoskeletal deformation at high strains and the role of cross-link unfolding or unbinding," *Cellular and Molecular Bioengineering*, vol. 2, no. 1, pp. 28–38, 2009.

[170] G. Hummer and A. Szabo, "Kinetics from nonequilibrium single-molecule pulling experiments," *Biophysical Journal*, vol. 85, no. 1, pp. 5–15, 2003.

[171] J. Åström, P. Kumar, I. Vattulainen, and M. Karttunen, "Strain hardening, avalanches, and strain softening in dense cross-linked actin networks," *Physical Review E*, vol. 77, no. 5, p. 051913, 2008.

[172] A. Argon, *Strengthening Mechanisms in Crystal Plasticity*. Oxford University Press, USA, 2008, vol. 4.

244

[173] O. Lieleg, M. Claessens, Y. Luan, A. Bausch *et al.*, "Transient binding and dissipation in cross-linked actin networks," *Physical review letters*, vol. 101, no. 10, p. 108101, 2008.

[174] K. Kasza, C. Broedersz, G. Koenderink, Y. Lin, W. Messner, E. Millman, F. Nakamura, T. Stossel, F. MacKintosh, and D. Weitz, "Actin filament length tunes elasticity of flexibly cross-linked actin networks," *Biophysical journal*, vol. 99, no. 4, pp. 1091–1100, 2010.

[175] O. Lieleg and A. Bausch, "Cross-linker unbinding and self-similarity in bundled cytoskeletal networks," *Physical Review Letters*, vol. 99, no. 15, p. 158105, 2007.

[176] R. Tharmann, M. Claessens, and A. Bausch, "Viscoelasticity of isotropically cross-linked actin networks," *Physical review letters*, vol. 98, no. 8, p. 88103, 2007.

[177] C. Broedersz, K. Kasza, L. Jawerth, S. Münster, D. Weitz, and F. MacKintosh, "Measurement of nonlinear rheology of cross-linked biopolymer gels," *Soft Matter*, vol. 6, no. 17, pp. 4120–4127, 2010.

[178] E. Peña, "Prediction of the softening and damage effects with permanent set in fibrous biological materials," *Journal of the Mechanics and Physics of Solids*, vol. 59, no. 9, pp. 1808 – 1822, 2011. [Online]. Available: http://www.sciencedirect.com/science/article/pii/S0022509611001220

[179] J. Planas, G. Guinea, and M. Elices, "Constitutive model for fiber-reinforced materials with deformable matrices," *Physical Review E*, vol. 76, no. 4, p. 041903, 2007.

[180] A. Zaccone and E. Scossa-Romano, "Approximate analytical description of the nonaffine response of amorphous solids," *Physical Review B*, vol. 83,

no. 18, p. 184205, 2011.

[181] C. Storm, J. Pastore, F. MacKintosh, T. Lubensky, and P. Janmey, "Nonlinear elasticity in biological gels," *Nature*, vol. 435, no. 7039, pp. 191–194, 2005.

[182] H. Wu, *Continuum mechanics and plasticity*. CRC Press, 2005, vol. 3.

[183] S. Furuike, T. Ito, and M. Yamazaki, "Mechanical unfolding of single filamin a (abp-280) molecules detected by atomic force microscopy," *FEBS letters*, vol. 498, no. 1, pp. 72–75, 2001.

[184] C. Heussinger, B. Schaefer, and E. Frey, "Nonaffine rubber elasticity for stiff polymer networks," *Physical Review E*, vol. 76, no. 3, p. 031906, 2007.

[185] C. Broedersz, X. Mao, T. Lubensky, and F. MacKintosh, "Criticality and isostaticity in fibre networks," *Nature Physics*, 2011.

[186] S. Winder and K. Ayscough, "Actin-binding proteins," *Journal of cell science*, vol. 118, no. 4, pp. 651–654, 2005.

[187] G. Žagar, P. Onck, and E. Giessen, "Small strain topological effects of biopolymer networks with rigid cross-links," in *IUTAM Symposium on Cellular, Molecular and Tissue Mechanics*. Springer, 2010, pp. 161–169.

[188] M. Bai, A. R. Missel, A. J. Levine, and W. S. Klug, "On the role of the filament length distribution in the mechanics of semiflexible networks," *Acta Biomaterialia*, vol. 7, no. 5, pp. 2109 – 2118, 2011. [Online]. Available: http://www.sciencedirect.com/science/article/pii/S1742706110005891

[189] J. Howard, *Mechanics of Motor Proteins and the Cytoskeleton*, pp. Sinauer Associates Sunderland, MA, 2001.

[190] A. Missel, M. Bai, W. Klug, and A. Levine, "Affine-nonaffine transition in networks of nematically ordered semiflexible polymers," *Physical Review E*, vol. 82, no. 4, p. 041907, 2010.

[191] J. Wilhelm and E. Frey, "Elasticity of stiff polymer networks," *Physical review letters*, vol. 91, no. 10, p. 108103, 2003.

[192] C. Broedersz, C. Storm, and F. MacKintosh, "Nonlinear elasticity of composite networks of stiff biopolymers with flexible linkers," *Physical review letters*, vol. 101, no. 11, p. 118103, 2008.

[193] S. Kidoaki, I. K. Kwon, and T. Matsuda, "Structural features and mechanical properties of in situbonded meshes of segmented polyurethane electrospun from mixed solvents," *Journal of Biomedical Materials Research Part B: Applied Biomaterials*, vol. 76B, no. 1, pp. 219–229, 2006. [Online]. Available: http://dx.doi.org/10.1002/jbm.b.30336

[194] C. Baley, P. Davies, Y. Grohens, and G. Dolto, "Application of interlaminar tests to marine composites. a literature review," *Applied Composite Materials*, vol. 11, no. 2, pp. 99–126, 2004.

[195] A. Hodzic, J. Kim, A. Lowe, and Z. Stachurski, "The effects of water aging on the interphase region and interlaminar fracture toughness in polymer-glass composites," *Composites Science and Technology*, vol. 64, no. 13-14, pp. 2185–2195, 2004.

[196] J. L. Ferracane, "Hygroscopic and hydrolytic effects in dental polymer networks," *Dental Materials*, vol. 22, no. 3, pp. 211–222, 2006.

[197] K. Derrien and P. Gilormini, "The effect of applied stresses on the equilibrium moisture content in polymers," *Scripta Materialia*, vol. 56, no. 4, pp. 297–299, 2007.

[198] S. Roy, K. Vengadassalam, Y. Wang, S. Park, and K. Liechti, "Characterization and modeling of strain assisted diffusion in an epoxy adhesive layer," *International journal of solids and structures*, vol. 43, no. 1, pp. 27–52, 2006.

[199] Y. Weitsman, "Coupled damage and moisture-transport in fiber-reinforced polymeric composites," *International Journal of Solids and Structures*, vol. 23, no. 7, pp. 1003–1025, 1986.

[200] A. Apicella, L. Nicolais, G. Astarita, and E. Drioli, "Effect of thermal history on water sorption, elastic properties and the glass transition of epoxy resins," *Polymer*, vol. 20, no. 9, pp. 1143–1148, 1979, cited By (since 1996): 35.

[201] M. R. VanLandingham, R. F. Eduljee, and J. W. Gillespie Jr, "Moisture diffusion in epoxy systems," *Journal of Applied Polymer Science*, vol. 71, no. 5, pp. 787–798, 1999, cited By (since 1996): 64 Export Date: 15 November 2009 Source: Scopus.

[202] G. "Xiao and M. "Shanahan, "Irreversible effects of hygrothermal aging on dgeba/dda epoxy resin," *Journal of Applied Polymer Science*, vol. 69, no. 2, pp. 363–369, 1998.

[203] G. Z. Xiao, M. Delamar, and M. E. R. Shanahan, "Irreversible interactions between water and dgeba/dda epoxy resin during hygrothermal aging," *Journal of Applied Polymer Science*, vol. 65, no. 3, pp. 449–458, 1997, cited By (since 1996): 33 Export Date: 15 November 2009 Source: Scopus.

[204] G. Z. Xiao and M. E. R. Shanahan, "Water absorption and desorption in an epoxy resin with degradation," *Journal of Polymer Science, Part B: Polymer*

Physics, vol. 35, no. 16, pp. 2659–2670, 1997, cited By (since 1996): 54 Export Date: 25 December 2009 Source: Scopus.

[205] C. W. Kensche, "Fatigue of composites for wind turbines," *International Journal of Fatigue*, vol. 28, no. 10 SPEC. ISS., pp. 1363–1374, 2006.

[206] H. S. Choi, K. J. Ahn, J. D. Nam, and H. J. Chun, "Hygroscopic aspects of epoxy/carbon fiber composite laminates in aircraft environments," *Composites Part A: Applied Science and Manufacturing*, vol. 32, no. 5, pp. 709–720, 2001.

[207] S. S. Wang and X. Chen, "Computational micromechanics for high-temperature constitutive equations of polymer-matrix composites with oxidation reaction, damage, and degradation," *Journal of Engineering Materials and Technology, Transactions of the ASME*, vol. 128, no. 1, pp. 81–89, 2006.

[208] J. Zhou and J. P. Lucas, "Hygrothermal effects of epoxy resin. part i: the nature of water in epoxy," *Polymer*, vol. 40, no. 20, pp. 5505 – 5512, 1999. [Online]. Available: http://www.sciencedirect.com/science/article/pii/S0032386198007903

[209] C. Carfagna and A. Apicella, "Physical degradation by water clustering in epoxy resins," *Journal of applied polymer science*, vol. 28, no. 9, pp. 2881–2885, 1983.

[210] S. Popineau, C. Rondeau-Mouro, C. Sulpice-Gaillet, and M. Shanahan, "Free/bound water absorption in an epoxy adhesive," *Polymer*, vol. 46, no. 24, pp. 10 733–10 740, 2005.

[211] G. Xiao and M. Shanahan, "Water absorption and desorption in an epoxy resin with degradation," *Journal of Polymer Science Part B: Polymer Physics*,

vol. 35, no. 16, pp. 2659–2670, 1997.

[212] G. Xiao, M. Delamar, and M. Shanahan, "Irreversible interactions between water and dgeba/dda epoxy resin during hygrothermal aging," *Journal of Applied Polymer Science*, vol. 65, no. 3, pp. 449–458, 1997.

[213] G. Xiao and M. Shanahan, "Irreversible effects of hygrothermal aging on dgeba/dda epoxy resin," *Journal of applied polymer science*, vol. 69, no. 2, pp. 363–369, 1998.

[214] G. "Xiao and M. Shanahan, "Swelling of dgeba/dda epoxy resin during hygrothermal ageing," *Polymer*, vol. 39, no. 14, pp. 3253–3260, 1998.

[215] H. Ishida and J. Koenig, "The reinforcement mechanism of fiber-glass reinforced plastics under wet conditions: A review," *Polymer Engineering & Science*, vol. 18, no. 2, pp. 128–145, 1978.

[216] H. Kim and W. Marek, "Molecular level chain scission mechanisms of epoxy and urethane polymeric films exposed to uv/h2o. multidimensional spectroscopic studies," *Langmuir*, vol. 16, no. 12, pp. 5382–5390, 2000.

[217] K. Liao and Y. Tan, "Influence of moisture-induced stress on in situ fiber strength degradation of unidirectional polymer composite," *Composites Part B: Engineering*, vol. 32, no. 4, pp. 365–370, 2001.

[218] A. DiBenedetto, "Tailoring of interfaces in glass fiber reinforced polymer composites: a review," *Materials Science and Engineering: A*, vol. 302, no. 1, pp. 74–82, 2001.

[219] D. Olmos, R. Lopez-Moron, and J. Gonzalez-Benito, "The nature of the glass fibre surface and its effect in the water absorption of glass fibre/epoxy composites. the use of fluorescence to obtain information at the

interface," *Composites science and technology*, vol. 66, no. 15, pp. 2758–2768, 2006.

[220] A. Chateauminois, L. Vincent, B. Chabert, and J. Soulier, "Study of the interfacial degradation of a glass-epoxy composite during hygrothermal ageing using water diffusion measurements and dynamic mechanical thermal analysis," *Polymer*, vol. 35, no. 22, pp. 4766–4774, 1994.

[221] C. Tsenoglou, S. Pavlidou, and C. Papaspyrides, "Evaluation of interfacial relaxation due to water absorption in fiber–polymer composites," *Composites science and technology*, vol. 66, no. 15, pp. 2855–2864, 2006.

[222] N. Choi and J. Park, "Fiber/matrix interfacial shear strength measured by a quasi-disk microbond specimen," *Composites Science and Technology*, vol. 69, no. 10, pp. 1615–1622, 2009.

[223] X. Zhou, H. Wagner, and S. Nutt, "Interfacial properties of polymer composites measured by push-out and fragmentation tests," *Composites Part A: Applied Science and Manufacturing*, vol. 32, no. 11, pp. 1543–1551, 2001.

[224] Q. Yang and B. Cox, "Cohesive models for damage evolution in laminated composites," *International Journal of Fracture*, vol. 133, no. 2, pp. 107–137, 2005.

[225] J. Remmers, R. Borst, and A. Needleman, "A cohesive segments method for the simulation of crack growth," *Computational Mechanics*, vol. 31, no. 1, pp. 69–77, 2003.

[226] U. Gaur and B. Miller, "Microbond method for determination of the shear strength of a fiber/resin interface: evaluation of experimental parameters," *Composites science and technology*, vol. 34, no. 1, pp. 35–51, 1989.

[227] D. Biro, G. Pleizier, and Y. Deslandes, "Application of the microbond technique: effects of hygrothermal exposure on carbon-fiber/epoxy interfaces," *Composites science and technology*, vol. 46, no. 3, pp. 293–301, 1993.

[228] B. Miller, U. Gaur, and D. Hirt, "Measurement and mechanical aspects of the microbond pull-out technique for obtaining fiber/resin interfacial shear strength," *Composites science and technology*, vol. 42, no. 1-3, pp. 207–219, 1991.

[229] S. Kang, D. Lee, and N. Choi, "Fiber/epoxy interfacial shear strength measured by the microdroplet test," *Composites Science and Technology*, vol. 69, no. 2, pp. 245–251, 2009.

[230] X. Zhou, H. Wagner, and S. Nutt, "Interfacial properties of polymer composites measured by push-out and fragmentation tests," *Composites Part A*, vol. 32, no. 11, pp. 1543–1551, 2001.

[231] U. Gaur, C. Chou, and B. Miller, "Effect of hydrothermal ageing on bond strength," *Composites*, vol. 25, no. 7, pp. 609–612, 1994.

[232] A. Hodzic, Z. Stachurski, and J. Kim, "Nano-indentation of polymer–glass interfaces part i. experimental and mechanical analysis," *Polymer*, vol. 41, no. 18, pp. 6895–6905, 2000.

[233] A. Hodzic, J. Kim, and Z. Stachurski, "Nano-indentation and nano-scratch of polymer/glass interfaces. ii: model of interphases in water aged composite materials," *Polymer*, vol. 42, no. 13, pp. 5701–5710, 2001.

[234] A. Hodzic, J. Kim, A. Lowe, and Z. Stachurski, "The effects of water aging on the interphase region and interlaminar fracture toughness in polymer–glass composites," *Composites science and technology*, vol. 64, no. 13, pp.

252

2185–2195, 2004.

[235] A. Chateauminois, L. Vincent, B. Chabert, and J. Soulier, "Study of the interfacial degradation of a glass-epoxy composite during hygrothermal ageing using water diffusion measurements and dynamic mechanical thermal analysis," *Polymer*, vol. 35, no. 22, pp. 4766–4774, 1994.

[236] Y. Weitsman and Y. Guo, "A correlation between fluid-induced damage and anomalous fluid sorption in polymeric composites," *Composites Science and Technology*, vol. 62, no. 6, pp. 889–908, 2002.

[237] C. Tsenoglou, S. Pavlidou, and C. Papaspyrides, "Evaluation of interfacial relaxation due to water absorption in fiber-polymer composites," *Composites Science and Technology*, vol. 66, no. 15, pp. 2855–2864, 2006.

[238] U. Gaur, C. Chou, and B. Miller, "Effect of hydrothermal ageing on bond strength," *Composites*, vol. 25, no. 7, pp. 609–612, 1994.

[239] F. Ramirez, L. Carlsson, and B. Acha, "Evaluation of water degradation of vinylester and epoxy matrix composites by single fiber and composite tests," *Journal of Materials Science*, vol. 43, no. 15, pp. 5230–5242, 2008.

[240] P. Vaddadi, T. Nakamura, and R. Singh, "Transient hygrothermal stresses in fiber reinforced composites: a heterogeneous characterization approach," *Composites Part A*, vol. 34, no. 8, pp. 719–730, 2003.

[241] P. Vaddadi, T. Nakamura, and R. P. Singh, "Inverse analysis for transient moisture diffusion through fiber-reinforced composites," *Acta Materialia*, vol. 51, no. 1, pp. 177 – 193, 2003. [Online]. Available: http://www.sciencedirect.com/science/article/pii/S1359645402003907

[242] S. Roy, W. Xu, S. Patel, and S. Case, "Modeling of moisture diffusion in the presence of bi-axial damage in polymer matrix composite laminates,"

International Journal of Solids and Structures, vol. 38, no. 42-43, pp. 7627–7641, 2001.

[243] W. Loh, A. Crocombe, M. Abdel Wahab, and I. Ashcroft, "Modelling interfacial degradation using interfacial rupture elements," *Journal of Adhesion*, vol. 79, no. 12, pp. 1135–1160, 2003.

[244] S. Lee, H. Chiang, C. Lin, H. Huang, and D. Dong, "Finite element analysis of thermo-debonding mechanism in dental composites," *Biomaterials*, vol. 21, no. 13, pp. 1315–1326, 2000.

[245] D. Bond, "Moisture diffusion in a fiber-reinforced composite: Part i-non-fickian transport and the effect of fiber spatial distribution," *Journal of Composite Materials*, vol. 39, no. 23, p. 2113, 2005.

[246] K. Kondo and T. Taki, "Moisture diffusivity of unidirectional composites," *Journal of Composite Materials*, vol. 16, no. 2, p. 82, 1982.

[247] X. Chen and T. Papathanasiou, "Interface stress distributions in transversely loaded continuous fiber composites: parallel computation in multi-fiber rves using the boundary element method," *Composites Science and Technology*, vol. 64, no. 9, pp. 1101–1114, 2004.

[248] Y. Huang, K. Jin, and S. Ha, "Effects of fiber arrangement on mechanical behavior of unidirectional composites," *Journal of Composite Materials*, vol. 42, no. 18, p. 1851, 2008.

[249] R. Pyrz and B. Bochenek, "Topological disorder of microstructure and its relation to the stress field," *International Journal of Solids and Structures*, vol. 35, no. 19, pp. 2413–2427, 1998.

[250] S. Torquato, "Nearest-neighbor statistics for packings of hard spheres and disks," *Physical Review E*, vol. 51, no. 4, pp. 3170–3182, 1995.

[251] I. Sevostianov and V. Kushch, "Effect of pore distribution on the statistics of peak stress and overall properties of porous material," *International Journal of Solids and Structures*, vol. 46, no. 25-26, pp. 4419–4429, 2009.

[252] V. Kushch, S. Shmegera, and L. Mishnaevsky Jr, "Statistics of microstructure, peak stress and interface damage in fiber reinforced composites."

[253] S. Yoon, C. Jang, and B. Han, "Nonlinear stress modeling scheme to analyze semiconductor packages subjected to combined thermal and hygroscopic loading," *Journal of Electronic Packaging*, vol. 130, p. 024502, 2008.

[254] C. Wu and W. Xu, "Atomistic simulation study of absorbed water influence on structure and properties of crosslinked epoxy resin," *Polymer*, vol. 48, no. 18, pp. 5440–5448, 2007, cited By (since 1996): 7 Export Date: 24 December 2009 Source: Scopus.

[255] B. De Neve and M. Shanahan, "Physical and chemical effects in an epoxy resin exposed to water vapour," *The Journal of Adhesion*, vol. 49, no. 3, pp. 165–176, 1995.

[256] B. De'Nve and M. E. R. Shanahan, "Water absorption by an epoxy resin and its effect on the mechanical properties and infra-red spectra," *Polymer*, vol. 34, no. 24, pp. 5099–5105, 1993.

[257] T. Clancy, S. Frankland, J. Hinkley, and T. Gates, "Molecular modeling for calculation of mechanical properties of epoxies with moisture ingress," *Polymer*, vol. 50, no. 12, pp. 2736–2742, 2009.

[258] H. Zhang, M. Ericson, J. Varna, and L. Berglund, "Transverse single-fibre test for interfacial debonding in composites: 1. experimental observations," *Composites Part A*, vol. 28, no. 4, pp. 309–315, 1997.

[259] L. Shen and Z. Chen, "Critical review of the impact of tortuosity on diffusion," *Chemical engineering science*, vol. 62, no. 14, pp. 3748–3755, 2007.

[260] M. Carrion-Vazquez, A. Oberhauser, S. Fowler, P. Marszalek, S. Broedel, J. Clarke, and J. Fernandez, "Mechanical and chemical unfolding of a single protein: a comparison," *Proceedings of the National Academy of Sciences*, vol. 96, no. 7, p. 3694, 1999.

[261] M. Schlierf and M. Rief, "Single-molecule unfolding force distributions reveal a funnel-shaped energy landscape," *Biophysical journal*, vol. 90, no. 4, pp. L33–L35, 2006.

[262] E. Walton, S. Lee, and K. Van Vliet, "Extending bell's model: how force transducer stiffness alters measured unbinding forces and kinetics of molecular complexes," *Biophysical Journal*, vol. 94, no. 7, pp. 2621–2630, 2008.

[263] R. Merkel, P. Nassoy, A. Leung, K. Ritchie, and E. Evans, "Energy landscapes of receptorligand bonds explored with dynamic force spectroscopy," *Nature*, vol. 397, no. 6714, pp. 50–53, 1999.

[264] A. Maitra and G. Arya, "Model accounting for the effects of pulling-device stiffness in the analyses of single-molecule force measurements," *Physical Review Letters*, vol. 104, no. 10, p. 108301, 2010.

[265] M. Rief, M. Gautel, F. Oesterhelt, J. Fernandez, and H. Gaub, "Reversible unfolding of individual titin immunoglobulin domains by afm," *Science*, vol. 276, no. 5315, p. 1109, 1997.

[266] T. Fisher, A. Oberhauser, M. Carrion-Vazquez, P. Marszalek, and J. Fernandez, "The study of protein mechanics with the atomic force microscope," *Trends in Biochemical Sciences*, vol. 24, pp. 379–384, 1999.

[267] Z. Tshiprut, J. Klafter, and M. Urbakh, "Single-molecule pulling experiments: when the stiffness of the pulling device matters," *Biophysical journal*, vol. 95, no. 6, pp. L42–L44, 2008.

[268] A. Maitra and G. Arya, "Infuence of pulling handles and device stifness in single molecule force spectroscopy," *Physical Chemistry Chemical Physics*, vol. 13, pp. 1836–1842, 2010.

Appendix A

Single Crosslink Simulations

A.1   Introduction

Single molecule pulling experiments reveals interesting dynamics in the mechanical behavior of the proteins [166, 260, 261]. It is observed that the critical force at which proteins break, referred to as the rupture force F_r, shows a dependency on the applied velocity $\bar{v}$, also referred to as the pulling velocity [166]. This behavior is adequately captured by the Bell expression (Eq. A.1) [262]. The Bell model for crosslink dissociation is by nature a deterministic one in that the rupture force F_r is simply a logarithmic function of the applied velocity. However, it can be endowed with a stochastic feature by using appropriate probabilistic criterion [260, 261]. A Bell model equipped with stochastic crosslink scission criterion is capable of capturing the experimentally observed probabilistic nature of the phenomenon and resulting scatter.

A.2 Bell Model

Bell model gives the crosslink dissociation rate k

$$k = k_0 e^{\frac{Fa}{k_B T}} \tag{A.1}$$

where k_0 is the crosslink dissociation rate at zero force, a is the interaction distance, k_B is the Boltzmann constant, T is the temperature.

The local velocity v experienced by a crosslink can be written in terms of the dissociation rate k as

$$v = ka \tag{A.2}$$

Using Eq. A.2 in Eq. A.1, we obtain

$$v = v_0 e^{\frac{Fa}{k_B T}} \tag{A.3}$$

Inverting Eq. A.3, the rupture force F_r is given by

$$F_r = \frac{k_B T}{a} \frac{v}{v_0} \tag{A.4}$$

As mentioned in introduction, Eq. A.4 shows the logarithmic dependence of F_r on the local velocity. Note that the effects of the crosslink stiffness and/or the stiffness of the loading arrangement are implicitly embedded in the fact that v is the local velocity (Fig. A.2). However, a simplifying assumption is sometimes made in that $v = \bar{v}$. Such an assumption implies that the crosslink stiffness is much lower than the filaments it connects and the loading system. While,

this simplifies the result, it has been shown that F_r is substantially modulated by the stiffness of the loading system [262–267]. Recently, Maitra and Arya [268]have derived the governing kinetics of a single ABP extension accounting for the stiffnesses of the loading system and attached filament, but the solution requires a numerical treatment.

In comparison to aforementioned analytical and semi-analytical approaches, we have implemented Eq. A.1 in ABAQUS®using its user subroutine capabilities. What Eq. A.1 tells us is the rate at which crosslink can break under a given force. Therefore, it is imperative to ask: is the local rate supplied to a crosslink sufficient to break it? In other words, we must prescribe a criterion within the FE procedure that allows making a decision on the crosslink scission. To this end, we adopt the following steps:

- At time t, calculate the force F on the crosslink corresponding to the local deformation δ via a linear Hookean assumption $F = K_x\delta$, where K_x is the (known) crosslink stiffness.

- Calculate the crosslink dissociation rate k for this force using using Eq. A.1 .

- Compare k with the normalized local rate $\hat{k} = \dot{\varepsilon}/\varepsilon$, where $\dot{\varepsilon}$ is the local strain and ε_c is a critical strain (ref section A.3). If $k \geq \hat{k}$ then the crosslink breaks.

A.3   Breaking Criterion

This section briefly discusses a breaking criterion which is independent of the time increment chosen in the FE simulations. We have,

$$\hat{k} = \frac{\dot{\varepsilon}}{\varepsilon} = \frac{v/l_0}{\delta/l_0} \tag{A.5}$$

where $v = \Delta\delta/\Delta t$ is the local instantaneous velocity, δ is the local displacement, $\Delta\delta$ is the incremental displacement in Δt and l_0 is the initial length of the crosslink. Therefore,

$$\hat{k} = \frac{\dot{\varepsilon}}{\varepsilon} = \frac{\delta/\Delta t}{\delta} \tag{A.6}$$

Using a Hookean decription for the crosslink $F = K_x\delta$, we obtain

$$\hat{k} = \frac{(\delta/\Delta t)K_x}{F} \tag{A.7}$$

In the above expression $\hat{k}$ continuously changes with time because of F. Specifically, it monotonically decreases with increasing time as F increases with increasing δ. On the other hand, $k_{off} = k_0 e^{\frac{Fa}{k_B T}}$ increases with time. It can be systematically shown that in a deterministic single crosslink simulation, the force F at which $k_{off} \geq \hat{k}$ is satisfied, is lower for lower K_x.
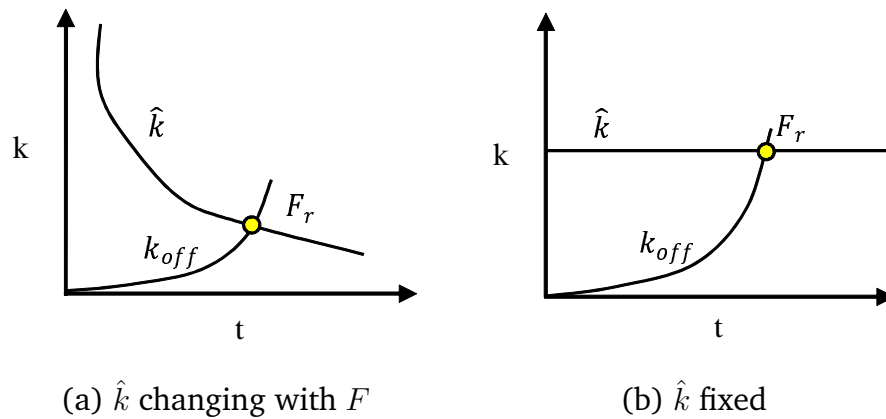

(a) $\hat{k}$ changing with F (b) $\hat{k}$ fixed

Figure A.1: Variation of $\hat{k}$ and k_{off} for varying and fixed $\hat{k}$.

The question arises: should $\hat{k}$ (a) change with time (Fig. A.1a) or (b) remain constant (Fig. A.1b)? Prima facie, it appears difficult to decide what would constitute a right choice. If we choose case a, we need to ensure that we choose appropriate K_x in order to match the experiments (see Fig. A.5). It turns out that a high value of K_x, even larger than the filament axial stiffness K_f (Fig. A.2), which creates an awkward situation. Instead, let us consider a different definition of $\hat{k}$,

$$\hat{k} = \frac{\dot{\varepsilon}}{\varepsilon_c} \tag{A.8}$$

where $\varepsilon_c = a/l_0$ is a constant strain (independent of force, perhaps a material parameter), with a= interaction distance (same as in $k_{off}, \sim 0.1-1 \; nm$ typically) and l_0 is the initial crosslink length ($\sim 10-200 \; nm$ typically).

The above expression reads as follows: It takes time $\hat{t} = 1/\hat{k}$ to reach a critical strain ε_c at a local strain rate $\dot{\varepsilon}$. If this time is smaller than $t_{life} = 1/k_{off}$, then a crosslink breaks. In other words, if $k_{off} \geq \hat{k}$ then the crosslink breaks. The only difference being that now $\hat{k}$ does not change with force. This liberates the solution from the choice of K_x, and allows predicting a correct rupture force provided we appropriately tune ε_c.

A.4   Stochastic Breaking Process

While Eq. A.1 gives a deterministic dissociation rate, the element of probability is incorporated through a KMC algorithm as follows: the probability distribution function corresponding to k is [167],

$$p(t) = ke^{-kt} \tag{A.9}$$

Then, the time corresponding this probability distribution is obtained as

$$t = -\frac{1}{k} ln(r) \tag{A.10}$$

where $0 < r < 1$ is a uniformly distributed random number. Finally, we rewrite Eq. A.10 in terms of a rate, i.e. $k = 1/t$. Then, the crosslink is ready to break if $k \geq \hat{k}$.
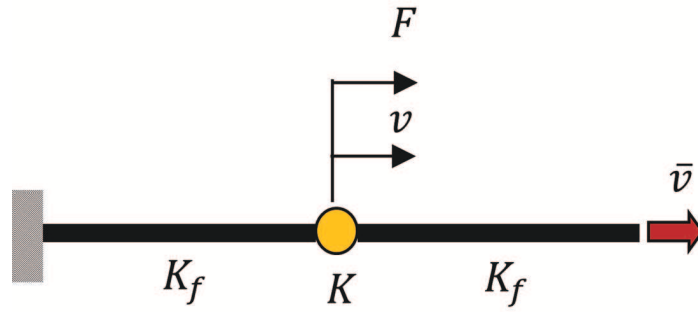
A.5 Simulation Results

Figure A.2: Single crosslink scission simulation setup.

Figure A.2 shows the schematic of a crosslink (yellow circle) with a stiffness K_x connecting two filaments each with stiffness K_f .The same setup is used to determine F_r as a function of $\bar{v}$ using (a) analytical model (Eq. A.4), (b) deterministic FE simulation, and (c) stochastic FE simulation. In the analytical model, we assume that $v = \bar{v}$ for simplicity. As this equation does not account for the K_x and K_f explicitly, in FE simulations too we tune K_x/K_f so that F_r matches with Eq. A.3 for one $\bar{v}$, but use the same stiffness for the other cases. In doing so, we set K_f to be sufficiently larger than K_x so that the crosslink experiences nearly the same local velocity as the applied one (that is the filament is nearly rigid

in comparison with the crosslink). Note that this assumption adopted in the FE simulations (both, deterministic and stochastic) is not a limitation of the method, but only a simplification for a meaningful comparison with the analytical model. In a general FE scenario, the effect of the filament stiffness and loading system stiffness will be captured through the local velocity experienced by the crosslink (spring nodes).

Figure A.3 shows the results of the deterministic and stochastic FE simulations along with the analytical result. For the stochastic simulations, the symbols represent the average value of five simulations for each loading rate and the error bars indicate their standard deviations. The values obtained from the deterministic FE simulations are slightly lower than those obtained by the analytical equation (Eq. A.3) due to the assumed value of K_x used in the former. Importantly, in both deterministic and stochastic FE simulations, the trends match very well with the analytical prediction. Further, the stochastic approach shows a scatter that is qualitatively akin to the experimentally observed variation. Moreover, the results are independent of the time increment chosen. This substantiates the validity of the present algorithm, which can now be used for different combinations of K_x/K_f.

A.6 A Note on Crosslink Constitutive Response

As mentioned earlier, here the crosslinks are assumed to possess a linear $F - \delta$ relation through stiffness K_x that is assumed to be independent of the applied rate. As shown in Fig. A.4, it is natural then that δ_r must increase with increasing F_r for increasing rate of loading[1].

---

[1] In an alternative scenario, δ_r may be fixed. Then, to reach a higher force with higher rate, the stiffness K should be rate-dependent. But, this rate-dependence of the crosslink would be a
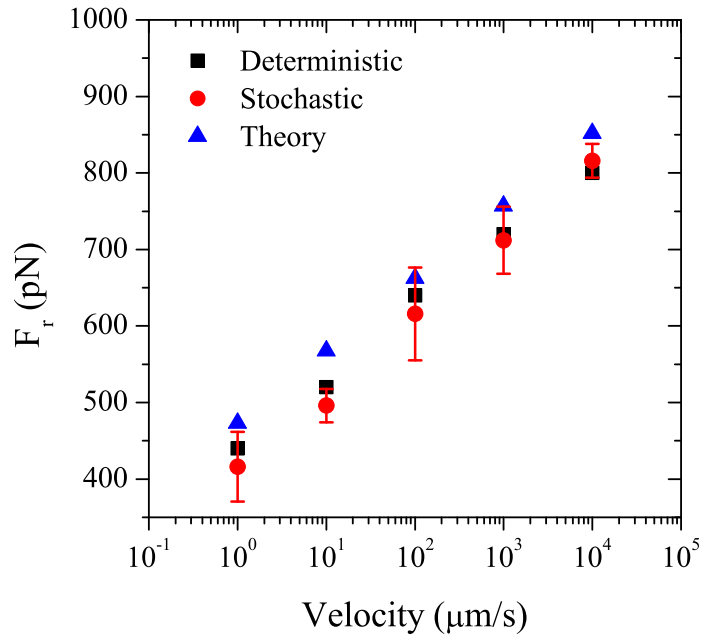
Figure A.3: Predicted dependence of the rupture force F_r on the pulling velocity.

It is commonly observed that compliant crosslinkers like Filamin first unfold (Fig. A.5), which requires very small force (stiffness), but beyond a critical extension δ_c at which it is fully stretched the force (stiffness) increases dramatically before dissociation. Such a behavior may be modeled using a nonlinear (or a bi-linear) $F - \delta$ relationship (Fig. A.5) [81]. Note that if this type of relationship is adopted the dissociation rate k must be calculated only beyond the point where nonlinearity initiates (i.e., δ_c), because the initial stage is related to unfolding rather than unbinding of the crosslink. Indeed, in our current simulations we choose K_x that corresponds to the stiffening regime (Fig. A.5) and the maximum displacement $\delta_{max} \sim a$ in calculating k (Eq. A.1).

constitutive prescription unlike the present case where the rate effect appears from the scission criterion.
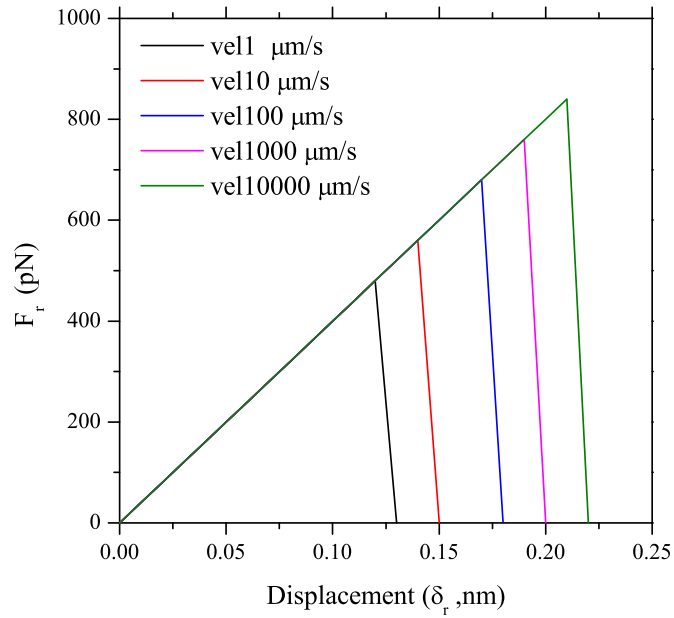
Figure A.4: $F - \delta$ relation obtained from the deterministic FE simulations. F_r and δ_r increase with increasing pulling velocity.
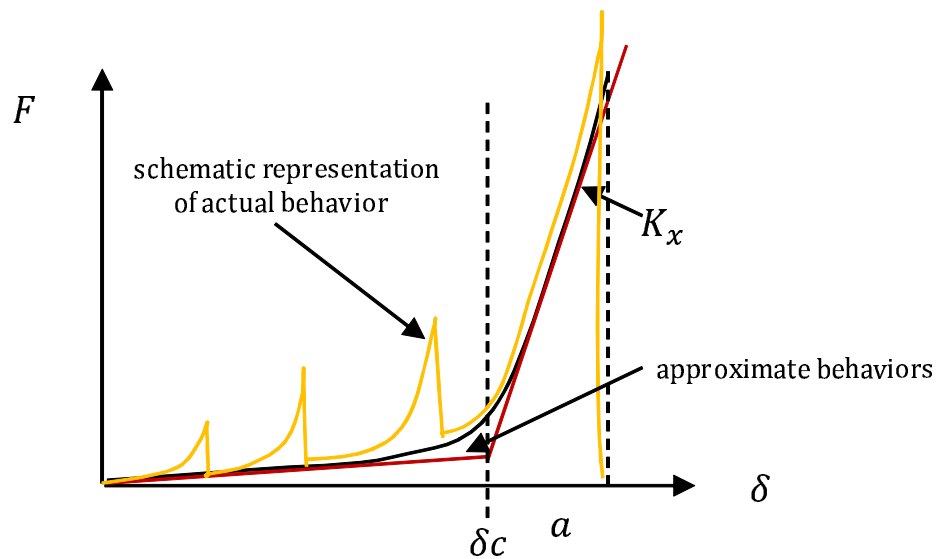

Figure A.5: Schematic of nonlinear constitutive response of Filamin.

Appendix B

# Probabilistic Damage Model for Polymers

B.1   Introduction

Polymers like elastomers, thermoplastics and thermosets undergo degradation of its properties when exposed to moisture, oxygen, ozone etc. Irreversible plasticization takes place in epoxies above glass transition temperatures when they are exposed to moisture, which is reflected in mechanical property as loss of elastic modulus [214]. One of the dominant mechanisms by which it takes place is due to the breaking of bonds in polymer chains, which we refer to as chain scission.

B.2   The Model

Based on the work of Xiao and Shanahan, we developed a model which accounts for the damage caused by moisture in epoxies assuming chain scission [202,

211–214]. The observation is that the damage is nearly reversible in the glassy regime where as irreversible in the rubbery regimes upon desorption. Diffusion is assumed to follow the Fick's Law and chain scission is proportional to the local concentration of diffusant. The diffused water reacts irreversibly with the polymer. This reaction is schematically written as

$$\sim A - B + H_2O \rightarrow \sim A - OH + \sim B - H \tag{B.1}$$
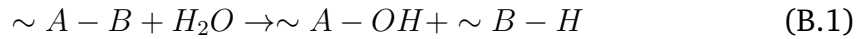
where A and B represents the main groups in epoxy chains. A fraction of the water diffusing into the polymer is residing in the free volume and the rest resides among the polymer chains and can react with it. This fraction is called bound water. Number moles of reacted water n_2 is directly proportional to the number of moles of the mobile water per unit volume of the polymer n_1

$$n_2 = rn_1 \ , \hat{r} \leq 1 \tag{B.2}$$

Diffusion is assumed to follow Fick's Law and is given by

$$D\frac{\partial^2 n_1}{\partial x^2} = \frac{\partial n_1}{\partial t} + \frac{\partial n_2}{\partial t} \tag{B.3}$$

Long term weight gain of the polymer without considering the leaching is given by

$$M_\infty = \frac{(n_{1\infty} + n_{2\infty})m_w}{\rho} \tag{B.4}$$

For a dry slab of thickness $\bar{d}$ and infinite dimension in other two orthogonal dimensions exposed to moisture at both sides, expression for *M(t)* , ignoring the leaching is given by

$$M(t) \approx 4\frac{M_\infty}{\bar{d}}\sqrt{\frac{D't}{\pi}} \quad \text{where } t \leq \frac{0.05\bar{d}^2}{D'} \tag{B.5}$$

$$M(t) \approx M_\infty \left[1 - \frac{8}{\pi^2}\exp\left(-\frac{D'\pi^2 t}{\bar{d}^2}\right) \right] \quad \text{where } t \leq \frac{0.05\bar{d}^2}{D'} \tag{B.6}$$

where $D' = D/(1 + \hat{r})$. Using the theory of rubber elasticity, the total number of inter cross link chains in unit volume of the polymer is given by

$$N^0 = \frac{\rho}{M_c^0} \tag{B.7}$$

where M_c^0 is the molecular mass between the chains in the undamaged state. When a chain is cut M times, it produces $M - 1$ leachable segments. Based on probability, total number of leachable segments per unit volume at a time t is given by

$$J(t) \approx \frac{N^0}{2}\left(-\frac{n_2(t)}{N^0}\right)^2 = \frac{[n_2(t)]^2}{2N^0} \tag{B.8}$$

If S mol of inter-crosslink chains are cut once or more than once, the remaining number of inter crosslink chains will be

$$\bar{N}(t) = N^0 - ZS \tag{B.9}$$

Where Z is the total number of chains lost when one chain is cut. Depending on the network architecture, when one when is cut, it will reduce the total number of effective chains by one or more than one. The numbers of moles of inter-crosslink chains having been cut per unit volume at time t is

$$S = N^0 \left[1 - \exp\left(\frac{-n_2(t)}{N^0}\right)\right]$$

(B.10)

The average number of moles of inter-crosslink chain at time t is,

$$N(t) = N^0 \left[Z \exp\left(\frac{-n_2(t)}{N^0} - (Z-1)\right)\right]$$

(B.11)

The damage is quantified using a parameter ϕ_m gives by

$$\phi_m(c) = \frac{N_0 - N}{N_0}$$

(B.12)

Using Eq. B.11 in Eq. B.13 gives the expression of damage in terms of moisture concentration as

$$\phi_m(c) = -\left[Z \exp\left(-\frac{\alpha c(t)}{N^0}\right) - Z\right]$$

(B.13)

The value of ϕ_m ranges from 0 which corresponds to the pristine material and 1 which correspond to fully damaged material. The parameter α controls the severity of degradation. It depends on the susceptibility of the polymer to moisture degradation. Its value should be < 1. If the polymer is highly sensitive to moisture, its value will be ≈ 1. At this value of α, the polymer degrades almost completely.

B.3 Results

The model is implemented in a FE software package ABAQUS$^{\circledR}$ using UMAT subroutines. A rectangular thin film geometry with moisture boundary conditions is considered. In the current analysis, only moisture boundary conditions are prescribed without any mechanical loads. Simulation is done till the moisture equilibrates in the domain and the value of the damage parameter is quantified. We consider two sets of analysis, one in which α is kept constant and Z is varied and in another set, Z is kept constant and α is varied.

Figure B.1 shows the results of cases with fixed α and varying Z. With the increasing Z, the intensity of damage increases as more chains are lost when a single crosslink breaks. The sensitivity of α in the response is checked by keeping Z fixed and varying α (Fig. B.2). It shows a similar response as in the case of varying Z. These two parameters together determine the intensity of degradation which may be inherently linked to the structure of the material (Z) and its propensity to react with moisture (α). Further investigations are to be done to establish the validity of the model with a variety of materials.
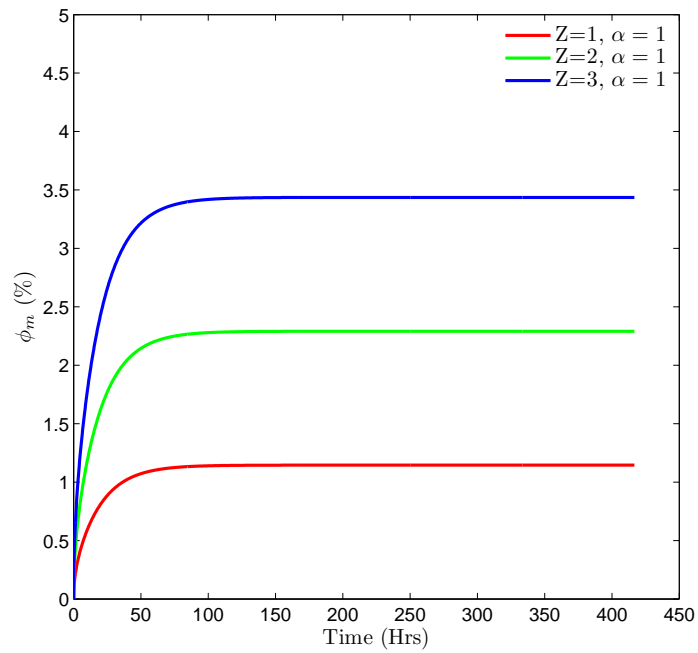
Figure B.1: Moisture induced chain scission for varying z and fixed α. The chain scission ceases with the moisture saturation at ≈ 100 Hrs. As the damage evel-oution depends on the moisture concentration, damage evolution curves looks similar to moisture evolution.
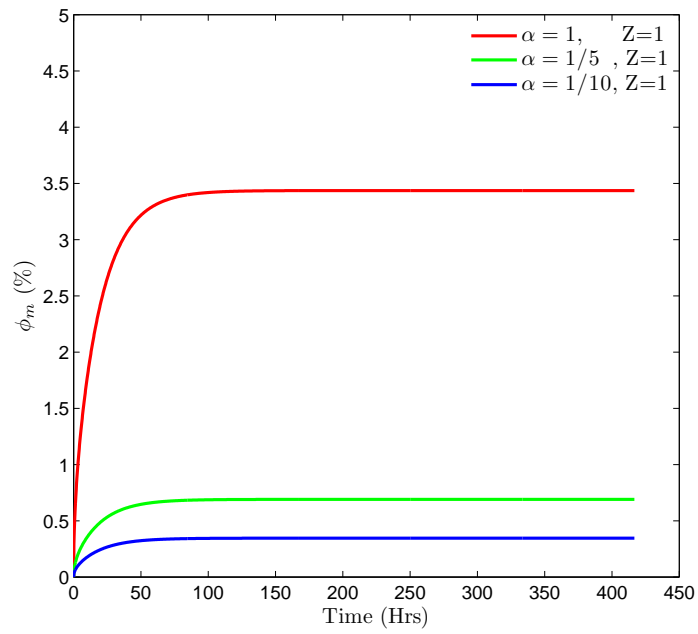
Figure B.2: Moisture induced chain scission for fixed z and varying α. The degradation is very sensitive to the value of α.

Appendix C

Publications

C.1 Journal Papers

1. Abhilash, AS., Joshi, SP., Mukherjee, A. and Mishnaevsky, L., Jr., "Microme-chanics of diffusion induced damage evolution in reinforced polymers", Composites Science and Technology, 71, 333-34, 2010.

2. Abhilash, AS., Joshi, SP. and Prashant K. Purohit., "Stochastic rate-dependent elasticity and failure of soft fibrous networks", Soft Matter, 2012, 8, 7004-7016.

3. Abhilash, AS., Joshi, SP. and Prashant K. Purohit., "Characterization of me-chanical response of filamentous networks", In preparation.

4. Abhilash, AS., Joshi, SP. and Prashant K. Purohit., "Response of filamentous networks: Toward a predictive map", In preparation.

C.2 Conference Oral Presentations

1. Abhilash, AS. and Joshi, SP., "Micromechanics of diffusion induced damage evolution in reinforced polymers", ACE-X 2010 Paris, France (July 08-09, 2010).

2. Abhilash, AS., Joshi, SP. and Prashant K. Purohit., "Rate-dependent stochastic response of discrete filament networks", ISCM-III, CSE II, Taipei, Taiwan (5-7 December 2011).

C.3 Poster Presentations

1. Abhilash, AS., Joshi, SP. and Prashant K. Purohit., "Stochastic modeling of discrete filament networks mimicking polymeric microstructures", ICMAT 2011, Singapore (26 June to 1 July, 2011).

2. Abhilash, AS., Joshi, SP. and Prashant K. Purohit., "Stochastic failure mechanics of F-actin networks: A computational approach", The 5th Mechanobiology Conference, Singapore (9-11 November 2011).